Stony Brook University

Investigation on Deformation of Olivine

at High Pressure and Low Temperature

A Dissertation Presented

by

Hongbo Long

to

The Graduate School

in Partial fulfillment of the

Requirements

for the Degree of

Doctor of Philosophy

in

Geosciences

Stony Brook University

December 2008

Stony Brook University

The Graduate School

Hongbo Long

We, the dissertation committee for the above candidate for the
Doctor of Philosophy degree, hereby recommend
acceptance of this dissertation.

Donald J. Weidner - Dissertation Advisor
Distinguished Professor, Department of Geosciences

Gilbert N. Hanson – Chairman of Defense
Distinguished Service Professor, Department of Geosciences

Robert C. Liebermann
Distinguished Service Professor, Department of Geosciences

Michael T. Vaughan
Research Associate Professor, Department of Geosciences

Paul Raterron, Professor
CNRS, Université des Sciences et Technologies de Lille, France

This dissertation is accepted by the Graduate School

Lawrence Martin
Dean of the Graduate School

Abstract of the Dissertation

Investigation on Deformation of Olivine at High Pressure and Low Temperature

by

Hongbo Long

Doctor of Philosophy

in

Geosciences

Stony Brook University

2008

Olivine is the dominant mineral in the upper mantle. Several deformation experiments of polycrystalline powdered San Carlos olivine at subduction zone conditions (pressures of 3-5 GPa and temperatures of 25-1100°C) have been performed on a deformation DIA (D-DIA) apparatus, SAM85, at X17B2, National Synchrotron Light Source (NSLS). Enstatite ($MgSiO_3$) (3-5% total quality of sample) is used as buffer to control the activity of silica. Ni foil is used in some experiments to buffer the oxygen fugacity. Water content is confirmed by IR spectra of the recovered samples. The Total (plastic and elastic) strains (macroscopic) are derived from the direct measurements of the images taken by X-ray radiograph technique. Differential stresses are measured at constant strain rate ($\sim 10^{-5}$-$10^{-7} s^{-1}$) and at different pressures and temperatures with synchrotron x-ray. It can be concluded that in the regime of 25-400°C, there is a small

increase stress at steady state along with the temperature drop; in the regime of 400°C to transition temperature, the differential stress at steady state is a constant (~3 GPa) and is relatively insensitive to the changes of temperature and strain rate; however, it drastically decreases to about 1 GPa and becomes temperature-dependent above the transition temperature and thereafter. The transition temperature is between 700°C and 900°C. No significant difference of differential stress and strain is observed between the samples with/without Ni foil buffered below 700°C. Two regimes with different deformation mechanisms for olivine have been determined in this study: regime of low temperature plasticity at low temperature (below transition temperature) and regime of power law creep at high (above the transition temperature). The annealing process can obviously shift up the transition temperature between regimes of temperature insensitive and sensitive. Grain size affects the rheological properties of olivine in the low temperature dislocation regime. Existence of water obviously decreases the transition temperature of the boundary between the regimes of low temperature plasticity and paw-law creep. (100)[001] and {hk0}[001] (h>k) are the predominant active slip systems in the deformation at low temperature. The instability of olivine could be the mechanism for the deep-focus earthquake happened in the subduction zone slab.

Table of Contents

List of Figures

Chapter Two

Chapter Three

Chapter Four

List of Tables

Chapter Two

Acknowledgements

I would like to express my sincere gratitude to my advisor, Donald J Weidner, for his guidance throughout this project and his help in the preparation of this dissertation. His enthusiastic advice and encouragement made this dissertation possible.

I would also like to sincerely appreciate Jiuhua Chen for his kindly showing me hand by hand how to set up the high pressure experiment, also for his helpful discussion and suggestion.

Special thanks to Liping Wang, Li Li, Helene Couvy for their kindness and assistance during my experiments, and their helpful discussion.

I also wish to thank Kenneth Baldwin for his heating-control program which I used in my experiments. I thank Zhenxian Liu for his helping my IR analysis. Special thank Tony Yu for his help during the overnight experiments.

Special thank Hanna Nekvasil for kindly letting me prepare the thin sections in her lab.

I thank Gilbert N. Hanson, Robert C. Liebermann, Michael Vaughan and Paul Raterron for serving in my dissertation committee.

I gratefully acknowledge my family—my two brothers, my mother, and my father who is now in heaven. Without their encouragement and support, I would not have kept my focus on this study.

I especially appreciate my beloved, Haiyan. This work would be an impossible thing without her love and support every day and all the time.

Chapter 1

Introduction

1.1 Background

Olivine (α-$(Mg,Fe)_2SiO_4$) is the major constituent of the upper mantle. In subduction zone, where the earthquakes happen, the rheology of the slab is mainly controlled by that of olivine at low temperatures. Several different mechanisms for deep focus earthquakes have been suggested, which include olivine instability (Bridgman, 1936; Orowan, 1960; Post, 1977; Ogawa, 1987; Hobbs and Ord, 1988; Kao and Chen, 1995), shear/fault-induced melting (Griggs, 1954, 1972; Griggs and Handin, 1960; Griggs and Baker, 1969; Zhang et al., 2004), phase transformation (Bridgman, 1945; Benioff, 1963; Meade and Jeanloz, 1989), dehydration of hydrous specimens (Raleigh and Paterson, 1965; Meade and Jeanloz, 1991; Peacock, 2001; Dobson et al., 2002; Jung et al., 2004), and olivine metastability-induced anti-crack (Green and Houston, 1995). Since the low temperature of the "cold" slab, which can be as low as 600°C in the transition zone, it has been argued that olivine may still exist there and thus its instability may be the possible mechanism for the deep-focus earthquakes.

Despite of its importance, rheological studies on olivine at high pressure (>3 GPa) and low temperature (subduction zone condition) is limited due to the experimental technical difficulty. Development of multi-anvil apparatus made a great progress in doing deformation experiment at high pressure and high temperature (Durham and Rubie, 1998). In order to carry out deformation experiments at high pressure and temperature, the Deformation DIA (D-DIA) apparatus has been recently developed (Durham et al. 2002; Wang et al. 2003). One of the characteristics of the D-DIA is that it can keep a constant strain rate at pressure up to over 10 GPa, which allows performing the steady state deformation experiment at high pressure. It also has an advantage in fitting the *in situ* synchrotron X-ray measurement for stress and strain (Chen et al. 2004; Li et al. 2003; Li et al. 2004a and b; Li et al. 2006a and b; Uchida et al. 2004).

Recently, *in situ* X-ray measurement on stress and strain on the large volume multi-anvil press (e.g. Weidner *et al*., 1992; Li *et al*., 2003; Li *et al*., 2004; Chen *et al*., 2004) has also made a significant progress in the deformation experiments. A method has been developed to measure microscopic elastic stress and strain in powder sample from the broadening of the deformed mineral's X-ray diffraction peaks (Weidner et al. 1992a and b; Weidner et al. 1994; Weidner; 1998; Weidner et al. 1998). However, it is not a direct extension of traditional strain and stress measurement. The assumption of constant total microscopic strain (sum of both elastic and plastic strain) yield additional uncertainties to construct a flow law from the experimental data (Chen et al. 2004). So a new technique has been developed to carry out the deformation experiment on a large volume multi-anvil apparatus with *in situ* X-ray measurements (Chen et al. 2004; Li et al.,

2004a and b). By using this method, the macroscopic plastic strain is measured by a direct sample length imaging system. The microscopic elastic strain is measured by the multiple X-ray diffraction pattern of the sample along different stress axis. Then the differential stress is derived according to Hook Law: $\sigma_{ij} = c_{ijkl}\varepsilon_{kl}$, where σ is stress, ε is strain, and c is the elastic constants tensor.

1.2 Review of Previous Research

For decades numerous literatures related to olivine rheology have been published mainly in the field of low pressure and high temperature, including the dependences of temperature, pressure, activity of constituent oxide phase, oxygen fugacity, water fugacity and grain size.

Temperature

The effect of temperature plays an important role in the deformation of olivine. According to Frost and Ashby (1982), the deformation of olivine can be divided into four regimes: low temperature plasticity or dislocation glide controlled by a lattice resistance, low temperature plasticity or dislocation glide controlled by discrete obstacles, high temperature plasticity or power-law creep, and diffusional flow. The rheological properties of olivine are quite different in one regime comparing to the others. Furthermore, dynamic recrystallization, which results in removing or drastically changing the dislocation substructure and allowing a period of primary creep, may accompany at

high temperature when temperature/melting temperature is about 0.6 or more. The dynamic recrystallization of olivine can occur at about 1200°C at mantle condition (Li et al. 2003). At low temperature, the differential stress in olivine can be very high. Evans and Geotze (1979) reported that it can be up to 5 GPa at about 100°C. Several literatures reported related study on olivine rheology at high pressures and room temperature (Meade and Jeandoz, 1990; Chai *et al*., 1998). The relaxation experiments' results (Raterron *et al*., 2004) demonstrate a rapid decrease of differential stress from 3 GPa to 1 Gpa at 450-500°C. Li et al. (2004b) report a dramatic drop of differential stress from 1.7 GPa to about 0.6 GPa at hydrostatic pressure of 8 GPa and about 820°C. Chen et al. (2004) report a decrease of differential stress with the increase of temperature in an *in situ* measurement of deforming fayalite (Fe_2SiO_4). Using D-DIA apparatus, Li et al. (2006b) report at steady state the differential stress values of 2.4 GPa for fine olivine sample at 6.5 GPa and 900°C, and 2.0 GPa for coarse sample at 3.5 GPa, 800°C and at 6.5 GPa, 900°C. Up to now the study on olivine at steady state at high pressure is still limited, especially for high pressure and low temperature.

Pressure

Pressure dependence of the olivine deformation is still considered as somewhat a controversial and ambiguous issue up to now by some workers. The activation volume of olivine dislocation creep at high temperature is from 13-27 cm^3mol^{-1} at low pressure (<0.3 GPa) (Ross et al. 1979; Borch and Green, 1987; Green and Borch, 1987; Karato and Wu, 1993; Kohlstedt and Wang, 2001), and 11 cm^3mol^{-1} at 0.5 GPa (Kohlstedt et al.

1980). Karato and Jung (2003) give values of 14 cm^3mol^{-1} for "dry" condition and 24 cm^3mol^{-1} for "wet" condition at 1-2 GPa and 1300°C. However, at high pressure it is suggested to be small. Karato et al. (1993) give a value of 6 cm^3mol^{-1} at up to 10 GPa and 1500°C from the recovered sample run on a multi-anvil apparatus. Bejina et al. (1997) give a zero value at 9 GPa and 1590°C from the sample run on a uniaxial split-sphere apparatus. Karato and Rubie (1997) also give a value of 14 cm^3mol^{-1} at 15 GPa and up to 1600°C. Using synchrotron *in situ* X-ray diffraction measurement on a multi-anvil apparatus and TEM investigation of recovered experiment sample, Li et al. (2004) conclude that the activation volume of San Carlos olivine is less than 10 cm^3mol^{-1} at high pressure and high temperature. Li et al. (2006) also report that little or no dependence of the dislocation creep flow with pressure is shown and give an activation volume value of zero for San Carlos olivine at up to 9.6 GPa and up to 1200°C on a D-DIA apparatus along with *in situ* X-ray measurement. Based on the review above, one may conclude that the activation volume of olivine is significantly smaller at high pressure than that at low pressure by several tenths. Just as suggested, the activation volume of olivine may decrease while the pressure increases (Borch and Green, 1987; Green and Borch, 1987). In fact a recent study shows that the active slip system of olivine transforms from [100] direction to [001] direction along with the increase of the pressure, and suggests that such kind of transition in olivine may be responsible for the difference of the big V* value at low pressure and the small value of V* at high pressure (Raterron et al., 2007). Nevertheless, an increase of water or hydrogen fugacity in olivine also drastically increases the activation volume.

Activity of Constituent Oxide Phase

The effects of activity of constituent oxide phase in olivine can be described as the effects of activities of silica and metal oxides (e.g. activities of MgO and FeO, or the Mg-Fe partition in the olivine). Difference of creep properties between pure forsterite and iron-bearing olivine has been investigated (Durham and Geotze, 1977). Bai et al. (1991) report wide variations in activation energy and oxygen fugacity dependence in the systematic experiments on olivine buffered against orthopyroxene or magnesiowustite at low pressure (0.1 MPa) and high temperature. Bai and Kohlstedt (1992) further report that along [110]c orientation of San Carlos olivine, the creep behavior of unbuffered sample is substantially different from that of the Opx buffered samples while for the samples compressed along [101]c or [011]c, the results are similar in both buffered and unbuffered cases. Opx activity dependence is proposed to interpret their results. Experimental study at low pressure (15-175 Mpa) and high temperature (1200-1500°C) shows that moderate differences in forsterite content (Fo89-Fo93) and in the concentrations of minor elements, such as Ni, Cr, and Mn do not have significant effect on the creep behavior of olivine (Jin et al. 1994). Chen et al. (2004) proposed a weakening mechanism by increasing iron partitioning in olivine structure with comparison of activation energy and Peierls stress of fayalite with those of San Carlos olivine.

Oxygen Fugacity

Influence of oxygen fugacity on olivine deformation has been investigated at high temperature by many researchers (e.g. Kohlstedt and Hornack, 1981; Poumellec and Jaoul, 1984; Bai et al. 1991; Bai and Kohlstedt, 1992a, 1992b). Karato and Sato (1982) report that the dislocation annihilation rate decreases with the increase of oxygen partial pressure (P_{O2}), which is controversial with the former reported P_{O2} dependence of creep rate. To simulate the mantle condition, Ni/NiO buffer has been widely accepted to maintain the oxygen fugacity in the deformation experiment (e.g. Karato et al. 1993; Mei and Kohlstedt, 2000a, 2000b).

Water fugacity

Water is the most important volatile in the silicate earth. In the earth mantle, water content may significantly change in different environments (Mei and Kohlstedt, 2000a). The water content in olivine can range from 10 to 2000 H/Si 10^6 (Bell and Rossman, 1992) and the solubility of water in olivine can be up to 20000 H/Si 10^6 (1200ppm) (Kohlstedt et al. 1996). Many related literatures have published on the effect of water fugacity on olivine rheology at low pressure and high temperature, demonstrating significant weakening effect of even a trace amount of water on olivine deformation (Carter and Ave Lallemant, 1970; Post, 1977; Chopra and Paterson, 1981, 1984; Mackwell et al. 1985; Karato et al. 1986). The creep rate of deformed olivine can be up to 5-6 times faster at water fugacity of 0.3 GPa than that at anhydrous condition at similar temperature and differential stress (Mei and Kohlstedt, 2000a, 2000b). Kohlstedt et al. (1995) and Hirth and Kohlstedt (1996) suggest that creep rate increases nearly linearly

with increasing water fugacity. As discussed in pressure dependence paragraph above, water fugacity drastically change the activation volume of olivine at high temperature. Water fugacity also has effect on the dynamic recrystallization of olivine (see the next paragraph for detail). Point defect theory is proposed for the mechanism of water weakening in deforming olivine (Hobbs, 1983, 1984; Mackwell et al. 1985; Karato, 1989).

Grain Size

Effect of grain size on deformation of olivine is also investigated by workers. Based on the experiments at low pressure (0.3 GPa) and high temperature (1300°C), Karato et al. (1986) report two distinct regimes of olivine deformation depending on stress level and grain size: independence of grain size for strain rate at high stress and large grain size, and decreasing strain rate with increasing grain size at low stress and small grain size. Two different deformation mechanisms are further suggested: dislocation creep for the grain size insensitive regime and diffusion creep for the grain size sensitive regime. Dynamic recrystallization grain size of olivine is larger at "wet" condition than that at "dry" condition (Jung and Karato, 2001).

Limitations of previous studies

Although a number of literatures about rheology of olivine have been published, research on the deformation of olivine at high pressure and low temperature is still

limited and need to be explored. Especially, no study of olivine at steady states is yet reported at high pressure and low temperature. *In situ* X-ray measurement combined with D-DIA apparatus is a good tool and help one constrain the rheological properties of olivine and understand the mantle and subduction zone.

1.3 About the Study of this Dissertation

The nature of deformation of olivine in low temperature plasticity regime and the boundary between the regimes of low temperature plasticity and power law creep have been investigated. The objectives of this study are: (1) to determine the yield stress of olivine at different temperatures in the low temperature regime of deformation; (2) to construct a deformation mechanism map of olivine based on the experimental results; and (3) to constrain models of the mechanism of deep focus earthquakes based on the experimental results.

In Chapter Two I present the results of deformation experiments on San Carlos olivine, whose composition is $(Mg_{0.9}Fe_{0.1})_2SiO_4$ and which is believed to present the same Mg:Fe ratio in the earth mantle. On a D-DIA type apparatus, SAM 85, at X17B2, NSLS, Both image and diffraction data of olivine are *in-situ* investigated at high pressure (3-5 GPa) and low temperatures (25-900°C). The strain and differential stress are derived from *the in-situ* measurements. A deformation map is constructed based on the experimental results.

The results of SEM/EBSD study are presented in Chapter Three. The SEM results show that compression and deformation make the grain size of olivine into sub-micron level. The EBSD study demonstrates that the dominant active slip systems of olivine in the low temperature regime are [001](100) and [001]{hk0} (h>k).

The Chapter Four presents the results of study on the shift of transition temperature boundary between regimes of low temperature and high temperature, both annealing and unannealing system are investigated. The effects of grain size and water content are documented. A model of instable olivine for the deep focus earthquakes is established thereafter.

References

Bai, Q., Mackwell, S.J., Kohlstedt, D.L. 1991. High-temperature creep of olivine single crystal, 1. Mechanical results for buffered sample. Journal of Geophysical Research 96(B2): 2441-2463.

Bai, Q., Kohlstedt, D.L. 1992a. High-temperature creep of olivine single crystals, 2. dislocation structures. Tectonophysics 206(1-2): 1-29.

Bai, Q., Kohlstedt, D.L. 1992b. High-temperature creep of olivine single-crystals. 3. Mechanical results for unbuffered sample and creep mechanisms. Philosophical Magazine A-Physics of Condensed Matter Structure Defects and Mechanical Properties 66(6): 1149-1181.

Bejina, F., Raterron, P., Zhang, J.Z., Jaoul, O., Liebermann, R.C. 1997. The Activation volume of silicon diffusion in San Carlos olivine. Geophysical Research Letters 24(21): 2597-2600.

Bell, D. R., Rossman, G.R. 1992. Water in Earth's mantle: The role of nominally anhydrous minerals. Science 255(5050): 1391-1397.

Bell, D. R., Rossman, G.R., Maldener, J., Endisch, D., Rauch, F. 2003. Hydroxide in olivine: A quantitative determination of the absolute amount and calibration of the IR spectrum. Journal of Geophysical Research 108(B2): 2105, doi: 10.1029/2001 JB000679.

Benioff, H. 1963. Source wave forms of three earthquakes. Bulletin of Seismological Society of America 53(5): 893-903.

Borch, R. S., Green, H.W.II 1987. Dependence of greep in olivine on homologous temperature and its implications for flow in the mantle. Nature 330(6146): 345-348.

Bridgman, P. W. 1936. Shearing phenomena at high pressure of possible importance for geology. Journal of Geology 44: 653-669.

Carter, N. C., Ave Lallemant, H.G. 1970. High temperature flow of dunite and peridotite. Geological Society of America Bulletin 81: 2181-2202.

Chai, M., Brown, M., Wang, Y. 1998. Yield strength, slip systems and deformation induced phase transition of San-Carlos olivine up to the transition zone pressure at room temperature. Properties of Earth and Planetary Materials. M. H. Manghnani, Yagi, T., American Geophysical Union. Geophysical Monograph Series 101: 483-493.

Chen, J., Li, L., Weidner, D.J., Vaughan, M.T. 2004. Deformation experiments using synchrontron X-rays: in situ stress and strain measurements at high pressure and temperature. Physics of the Earth and Planetary Interiors 143-144: 347-356.

Chopra, P. N., Paterson, M.S. 1981. The experimental deformation of dunite. Tectonophysics 78: 453-473.

Chopra, P. N., Paterson, M.S. 1984. The role of water in the deformation of dunite. Journal of Geophysical Research 89(NB9): 7861-7876.

Durham, W. B., Goetze, C. 1977. A comparison of creep properties of pure forsterite and iron-bearing olivine. Tectonophysics 40: 15-18.

Durham, W. B., Rubie, D.C. 1998. Can the multianvil apparatus really be used for high-pressure deformation experiments. Properties of Earth and Planetary Materials at High Pressure and Temperature. M. H. Manghnani, Yagi, T., American Geophysical Union. Geophysical Monograph 101: 63-70.

Durham, W. B., Weidner, D.J., Karato, S.-I., Wang, Y. 2002. New developments in deformation experiments at high pressure. Plastic Deformation of Minerals and Rocks, Reviews in Mineralogy and Geochemistry. S.-I. Karato, Wenk, H.R. Chantilly, Virginia, Mineralogy Society of America. 51: 21-50.

Evans, B., Geotze, C. 1979. The temperature variation of hardness of olivine and its implication for polycrystalline yield stress. Journal of Geophysical Research 84(NB10): 5505-5524.

Frost, H. J., Ashby, M.F. 1982. Deformation-Mechanism Maps The Plasticity and Creep of Metals and Ceramics. Oxford, New York, Toronto, Sydney, Paris, Frankfurt, Pergamon Press.

Green, H. W. I., Borch, R.S. 1987. The pressure-dependence of creep. Acta Metallurgica 35(6): 1301-1305.

Green, H. W. I., Houston, H. 1995. The Mechanics of deep earthquakes. Annual Review of Earth and Planetary Sciences 23: 169-213.

Griggs, D. T. 1954. High-pressure phenomena with applications to geophysics. Modern Physics for the Engineer. L. N. Ridenour. New York, McGraw Hill: 272-305.

Griggs, D. T., Handlin, J. 1960. Observations on fracture and a hyphothesis of earthquakes. Rock Deformation. D. T. Griggs, Handlin, J., Memoir of Geological Society of America. 79: 347-373.

Griggs, D. T., Baker, D.W. 1969. The origin of deep-focus earthquakes. Properties of matter under unusual conditions. H. Mark, Fernbach, S. New York /London /Sydney /Toronto, Interscience Publishers 23-42.

Griggs, D. T. 1972. The sinking lithophere and the focal mechanism of deep earthquakes. The Nature of Solid Earth. E. C. Robertson. New York, McGraw Hill: 361-384.

Hirth, G., Kohlstedt, D.L. 1996. Water in the oceanic upper mantle: Implications for rheology, melt extraction and the evolution of the lithosphere. Earth and Planetary Science Letters 144(1-2): 93-108.

Hobbs, B. E. 1983. Constraints on the mechanism of deformation of olivine imposed by defect chemistry. Tectonophysics 92(1-3): 35-69.

Hobbs, B. E. 1984. Point-defect chemistry of minerals under a hydrothermal environment. Journal of Geophysical Research 89(NB6): 4026-4038.

Hobbs, B. E., Ord, A. 1988. Plastic instabilities: implications for the origin of intermediate and deep focus earthquakes. Journal of Geophysical Research 93(B9): 10521-10540.

Jin, Z. M., Bai, Q., Kohlstedt, D.L. 1994. High-temperature creep of olivine crystal from 4 localities. Physics of the Earth and Planetary Interiors 82(1): 55-64.

Jung, H., Karato, S.-I. 2001. The effect of water on dynamically recrystallized grain-size of olivine. Journal of Structural Geology 23(9): 1337-1344.

Kao, H., Chen, W.P. 1995. Transition from interplate slip to double seimic zone along the Kuril-Kamchatka arc. Journal of Geophysical Research 100(B6): 9881-9904.

Karato, S.-I., Sato, H. 1982. Effect of oxygen partial pressure on the dislocation recovery in olivine: a new constraint on creep mechanisms. Physics of the Earth and Planetary Interiors 28(4): 312-319.

Karato, S.-I., Paterson, M.S., FitzGerald, J.D. 1986. Rheology of synthetic olivine aggregates: influence of grain size and water. Journal of Geophysical Research 91(B8): 8151-8176.

Karato, S.-I. 1989. Defect and plastic deformation in olivines. Rheology of Solids and of the Earth. S.-I. Karato, Toriumi, M. New York, Oxford University Press: 176-208.

Karato, S.-I., Rubie, D.C., Yan, H. 1993. Dislocation recovery in olivine under deep upper mantle conditions - implications for creep and diffusion. Journal of Geophysical Research 98(B6): 9761-9768.

Karato, S.-I., Wu, P. 1993. Rheology of the upper mantle: a synthesis. Science 260(5109): 771-778.

Karato, S.-I., Rubie, D.C. 1997. Toward an experimental study of deep mantle rheology: A new multianvil sample assembly for deformation studies under high pressures and temperatures Journal of Geophysical Research 102(B9): 20111-20122.

Karato, S.-I., Jung, H. 2003. Effects of pressure on high-temperature dislocation creep in olivine. Philosophical Magazine 83(3): 401-414.

Kohlstedt, D. L., Nicholas, H.P.K., Hornack, P. 1980. The effect of pressure on the rate of dislocation recovery in olivine. Journal of Geophysical Research 85(NB6): 3122-3130.

Kohlstedt, D. L., Hornack, P. 1981. The effect of oxygen partial pressure on the creep of olivine. Anelasticity in the Earth, Geodynamics Series. F. D. Stacey, Paterson, M,S, Nicolas, A. Washington, D.C., American Geophysical Union. 4: 101-107.

Kohlstedt, D. L., Evan, B., Mackwell, S.J. 1995. Strength of the lithosphere: Constraints imposed by laboratory experiments. Journal of Geophysical Research 100(B9): 17587-17602.

Kohlstedt, D. L., Keppler, H., Rubie, D.C. 1996. Solubility of water in the alpha, beta and gamma phases of (Mg,Fe)2SiO4. Contributions to Mineralogy and Petrology 123(4): 345-357.

Kohlstedt, D. L., Wang, Z.Y. 2001. Grain boundary sliding accomodated dislocation creep in dunite. EOS, Transactions, American Geophysical Union 82(47): F1137.

Li, L., Raterron, P., Weidner, D.J., Chen, J. 2003. Olivine flow mechanisms at 8 GPa. Physics of the Earth and Planetary Interiors 97: 121-131.

Li, L., Weidner, D.J., Raterron, P., Chen, J., Vaughan, M.T. 2004a. Stress measurement of deforming olivine at high pressure. Physics of the Earth and Planetary Interiors 143-144: 357-367.

Li, L., Weidner, D.J., Chen, J., Vaughan, M.T., Davis, M. 2004b. X-ray strain analysis at high pressure: effect of plastic deformation in MgO. Journal of Applied Physics 95(12): 8357-8365.

Li, L., Weidner, D.J., Raterron, P., Chen, J.H., Vaughan, M., Mei, S., Durham, W. 2006. Deformation of olivine at mantle pressure using the D-DIA. European Journal of Mineralogy 18(1): 7-19.

Mackwell, S. J., Kohlstedt, D.L., Paterson, M.S. 1985. The role of water in the deformation of olivine single crystals. Journal of Geophysical Research 90(NB13): 11319-11333.

Meade, C., Jeanloz, R. 1989. Acoustic emissions and shear instabilities during phase transformation in Si and Ge at ultrahigh pressure. Nature 339: 616-618.

Meade, C., Jeanloz, R. 1990. The strength of mantle silicates at high pressure and room temperature: implications for the viscosity of the mantle. Nature 348: 533-535.

Meade, C., Jeanloz, R. 1991. Deep focus earthquakes and recycling of water into the Earth's mantle. Science 252: 68-72.

Mei, S., Kohlstedt, D.L. 2000a. Influence of water on plastic deformation of olivine aggregates 1: diffusion creep regime. Journal of Geophysical Research 105(B9): 21457-21469.

Mei, S., Kohlstedt, D.L. 2000b. Influence of water on plastic deformation of olivine aggregates 2: dislocation creep regime. Journal of Geophysical Research 105(B9): 21471-21481.

Ogawa, M. 1987. Shear instability in a viscoelastic material as the cause of deep focus earthquake. Journal of Geophysical Research 92(B13): 13801-13810.

Orowan, E. 1960. Mechanism of seismic faulting. Deformation. D. T. Griggs, Handlin, J. London, Geological Society Memoir. 79: 323-345.

Peterson, M. S. 1982. The determination of hydroxyl by infrared absorption in quartz, silicate glass and similar materials. Bulletin Mineralogie 105: 20-29.

Post, J. P. J. 1977. High temperature creep of Mt. Burnet dunite. Tectonics 7: 1243-1256.

Poumellec, B., Jaoul, O. 1984. Influence of PO2 and PH2O on the high temperature plasticity of olivine. Deformation of Ceramic Materials II. R. E. Tressler, Bradt, R.C. New York, Plenum: 281-305.

Raterron, P., Wu, Y.J., Weidner, D.J., Chen, J.H. 2004. Low-temperature olivine rheology at high pressure. Physics of the Earth and Planetary Interiors 145: 149-159.

Raterron, P., Chen, J., Li, L., Weidner, D., Cordier, P. 2007. Pressure-induced slip-system transition in forsterite: Single-crystal rheological properties at mantle pressure and temperature. American Mineralogist, 92: 1436-1445.

Ross, J. V., Avelallemant, H.G., Carter, N.L. 1979. Activation volume for creep in the upper mantle. Science 203(4377): 261-263.

Singh, A. K., Balasingh, C., Mao, H.K., Hemley, R.J., Shu, J.F. 1998. Analysis of lattice strains measured under nonhydrostatic pressure. Journal of Applied Physics 83(12): 7567-7575.

Uchida, T., Wang, Y., Rivers, M.L., Sutton, S.R. 2004. Yield strength and strain hardening of MgO up to 8 GPa measured in deformation DIA with monochromatic X-ray diffraction. Earth and Planetary Science Letters 226: 117-126.

Wang, Y., Durham, W.B., Getting, I.C., Weidner D.J. 2003. The deformation DIA: a new apparatus for high temperature trialxial deformation for pressure up to 15 GPa. Review of Scientific Instruments 74: 3002-3011.

Weidner, D. J., Vaughan, M.T., Ko, J., Wang, Y., Leinenweber, K., Liu, X., Yeganeh-Haeri, A., Pacalo, R.E., Zhao, Y.S. 1992a. Large volumn high pressure research using the wigger port at NSLS. High Pressure Research 8: 617-623.

Weidner, D. J., Vaughan, M.T., Ko, J., Wang, Y., Liu, X., Yeganeh-Haeri, A., Pacalo, R.E., Zhao, Y.S. 1992b. Characterization of stress, pressure, and temperature in SAM-85, a DIA type high pressure apparatus. High-Pressure Research: Application to Earth and Planetary Sciences. Y. Syono, Manghnani, H. Tokyo / American Geophysical Union, Washington, D.C., Terra Scientific Publishing Company: 13-17.

Weidner, D. J., Wang, Y., Ando, J., Vaughan, M.T. 1994. Yield stress at high pressure and temperature. Geophysical Research Letters 21: 753-756.

Weidner, D. J. 1998. Rheological studies at high pressure. Ultrahigh-Pressure Mineralogy: Physics and Chemistry of the Earth's Deep Inerior. R. J. Hemley. Washington, DC, Mineralogical Society of America. 37: 493-524.

Weidner, D. J., Wang, Y., Chen, J., Ando, J., Vaughan, M.T. 1998. Rheology measurements at high pressure and temperature. Properties of the Earth and Planetary Materials at High Pressure and Temperature. M. H. Manghnani, Yagi, T., American Geophysical Union. Geophysical Monograph 101: 473-482.

Chapter 2

In situ Measurement of Deformation of Olivine at Subduction Zone Conditions Using Synchrotron X-Ray

2.1 Abstract

Several deformation experiments of San Carlos olivine at subduction zone conditions (pressures of 3-5 GPa and temperatures of 25-900°C) have been carried out on a deformation DIA (D-DIA) apparatus, Sam85, at X17B2, NSLS. Powder samples are used in these experiments. Enstatite ($MgSiO_3$) (3-5% total quality of sample) is used as the buffer to control the activity of silica. Ni foil is used in some experiments to buffer the oxygen fugacity. Water content is confirmed by IR spectra of the recovered samples. Samples are compressed at room temperature and are then annealed at 1200°C for at least 2 hours before deformation. The total (plastic and elastic) strains (macroscopic) are derived from the direct measurements of the images taken by X-ray radiograph technique. The differential stresses are deduced from elastic strains, which are calculated from olivine elastic. Respecting to the incident synchrotron X-ray beam, the elastic constraints are *in situ* measured in different directions and are collected as a function of time by the X-ray multi-detector EDS. At different pressures and temperatures, the experiments are preformed at constant strain rates (~10^{-5}-$10^{-7}s^{-1}$). It can be concluded that in the regime of

25-400°C, there is a small increase of stress at steady state along with the temperature drop; in the regime of 400°C to transition temperature, the differential stress at steady state is a constant (~3 GPa) and is relatively insensitive to the changes of temperature and strain rate; however, it drastically decreases to about 1 GPa and becomes temperature-dependent above the transition temperature and thereafter. The transition temperature is between 700°C and 900°C. No significant difference of differential stress and strain is observed between the samples with/without Ni foil buffered below 700°C. Two regimes with different deformation mechanisms for olivine have been determined in this study: regime of low temperature plasticity at low temperature (below transition temperature) and regime of power law creep at high temperature (above the transition temperature). Comparing to the natural system, the transition temperature for the olivine in the slab is most likely in the range of 550-600°C.

2.2 Introduction

Olivine is the dominant mineral in the upper mantle and the ocean lithosphere. In the subduction zone, where earthquakes happen, the rheology of the slab is mainly controlled by that of olivine at low temperatures. Several different mechanisms for deep focus earthquakes have been suggested, which include olivine instability (Bridgman, 1936; Orowan, 1960; Post, 1977; Ogawa, 1987; Hobbs and Ord, 1988; Kao and Chen, 1995), shear/fault-induced melting (Griggs, 1954, 1972; Griggs and Handin, 1960; Griggs and Baker, 1969; Zhang et al., 2004), phase transformation (Bridgman, 1945; Benioff, 1963; Meade and Jeanloz, 1989), dehydration of hydrous specimens (Raleigh

and Paterson, 1965; Meade and Jeanloz, 1991; Peacock, 2001; Dobson et al., 2002; Jung et al., 2004), and olivine metastability-induced anti-crack (Green and Houston, 1995). Since the low temperature of the "cold" slab, which may be as low as 600°C in the transition zone, it has been argued that olivine may still exist there and thus its instability may be the possible mechanism for the deep-focus earthquakes.

Although it is important, rheological studies on olivine at high pressure (>3 GPa) and low temperature (subduction zone condition) is limited due to the experimental technical difficulty. Development of multi-anvil apparatus made a great progress in doing deformation experiments at high pressure and high temperature (Durham and Rubie, 1998). In order to carry out deformation experiments at high pressure and temperature, the Deformation DIA (D-DIA) apparatus has been recently developed (Durham et al. 2002; Wang et al. 2003). One of the characteristics of the D-DIA is that it can keep a constant strain rate at pressure up to over 10 GPa, which allows performing the steady state deformation experiments at high pressure. It also has an advantage in fitting the *in situ* synchrotron X-ray measurements for stress and strain (Chen et al. 2004; Li et al. 2003; Li et al. 2004a and b; Li et al. 2006a and b; Uchida et al. 2004).

Recently, *in situ* X-ray measurements of stress and strain on the large volume multi-anvil press (e.g. Weidner *et al*., 1992; Li *et al*., 2003; Li *et al*., 2004; Chen *et al*., 2004) has also made a significant progress in the deformation experiments. A method was been developed to measure microscopic elastic stress and strain in powder sample from the broadening of the deformed mineral's X-ray diffraction peaks (Weidner et al.

1992a and b; Weidner et al. 1994; Weidner; 1998; Weidner et al. 1998). However, it is not a direct extension of traditional strain and stress measurement. The assumption of constant total microscopic strain (sum of both elastic and plastic strain) yields additional uncertainties to construct a flow law from the experimental data (Chen et al. 2004). Furthermore, the experimental sample can not be annealed before the deformation starts because such a process releases stress, which can only build up during the compression in this kind of experiments. So a new technique has been developed to carry out the deformation experiment on a large volume multi-anvil apparatus with *in situ* X-ray measurements (Chen et al. 2004; Li et al., 2004a and b). By using this method, the macroscopic plastic strain is measured by a direct sample length imaging system. The microscopic elastic strain is measured by the multiple X-ray diffraction pattern of the sample along different stress axis. Then the differential stress is derived according to Hook Law:

$$\sigma_{ij} = c_{ijkl}\varepsilon_{kl} \quad (1)$$

where σ is stress, ε is strain, and c is the elastic constants tensor.

Temperature plays an important role in the deformation of olivine. According to Frost and Ashby (1982), the deformation of olivine can be divided into four regimes: low temperature plasticity or dislocation glide controlled by a lattice resistance, low temperature plasticity or dislocation glide controlled by discrete obstacles, high temperature plasticity or power-law creep, and diffusional flow. The rheological properties of olivine are quite different in one regime comparing to the others. Furthermore, dynamic recrystallization, which results in removing or drastically changing

the dislocation substructure and allowing a period of primary creep, may accompany at high temperature when temperature/melting temperature is about 0.6 or more. The dynamic recrystallization of olivine can be very active at about 1200°C at mantle condition (Li et al. 2003). At low temperature, the differential stress in olivine can be very high. Evans and Geotze (1979) reported that it can be up to 5 GPa at about 100°C. Several literatures reported related studies on olivine rheology at high pressures and room temperature (Meade and Jeandoz, 1990; Chai *et al*., 1998). The relaxation experiments' results (Raterron *et al*., 2004) demonstrate a rapid decrease of differential stress from 3 GPa to 1 Gpa at 450-500°C. Li et al. (2004b) report a dramatical drop of differential stress from 1.7 GPa to about 0.6 GPa at hydrostatic pressure of 8 GPa and about 820°C. Chen et al. (2004) report a decrease of differential stress with the increase of temperature in an *in situ* measurement of deforming fayalite (Fe_2SiO_4). Using D-DIA apparatus, Li et al. (2006b) report that at steady state the differential stress values are 2.4 GPa for fine olivine sample at 6.5 GPa and 900°C, and 2.0 GPa for coarse sample at 3.5 GPa, 800°C and at 6.5 GPa, 900°C. Up to now the study on olivine at steady state at high pressure is still limited, especially at high pressure and low temperature.

In this study, several deformation experiments of San Carlos olivine have been performed at subduction zone conditions (pressures of 3-5 GPa and temperatures of 25-900°C) on a deformation DIA (D-DIA) apparatus, SAM85, at X17B2, National Synchrotron Light Source (NSLS). Differential stresses are measured at constant strain rate ($\sim 10^{-5}$-10^{-7} s^{-1}) and at different pressures and temperatures with synchrotron x-ray.

2.3 Starting Material

San Carlos olivine, whose composition is $(Mg_{0.9}Fe_{0.1})_2SiO_4$ and which is believed to present the same Mg:Fe ratio in the earth mantle, is used as the sample in the deformation experiments. Optically clear (gem quality) grains of San Carlos olivine with maximum dimension of 3-10 mm are well ground into powder in an agate mortar. Powdered San Carlos Olivine samples are used in these experiments. Powdered enstatite ($MgSiO_3$) (3-5% total quality of sample) is mixed into the olivine samples as a buffer to control the activity of silica. To determine the effect of oxygen fugacity, two samples, one with Ni-NiO foil buffered and another without buffered, are put in one cell assembly during the deformation experiment. In order to explore the effect of water fugacity on deformation of olivine, both "normal" and "wet" samples are investigated. Amorphous boron epoxy (BE) cells are used in this study. To keep away from the moisture, "normal" samples are placed in a vacuum oven at 135°C for at least 2 hours before experiments. In "wet" samples, talc instead of enstatite is used as both water source and the buffer of controlling the activity of silica. Samples are compressed at room temperature and are then annealed at 1200°C for at least 2 hours before dropping to the designed temperature and deformation.

2.4 Grain Size

The grain size of starting powdered San Carlos olivine is mainly in the range of 10-20 μm (**Fig. 2-1**). During the anneal process at 1200°C, however, the grain self-growth

process is active. As a result some grains become bigger and the others become much smaller or disappear. Li et al. (2003, 2006b) report the similar situation at similar conditions. It is also observed that the grain size become smaller during cold compression (Brearley et al., 1992; Raterrron et al., 2004). In addition, Raterron et al. (2004) notice that the number of large grains (≥ 1 μm) becomes more popular in the recovered sample performed at higher temperature. In our experiments, we also observe that the big grains become smaller during the deformation. Thus the grain size can not be controlled in the experiments with compression, annealing and deformation processes. In the dislocation regime, however, deformation of olivine is insensitive to the grain size (Karato et al., 1986; Li et al., 2003, 2006b). So the process of dynamic recrystallization may not affect the experiments in this study.

2.5 Water Content

The water content in the starting San Carlos olivine crystal is less than 1 ppm wt, which is measured at the infrared (IR) facility of beam line U2A, NSLS (Raterron et al. 2004). However, although the whole cell assemblies are placed in a vacuum oven at 135°C to keep away from the moisture in the air prior to the deformation experiments, the water content in the recovered sample is significant, as measured at the IR spectra of U2A, NSLS. The zirconia cement, which is used to coat the thermal couple (TC) and fill the space around the TC in the cell assembly, may be the most important source of water in the recovered sample. The BE may be another main source of water. The IR results of the recovered deformed samples are presented in **Fig 2-2** based on a diagram of

absorption coefficient vs. wavenumber. It shows that there is no sharp peak in the range of wavenumber 3000-3780 cm^{-1}. Instead, a big hump appears in this area. It indicates that the amount of molecular water among the olivine grains is significant. Showing very similar IR absorption spectra with a hump in the recovered deformed "wet" olivine aggregate, Karato et al. (1986) suggest that two kinds of peaks, free water and the OH-related species, are combined together in the spectra and the ratio of molecular water vs. OH-related species changes from 1:2 to 2:1 in the different specimens. They observe that the fraction of free water tends to be larger in hot-pressed samples than that in the deformed polycrystalline olivine, thus suggest that the olivine specimen loses water during deformation. Mei and Kohlstedt (2000a) also show very similar IR diagrams with huge hump for their deformed polycrystalline olivine samples, which suggest that the polycrystalline samples have 5-20 times higher values of hydroxyl concentration than that in the single crystal and indicate that a large portion of water resides in the grain boundaries and fluid inclusions. In this study, a sharp peak or peaks presenting bonding hydroxyl can be found with no or much smaller hump in the IR diagrams (**Fig 2-3**) in the recovered San Carlos olivine samples from undeformed experiments with the similar cell assemblies at similar pressure and temperature. We therefore suggest that either the bonding hydroxyl is driven off from the olivine structure, or the peak presenting such bounding hydroxyl is buried in the background of molecular water.

2.6 Experimental Protocol

The deformation experiments are carried out on a D-DIA facility, SAM85, at X17B2 beamline, NSLS. Sample in each experiment is placed in a boron nitride tube, which is

used as a capsule to separate the sample from the graphite furnace. Sample(s) is (are) separated from each other or from alumina pistons by Ni/Pt foils, which are also used as strain markers. Surrounded by a machinable alumina sleeve, the furnace is inserted inside a pressure media cube, which is made from amorphous boron powder and expoxy (BE) or mullite. Differential stress is produced by the hard alumina pistons on the top and the bottom in the cell assembly (**Fig. 2-4**). Each of the hard alumina pistons is driven by an independent vertical anvil of the D-DIA, which is driven by an independent ram. The W3%Re-W25%Re thermal couple is used in the experiments. To measure the elastic strain of deformed samples, a solid-state multi-detectors (energy dispersive spectrometer, EDS) is used with a conical slit. Transparent to the X-ray, sintered diamond anvils or cubic boron nitride anvils are used so that the X-ray diffraction data of sample can be properly collected with a two theta angle of about 6.5 degree.

The data of macroscopic strain along the uniaxial direction is measured from the X-ray radiograph of the sample. Using a white incident X-ray beam with 2 x 2 mm^2 in size, the image of the experimental sample is *in situ* captured and magnified by a CCD camera with the X-ray radiographic technique (**Fig.2-5**). The length of the specimen is measured and plotted as a function of time in a diagram, which is used as a strain indicator.

The differential stresses are deduced from elastic strains, which are calculated from olivine elastic constraints which are *in situ* collected as a function of time by the X-ray multi-detector EDS. With a white X-ray beam of 50 x 50 μm^2 in size going through the

samples, the samples' elastic constraints are *in situ* measured in different directions respecting to the incident X-ray beam (**Fig. 2-6**).

In this study, the D-DIA apparatus gives the capacity to drive the top and bottom rams at a certain speed to maintain a constant strain rate while the main ram is also driven at a related certain speed to keep the pressure constant (Durham et al., 2002; Wang et al., 2003). During the experiments, the equation of state for the olivine is used as the pressure standard. The experimenter has the capability to control the speeds of differential rams and the directions of the rams, either advance or retreat (**Fig 2-7**).

2.7 Data Analysis

2.7.1 Pressure Calibration

The San Carlos olivine sample itself is used as the pressure standard. The 3rd order Birch-Murnaghan equation of state is applied to calculate the pressure. The parameters for the calculation are from Liu et al. (2005), Isaak (1992) and Suzuki (1975). We also use the data from zha et al. (1996) to do a comparison with Liu et al (2005) and no significant difference is founded. The parameters are listed in **Table 2-1**. The X-ray diffraction data of San Carlos olivine at ambient condition (10^5 Pa, 25°C) is used to calculate the reference unit cell volume V_0. The value of hydrostatic d-spacing is derived from:

$$d(P,T)(hkl) = \frac{d_V(P,T)(hkl) + 2d_H(P,T)(hkl)}{3} \quad (2)$$

in which d is the hydrostatic d-spacing value, d_V and d_H are the d-spacing values collected with vertical and horizontal detectors, respectively, at certain pressure (P) and temperature (T). (*hkl*) represents the inter-planar.

For the orthorhombic structure of olivine, the cell parameters *a*, *b* and *c* are from:

$$\frac{1}{d^2} = \frac{a^2}{h^2} + \frac{b^2}{k^2} + \frac{c^2}{l^2} \quad (3)$$

where *d* is the hydrostatic d-spacing value, *h, k, l* are the planar parameters of the olivine crystal. *a, b* and *c* are the unit cell parameters of olivine structure.

The unit cell volume is from:

$$V = a \times b \times c \quad (4)$$

in which V is the unit cell volume, *a, b* and *c* are the unit cell parameters.

2.7.2 Strain Analysis

The total (plastic and elastic) strain (macroscopic) is derived from the direct measurement of the images taken by X-ray radiograph technique. The strain markers, Ni/Pt foils with thickness of 25 μm, are shown as dark lines in the images. The resolution is at pixel level.

2.7.3 Stress Analysis

Elastic deformation is measured by X-ray powder diffraction pattern analysis (Chen *et al*., 2004; Li *et al*., 2004; Li et al., 2006). Following Singh *et al*. (1998), differential stress is deduced from elastic strain, which is calculated from olivine elastic constraints measured by a solid state multi-detector, energy dispersive spectrometer (EDS):

$$\varepsilon(hkl) = \frac{d_V(hkl) - d_H(hkl)}{\frac{d_V(hkl) + 2d_H(hkl)}{3}} \tag{5}$$

$$\varepsilon(hkl) == \tau(hkl)\alpha[2G_R(hkl)]^{-1} + \tau(hkl)(1-\alpha)(2G_V)^{-1} \tag{6}$$

where ε is the elastic strain; d_V and d_H are the d-space values for vertical and horizontal directions, respectively; is the differential stress, G_R and G_V are the aggregate shear modulus under Reuss condition (iso-stress) and voigt condition (iso-strain), respectively; and α weight parameter for *reuss* and *voigt* conditions. (*hkl*) represents the inter-planar. In this study, we assume that our experiments are at Reuss condition so α=1.

2.8 Experimental Results

At 3-5 GPa, the deformation experiments of olivine at 25°C, 400°C, 500°C, 700°C and 900°C are performed in this study. Two distinguished deformation regimes have been found above 400°C in this study: temperature-independent regime at low temperature and temperature-dependent regime at high temperature. In order to observe the boundary between these two regimes, several experiments are designed to investigate the deformation behavior of olivine along the temperature increase and decrease cycles

after steady state has been reached at 400°C. The strategy of these investigations is that the observed stress should be higher than or equal to the stress at steady state along increase cycle, whereas it should be equal to or lower than that at steady state along decrease cycle at the same temperature. Thus the value of stress at steady state is right between these two values.

During the experiments, steady state is reached and is checked by a quick analysis of a single diffraction peak of olivine (130). The final results of the differential stress are from the average values of five diffraction peaks of olivine, which are (021), (101), (130), (131) and (112).

The diagrams of differential stress versus total strain and total strain versus time during the deformation experiments at 25°C and 500°C are shown in **Fig 2-8a**, **Fig. 2-8b** and **Fig 2-9a**, **Fig 2-9b**, respectively. The relationships of stress versus time and strain versus time during deformation at 700°C are shown in **Fig. 2-10a** and **Fig. 2-10b**, respectively. The relationships of differential stress versus total strain during the deformation at 900°C and 400°C are illuminated in **Fig. 2-11a** and **Fig. 2-11b**, whereas the strain versus time is shown in **Fig. 2-11c**. The relationship of differential stress versus temperature during the deformation experiment of olivine in temperature increase and decrease cycles is illuminated in **Fig. 2-12a** and **Fig. 2-12b**, respectively.

Most of the strain rates in the experiments are in the scale of 10^{-5} s^{-1}. However, to investigate the relationship of stress and strain rate, some experiments are applied to a very slow D-DIA speed and a low strain rate of $10^{-7}s^{-1}$ level is obtained.

It is shown that in the experiments of deformation at 25°C, 400°C, 500°C and 700°C, the differential stress builds up along with the strain increase at the beginning due to the work (strain) hardening. After overcoming the work hardening, however, it finally reaches steady state (constant flow stress) and becomes a constant. It should be mentioned that at low temperature, the stress at steady state is not a constant strait line parallel to the X-axis; instead, it fluctuates with time. The lower the temperature is, the bigger the amplitude is. We conclude that it is due to the contribution of work hardening at low temperature. However, the mean line is strait. Thus it is no doubt that the deformation has reached steady state. “Quasi” steady state may be a better name for it.

At steady state, the differential stress of olivine at 25°C is as high as 4.4 GPa. It drops to about 3.0 GPa at 400°C and keeps the similar value at 500°C and 700°C. At 900°C, however, it drops to about 1 GPa.

In the deformation experiment applying cycles of increasing and decreasing temperature, it shows a textbook’s perfect diagram of stress versus temperature. During the temperature increasing cycle, the stress remains a constant with a characteristic of temperature independence in the low temperature regime until it reaches the boundary, about 990°C. After this transition point, the stress becomes temperature dependent.

During the temperature decreasing cycle, the stress keeps its characteristics of temperature dependence in the high temperature regime and finally when reaching the transition point at about 830°C, stress becomes a constant again in the low temperature regime. We have talked about our strategy for this investigation in the early paragraph in this paper. The real transition temperature thus should be between the values of increase and decrease cycles. A mean of these two values, 910°C, may be an acceptable value for the boundary transition point.

In the low temperature regime during deformation, no significant difference in both differential stress and strain rate at steady state is observed between the specimens with and without Ni foil buffered though specimen with Ni buffered shows an obvious lower value of stress than the one without Ni buffered in the high temperature regime.

2.9 Discussion

2.9.1 Comparison to the previous work

The study on deformation of olivine at high pressure and low temperature is very limited, though there are a lot of literatures about the deformation of olivine at high temperature regime in decades. This study takes full benefit of D-DIA technique and *in situ* measurements of stress and strain using synchrotron X-ray and presents the first steady state data of deformed San Carlos olivine at mantle pressure and low temperature. The data presented here has limited range of strain rate, most in scale of $10^{-5}s^{-1}$ and one in scale of $10^{-7}s^{-1}$. The temperature range is wide enough to constrain the temperature

dependent characteristics of olivine in low temperature regime and at the boundary of low and high temperature regimes. Here we compare the data in this study to the other existing results, including the data at low pressure and low temperature, some *in situ* X-ray measurement data but by different technique, and the other isolated data by in situ X-ray technique at the D-DIA facility, SAM85 from colleagues.

Some studies related to the deformation of olivine have been performed at high pressure and low temperature condition. Using the Vickers diamond pyramid technique (up to 800°C) and the mutual indentation technique (up to 1500°C), Evans and Goetze (1979) give the hardness data at ambient pressure. Based on the momentum balance of olivine specimen in the Mao-Bell diamond cell with a spring steel gasket and considering the maximum shear stress τ as the yield stress of the specimen, the shear stress τ is calculated from the maximum pressure gradient and the thickness of the specimen (Meade and Jeanloz, 1990). Studies have been reported using *in situ* synchrotron X-ray measurement on the relaxation experiments of San Carlos olivine at high pressure on a DIA facility by peak broadening method (Wu, 2000; Weidner et al., 2001; Raterron *et al*., 2004) or solid state multi-detectors (Li et al., 2004b). Li et al. (2006b) also recently report a study with *in situ* synchrotron X-ray measurement using solid state multi-detectors on a D-DIA apparatus.

Our data presented here generally make a good agreement with the other colleagues' about the very high stress value in the low temperature regime. The relaxation experiments (Weidner et al., 2001; Raterron *et al*., 2004) report a stress value of 6 GPa at

the hydrostatic pressure of 9 GPa and room temperature, which is consistent to the value given by Meade and Jeanloz (1990) at 8 GPa and room temperature. They also give a value of about 5 GPa in stress at pressure of 4.9 GPa, which is close to our data, 4.4 GPa at steady state, but a little bit lower than the hardness data (Evans and Goetze, 1979). The high stress value remains in the low temperature regime. Raterron *et al*. (2004) observe the differential stress of olivine changes when crossing the boundary, from 3 GPa or more at 400°C to 1 GPa or less at 625°C. Chen et al. (1998) also observe a rapid drop in differential stress between 400°C and 600°C in the dry olivine polycrystalline powder specimen by using the peak broadening method. The values of differential stress in both high and low temperature regimes in this study get a very good agreement with theirs. However, in this study the determined low and high temperature ranges are quite higher than their data. A transition temperature range of 450-500°C for the boundary is observed in the relaxation experiments (Weidner et al., 2001; Raterron et al., 2004), which is much lower than the value observed in this paper, a range between 700°C and 900°C in the measurement at steady state, or 910°C determined in the deformation applying temperature increase and decease cycles. The hardness data at ambient pressure (Evans and Goetze, 1979) show a similarly rapid drop of yield stress around 770°C though they don't realize it, which agrees with the result in this study. A diagram demonstrates our data at steady state in this study and a comparison with the colleagues' results is illuminated in **Fig. 2-13**.

The difference in transition temperature reflects not only the different properties between the annealed and unannealed specimens, also the water effect. In fact, all the

data we present here are from the annealed specimens before deformation while all the data using peak broadening method have to be from the unannealed olivine samples because the annealing process certainly eliminates the yield stress. The details will be discussed in our another paper.

2.9.2 Anisotropy of stress on different planes

As we mentioned in the early paragraph, our stress data presented here is a mean value of several crystal planes. We explore the behaviors of different planes during the deformation. The stress on planes of (021), (101), (130), (131) and (112) as a function of strain is demonstrated in **Fig. 2-14**. The strength of all planes reaches steady state at the same time when the strain arrives about 5%. However, the values of stress from these planes at steady state are significantly different. The stress in group of (021), (130) and (131) is obviously higher than that in group of (101) and (112). The stress of (112) is obviously higher than that of (101), too. It can be seen that the stress in planes (*hkl*) tends to be higher if *k* is relatively big. This phenomenon may reflect the effect of active slip system. At low temperature, the dominant active slip systems are [001](100), [001](110) and [001]{hk0} (Raileigh, 1968; Raterron et al., 2004; our paper elsewhere). More work is needed.

2.9.3 Plastic flow law and deformation map

The mechanisms of deformation have been well developed. According to Frost and Ashby (1982), our data can be in the regimes of low temperature plasticity by dislocation glide and/or power law creep at high temperature. In order to determine

whether our data presented here is in the regime of power law creep, a test is performed. In this test we use the flow law equation for the power law creep to fit our data:

$$\dot{\varepsilon} = A\sigma^n \exp(-\frac{E^* + PV^*}{RT}) \quad (7)$$

where A is constant, $\dot{\varepsilon}$, E*, P, V*, R, T are the strain rate, activation energy, hydrostatic pressure, activation volume, standard gas constant and temperature, respectively.

Following the parameters derived by Mei and Kohlstedt (2000b) and applying a small V* suggested by Li et al. (2006b) (we set V* = $2 \times 10^{-6} m^3 mol^{-1}$), we obtain the value of n from 20.8 to 8.1 for the temperature range of 25-400°C, 8.1-3.5 for the range from 400°C to transition point, and 3.4-3.0 for the temperature above the transition point to up to 1145°C, respectively (**Table 2-4**). In general the n value for the power law creep is 3-3.5. Thus the deformation of olivine below the transition temperature is in the regime of low temperature plasticity instead of power law creep. As temperature increases and gets across the transition boundary, however, the mechanism of deformation finally evolves into the regime of power-law creep.

For decades several models have been developed to describe the flow law of the low temperature plasticity (refer to Evans and Kohlstedt, 1995 for details). The plastic deformation in this regime is actually the motion of dislocation glide. The velocity of the dislocation is determined by the strength and density of the discrete obstacle (obstacle-limited) frequently or limited by a barrier of so-called Peierls force: lattice resistance

(lattice-limited). The Gibbs free energy of activation for the dislocation is a function of the flow stress. The flaw law can be expressed as:

$$\dot{\varepsilon} = \dot{\varepsilon}_0 (\frac{\sigma}{\mu})^2 \exp(-\frac{\Delta G(\sigma)}{RT}) \quad (8)$$

where $\dot{\varepsilon}_0$ is a pre-exponential factor depending on the nature of obstacles and the stress level. The $\Delta G(\sigma)$ can be expressed as:

$$\Delta G(\sigma) = \Delta F_0 [1 - (\frac{\sigma}{\tau})^p]^q \quad (9)$$

where ΔF_0 is the total free energy of activation of an isolated pair of kinks, or required to overcome the obstacle without aid from the external strength; τ is the flow stress at zero K. p and q are constants and $0 \leq p \leq 1$, $1 \leq q \leq 2$.

Putting equation 9 in to equation 8, we can finally get

$$\sigma^p = \tau^p - KT^{1/q} \quad (10)$$

where

$$K = \tau^p \{\frac{R}{F_0} \cdot \ln[\frac{\dot{\varepsilon}_0}{\dot{\varepsilon}} \cdot (\frac{\sigma}{\mu})^2]\}^{1/q} \quad (11)$$

For a given constant strain rate, K is a constant.

Plotting and fitting the data in the diagram of stress versus temperature, we can obtain the parameters of p, q, τ and K.

For the deformation of olivine below 400°C, we only have two data, about 4.4 GPa at 25°C and about 3.5 GPa at 400°C. Thus it is difficult to derive an accurate flow law

equation for this temperature range in this study. However, we can roughly fit the data and obtain:

$$\sigma = 5.1 - 0.0024T \quad (12)$$

in which we roughly estimate the evaluation of $\tau = 5.1$ GPa.

For the deformation above 400°C, as we report in the early section of this paper, our data show two different regimes of deformation of olivine: temperature insensitive regime in the temperature range from 400°C to the transition temperature and temperature sensitive regime at the temperature higher than the transition point. It means that in the regime of 400°C to transition temperature there exists an athermal flow strength, which is insensitive to the temperature at steady state. The value of the maximum strength, or the stress at steady state, is about 3.0 GPa. We also find that the strain rate has little effects on the stress at steady state in this regime comparing the deformation in scale of $10^{-5}s^{-1}$ to that in scale of $10^{-7}s^{-1}$. We thus conclude that the differential stress at steady state is independent to both temperature and strain rate in this regime. The flow law in this regime can be described as a very simple form:

$$\sigma = C \quad (13)$$

Where σ is the stress, *C* is a constant. In this study, C is equal to 3.0 GPa.

2.9.4 Implications

Our data demonstrate that for the annealed olivine polycrystalline at mantle pressure and temperature, there are two distinctive deformation regimes above 400°C:

temperature insensitive regime with stable high value of stress at steady state from 400°C to the transitional temperature and temperature sensitive regime with quick stress drop along with temperature increase above the transitional temperature. The transition temperature is between 700°C and 900°C. The strain rate also has little effect on the stress at steady state.

We compare our laboratory results with the cases in the natural environment. Although for olivine it shows little effect on the stress at steady state in the regime of low temperature plasticity, as we discover in this study, the strain rate obviously affects the stress at steady state in the power-law regime, as many workers have demonstrated (Frost and Ashby, 1982; Mei and Kohlstedt, 2000b; etc). As we mentioned, our results are from the conditions where the strain rate is in the scales of 10^{-5} to $10^{-7}s^{-1}$. It is far away from the subduction zone condition, where the strain rate is about $10^{-15}s^{-1}$ (Holt, 1995). So we cannot apply the transitional temperature from our experimental results directly to the natural earth mantle. To consider the situation of natural system, following the parameters of the power-law equation suggested by Mei and Kohlstedt (2000b) and giving a small V* suggested by Li et al. (2006b) (we set $V^* = 2 \times 10^{-6} m^3 mol^{-1}$), we calculate the stress at steady state in power-law creep at different temperatures with unique strain rates: lab condition ($10^{-5}s^{-1}$) and natural plate's condition (10^{-12}-$10^{-15}s^{-1}$). We plot the calculation results as the function of temperature together with the data sets we get from the temperature increase and decrease cycles' experiment in **Figure 12a**. It shows that in lab conditions, the calculated data are in good agreement with our experiment data obtained above the transition temperature and demonstrates that in the

regime of high temperature (higher than the transition temperature), the deformation mechanism of olivine follows power-law creep. On the other hand, the transition temperature at natural condition is significantly lower. For the slab condition ($10^{-15}s^{-1}$ level), the transitional temperature is about 550-600°C. For the quickly moving plates ($10^{-12}s^{-1}$ level), the transition happens at 670-720°C. The value of transitional temperature should not changed much due to the sharp slope of the olivine deformation curve in the power-law creep in natural condition, although the stress of olivine in the geological environments may be much lower than that at steady state.

2.10 Conclusions

Here we present that the olivine deformation properties on a D-DIA apparatus using synchrotron X-ray *in situ* facility. Our data show that the olivine flow reaches steady state in this study.

Beside the regime of 25-400°C, in which there is a small increase of stress at steady state along with the temperature drop, two regimes with different deformation mechanisms for olivine have been determined in this study: low temperature plasticity at 400°C to transition temperature and power law creep above the transition temperature. The transition boundary of these two deformation regimes is between 700-900°C. The differential stress at steady state is a constant (~3 GPa) and is relatively insensitive to the changes of temperature and strain rate between 400°C and transition temperature in the

annealed olivine polycrystalline. However, it has a rapid decrease above the transition temperature and becomes temperature-dependent thereafter.

No significant difference in differential stress and strain is observed between the samples with/without Ni foil buffered below 700°C.

Comparing to the natural system, the transition temperature for the olivine in the slab is most likely in the range of 550-600°C.

References

Benioff, H., 1963. Source wave forms of three earthquakes. *Bulletin of Seismological Society of America* **53**, 893-903.

Bridgman, P. W., 1936. Shearing phenomena at high pressure of possible importance for geology. *Journal of Geology* **44**, 653-669.

Bridgman, P. W., 1945. Polymorphic Transitions and Geological Phenomena. *American Journal of Science* **243A**, 90-97.

Chai, M., Brown, M., and Wang, Y., 1998. Yield strength, slip systems and deformation induced phase transition of San-Carlos olivine up to the transition zone pressure at room temperature. In: Manghnani, M. H., Yagi, T. (Ed.), *Properties of Earth and Planetary Materials*. American Geophysical Union.

Chen, J., Li, L., Weidner, D. J., and Vaughan, M. T., 2004. Deformation experiments using synchrontron X-rays: in situ stress and strain measurements at high pressure and temperature. *Physics of the Earth and Planetary Interiors* **143-144**, 347-356.

Dobson, D. P., Meredith, P. G., and Boon, S. A., 2002. Simulation of subduction zone seismicity by dehydration of serpentine. *Science* **298**, 1407-1410.

Durham, W. B. and Rubie, D. C., 1998. Can the multianvil apparatus really be used for high-pressure deformation experiments. In: Manghnani, M. H., Yagi, T. (Ed.), *Properties of Earth and Planetary Materials at High Pressure and Temperature*. American Geophysical Union.

Durham, W. B., Weidner, D. J., Karato, S.-I., and Wang, Y., 2002. New developments in deformation experiments at high pressure. In: Karato, S.-I., Wenk, H.R. (Ed.), *Plastic Deformation of Minerals and Rocks, Reviews in Mineralogy and Geochemistry*. Mineralogy Society of America, Chantilly, Virginia.

Evans, B. and Geotze, C., 1979. The temperature variation of hardness of olivine and its implication for polycrystalline yield stress. *Journal of Geophysical Research* **84**, 5505-5524.

Evans, B. and Kohlstedt, D., 1995. Rheology of Rocks. In: Ahren, T. (Ed.), *Rock Physics and Phase Relations: a Handbook of Physical Constants*. The american Geophysical Union, Washington DC.

Frost, H. J. and Ashby, M. F., 1982. *Deformation-Mechanism Maps The Plasticity and Creep of Metals and Ceramics*. Pergamon Press, Oxford, New York, Toronto, Sydney, Paris, Frankfurt.

Green II, H. W. and Houston, H., 1995. The Mechanics of deep earthquakes. *Annual Review of Earth and Planetary Sciences* **23**, 169-213.

Griggs, D. T., 1954. High-pressure phenomena with applications to geophysics. In: Ridenour, L. N. (Ed.), *Modern Physics for the Engineer*. McGraw Hill, New York.

Griggs, D. T., 1972. The sinking lithophere and the focal mechanism of deep earthquakes. In: Robertson, E. C. (Ed.), *The Nature of Solid Earth*. McGraw Hill, New York.

Griggs, D. T. and Baker, D. W., 1969. The origin of deep-focus earthquakes. In: Mark, H., Fernbach, S. (Ed.), *Properties of matter under unusual conditions*. Interscience Publishers New York/London/Sydney/Toronto.

Griggs, D. T. and Handlin, J., 1960. Observations on fracture and a hyphothesis of earthquakes. In: Griggs, D. T., Handlin, J. (Ed.), *Rock Deformation*. Memoir of Geological Society of America.

Hobbs, B. E. and Ord, A., 1988. Plastic instabilities: implications for the origin of intermediate and deep focus earthquakes. *Journal of Geophysical Research* **93**, 10521-10540.

Holt, W. E., 1995. Flow-Fields within the Tonga Slab Determined from the Moment Tensors of Deep Earthquakes. *Geophysical Research Letters* **22**, 989-992.

Isaak, D. G., 1992. High-temperature elasticity of iron-bearing olivines. *Journal of Geophysical Research-Solid Earth* **97**, 1871-1885.

Jung, H., Green, H. W., and Dobrzhinetskaya, L. F., 2004. Intermediate-depth earthquake faulting by dehydration embrittlement with negative volume change. *Nature* **428**, 545-549.

Kao, H. and Chen, W. P., 1995. Transition from interplate slip to double seimic zone along the Kuril-Kamchatka arc. *Journal of Geophysical Research* **100**, 9881-9904.

Karato, S.-I., Paterson, M. S., and FitzGerald, J. D., 1986. Rheology of synthetic olivine aggregates: influence of grain size and water. *Journal of Geophysical Research* **91**, 8151-8176.

Li, L., Long, H., Raterron, P., and Weidner, D., 2006a. Plastic flow of pyrope at mantle pressure and temperature. *American Mineralogist* **91**, 517-525.

Li, L., Raterron, P., Weidner, D. J., and Chen, J., 2003. Olivine flow mechanisms at 8 GPa. *Physics of the Earth and Planetary Interiors* **97**, 121-131.

Li, L., Weidner, D. J., Chen, J., Vaughan, M. T., and Davis, M., 2004a. X-ray strain analysis at high pressure: effect of plastic deformation in MgO. *Journal of Applied Physics* **95**, 8357-8365.

Li, L., Weidner, D. J., Raterron, P., Chen, J., and Vaughan, M. T., 2004b. Stress measurement of deforming olivine at high pressure. *Physics of the Earth and Planetary Interiors* **143-144**, 357-367.

Li, L., Weidner, D., Raterron, P., Chen, J. H., Vaughan, M., Me, S. H., and Durham, B., 2006b. Deformation of olivine at mantle pressure using the D-DIA. *European Journal of Mineralogy* **18**, 7-19.

Liu, W., Kung, J., and Li, B. S., 2005. Elasticity of San Carlos olivine to 8 GPa and 1073 K. *Geophysical Research Letters* **32**.

Meade, C. and Jeanloz, R., 1990. the strength of mantle silicates at high pressure and room temperature: implications for the viscosity of the mantle. *Nature* **348**, 533-535.

Meade, C. and Jeanloz, R., 1991. Deep focus earthquakes and recycling of water into the Earth's mantle. *Science* **252**, 68-72.

Mei, S. and Kohlstedt, D. L., 2000a. Influence of water on plastic deformation of olivine aggregates 1: diffusion creep regime. *Journal of Geophysical Research* **105**, 21457-21469.

Mei, S. and Kohlstedt, D. L., 2000b. Influence of water on plastic deformation of olivine aggregates 2: dislocation creep regime. *Journal of Geophysical Research* **105**, 21471-21481.

Ogawa, M., 1987. Shear instability in a viscoelastic material as the cause of deep focus earthquake. *Journal of Geophysical Research* **92**, 13801-13810.

Orowan, E., 1960. Mechanism of seismic faulting. In: Griggs, D. T., Handlin, J. (Ed.), *Deformation*. Geological Society Memoir, London.

Peacock, S. M., 2001. Are the lower planes of double seismic zones caused by serpentine dehydration in subducting oceanic mantle? *Geology* **29**, 299-302.

Post, J. P. J., 1977. High temperature creep of Mt. Burnet dunite. *Tectonics* **7**, 1243-1256.

Raleigh, C. B., 1968. Mechanisms of Plastic Deformation of Olivine. *Journal of Geophysical Research* **73**, 5391-&.

Raleigh, C. B. and Paterson, M. S., 1965. Experimental Deformation of Serpentinite and Its Tectionic Implications. *Journal of Geophysical Research* **70**, 3965-&.

Raterron, P., Wu, Y. J., Weidner, D. J., and Chen, J. H., 2004. Low-temperature olivine rheology at high pressure. *Physics of the Earth and Planetary Interiors* **145**, 149-159.

Singh, A. K., Balasingh, C., Mao, H. K., Hemley, R. J., and Shu, J. F., 1998. Analysis of lattice strains measured under nonhydrostatic pressure. *Journal of Applied Physics* **83**, 7567-7575.

Suzuki, I., 1975. Thermal expansion of periclase and olivine and their anharmonic properties, *Journal of Physics of the Earth*, 23, 145-159.

Uchida, T., Wang, Y., Rivers, M. L., and Sutton, S. R., 2004. Yield strength and strain hardening of MgO up to 8 GPa measured in deformation DIA with monochromatic X-ray diffraction. *Earth and Planetary Science Letters* **226**, 117-126.

Wang, Y., Durham, W. B., Getting, I. C., and Weidner, D. J., 2003. The deformation DIA: a new apparatus for high temperature trialxial deformation for pressure up to 15 GPa. *Review of Scientific Instruments* **74**, 3002-3011.

Weidner, D. J., 1998. Rheological studies at high pressure. In: Hemley, R. J. (Ed.), *Ultrahigh-Pressure Mineralogy: Physics and Chemistry of the Earth's Deep Inerior*. Mineralogical Society of America, Washington, DC.

Weidner, D. J., Chen, J., Xu, Y., Wu, Y., Vaughan, M. T., and Li, L., 2001. Subduction zone rheology. *Physics of the Earth and Planetary Interiors* **127**, 67-81.

Weidner, D. J., Vaughan, M. T., Ko, J., Wang, Y., Leinenweber, K., Liu, X., Yeganeh-Haeri, A., Pacalo, R. E., and Zhao, Y. S., 1992a. Large volumn high pressure research using the wigger port at NSLS. *High Pressure Research* **8**, 617-623.

Weidner, D. J., Vaughan, M. T., Ko, J., Wang, Y., Liu, X., Yeganeh-Haeri, A., Pacalo, R. E., and Zhao, Y. S., 1992b. Characterization of stress, pressure, and temperature in SAM-85, a DIA type high pressure apparatus. In: Syono, Y., Manghnani, H. (Ed.), *High-Pressure Research: Application to Earth and Planetary Sciences*. Terra Scientific Publishing Company, Tokyo / American Geophysical Union, Washington, D.C.

Weidner, D. J., Wang, Y., Ando, J., and Vaughan, M. T., 1994. yield stress at high pressure and temperature. *Geophysical Research Letters* **21**, 753-756.

Weidner, D. J., Wang, Y., Chen, J., Ando, J., and Vaughan, M. T., 1998. Rheology measurements at high pressure and temperature. In: Manghnani, M. H., Yagi, T. (Ed.), *Properties of the Earth and Planetary Materials at High Pressure and Temperature*. American Geophysical Union.

Wu, Y., 2000. Rheological Studies of Olivine under high pressure and high temperature, Ph.D Thesis, State University of New York at Stony Brook.

Zha, C. S., Duffy, T. S., Downs, R. T., Mao, H. K., and Hemley, R. J., 1996. Sound velocity and elasticity of single-crystal forsterite to 16 GPa. *Journal of Geophysical Research-Solid Earth* **101**, 17535-17545.

Zhang, J. F., Green, H. W., Bozhilov, K., and Jin, Z. M., 2004. Faulting induced by precipitation of water at grain boundaries in hot subducting oceanic crust. *Nature* **428**, 633-636.

Table Captions

Figure Captions

Fig. 2-7 Sketch map for the Deformation DIA

Fig. 2-8a Stress vs. strain for San Carlos olivine during the deformation experiment of run San113 at 25°C. The strain is the macroscopic strain including the elastic and plastic strain, which is measured from the X-ray radiograph images. The stress is the average of the values deduced from five peaks (021), (101), (130), (131) and (112).

Fig. 2-8b Strain as a function of time for San Carlos olivine during the deformation experiment of run San113 at 25°C, 5 PGa. The strain rate is about 3 x 10^{-5} s^{-1}. A little fluctuation is found during the experiment.

Fig. 2-9a Stress vs. strain for San Carlos olivine during the deformation experiment of run San 114 at 500°C, 5 GPa. The strain is the macroscopic strain including the elastic and plastic strain, which is measured from the X-ray radiograph images. The stress is the average of the values deduced from five peaks (021), (101), (130), (131) and (112).

Fig. 2-9b Strain as a function of time for the San Carlos olivine deformation experiment of run San 114 at 500°C, 5 PGa. The strain rate is about 2.5 x 10^{-5} s^{-1}. A little fluctuation is found during the experiment

Fig. 2-10a Stress vs. time at 700°C. The strain is the macroscopic strain including the elastic and plastic strain, which is measured from the X-ray radiograph images. The stress is the average of the values deduced from five peaks (021), (101), (130), (131) and (112). Pink square, Ni foil buffered specimen; blue diamond, unbuffered specimen.

Fig. 2-10b Strain as a function of time for San Carlos olivine deformation experiment of run San 80 at 700°C and 5 GPa. Pink square, Ni foil buffered specimen; blue diamond, unbuffered specimen.

Fig. 2-11a Stress vs. time for the deformation of San 83. The stress is the average of the values deduced from five peaks (021), (101), (130), (131) and (112). Pink square, Ni foil buffered specimen; blue diamond, unbuffered specimen.

Fig. 2-11b Stress vs. time for the deformation of San 106. The stress is the average of the values deduced from five peaks (021), (101), (130), (131) and (112).

Fig. 2-11c Strain as a function of time for San Carlos olivine deformation experiment of run San 106. Pink square, Ni foil buffered specimen; blue diamond, unbuffered specimen.

Fig. 2-12a Stress vs. temperature for San Carlos olivine during the deformation of olivine in increase and decrease temperature cycles at 5 GPa. The temperature is measured by the W3%Re-W25%Re thermalcouple. The stress is the average of the values deduced from five peaks (021), (101), (130), (131) and (112). Blue diamond, temperature increase cycle; open square, temperature decrease cycle. The three shadow areas are the calculated power-law creep data with strain rates of $10^{-5}s^{-1}$ (dark green), $10^{-12}s^{-1}$ (light blue) and $10^{-15}s^{-1}$ (red), repectively. The parameters are from Mei and Kohlstedt (2000b). V* is set to 2 x 10^{-6} m^3mol^{-1}. The left boundary (solid line in the same color) in each area is the line with n=3.5 and the right one (solid line in the same color) is the line with n=3.

Fig. 2-12b Strain as a function of time for San Carlos olivine deformation experiment of run San 80 at 700°C and 5 GPa

Fig.2-13 Differential stress vs. temperature for San Carlos olivine during deformation. Pink square, this study; open circle, Raterron et al. (2004); blue diamond, Weidner et al. (2001); open triangle, Evans and Geotze (1979); open square, Meade and Jeanloz (1990).

Fig. 2-14 Stress as a function of strain for different planes, 5 GPa, 500°C. Blue Diamond: (021); pink square: (101); open triangle: (130); black X: (131); green circle: (112).

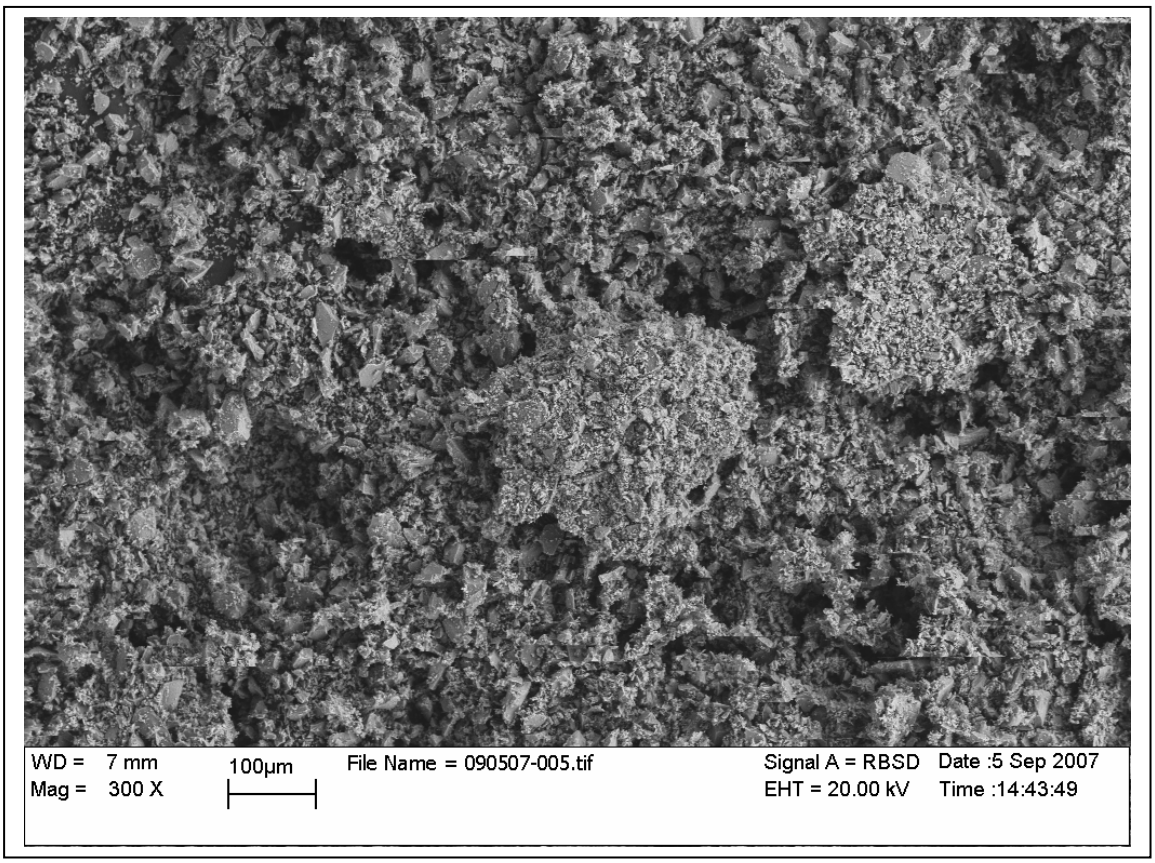

Fig. 2-1 SEM image of San Carlos olivine powder used as starting material in this study.

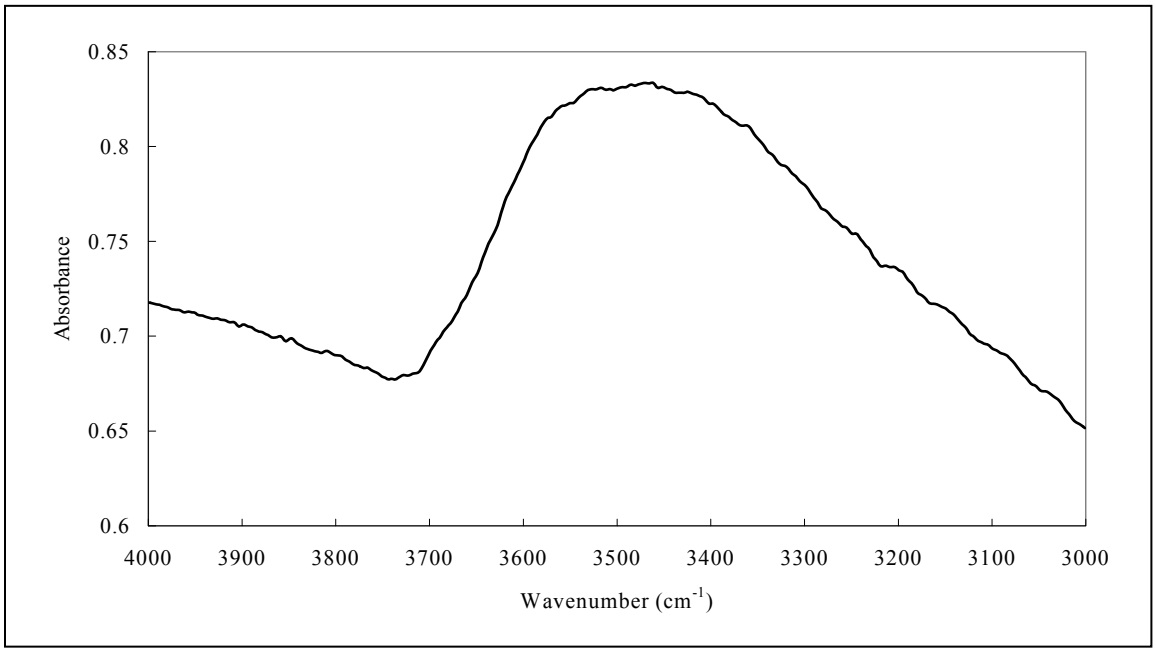

Fig. 2-2A Diagram of absorbance vs. wavenumber of recovered San Carlos olivine polycrystalline sample, San 113. Sample is deformed at 5 GPa, 25°C.

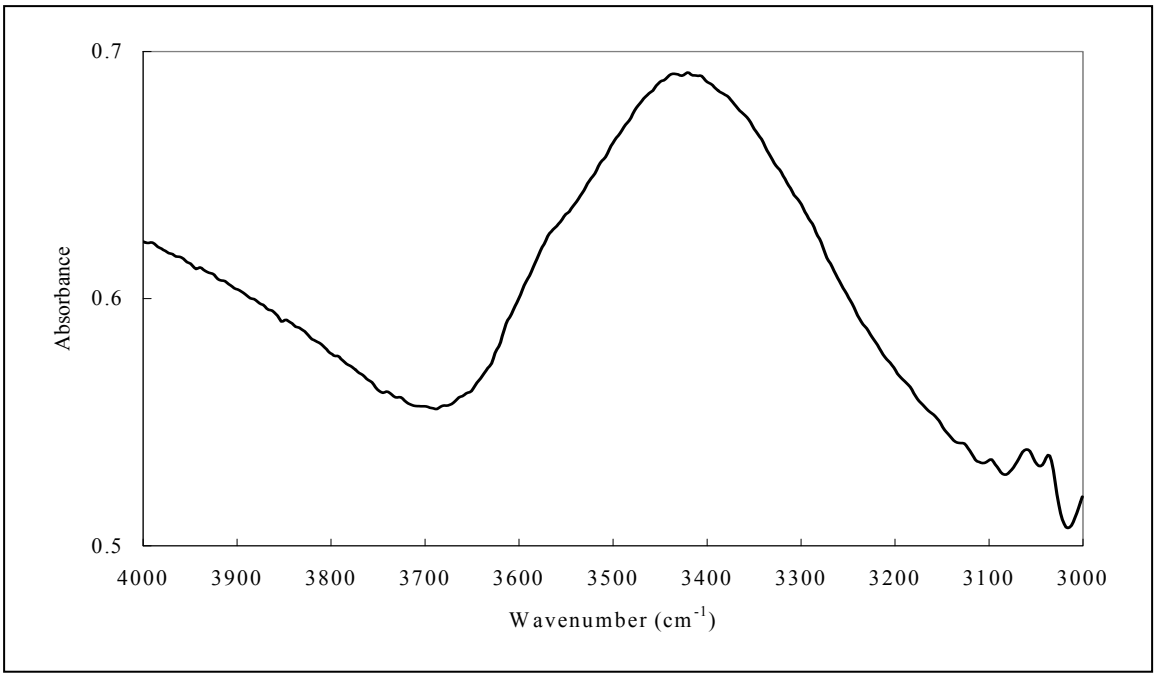

Fig. 2-2B Diagram of absorbance vs. wavenumber of recovered San Carlos olivine polycrystalline sample, San 114. Sample is deformed at 5 GPa, 500°C.

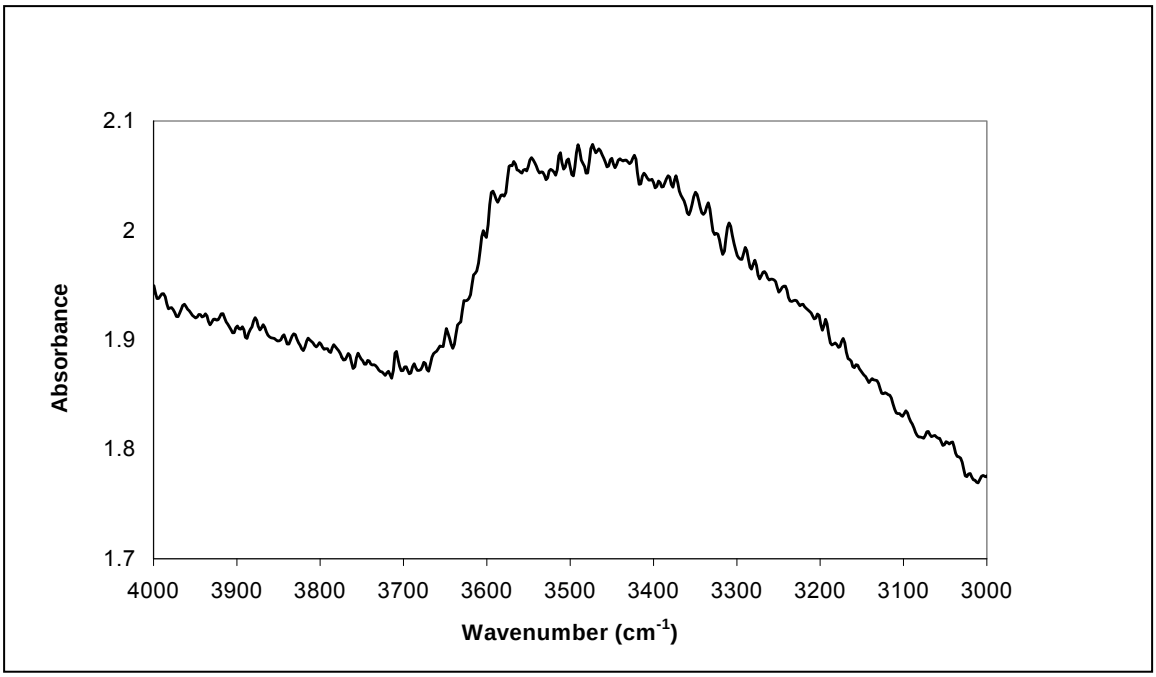

Fig. 2-2C Diagram of absorbance vs. wavenumber of recovered San Carlos olivine polycrystalline sample, San 80. Sample is deformed at 5 GPa, 700°C.

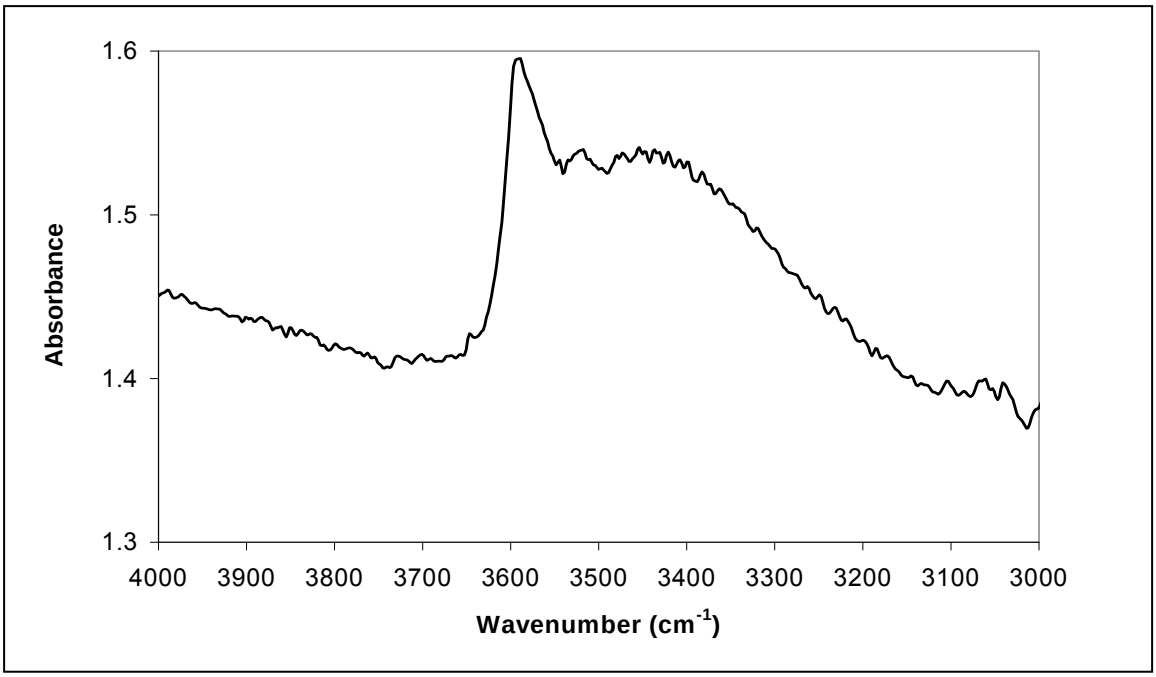

Fig. 2-2D Diagram of absorbance vs. wavenumber of recovered San Carlos olivine polycrystalline sample, San 83. Sample is deformed at 5 GPa, 900°C.

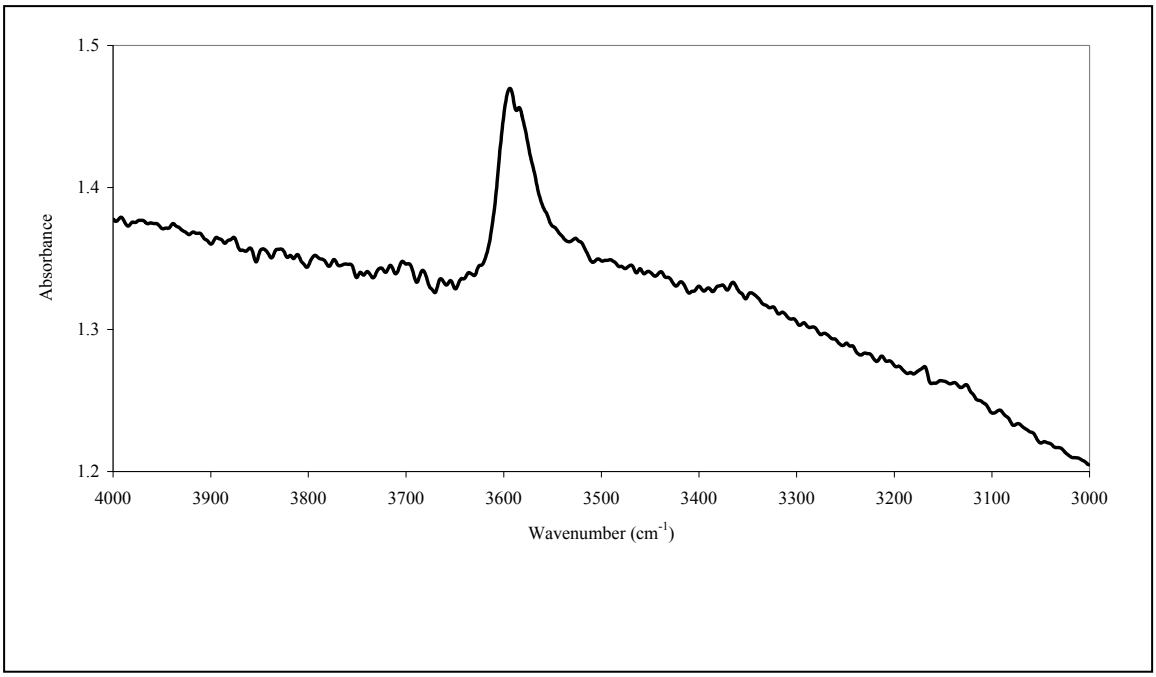

Fig. 2-3 Diagram of absorbance vs. wavenumber of recovered San Carlos olivine polycrystalline sample, San 63. Sample is cold compressed and then is heated at 1200°C for 2 hours before it gets quenched. No deformation is applied.

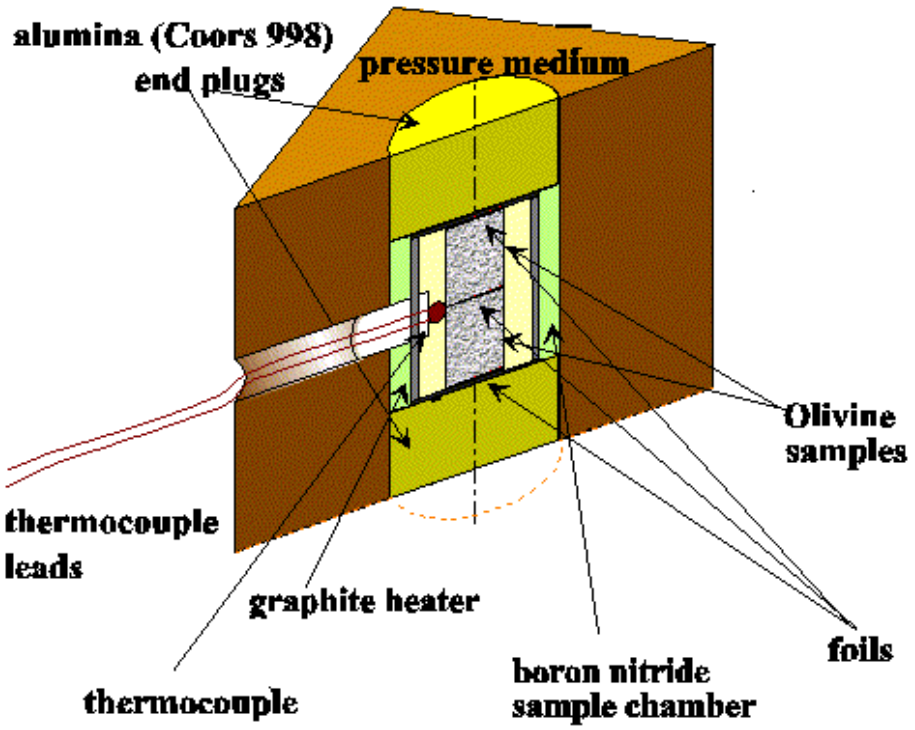

Fig. 2-4 Cell assembly with side-entry thermalcouple used in the deformation experiments on a D-DIA apparatus, SAM 85. The pressure media is a 6.25 mm-edge length cube, made from boron epoxy or mullite. A W3%Re-W25%Re thermalcouple is placed next to the olivine sample and is used to measure the temperature during the experiment. Two alumina pistons are placed at the top and the bottom of the specimen to yield the stress in the experiment. Cell assembly with top-entry thermalcouples, which is similar to this assembly except the entry of thermalcouple, is also used in this study.

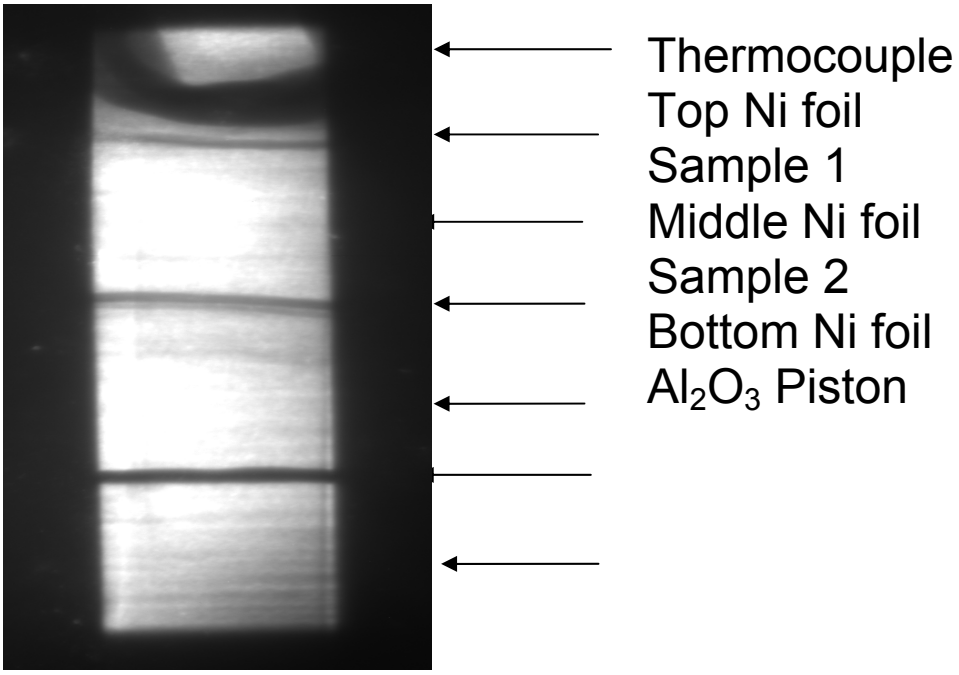

Fig. 2-5 Sample image taken by the in situ X-ray radiograph technique during the deformation experiment. The dark shadow surrounding is the gap of the anvils. The dark wires on the top are the thermalcouple. The light material surrounding the thermalcouple is the hard alumina piston with four holes on, which allows thermalcouple to go through and work properly. The three dark lines are Ni foils used as the strain markers. The light materials between the Ni markers are olivine specimens. The bottom is the hard alumina piston.

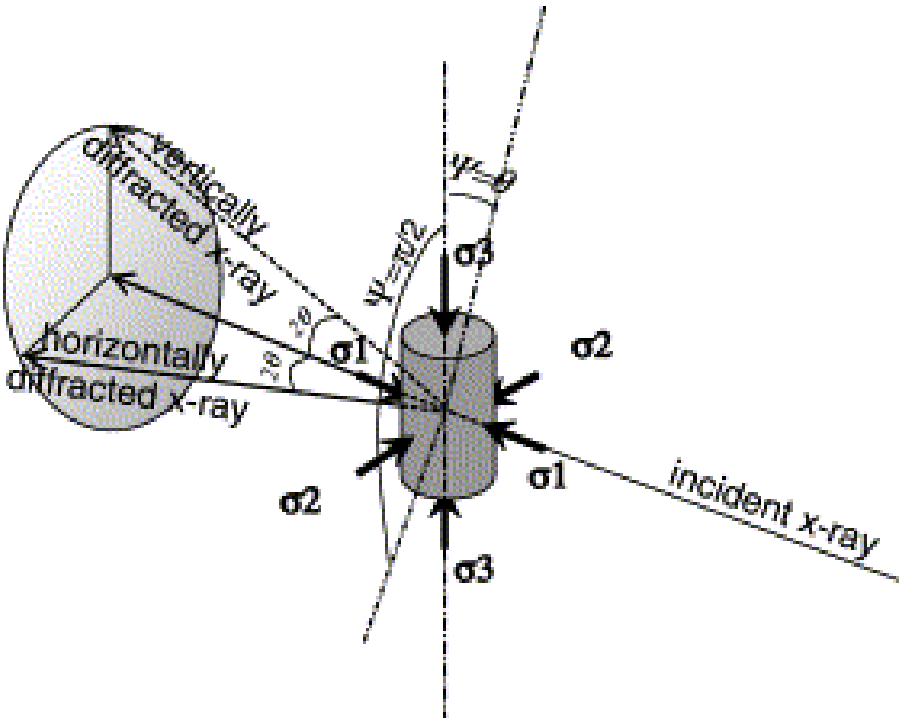

Fig. 2-6 Geometry of X-ray diffraction and stress field in a multi anvil high pressure apparatus. θ the Bragg angle of the X-ray diffraction, ψ the angle between diffraction vector and principal stress ($\sigma 3$) axis. (Following Chen *et al*. 2004)

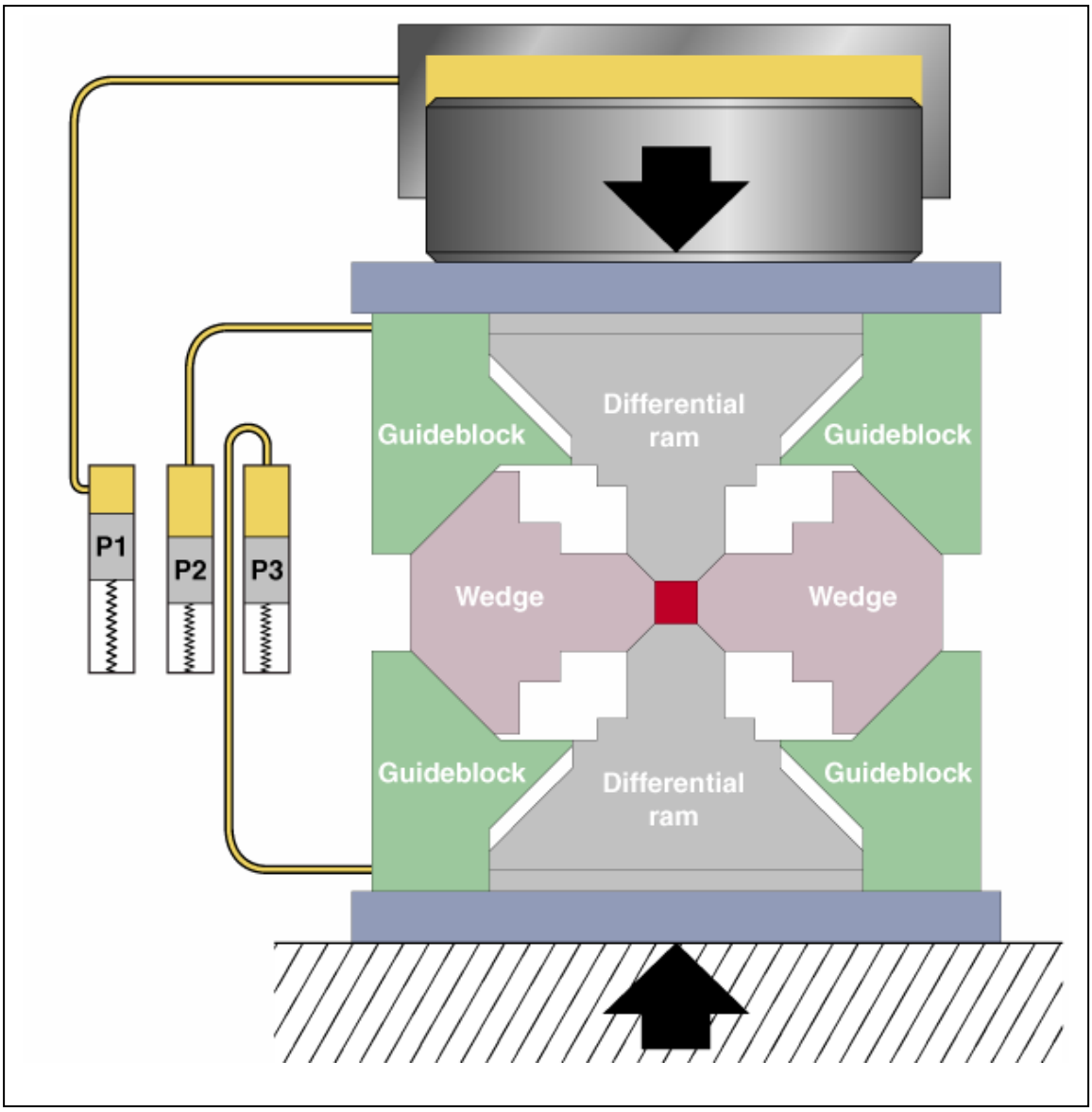

Fig. 2-7 Sketch map for the Deformation DIA

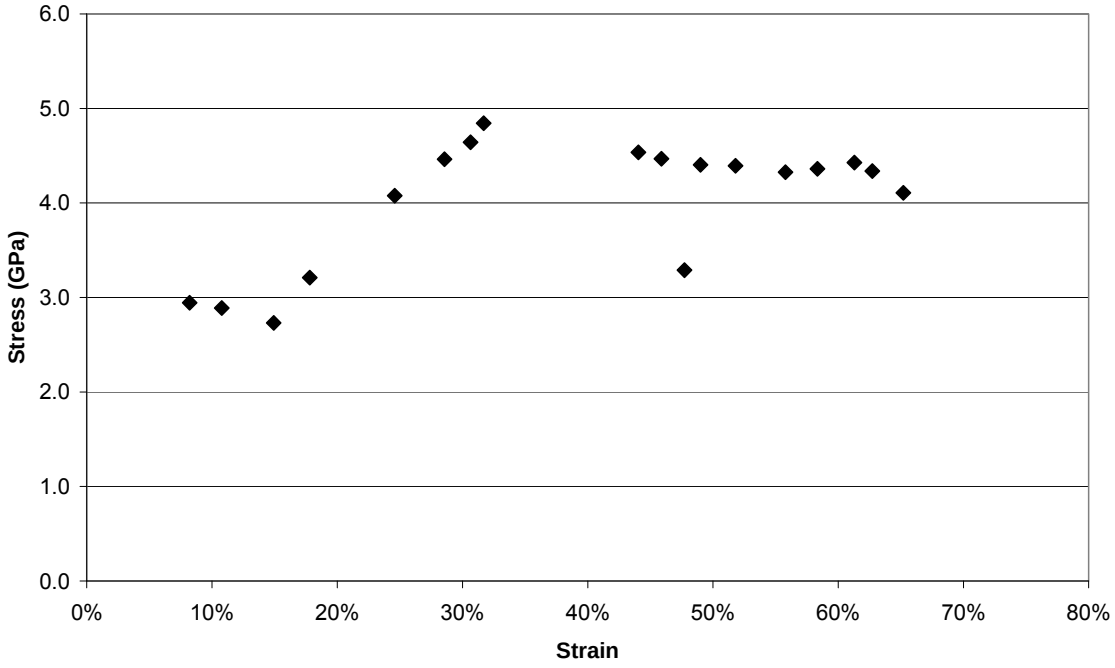

Fig. 2-8a Stress vs. strain for San Carlos olivine during the deformation experiment of run San113 at 25°C. The strain is the macroscopic strain including the elastic and plastic strain, which is measured from the X-ray radiograph images. The stress is the average of the values deduced from five peaks (021), (101), (130), (131) and (112).

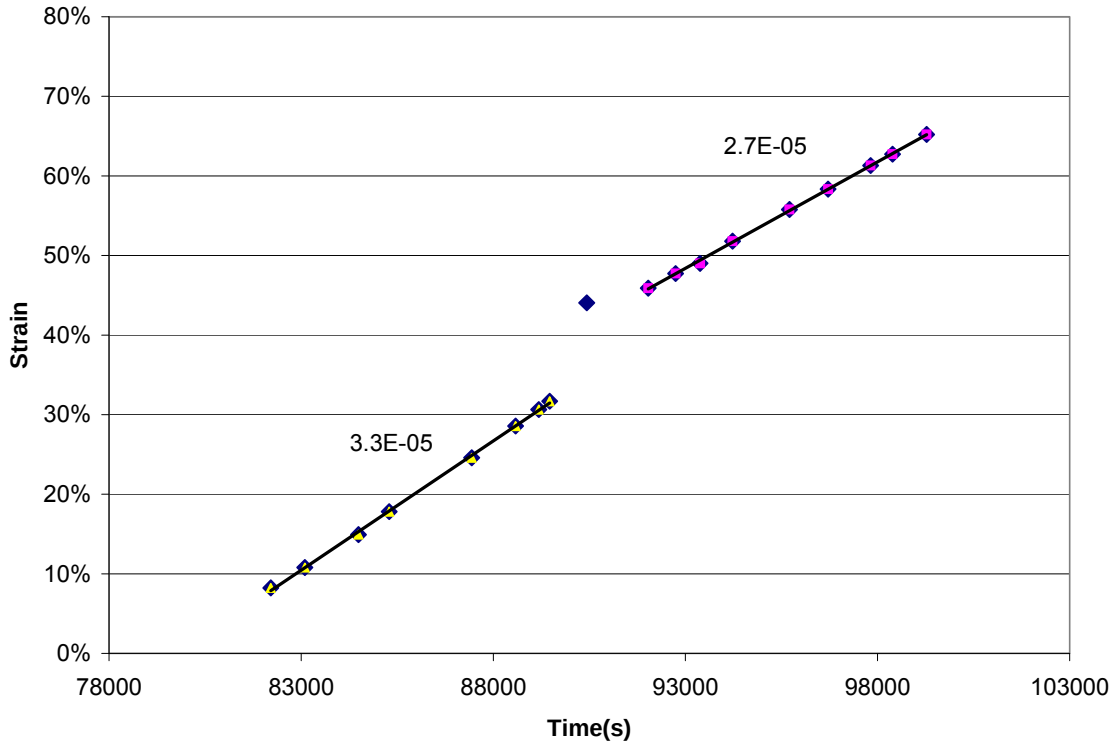

Fig. 2-8b Strain as a function of time for San Carlos olivine during the deformation experiment of run San113 at 25°C, 5 PGa. The strain rate is about 3 x 10^{-5} s^{-1}. A little fluctuation is found during the experiment.

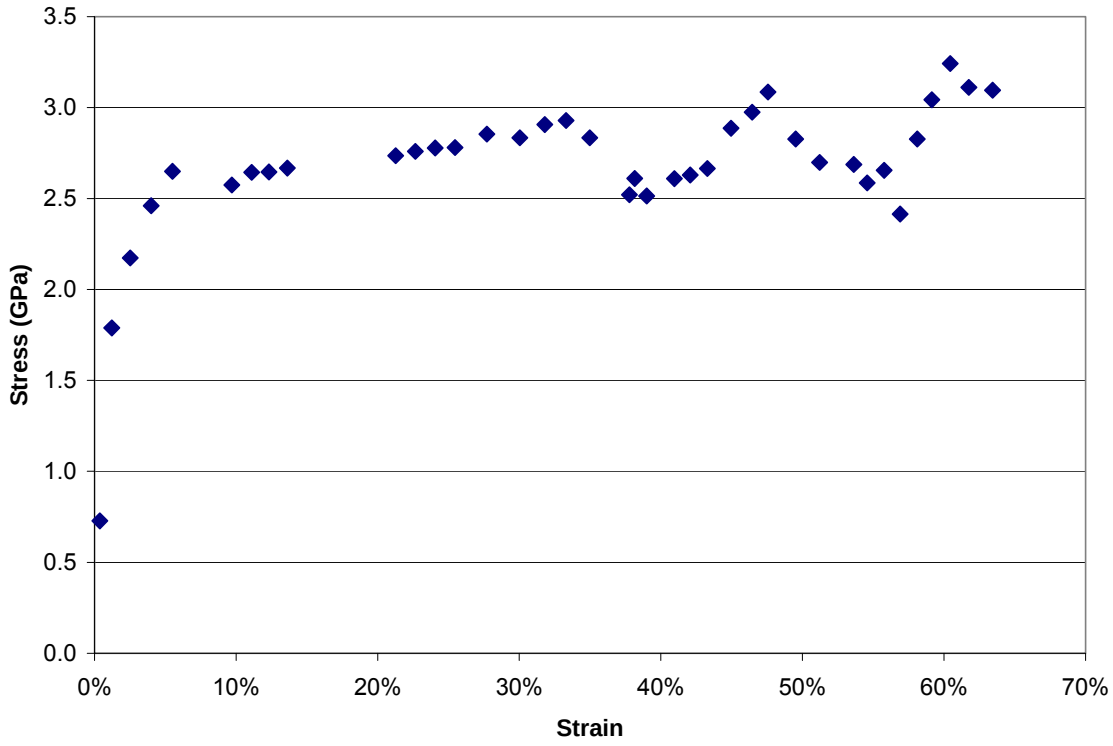

Fig. 2-9a Stress vs. strain for San Carlos olivine during the deformation experiment of run San 114 at 500°C, 5 GPa. The strain is the macroscopic strain including the elastic and plastic strain, which is measured from the X-ray radiograph images. The stress is the average of the values deduced from five peaks (021), (101), (130), (131) and (112).

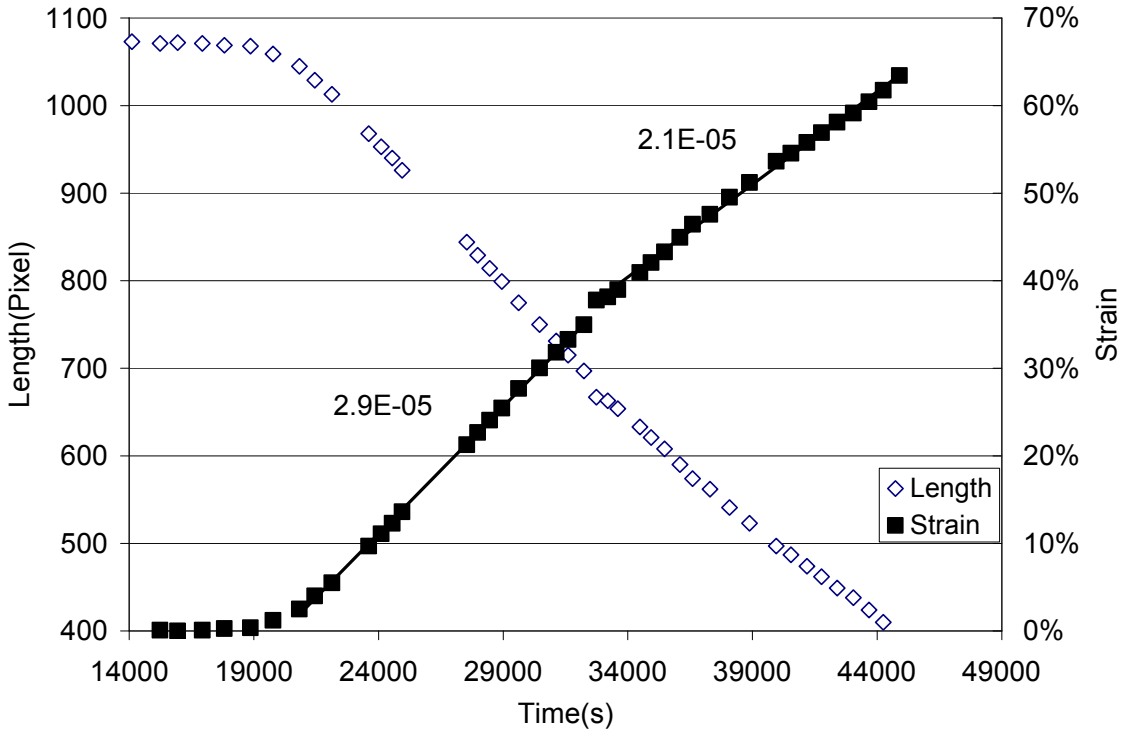

Fig. 2-9b Strain as a function of time for the San Carlos olivine deformation experiment of run San 114 at 500°C, 5 PGa. The strain rate is about 2.5 x 10^{-5} s^{-1}. A little fluctuation is found during the experiment

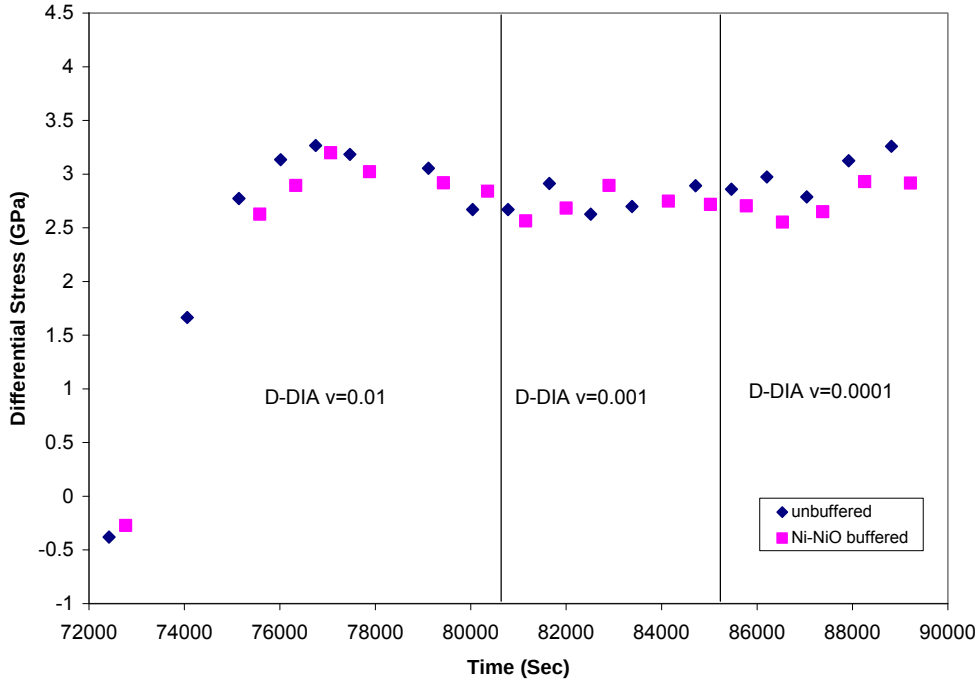

Fig. 2-10a Stress vs. time at 5 GPa, 700°C, San 80. The stress is the average of the values deduced from five peaks (021), (101), (130), (131) and (112). Pink square, Ni foil buffered specimen; blue diamond, unbuffered specimen.

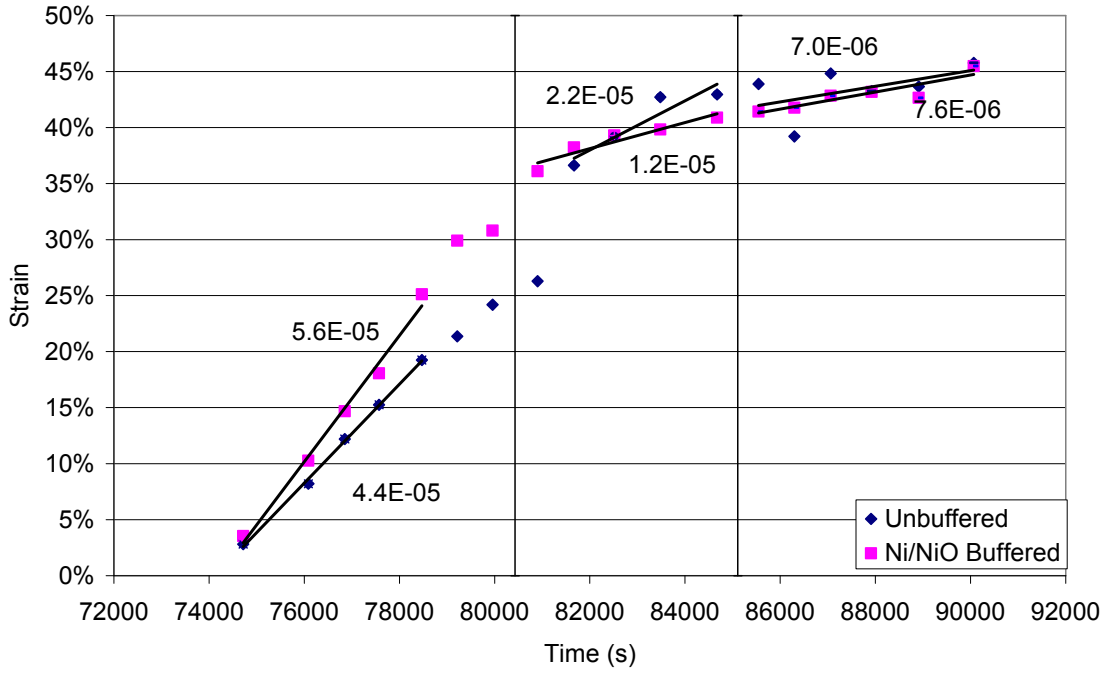

Fig. 2-10b Strain as a function of time for San Carlos olivine deformation experiment of run San 80 at 700°C and 5 GPa. Pink square, Ni foil buffered specimen; blue diamond, unbuffered specimen.

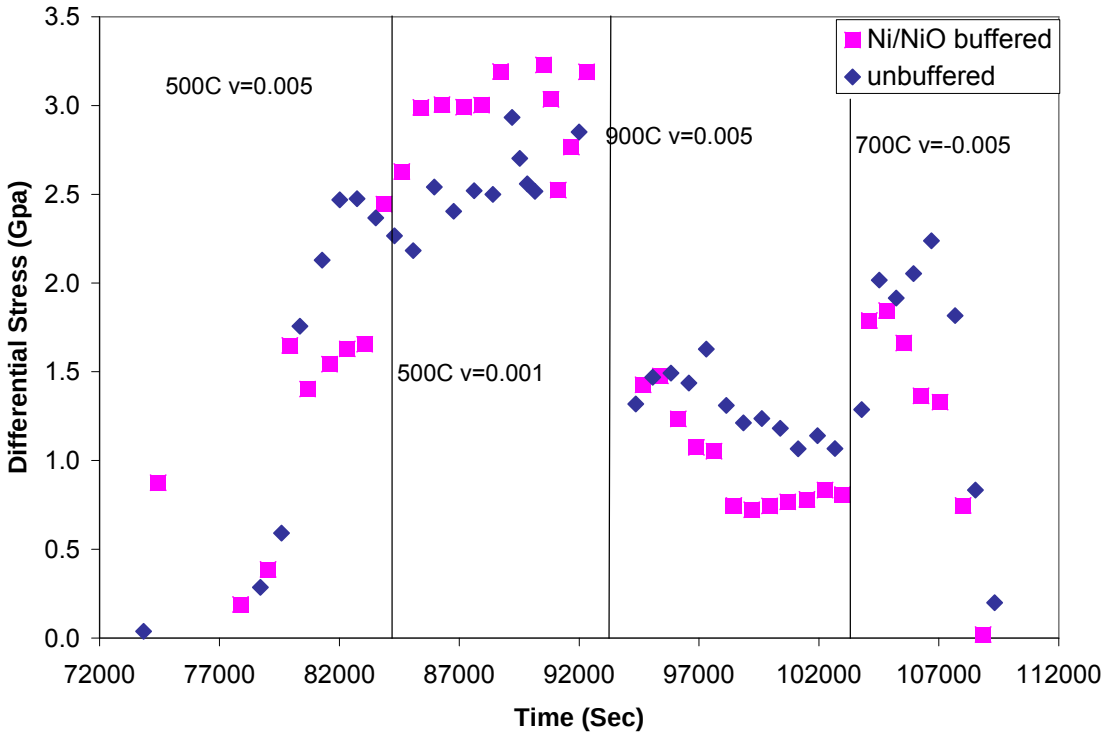

Fig. 2-11a Stress vs. time for the deformation of San 83. The stress is the average of the values deduced from five peaks (021), (101), (130), (131) and (112). Pink square, Ni foil buffered specimen; blue diamond, unbuffered specimen.

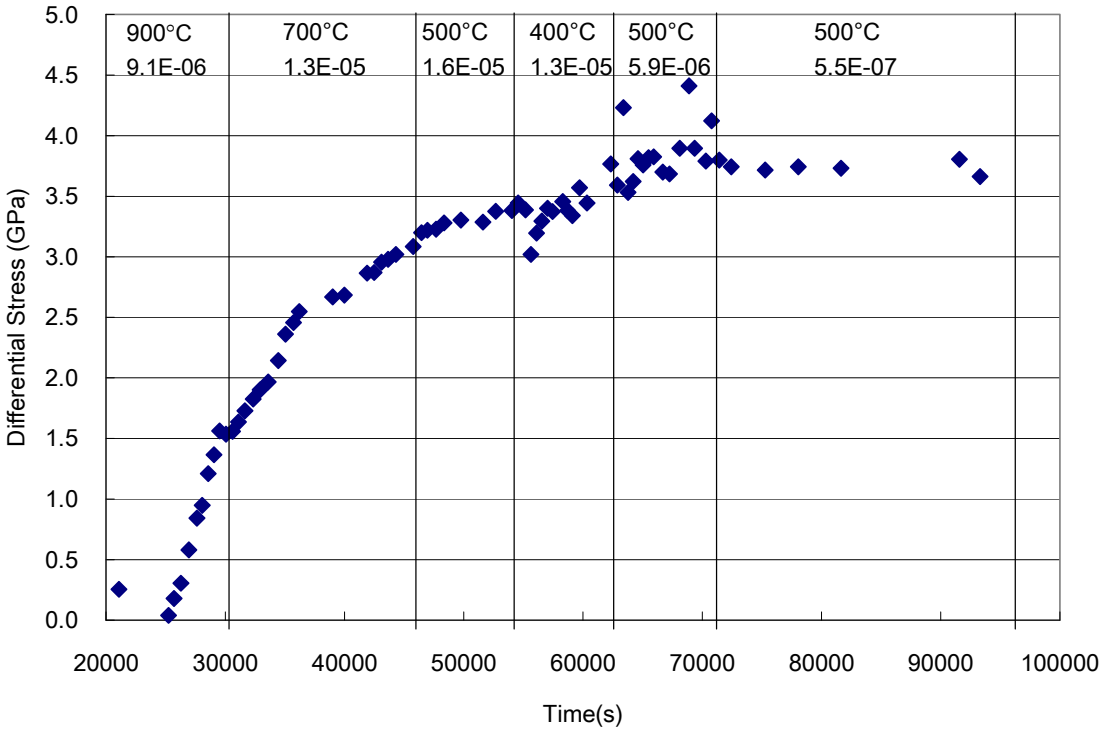

Fig. 2-11b Stress vs. time for the deformation of San 106. The stress is the average of the values deduced from five peaks (021), (101), (130), (131) and (112).

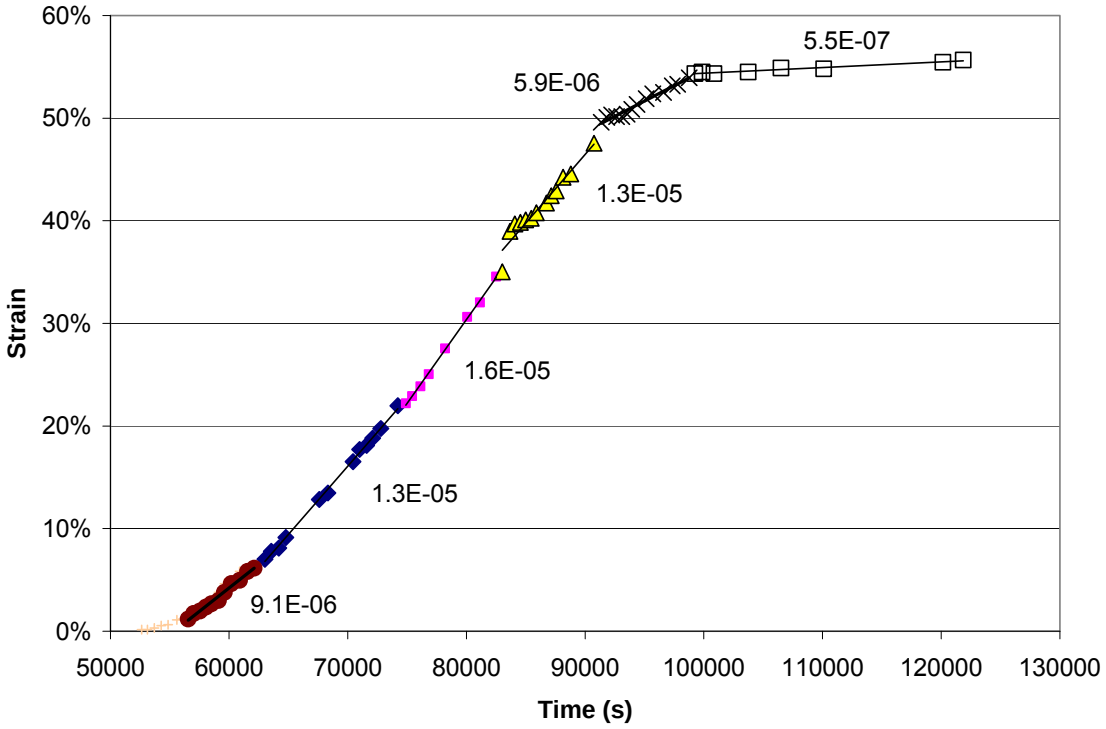

Fig. 2-11c Strain as a function of time for San Carlos olivine deformation experiment of run San 106.

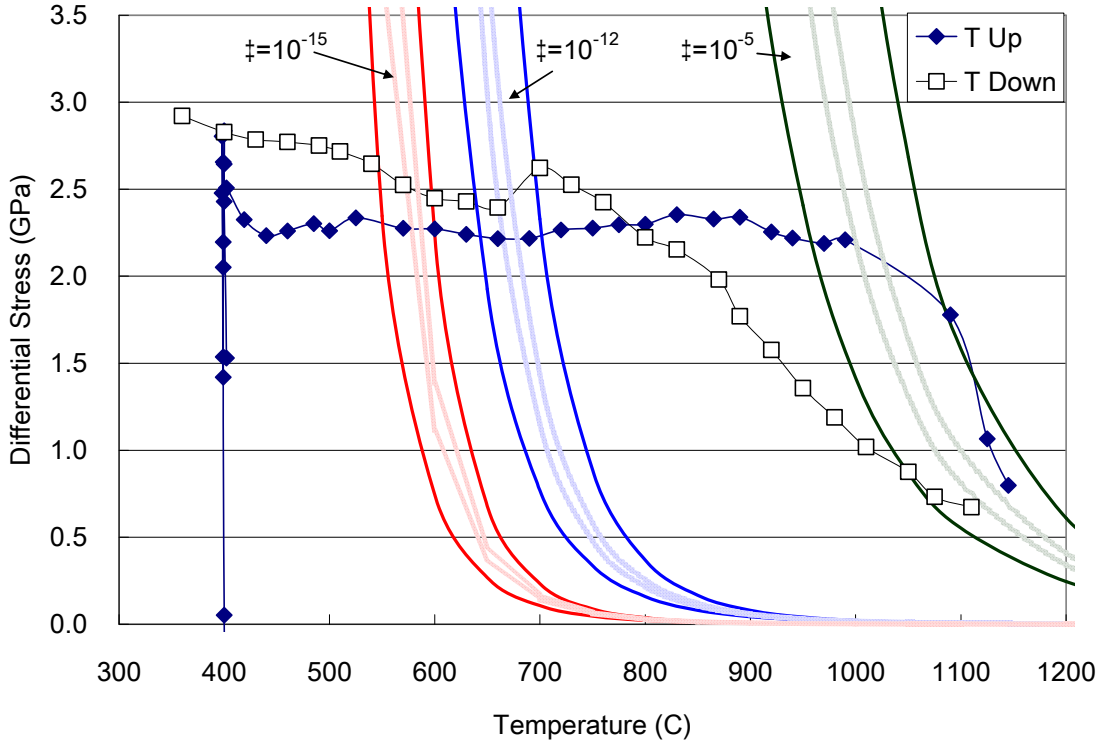

Fig. 2-12a Stress vs. temperature for San Carlos olivine during the deformation of olivine in increase and decrease temperature cycles at 5 GPa, San 123. The temperature is measured by the W3%Re-W25%Re thermalcouple. The stress is the average of the values deduced from five peaks (021), (101), (130), (131) and (112). Blue diamond, temperature increase cycle; open square, temperature decrease cycle. The three shadow areas are the calculated power-law creep data with strain rates of $10^{-5}s^{-1}$ (dark green), $10^{-12}s^{-1}$ (light blue) and $10^{-15}s^{-1}$ (red), repectively. The parameters are from Mei and Kohlstedt (2000b). V* is set to 2 x 10^{-6} m^3mol^{-1}. The left boundary (solid line in the same color) in each area is the line with n=3.5 and the right one (solid line in the same color) is the line with n=3.

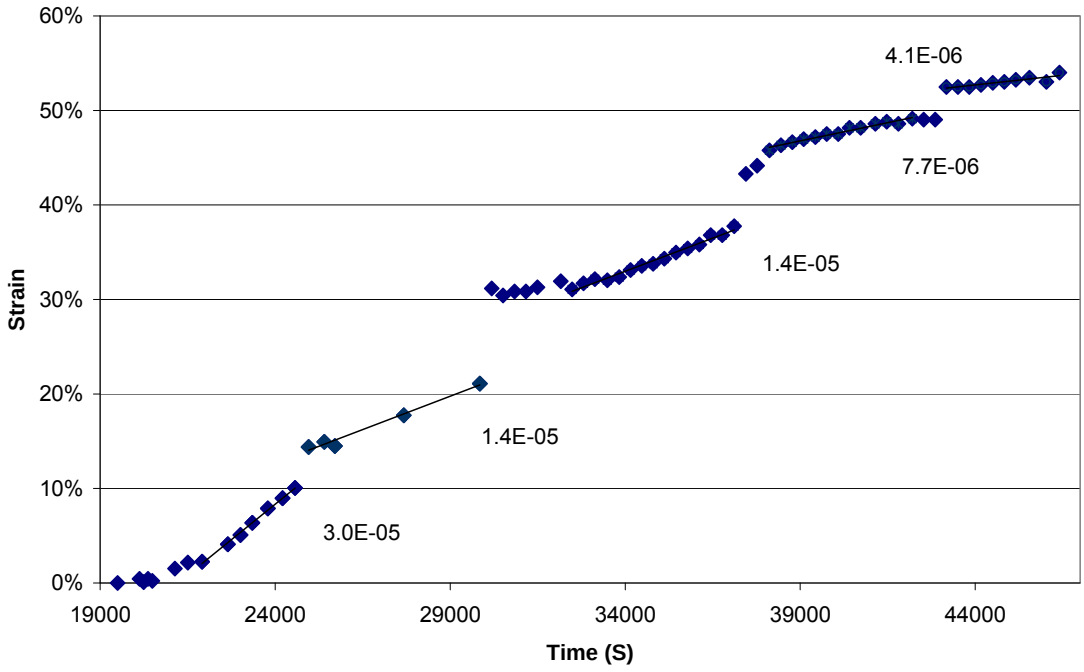

Fig. 2-12b Strain as a function of time for San Carlos olivine deformation experiment of run San 123, 5 GPa.

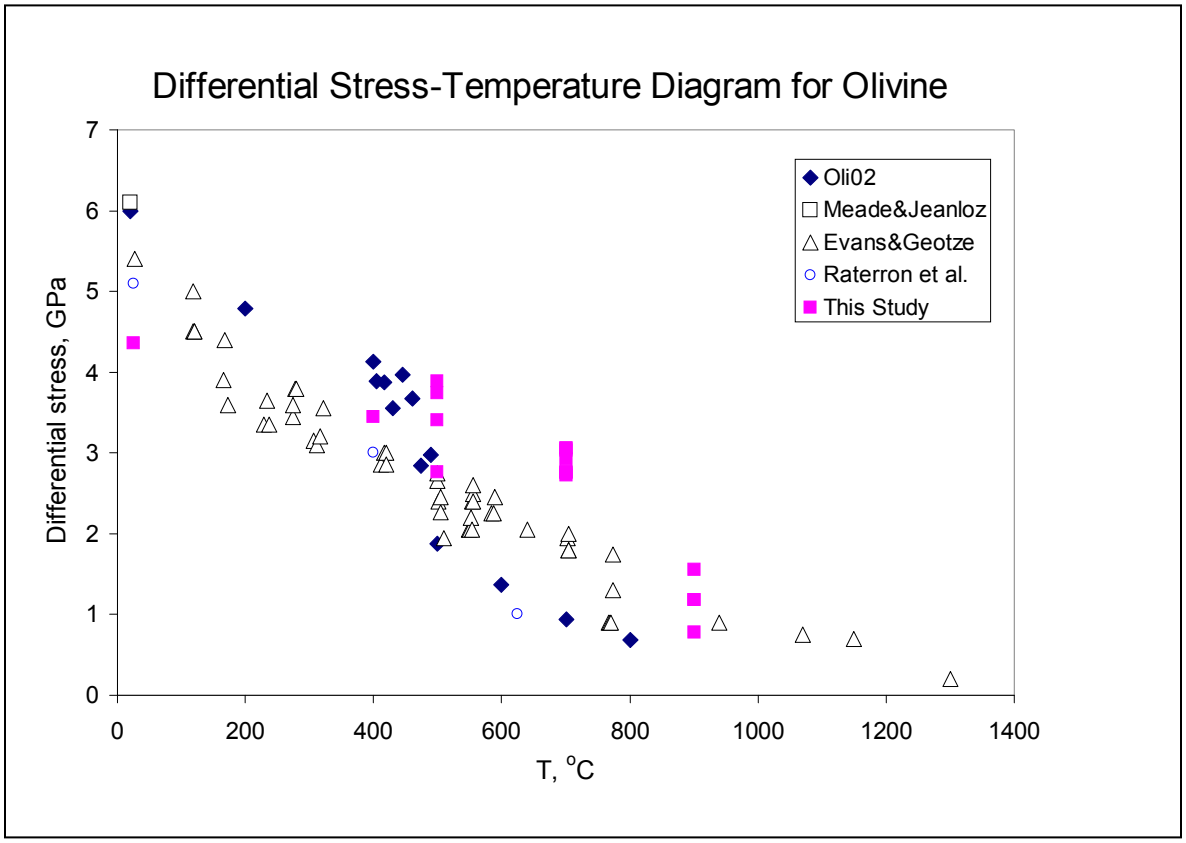

Fig.2-13 Differential stress vs. temperature for San Carlos olivine during deformation. Pink square, this study; open circle, Raterron et al. (2004); blue diamond, Weidner et al. (2001); open triangle, Evans and Geotze (1979); open square, Meade and Jeanloz (1990).

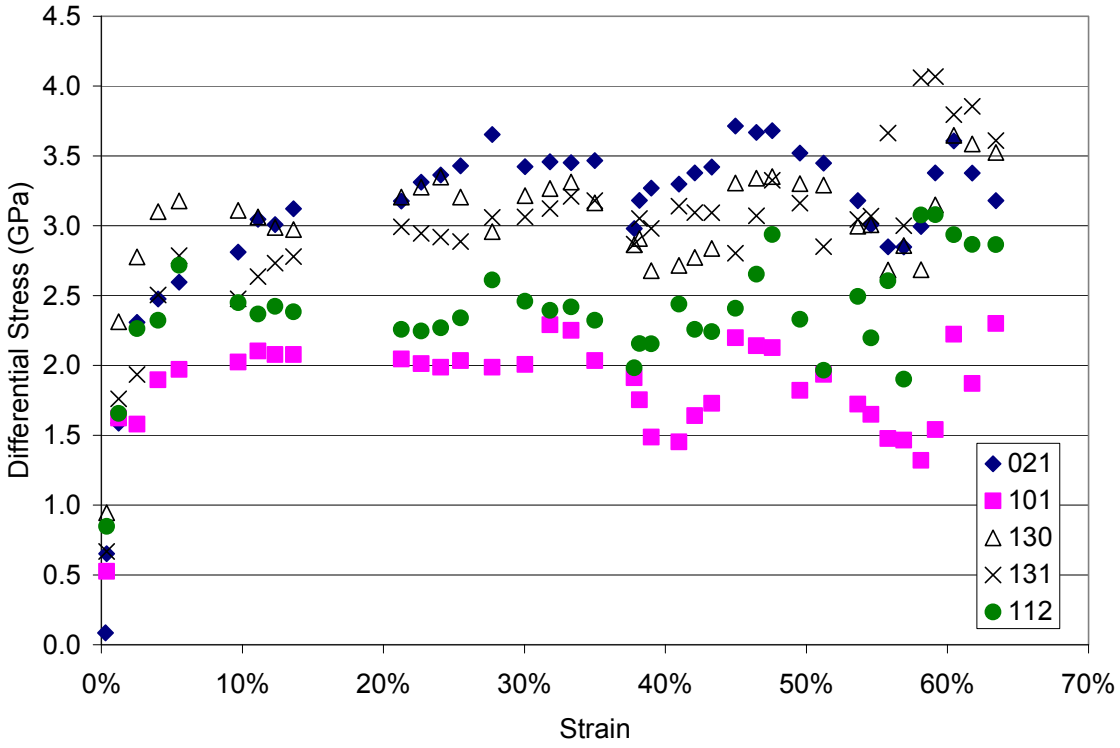

Fig. 2-14 Stress as a function of strain for different planes, 5 GPa, 500°C. San 114. Blue Diamond: (021); pink square: (101); open triangle: (130); black X: (131); green circle: (112).

Table 2-1 Parameters in the EoS Calculation [1]

K_{S0} [2]	130.3
K_{S0}' [2]	4.61
α [3]	26.3 x 10^{-6}
γ [4]	1.28
$1+\alpha\gamma T$	1.010032
K_{0T} [5]	129.1048
K_{0T}' [5]	4.564212
T(*ref*),K	298.15

1. K_S and K_T are the isothermal and adiabatic incompressibilities, respectively.

2. From Liu et al. (2005).

3. The volume coefficient of thermal expansivity (From Suzuki, 1975).

4. The Gruneisen parameter (From Isaak, 1992).

5. $K_{0T} = K_{S0}/(1+\alpha\gamma T)$, $K_{0T}' = K_{S0}'/(1+ \alpha\gamma T)$.

Table 2-2 Elastic constants for olivine

C =	325.4700	70.7700	72.8600	0	0	0
	70.7700	199.0600	75.8400	0	0	0
	72.8600	75.8400	237.0100	0	0	0
	0	0	0	64.5900	0	0
	0	0	0	0	78.4200	0
	0	0	0	0	0	79.0700

Table 2-3 Elastic constants for olivine (Continued)

S =	0.0034	-0.0009	-0.0008	0	0	0
	-0.0009	0.0060	-0.0016	0	0	0
	-0.0008	-0.0016	0.0050	0	0	0
	0	0	0	0.0155	0	0
	0	0	0	0	0.0128	0
	0	0	0	0	0	0.0126

Table 2-4 Summary of Deformation Experiment Results for San Carlos Olivine at Subduction Zone Conditions

		T (K)[a]	P (Gpa)	Strain Rate	Stress (Gpa)					
					(021)[b]	(101)	(130)	(131)	(112)	Average
San80	Unbuffered[c]	973	5.3	4.42E-05			3.14	3.33	2.72	3.06
			4.8	3.38E-05			2.99	2.74	2.55	2.76
			5.1				3.06	3.19	2.86	3.04
	Buffered	973	5.8	5.63E-05			2.85	3.35	2.55	2.92
			4.0	1.16E-05			2.98	2.95	2.24	2.72
			4.6				2.88	2.94	2.44	2.75
San83	Unbuffered	1173	5.0				1.35	1.33	0.84	1.17
	Buffered		5.0				0.66	1.00	0.66	0.77
San105	Unbuffered	1173	5.1	8.63E-06	1.05	0.93	1.53	1.45	0.93	1.18
		973	5.2	1.05E-05	3.21	2.01	3.17	3.18	2.28	2.77
San106	Unbuffered	1173	5.2	9.12E-06	1.42	1.37	1.81	1.93	1.21	1.55

		973	4.6	1.33E-05	3.71	2.06	3.56	3.68	2.31	3.06
		773	4.6	1.64E-05	4.20	2.59	3.82	3.73	2.71	3.41
		673	4.3	1.33E-05	4.23	2.80	3.85	3.73	2.63	3.45
		773	4.9	5.94E-06	4.50	3.29	4.20	4.28	3.15	3.88
		773	4.7	5.55E-07	4.38	3.32	4.10	3.88	3.02	3.74
San113	Unbuffered	298	4.8	3.25E-05	4.81	3.94	4.57	4.41	4.05	4.36
San114	Unbuffered	773	5.0	2.92E-05	3.25	1.90	3.11	3.11	2.44	2.76

a. W3%Re-W25%Re thermalcouple. T in San 80 is calibrated from the existing power-temperature relationship. b. individual X-ray diffraction peak. c. Ni foil buffered/unbuffered.

Table 2-5 Calculated **n** from the experimental data using power-law equation

T	$\dot{\varepsilon}$	σ	n
298.15	3.0×10^{-5}	4.4	20.8
673.15	1.4×10^{-5}	3.5	8.1
773.15	1.4×10^{-5}	2.8	6.9
823.15	1.4×10^{-5}	2.3	6.5
873.15	1.4×10^{-5}	2.3	6.0
973.15	1.4×10^{-5}	2.3	5.1
1073.15	1.4×10^{-5}	2.3	4.4
1173.15	1.4×10^{-5}	2.3	3.8
1213.15	1.4×10^{-5}	2.3	3.6
1243.15	1.4×10^{-5}	2.2	3.5
1263.15	1.4×10^{-5}	2.2	3.4
1373.15	1.4×10^{-5}	1.8	3.0
1398.15	1.4×10^{-5}	1.1	3.1
1418.15	1.4×10^{-5}	0.8	3.1

The equation $\dot{\varepsilon} = A\sigma^n \exp(-\frac{E^* + PV^*}{RT})$ is used in calculation. The value of active volume (V*) is given to be $2 \times 10^{-6} m^3 mol^{-1}$. The other parameters in the equation are from Mei and Kohlstedt (2000b).

Chapter 3

SEM and EBSD Study on the Microstructure of Deformed Olivine at High Pressure and Low Temperature

3.1 Abstract

SEM and EBSD studies have been done for the recovered olivine specimens from the deformation experiments performed at subduction zone conditions and mantle pressure, on a D-DIA apparatus, SAM85, at X17B2 of NSLS. The SEM results show that compression and deformation make the grain size of olivine into sub-micron level. The pseudo grains in the recovered sample may be the relics developed from the starting olivine grains and become foliations vertical to the deforming axis undergoing the deformation. In the EBSD study, The LPO shows that the predominant active slip systems of olivine at subduction zone condition and mantle pressure evolve from {*hk0*}[001] ($h > k$) and {110}[001] at 500°C to {*hk0*}[001] ($h > k$) and (100)[001] at 700°C. The occurrence of active (100)[001] represents that power-law creep has involved in playing an important role together with the low temperature plasticity. Predominant active (100)[001] system of olivine in the slab may result in the seismic anisotropy different from the conventional mantle.

3.2 Introduction

Olivine is the dominant mineral in the upper mantle and the ocean lithosphere. Its chemical composition can be written as α-M_2SiO_4, in which M is the metal atom. In nature, olivine is the solid solution of two end members: forsterite (Mg_2SiO_4) and fayalite (Fe_2SiO_4). The composition of olivine in the earth's mantle is believed to be near $(Mg_{0.9}Fe_{0.1})_2SiO_4$. In subduction zones, the rheology of the slab is mainly controlled by that of olivine at "low" temperatures. Here we define the range of "low" temperature to be less than the temperature in which the deformation is dominated by power-law creep. The common slip system of olivine is reported to be (100)[001] (Raleigh, 1968), {110}[001] (Evans and Geotze, 1979; Mercier, 1985) and {*hk0*}[001] (Raleigh, 1968) at low temperature while (010)[100] (Nicolas et al., 1973) and {*hk0*}[001] (Couvy et al., 2004) at high temperature in the regime of power-law creep. (010)[001] is also found to be active above 500°C in the low temperature plasticity regime (Li et al., 2003; Raterron et al., 2004). A recent study shows that the active slip system of olivine transforms from [100] direction to [001] direction along with the increase of the pressure at high pressure and temperature (Raterron et al., 2007).

Despite of its importance, rheological studies on olivine at high pressure (>3 GPa) and low temperature, the subduction zone conditions, are limited due to experimental technical difficulties. Only a few related literatures (Evans and Geotze, 1979; Meade and Jeanloz, 1990) are published by other means other than the high pressure and temperature experimental apparatus. With the development of multi-anvil apparatus (Durham and

Rubie, 1998) and the development of synchrotron *in situ* X-ray measurement of stress and strain on the large volume multi-anvil press (Weidner et al. 1992a and b; Weidner et al. 1994; Weidner; 1998; Weidner et al. 1998), literatures based on the relaxation experiments have been reported regarding olivine at high pressure and low temperature (Chen et al., 1998; Raterron et al., 2004). However, it is neither a direct extension of traditional deformation experiment, nor a direct extension of traditional strain and stress measurements. In such experiments the strain rate can not be controlled. Yet the stress at steady state can not be determined. Furthermore, the assumption of constant total microscopic strain (sum of both elastic and plastic strain) yields additional uncertainties to construct a flow law from the experimental data (Chen et al. 2004). Deformation DIA (D-DIA) apparatus has been recently developed (Durham et al. 2002; Wang et al. 2003). One of the characteristics of D-DIA is that it can keep a constant strain rate at pressure up to over 10 GPa, which allows performing the steady state deformation experiment at high pressure. It also has an advantage in fitting the *in situ* synchrotron X-ray measurements for stress and strain, which have been recently developed (Chen et al. 2004; Li et al. 2003; Li et al. 2004a and b; Li et al. 2006a and b; Uchida et al. 2004).

We perform a number of deformation experiments of San Carlos olivine polycrystalline based on a D-DIA facility, SAM85, at X17B2 of National Synchrotron Light Source (NSLS) (see our other paper for details). Here we report our results of SEM and EBSD analysis for the recovered olivine specimens after the experiments.

3.3 Sample preparation

The samples for the SEM and EBSD study are the recovered samples from the online deformation experiments at 5 GPa and 25°C, 500°C and 700°C performed on a D-DIA facility, SAM85, at X17B2 of NSLS. Cross-section parallel to the deforming direction of samples are made and well mechanically polished. Colloidal silica permanent suspension with grain size of 0.06 μm is used to provide a final chemical polish to remove the shallow layers damaged by the mechanical sample preparation. Sample surface is lightly carbon coated before applying to the SEM and EBSD analysis.

3.4 Analytical Techniques

The Scanning Electronic Microscope (SEM) and Electronic BackScattering Diffraction (EBSD) analysis are performed at the University of California-riverside. SEM is a kind of electronic microscope to scan the sample surface by the electronic beam with high energy and get its image. Back Scattered Electron (BSE) technique is applied to take the images of surface structure.

EBSD is a technique based on the SEM to obtain the microstructural-crystallographic information to elucidate the crystallographic texture or preferred orientation of any crystalline or polycrystalline materials. In the decade EBSD has been well developed. It can automatically determine the crystallographic orientation of an object grain on the polished sample surface. The spatial resolution is about 1 μm and the absolute angular resolution is 1-2°. In this study the EBSD patterns of the samples are collected on Philps XL30 SEM with 20 KV accelerating voltage and 15 mm working

distance, 70° inclining to the sample's surface. The Electron BackScattering Pattern (EBSP) is indexed by the HKL software Channel 5. A freeware developed by David Mainprice (Laboratoire de Tectonophysique, University of Montpellier II, France), PFch5, is used to plot the pole figures. The orientation of each identified crystal is manually collected and confirmed to avoid the unnecessary noise. The reference coordinates are determined as: X-normal to the compression direction in the surface plane of sample, Y-normal to the surface plane, and Z-parallel to the compression direction. Pole figures are projected using equal area to the lower hemisphere with a half width of 20° and a cluster size of 5°.

3.5 Analytical Results and Discussion

3.5.1 SEM

The SEM images for the samples at 25°C and 500°C are shown in **Fig 3-1a** and **b** and **Fig3-2**, respectively. In the images we find that there are numbers of flat "grains" with the long axis from *n* to 40 μm, most of which are perpendicular to the deformation direction or so. We further examine these "grains" by EBSD and find that they are not real single crystal grains. In fact we can only get EBSP at a few points in the area we examine. Since the resolution of EBSD is about 1 μm, it demonstrates that the dominant population of the olivine grains is in sub-micron level and only a few single crystalline grains larger than 1 μm exist in the recovered sample. Similar phenomena have been observed in the recovered olivine samples after compression (Brearley et al., 1992;

Raterron et al., 2004). Raterron et al. (2004) also notice that the number of larger grains (≥ 1 μm) becomes more popular in the recovered sample performed at higher temperature. The pseudo grains in our recovered sample may be the relics developed from the olivine grains before the experiments. They are squeezed into flat shape and become foliations perpendicular to the deforming axis while undergoing the deformation.

3.5.2 EBSD

We try to apply EBSD analysis to the samples at 25°C, 500°C and 700°C. However, only a limited number of grains with good EBSP can be found after testing hundreds of points for about 12 hours per sample. From the recovered sample at 25°C, the number of available data is very limited. So we just report the data from the recovered samples at 500°C and 700°C here.

The Lattice Preferred Orientation (LPO) analysis for the recovered sample of 700°C is shown as pole figures in **Fig 3-3a** and **b**. It demonstrates that the [100] and [hk0] (h>k) align toward the compress axis while the [010] and [001] present a girdle in the plane perpendicular to the compression axis. Thus the predominant active slip systems are (100)[001] and {*hk0*}[001] ($h > k$). We don't observe (010)[001] slip system in our sample, which is reported to be active over 500°C (Li et al., 2003; Raterron et al., 2004). We don't either observe {110}[001] in our sample, which is reported to be the predominant slip systems at 500-900°C (Evans and Goetze, 1979; Mercier, 1985). The predominant active (100)[001] system is in good agreement not only with the previous

studies in both experimental (Raleigh, 1968) and simulated (Wenk, 2002) results, but also with the natural olivine texture in the garnet lherzolite and garnet peridotite in the subduction zone formed at 3 GPa and 750°C (Mockel, 1969; Frese et al., 2003; Xu et al., 2006).

The LPO analysis for the recovered sample at 500°C (**Fig 3-4a** and **b**) illustrates that [110] and [hk0] (h>k) are sub-parallel with the compression axis while [001] presents a girdle in the plane perpendicular to the compression direction. Thus the predominant active slip systems are {110}[001] and {*hk0*}[001] ($h > k$). Unlike the sample at 700°C, there is no sign for an active (100)[001]. Dominant {110}[001] is observed in the similar temperature range (Raleigh, 1968; evans and Goetze, 1979). However, the existence of active {*hk0*}[001] ($h > k$), occurring at 700°C as well in this study, has not yet been found in the low temperature range in other literatures. On the other hand, it is observed at high temperature (Couvy et al., 2004).

The existence of dominant {*hk0*}[001] ($h > k$) at both 500°C and 700°C demonstrates that the same deformation mechanism for olivine is in function for the range of 500-700°C. However, the activation of (100)[001] at 700°C indicates that a new mechanism of deformation joins along with the increase of temperature. Despite that the active (010)[100] is predominant at high temperature and therefore in power-law creep regime, Jung and Karato (2001) observe that a similar (100)[001] is dominant in a low stress and H_2O-rich condition (type C) at 1-2 GPa and 1200-1300°C, where it is determined as power-law creep. The activation of (100)[001] suggests that the mechanism of power-law

creep has been in function with the low temperature plasticity together as the temperature goes up at the subduction zone condition and the mantle pressure.

3.6 Application

That the LPO of olivine at the subduction zone condition differs from that in normal condition at mantle pressure may results in the anisotropy in the seismic observation. Since the difference of dominant active slip system of olivine between the conventional mantle, (010)[100], and subduction zone slab, (100)[001] and {*hk0*}[001] ($h > k$), is significant, the seismic anisotropy should also be of significance.

3.7 Conclusion

Compression and deformation processes make the grain size of olivine into sub-micron level. The pseudo grains in the recovered samples may be the relics developed from the starting olivine grains. They are squeezed and become foliations vertical to the deforming axis during the deformation. The LPO shows the predominant active slip systems of olivine at subduction zone condition and mantle pressure evolve from {*hk0*}[001] ($h > k$) and {110}[001] at 500°C to {*hk0*}[001] ($h > k$) and (100)[001] at 700°C. The occurrence of active (100)[001] represents that power-law creep involves in playing an important role together with the low temperature plasticity. Predominant active (100)[001] system of olivine in the slab may result in the seismic anisotropy different from the conventional mantle.

References

Brearley, A. J., Rubie, D. C., and Ito, E., 1992. Mechanisms of the transformations between the alpha-polymorphs, beta-polymorphs and gamma-polymorphs of Mg_2SiO_4 at 15 GPa. *Physics and Chemistry of Minerals* **18**, 343-358.

Chen, J., Inoue, T., Weidner, D. J., Wu, Y. J., and Vaughan, M. T., 1998. Strength and water weakening of mantle minerals, olivine, wadsleyite and ringwoodite. *Geophysical Research Letters* **25**, 575-578.

Chen, J., Li, L., Weidner, D. J., and Vaughan, M. T., 2004. Deformation experiments using synchrontron X-rays: in situ stress and strain measurements at high pressure and temperature. *Physics of the Earth and Planetary Interiors* **143-144**, 347-356.

Couvy, H., Frost, D. J., Heidelbach, F., Nyilas, K., Ungar, T., Mackwell, S., and Cordier, P., 2004. Shear deformation experiments of forsterite at 11GPa-1400 degrees C in the multianvil apparatus. *European Journal of Mineralogy* **16**, 877-889.

Durham, W. B. and Rubie, D. C., 1998. Can the multianvil apparatus really be used for high-pressure deformation experiments. In: Manghnani, M. H., Yagi, T. (Ed.), *Properties of Earth and Planetary Materials at High Pressure and Temperature*. American Geophysical Union.

Durham, W. B., Weidner, D. J., Karato, S.-I., and Wang, Y., 2002. New developments in deformation experiments at high pressure. In: Karato, S.-I., Wenk, H.R. (Ed.), *Plastic Deformation of Minerals and Rocks, Reviews in Mineralogy and Geochemistry*. Mineralogy Society of America, Chantilly, Virginia.

Evans, B. and Geotze, C., 1979. The temperature variation of hardness of olivine and its implication for polycrystalline yield stress. *Journal of Geophysical Research* **84**, 5505-5524.

Frese, K., Trommsdorff, V., and Kunze, K., 2003. Olivine [100] normal to foliation: lattice preferred orientation in prograde garnet peridotite formed at high H2O activity, Cima di Gagnone (Central Alps). *Contributions to Mineralogy and Petrology* **145**, 75-86.

Jung, H. and Karato, S.-I., 2001. The effect of water on dynamically recrystallized grain-size of olivine. *Journal of Structural Geology* **23**, 1337-1344.

Li, L., Long, H., Raterron, P., and Weidner, D., 2006a. Plastic flow of pyrope at mantle pressure and temperature. *American Mineralogist* **91**, 517-525.

Li, L., Raterron, P., Weidner, D. J., and Chen, J., 2003. Olivine flow mechanisms at 8 GPa. *Physics of the Earth and Planetary Interiors* **97**, 121-131.

Li, L., Weidner, D. J., Chen, J., Vaughan, M. T., and Davis, M., 2004a. X-ray strain analysis at high pressure: effect of plastic deformation in MgO. *Journal of Applied Physics* **95**, 8357-8365.

Li, L., Weidner, D. J., Raterron, P., Chen, J., and Vaughan, M. T., 2004b. Stress measurement of deforming olivine at high pressure. *Physics of the Earth and Planetary Interiors* **143-144**, 357-367.

Li, L. L., Weidner, D., Raterron, P., Chen, J. H., Vaughan, M., Me, S. H., and Durham, B., 2006b. Deformation of olivine at mantle pressure using the D-DIA. *European Journal of Mineralogy* **18**, 7-19.

Meade, C. and Jeanloz, R., 1990. The strength of mantle silicates at high pressure and room temperature: implications for the viscosity of the mantle. *Nature* **348**, 533-535.

Mercier, J. C., 1985. Olivine and pyroxenes. In: Wenk, H. R. (Ed.), *Preferred Orientation in Deformed Metals and Rocks: An Introduction to Modern Texture Analysis*. Academic Press, Orlando, FL.

Mockel, J. R., 1969. Structural petrology of the garnet-peridotite of Alpe Arami (Ticino, Switzerland). *Leidse Geol Meded* **42**, 61-130.

Nicolas, A., Boudier, F., and Boullier, A. M., 1973. Mechanisms of Flow in Naturally Deformed Peridotites. *American Journal of Science* **273**, 853-876.

Raleigh, C. B., 1968. Mechanisms of Plastic Deformation of Olivine. *Journal of Geophysical Research* **73**, 5391-&.

Raterron, P., Chen, J., Li, L., Weidner, D., and Cordier, P., 2007. Pressure-induced slip-system transition in forsterite: Single-crystal rheological properties at mantle pressure and temperature. *American Mineralogist* **92**, 1436-1445.

Raterron, P., Wu, Y. J., Weidner, D. J., and Chen, J. H., 2004. Low-temperature olivine rheology at high pressure. *Physics of the Earth and Planetary Interiors* **145**, 149-159.

Uchida, T., Wang, Y., Rivers, M. L., and Sutton, S. R., 2004. Yield strength and strain hardening of MgO up to 8 GPa measured in deformation DIA with monochromatic X-ray diffraction. *Earth and Planetary Science Letters* **226**, 117-126.

Wang, Y., Durham, W. B., Getting, I. C., and D.J., W., 2003. The deformation DIA: a new apparatus for high temperature trialxial deformation for pressure up to 15 GPa. *Review of Scientific Instruments* **74**, 3002-3011.

Weidner, D. J., 1998. Rheological studies at high pressure. In: Hemley, R. J. (Ed.), *Ultrahigh-Pressure Mineralogy: Physics and Chemistry of the Earth's Deep Inerior*. Mineralogical Society of America, Washington, DC.

Weidner, D. J., Vaughan, M. T., Ko, J., Wang, Y., Leinenweber, K., Liu, X., Yeganeh-Haeri, A., Pacalo, R. E., and Zhao, Y. S., 1992a. Large volumn high pressure research using the wigger port at NSLS. *High Pressure Research* **8**, 617-623.

Weidner, D. J., Vaughan, M. T., Ko, J., Wang, Y., Liu, X., Yeganeh-Haeri, A., Pacalo, R. E., and Zhao, Y. S., 1992b. Characterization of stress, pressure, and temperature in SAM-85, a DIA type high pressure apparatus. In: Syono, Y., Manghnani, H. (Ed.), *High-Pressure Research: Application to Earth and Planetary Sciences*. Terra Scientific Publishing Company, Tokyo / American Geophysical Union, Washington, D.C.

Weidner, D. J., Wang, Y., Ando, J., and Vaughan, M. T., 1994. yield stress at high pressure and temperature. *Geophysical Research Letters* **21**, 753-756.

Weidner, D. J., Wang, Y., Chen, J., Ando, J., and Vaughan, M. T., 1998. Rheology measurements at high pressure and temperature. In: Manghnani, M. H., Yagi, T. (Ed.), *Properties of the Earth and Planetary Materials at High Pressure and Temperature*. American Geophysical Union.

Wenk, H. R., 2002. Texture and Anisotropy. In: Karato, S.-I. and Wenk, H. R. Eds., *Plastic Deformation of Minerals and Rocks, Reviews in Mineralogy and Geochemistry*. Mineralogical Society of America Geochemical Society, Chantilly, Virginia.

Xu, Z. Q., Wang, Q., Ji, S. C., Chen, J., Zeng, L. S., Yang, J. S., Chen, F. Y., Liang, F. H., and Wenk, H. R., 2006. Petrofabrics and seismic properties of garnet peridotite from the UHP Sulu terrane (China): Implications for olivine deformation mechanism in a cold and dry subducting continental slab. *Tectonophysics* **421**, 111-127.

Figure Captions

Fig 3-1a SEM images for the deformed polycrystalline olivine, 5GPa, room temperature, San 113. 700x.

Fig 3-1b SEM images for the deformed polycrystalline olivine, 5GPa, room temperature, San 113. 1000x

Fig 3-2 SEM images for the deformed polycrystalline olivine, 5GPa, 500°C, San 114. 700x.

Fig 3-3a EBSD pole figures of crystal axis for the recovered deformed polycrystalline olivine, at 5 GPa and 700°C, San 80. up, scattering plot; down, contour. 51 data points. The reference coordinates are determined as: X-normal to the deformation direction in the surface plane of sample, Y-normal to the surface plane, and Z-parallel to the compression direction. Pole figures are projected using equal area, lower hemisphere with a half width of 20° and a cluster size of 5°.

Fig 3-3b EBSD pole figures of crystal axis for the recovered deformed polycrystalline olivine, at 5 GPa and 700°C, San 80. Total 51 points. The reference coordinates are determined as: X-normal to the deformation direction in the surface plane of sample, Y-normal to the surface plane, and Z-parallel to the compression direction. Pole figures are projected using equal area, lower hemisphere with a half width of 20° and a cluster size of 5°.

Fig 3-4a EBSD pole figures of crystal axis for the recovered deformed polycrystalline olivine, at 5 GPa and 500°C, San 114. up, scattering plot; down, contour. 47 data points. The reference coordinates are determined as: X-normal to the deformation direction in the surface plane of sample, Y-normal to the surface plane, and Z-parallel to the deformation direction. Pole figures are projected using equal area, lower hemisphere with a half width of 20° and a cluster size of 5°.

Fig 3-4b EBSD pole figures of crystal axis for the recovered deformed polycrystalline olivine, at 5 GPa and 500°C, San 114. 47 data points. The reference coordinates are determined as: X-normal to the deformation direction in the surface plane of sample, Y-normal to the surface plane, and Z-parallel to the deformation direction. Pole figures are projected using equal area, lower hemisphere with a half width of 20° and a cluster size of 5°.

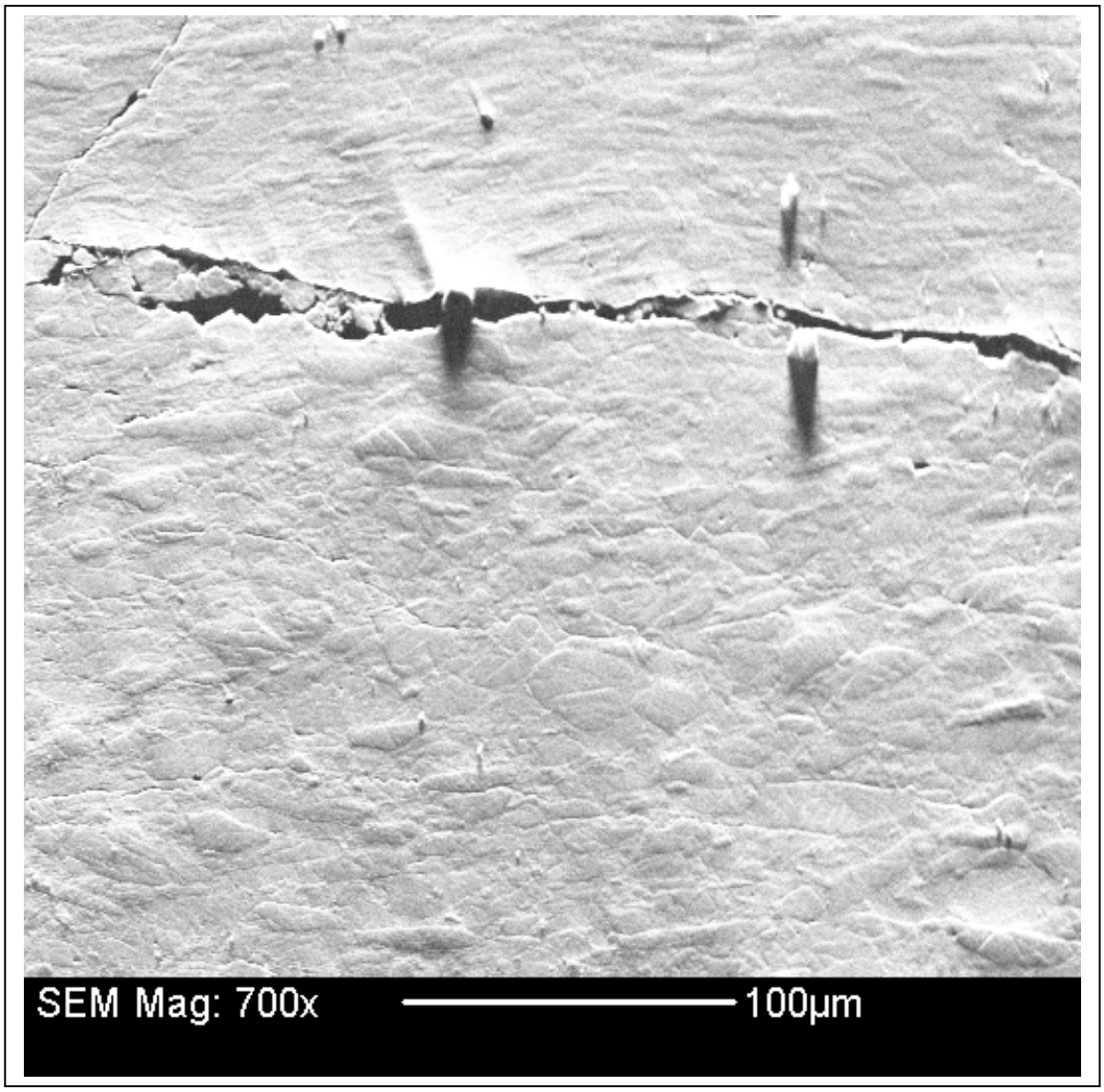

Fig 3-1a SEM images for the deformed polycrystalline olivine, 5GPa, room temperature, San 113. 700x.

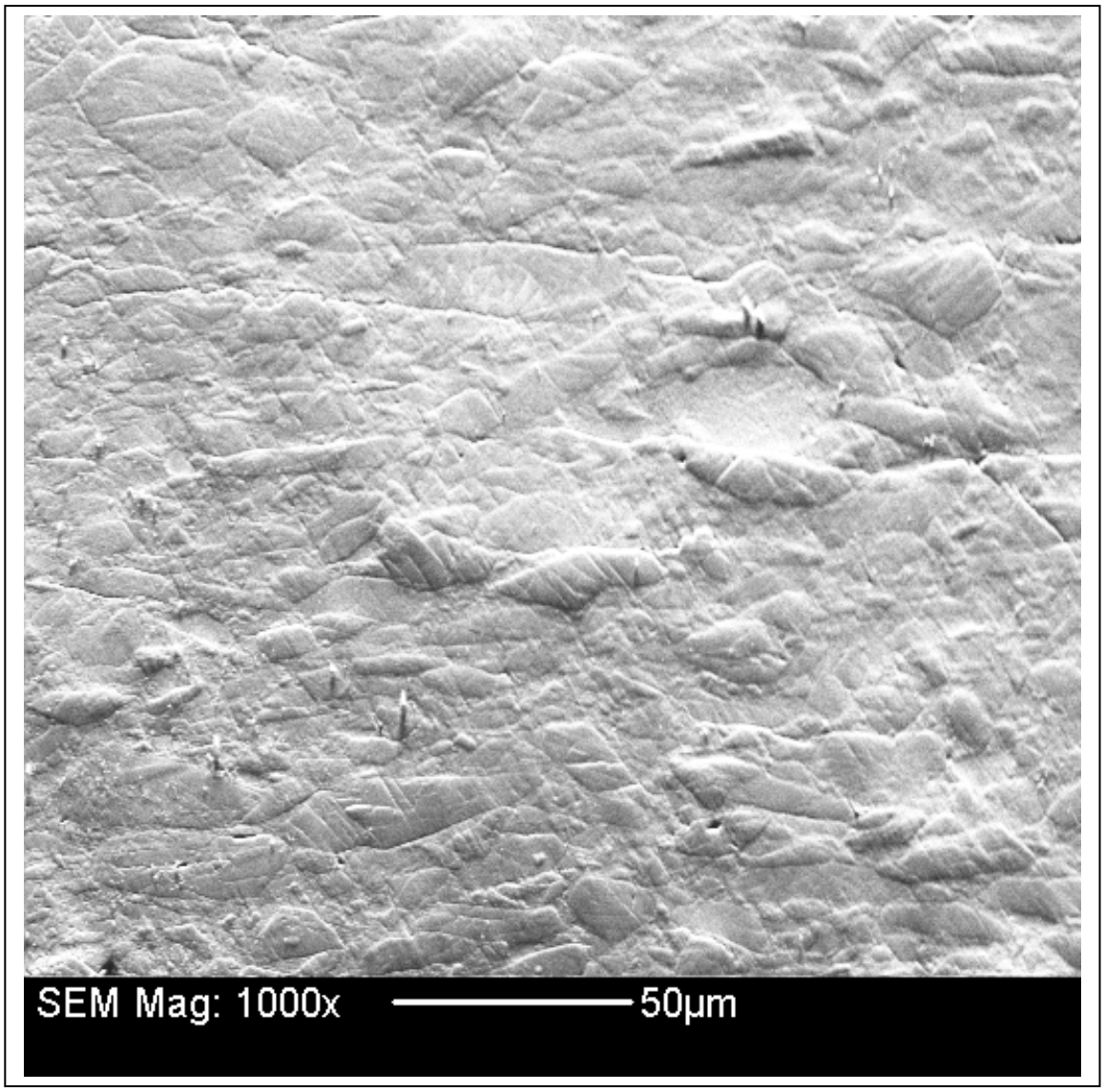

Fig 3-1b SEM images for the deformed polycrystalline olivine, 5GPa, room temperature, San 113. 1000x.

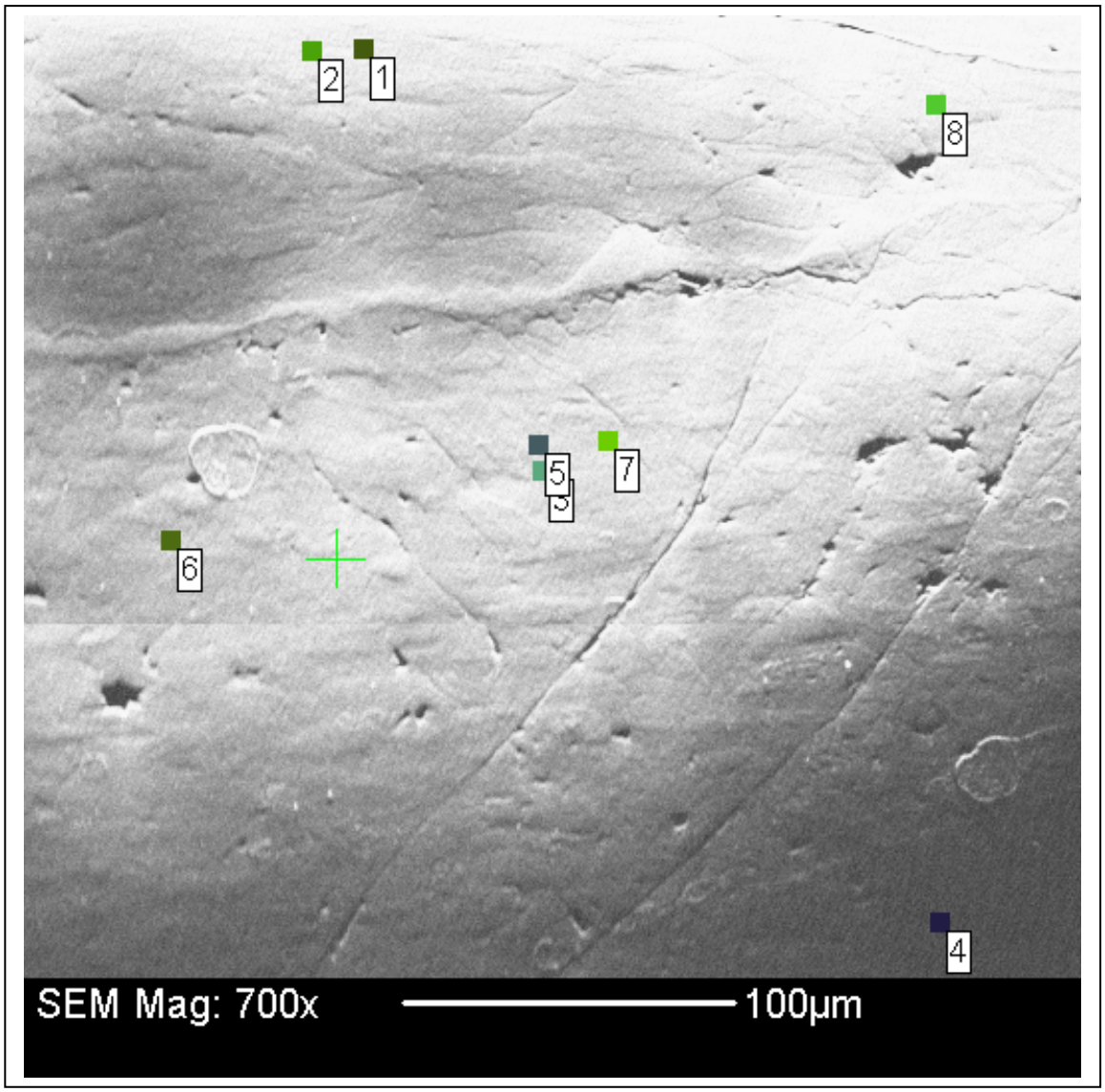

Fig 3-2 SEM images for the deformed polycrystalline olivine, 5GPa, 500°C, San 114. 700x.

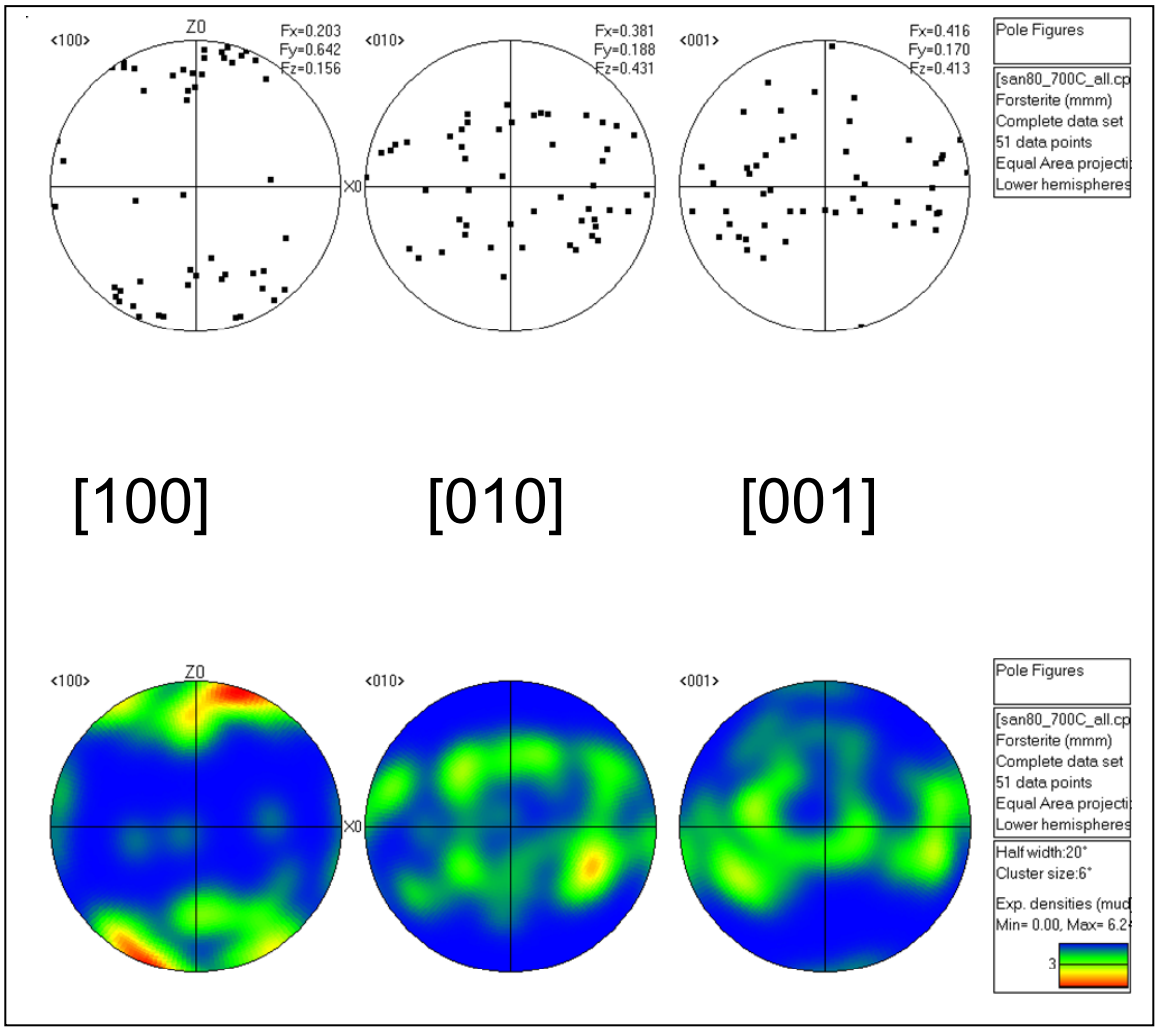

Fig 3-3a EBSD pole figures of crystal axis for the recovered deformed polycrystalline olivine, at 5 GPa and 700°C, San 80. up, scattering plot; down, contour. 51 data points. The reference coordinates are determined as: X-normal to the deformation direction in the surface plane of sample, Y-normal to the surface plane, Z-parallel to the compression direction. Pole figures are projected using equal area, lower hemisphere with a half width of 20° and a cluster size of 5°.

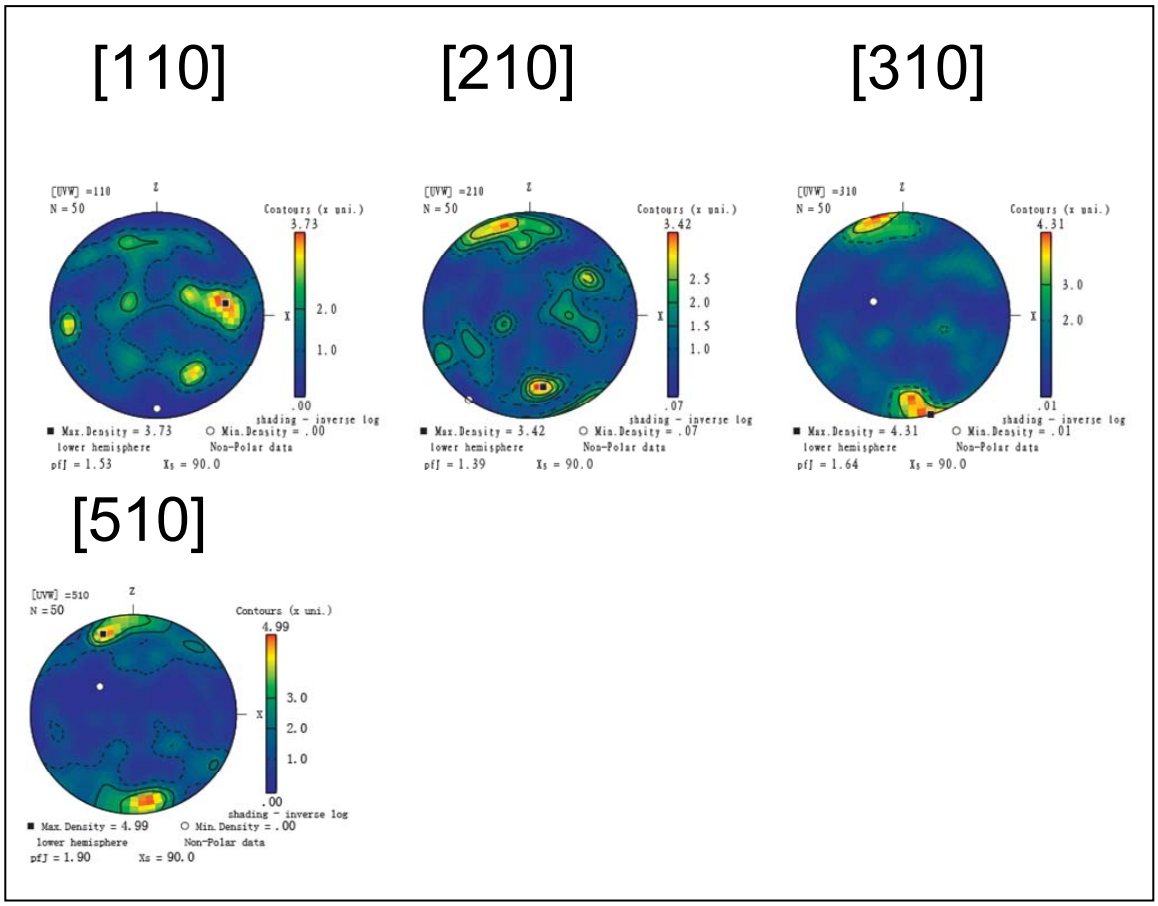

Fig 3-3b EBSD pole figures of crystal axis for the recovered deformed polycrystalline olivine, at 5 GPa and 700°C, San 80. Total 51 points. The reference coordinates are determined as: X-normal to the deformation direction in the surface plane of sample, Y-normal to the surface plane, Z-parallel to the compression direction. Pole figures are projected using equal area, lower hemisphere with a half width of 20° and a cluster size of 5°.

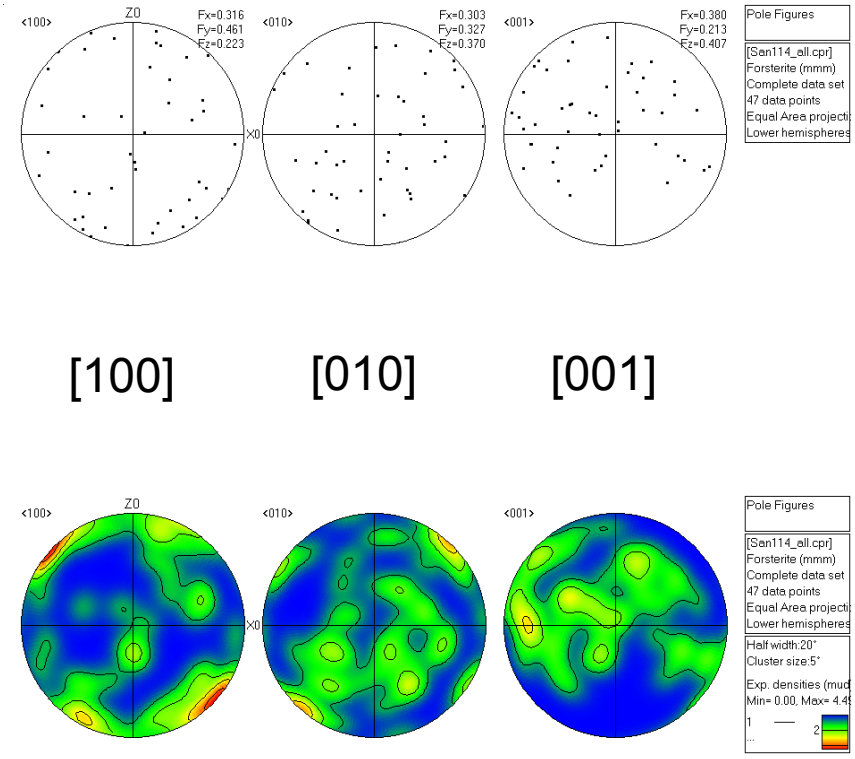

Fig 3-4a EBSD pole figures of crystal axis for the recovered deformed polycrystalline olivine, at 5 GPa and 500°C, San 114. up, scattering plot; down, contour. 47 data points. The reference coordinates are determined as: X-normal to the deformation direction in the surface plane of sample, Y-normal to the surface plane, Z-parallel to the deformation direction. Pole figures are projected using equal area, lower hemisphere with a half width of 20° and a cluster size of 5°.

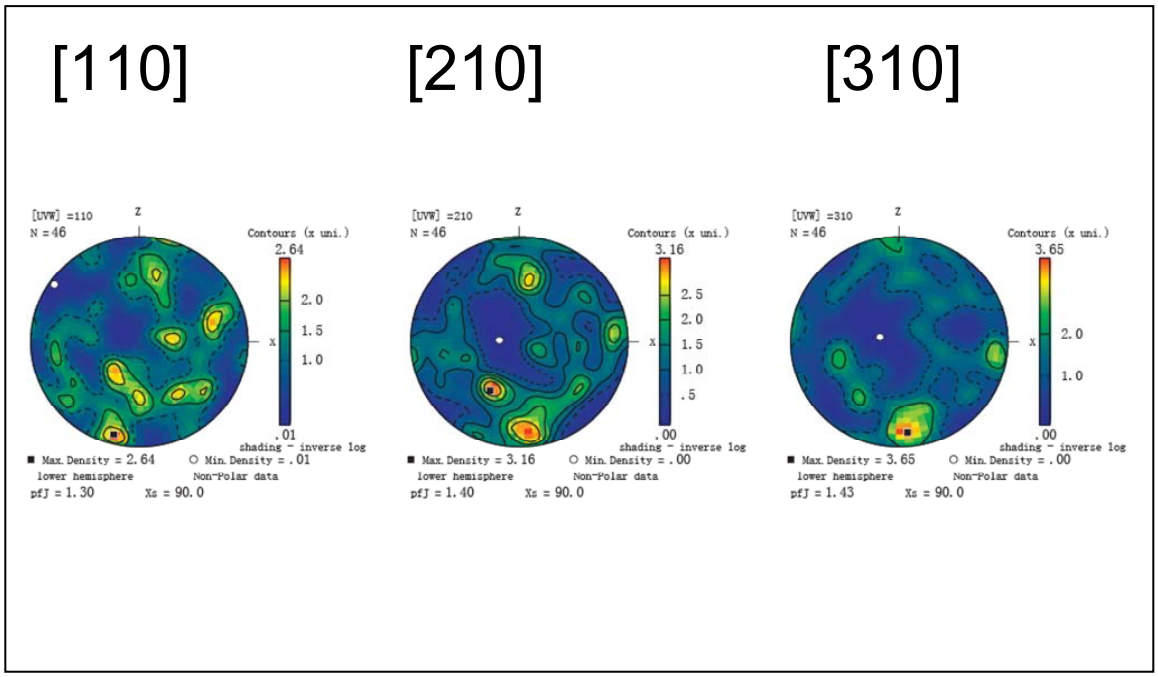

Fig 3-4b EBSD pole figures of crystal axis for the recovered deformed polycrystalline olivine, at 5 GPa and 500°C, San 114. 47 data points. The reference coordinates are determined as: X-normal to the deformation direction in the surface plane of sample, Y-normal to the surface plane, Z-parallel to the deformation direction. Pole figures are projected using equal area, lower hemisphere with a half width of 20° and a cluster size of 5°.

Chapter 4

Olivine Instability: An Experimental View of Mechanism of Deep Earthquakes

4.1 Abstract

Experimental study regarding to the effects of annealing process, grain size and water existence on the deformation of polycrystalline San Carlos olivine has been performed on a D-DIA facility at X17B2, NSLS. The total macroscopic strain is derived from the direct measurements of the images taken by X-ray radiograph technique. The differential stresses are deduced from elastic strains, which are calculated from olivine elastic. In respect to the incident synchrotron X-ray beam, the elastic constraints are *in situ* measured in different directions and are collected as a function of time by the X-ray multi-detector EDS. At constant strain rates ($\sim 10^{-5}$-$10^{-7} s^{-1}$), the experiments are preformed at different pressures and temperatures. Olivine in the annealed/unannealed system shows similar properties during the deformation. However, the annealing process can shift the transition temperature between regimes of temperature insensitive and sensitive to the high value side as much as 370°C. Grain size affects the rheological properties of olivine in the low temperature dislocation regime. Existence of water decreases the transition temperature of the boundary between the regimes of low

temperature plasticity and power-law creep. The instability of olivine could be the mechanism for the deep-focus earthquake happened in the subduction zone slab.

4.2 Introduction

Olivine (α-$(Mg,Fe)_2SiO_4$) is the major constituent of the upper mantle. In subduction zone, where the earthquakes happen, the rheology of the slab is mainly controlled by that of olivine at low temperatures. Several different mechanisms for deep focus earthquakes have been suggested, which include olivine instability (Bridgman, 1936; Orowan, 1960; Post, 1977; Ogawa, 1987; Hobbs and Ord, 1988; Kao and Chen, 1995), shear/fault-induced melting (Griggs, 1954, 1972; Griggs and Handin, 1960; Griggs and Baker, 1969; Zhang et al., 2004), phase transformation (Bridgman, 1945; Benioff, 1963; Meade and Jeanloz, 1989), dehydration of hydrous specimens (Raleigh and Paterson, 1965; Meade and Jeanloz, 1991; Peacock, 2001; Dobson et al., 2002; Jung et al., 2004), and olivine metastability-induced anti-crack (Green and Houston, 1995). Since the low temperature of the "cold" slab, which can be as low as 600°C in the transition zone, it has been argued that olivine may still exist there, thus its instability may be the possible mechanism for the deep-focus earthquakes.

Compare to the rheology of olivine at high pressure and high temperature, the study on rheology of olivine at subduction zone condition (high pressure and low temperature) is limited. Furthermore, the present results from different workers are contradictory. Several literatures have also reported related studies on the rheology of olivine at high pressures and room temperature (Meade and Jeandoz, 1990; Chai *et al*.,

1998). Evans and Goetze (1979) give the hardness data at ambient pressure up to 1500°C. A relaxation experiments study (Raterron *et al*., 2004) demonstrates a rapid decrease of differential stress from 3 GPa to 1 GPa at 450-500°C. Li et al. (2004) show a dramatic drop of differential stress from 1.7 GPa to 0.6 GPa at hydrostatic pressure of 8 GPa and 820°C. Using D-DIA apparatus, Li et al. (2006) that represent at steady state the differential stress values are 2.4 GPa for fine sample at 6.5 GPa and 900°C, and 2.0 GPa for coarse sample at 3.5 GPa, 800°C and at 6.5 GPa, 900°C. Using a D-DIA facility, we present our data of deformation of olivine in the annealed system in another paper and demonstrate there is a rapid stress drop at steady state from about 3 GPa to below 1 GPa between 700-900°C along with the increase of temperature. Besides, Chen et al. (2004) present a decrease of differential stress with the increase of temperature in an *in situ* measurement of deforming fayalite (Fe_2SiO_4).

The contradiction of present results from different workers makes it difficult for us to understand the rheological properties of olivine at subduction zone condition, which is important for one to explore the nature of slab's behavior during its diving into the deep mantle. Looking back at the literatures above, we may find that the experimental conditions for these studies are quite different. There are some important issues we concern about: only a few studies are based on the deformation experiments, and only a few data are from the deformation experiments at steady state (Li et al., 2006; our paper elsewhere). For the olivine samples applied in these studies, some of them are annealed before deformation (Li et al., 2006; our paper elsewhere), some are not (Ratteron et al., 2004; Li et al., 2004) due to the technical difficulty.

The annealing process before deformation helps removing the residue stress obtained from the sample's history. It also helps the formation of the chemical homogenous environment during the experiment. So it is generally used in the experiment whenever possible. When the annealing process is applied, the sample is also sintered.

In the ocean lithosphere, things are annealed and sintered by the heat from middle ocean ridge and the earth mantle until it reaches subduction zone. In the subduction zone, however, the slab may retain some damage zone due to the previous fractural activities during diving process. Thus it is worth exploring the properties of olivine in the damaged zone condition and comparing the results to the previous study on olivine in the undamaged zone. For the study of rheological purpose, the annealed olivine specimen in the experiment can represent the olivine in the undamaged zone while the unannealed olivine sample can represent the olivine in the damaged zone condition.

Here, we present a comparative study on the deformation of olivine at steady state under different sample conditions. We compare the result from the annealed polycrystalline with that from the unannealed one. We also present the results of the effects of grain size and water on the deformation of olivine at subduction condition. The deformation experiments are performed on a deformation DIA (D-DIA) apparatus, SAM85 at X17B2, National Synchrotron Light Source (NSLS).

4.3 Starting Material

We use San Carlos olivine powder, chemical formation $(Mg_{0.9}Fe_{0.1})_2SiO_4$, as the sample in the deformation experiments. San Carlos olivine is believed to represent the same Mg:Fe ratio in the earth mantle. Optically clear (gem quality) grains of San Carlos olivine with maximum dimension of 3-10 mm are well ground into powder in an agate mortar. The final grain size of powdered olivine is in the range of 10-20 μm. Powdered enstatite ($MgSiO_3$) (3-5% total quality of sample) is mixed into the olivine samples as a buffer to control the activity of silica. In order to explore the effect of water fugacity on deformation of olivine, "normal" and "wet" samples are investigated. Amorphous boron epoxy (BE) cells are used for both "normal" and "wet" samples. To keep away from the moisture, "normal" sample is placed in a vacuum oven at 135°C for at least 2 hours before experiment. "Wet" sample does not undergo such a process. In annealed "wet" samples, powdered talc instead of enstatite is used as both water source and the buffer controlling the activity of silica. Samples are compressed at room temperature. For the experiments exploring the properties of olivine in the undamaged zone, samples are annealed at 1200°C for at least 2 hours before dropping to the designed temperature and being deformed. To explore the properties of olivine in the damaged zone condition, no annealing process is performed.

4.4 Water Content and Water Fugacity

The water content in the starting olivine crystal is very limited (Raterron et al. 2004). However, the cell assembly provides water during the heating process and the water amount is determined to be significant in the recovered sample (our paper elsewhere, see chapter 2). Besides, powdered talc contributes some water in the "wet" sample when it is heated during the annealing process before the deformation. The water content of recovered samples from the deformation experiments are determined on a synchrotron infrared (IR) facility at U2A, NSLS. The IR diagrams with absorbance versus wavenumber are shown in **Fig 4-1a**, **b**, and **c**, respectively. From the diagram we can find that in all the recovered samples there is a big hump in the range of wavenumbers 3000-3780 cm^{-1}, just as we have observed in our paper elsewhere (see chapter 2). Similar obseration is also described by Karato et al. (1986) and Mei and Kohlstedt (2000a). It may indicate that the amount of molecular water is significant in the recovered specimens. By looking at the diagrams carefully, however, we find that there are sharp peaks between the wavenumbers of 3500-3650 cm^{-1}, which present the OH^- related species. We also observe that the peaks in "wet" specimen are obviously much higher than that in the "normal" olivine sample. Thus it demonstrates that the water fugacity is higher in the "wet" olivine specimen than that in the "normal" olivine sample.

4.5 Experiments

The deformation experiments are performed on a D-DIA apparatus, SAM85, at X17B2 beamline, NSLS. The cell assembly used in this study is similar as we used in our paper elsewhere (see chapter 2).

In the experiments of this study, the D-DIA apparatus gives the capacity to drive the top and bottom rams at a certain speed to maintain a constant strain rate while the main ram also chooses a related certain speed to keep the pressure constant (Durham et al., 2002; Wang et al., 2003). During the experiments, the equation of state for the olivine is used as the pressure standard. The experimenter has the capability to control the speeds of differential rams, and also the directions of the rams, either advance or retreat.

The macroscopic (plastic and elastic) strain along the uniaxial direction is derived from the specimen's length measured from the X-ray radiograph of the sample. Using a white incident X-ray beam with 2 x 2 mm^2 in size, the image of the experimental sample is *in situ* captured and magnified by a CCD camera with the X-ray radiographic technique. Ni foils with thickness of 25 μm as the strain markers are shown as dark lines in the images. The resolution is pixel level. The length of the specimen is measured and plotted as a function of time in a diagram, which is used as a strain indicator.

Elastic deformation is measured by X-ray powder diffraction pattern analysis (Chen *et al*., 2004; Li *et al*., 2004; Li et al., 2006). Following Singh *et al*. (1998), differential stress is deduced from elastic strain, which are calculated from olivine elastic constraints measured as a function of time by a solid state multi-detector, energy dispersive spectrometer (EDS):

$$\varepsilon(hkl) = \frac{d_V(hkl) - d_H(hkl)}{\frac{d_V(hkl) + 2d_H(hkl)}{3}} \tag{5}$$

$$\varepsilon(hkl) == \tau(hkl)\alpha[2G_R(hkl)]^{-1} + \tau(hkl)(1-\alpha)(2G_V)^{-1} \tag{6}$$

where ε is the elastic strain; d_V and d_H are the d-space values for vertical and horizontal directions, respectively; is the differential stress, G_R and G_V are the aggregate shear modulus under Reuss condition (iso-stress) and voigt condition (iso-strain), respectively; and α weight parameter for *reuss* and *voigt* conditions. (*hkl*) represents the inter-planar. In this study, we assume that our experiments are at Reuss condition so α=1.

With a white X-ray beam of 50 x 50 μm^2 in size going through the samples, the samples' elastic constraints are *in situ* measured in different directions respecting to the incident X-ray beam.

The San Carlos olivine sample itself is used as the pressure standard. The 3rd order Birch-Murnaghan equation of state is applied to calculate the pressure. The parameters for the calculation are from Issaak (1992), Zha et al. (1996) and Liu et al. (2005). The X-ray diffraction data of San Carlos olivine at ambient condition (10^5 Pa, 25°C) is used to calculate the reference unit cell volume V_0.

In order to observe the boundary between regimes of temperature independent at low temperature and temperature dependent at high temperature, experiments are designed to investigate the deformation behavior of olivine along temperature increase and decrease cycles after steady state has been reached at 400°C. The strategy of these investigations is that the observed stress should be higher than or equal to the stress at steady state along increase cycle whereas it should be equal to or lower than that at steady state along

decrease cycle at the same temperature. Thus the value of stress at steady state is well bounded and just between these two values.

To compare the properties of polycrystalline olivine specimens with/without annealing process, we run both deformation experiments with samples annealed and unannealed, respectively. We also run the experiments with olivine samples at "normal" and "wet" conditions to explore the effect of water fugacity on the behaviors of olivine.

4.6 Experiment Results and Discussion

At 5 GPa, deformation experiments are performed with the unannealed olivine specimens in "normal" condition and with the annealed olivine specimens in "normal" and "wet" conditions. The strain rates in the experiments are in the scale of $10^{-5}s^{-1}$. During the online *in-situ* experiments, steady state at 400°C is reached and is checked by a quick analysis of a single diffraction peak of olivine (130). The differential stress after 400°C is also monitored by such an analysis. The final results of the differential stress are from the average value of five diffraction peaks of olivine, which are (021), (101), (130), (131) and (112).

The diagrams of differential stress versus temperature are shown in **Fig 4-3a**, **b** and **c**, respectively. The diagram of strain versus time is shown in **Fig 4-4a**, **b** and **c**, respectively.

4.6.1 Comparison of annealed and unannealed samples

As we mention in our other paper, our experimental results give a much higher transition temperature from the low temperature plasticity to power-law creep regimes than the data from the relaxation experiments (Chen et al., 1998; Raterron et al., 2004) although the values of differential stress in our experiments get a good agreement with theirs at high and low temperatures, respectively. Comparing our experiment with theirs in detail, however, we find that the difference of transition temperature may be due to the different techniques of experiment specimen preparation. In order to get the homogeneous physical and chemical environment, we apply an annealing process at 1200°C for 2 hours at the designed pressure for the experiment before we start the deformation. For the relaxation experiment, however, no annealing process can be applied because the yield stress in the sample will be eliminated in such kind of process.

The result from the unannealed sample with "normal" condition is shown in **Fig 4-3a**. Here we just discuss the "coarse" specimen because the starting "coarse" olivine powder has the same grain size as the starting olivine sample we use in the annealed experiments. It can be seen that beginning at 400°C, the differential stress goes linearly down with the temperature going up. Although there is a data gap between 490°C and 580°C which is caused by the X-ray maintenance, from the trend of data points we can still see that there is a quick drop of differential stress around 480-490°C, which is consistent to the value of 450-500°C from Raterron et al. (2004) and the value of 400-600°C from Chen et al. (1998), but obviously higher than the value of between 300°C

and 400°C for the hydrous system (Chen et al., 1998). After the quick drop there looks likely a regime of temperature insensitive with stress value of 1.5 GPa until it arrives at 610-630°C. The differential stress becomes temperature-sensitive and again linearly decreases with the temperature increase over 610-630°C. The transition temperature for the regimes of temperatures insensitive and sensitive is thus determined as 620°C. From the diagram we can also find that the differential stress increases around 700°C along with the temperature increase. We believe that it is caused by the activation of the sintering/annealing process of olivine powder at such a temperature range.

We already give a flow law equation in our other paper (See Chapter 2) as:

$$\sigma^p = \tau^p - KT^{1/q} \tag{7}$$

where σ, τ and T are the stress, the flow stress at 0 K and temperature, respectively; p and q are constant and $0 \le p \le 1$, $1 \le q \le 2$, and

$$K = \tau^p \left(\frac{R}{F_0} \cdot \ln \frac{\dot{\varepsilon}_0}{\dot{\varepsilon}}\right)^{1/q} \tag{8}$$

where F_0 is the total free energy of activation of an isolated pair of kinks, or required to overcome the obstacle without aid from the external strength, R, $\dot{\varepsilon}$, and $\dot{\varepsilon}_0$ are gas constant, strain rate and constant, respectively.

Based on the increase cycle, the plastic flow law equations can be given as the following:

For temperature range of 400-480°C,

$$\sigma = 6.6076 - 5.455 \times 10^{3} \mathrm{T} \quad (9)$$

in which we get τ = 6.6 GPa.

For the temperature insensitive regime, although we lack the data to show where it starts, we know it ends around 620°C. Thus we can still give out a simple equation:

$$\sigma = C \quad (10)$$

in which C is a constant. In our experiment, C = 1.5 GPa.

For temperature range of 620-700°C,

$$\sigma = 8.3669 - 8.4876 \times 10^{3} \mathrm{T} \quad (11)$$

in which τ is given to be 8.4 GPa.

It should be stated that our data in the temperature range of 620-850°C get a good agreement with the flow law (500-740°C) given by Raterron et al. (2004) (**Fig. 4-3a**). As we mentioned earlier in this paper, however, there looks likely an activation of the sintering/annealing process for olivine powder at 700°C. Therefore the deformation above 700°C may be a mixture of partial annealing/unannealing system. The annealing system gets more and more dominant with the increase of temperature.

Since we lack the data for the quick drop of stress around 485°C, we can not give out the flow law and temperature range for this regime. As for the regime above 700°C, things become complicated because of the activation of annealing.

The transitional temperature between regimes of insensitive to temperature and sensitive to temperature can be as high as 990°C for the annealed polycrystalline olivine sample (see **Fig 4-3b**) at "normal" condition. We don't observe the starting temperature of first quick drop of differential stress before the regimes of temperature insensitive as the unannealed specimen undergoes around 480-490°C. However, we observe that there is most likely a stress drop at 400°C and finished around 420°C along with the temperature increase. The value of stress for the annealed specimen in the regime of temperature independent is 2.2 GPa. We therefore give the flow law for this regime as:

$$\sigma = C \tag{12}$$

in which C is a constant and C=2.2 GPa at our experiment condition.

It can be concluded that the behaviors of both annealed and unannealed polycrystalline olivine are similar in the deformation experiments at subduction zone condition. Along with the increasing temperature, they both undergo a quick drop of stress and then enter a temperature insensitive regime. As the temperature keeps up, they finally cross the transition boundary and go into the regime of power-law creep, where stress becomes temperature dependent as the result. However, the values of transition temperature are different for the annealed and unannealed polycrystalline olivine. The annealed polycrystal olivine has a lower temperature (≤400°C) for the first quick drop of stress and a higher temperature (up to 990°C) for the transition boundary from the regimes of low temperature plasticity to power-law creep. On the other hand, the unannealed one has a higher temperature (485°C) for the first quick drop of stress and lower temperature (620°C) for the boundary of regimes between low temperature

plasticity and power-law creep. The annealed olivine can hold higher stress than the unannealed one, 0.7 Gpa difference in our comparative experiments.

4.6.2 Effect of grain size

We investigate the effect of grain size on the deformation of olivine polycrystalline. Beginning about 900°C and above, the dynamic recrystallization becomes a more and more common phenomenon in the olivine polycrystalline. So it becomes difficult to control the grain size in the annealing process. For this purpose we use unannealed specimens in this investigation. Two specimens, one is bigger (10-20um) in grain size (**Fig 4-2a**) (we thus call it "coarse") and another is smaller (submicron) in grain size (**Fig 4-2b**) (we call it "fine") are placed in one cell assembly to compare with each other.

The diagram of stress vs. temperature for both coarse and fine samples is shown in **Fig 4-3a**. From this diagram it shows that the differential stress at steady states in the fine sample is obviously lower than that in the coarse sample. However, both of these two specimens have very similar stress-temperature relationship. In fact below 700°C the stress-temperature curves for both specimens are almost parallel to each other. It thus indicates that the mechanism of deformation for both specimens is the same and they both obey the same flow law. The only difference is the values of differential stress, which is due to the influence of grain size. The strain as a function of time for both samples is shown in **Fig 4-4a**. It demonstrates that at the same condition, the fine sample

is softer than the coarse one by factor of 2. Karato et al. (1986) report that during deformation the strain rate is independent to the grain size thus grain size is insensitive in the dislocation creep regime while grain size is sensitive and has effect on the strain rate in the diffusion creep. However, our experimental results illustrate that grain size is functional in the regime of low temperature dislocation creep. At 700°C both samples have a differential stress jump. But the differential stress for the fine sample increases dramatically by a factor of 2 from 0.5 Gpa to 1 GPa. This indicates that the activation of annealing process at 700°C influences the fine grain specimen more than it does on the coarse one.

4.6.5 Water influence on the deformation of olivine

Water plays an important role in the deformation of olivine. In decades a number of literatures have discussed the effect of water on the rheological properties of olivine. Water is found to enhance the deformation rate in both diffusion and power-law creep regimes (Carter and Ave Lallemant, 1970; Chopra and Paterson, 1984; Mackwell et al., 1985; Karato et al. 1986; Kohlstedt et al., 1995; Hirth and Kohlstedt, 1996; Mei and Kohlstedt, 2000a; Mei and Kohlstedt, 2000b). Water is also reported to weaken the olivine at 25-600°C in the unannealed experimental study (Chen et al., 1998). Since we use D-DIA apparatus with constant strain rate for our study, we don't have a comparison with them at this point. We perform a comparison study between the "normal" and "wet" annealed polycrystalline olivine at the similar condition. The stress versus temperature relationship is shown in **Fig 4-3b** and **c** and the strain versus time diagram is illustrated in

Fig 4-4b and **c**. Comparing these two diagrams, we find that in the increase cycle for the "wet" specimen, the transition temperature for the boundary of temperature insensitive to temperature sensitive is about 800°C while that for the "normal" sample is about 990°C, which are much higher than the unannealed data (Chen et al., 1998) for "dry" (400-600°C) and "wet" (300-400°C) experiments, respectively. The difference of 190°C demonstrates that the increase of water fugacity or concentration obviously decreases the transition temperature of the boundary between low temperature plasticity and paw-law creep regimes. Mei and Kohlstedt (2000b) give out a flow law equation for the power law creep at hydrous conditions $\dot{\varepsilon} = A\sigma^n f_{H_2O}^r \exp(-\frac{E^* + PV^*}{RT})$ in which $r = 0.69$ when V* = 0 $m^3 mol^{-1}$. Applying this equation in a constant strain rate case, we can find that the increase of the value of item $f_{H_2O}^r$ decreases the value of σ^n. As a result, value of n will be smaller at the hydrous condition than that at anhydrous condition if the other parameters are similar. Therefore for olivine the transition temperature of boundary between the regimes of low temperature plasticity and power-law creep will shift down in the hydrous environment comparing to that in the anhydrous environment. Our experiment result gets a good agreement with this deduced calculation. Our experiment results shows that in the temperature independent regime (low temperature plasticity) the differential stress is higher at hydrous condition than that at anhydrous condition, which is different from the result of Chen et al. (1998) showing olivine weakened by water at 25-400°C in the unannealed system. It also differs from the results for the power-law and diffusion creeps that water weakens the creep strength (Karato et al., 1986; Kohlstedt et al., 1995; Hirth and Kohlstedt, 1996; Mei and Kohlstedt, 2000a; Mei and Kohlstedt, 2000b). We argue that water may accelerate the dynamic recrystallization of olivine and

it results in a bigger grain size polycrystalline in the above experiment. Thus it gives a higher stress value as a result. Further work is needed.

4.6.6 Application

The annealed and unannealed olivine can represent the natural olivine in non-fault systems and that in pre-existing fault systems in subduction zone, respectively. We therefore propose a new olivine instability model with a "sandwich" formation for the deep focus earthquakes (**Fig 4-5**). In this model the pre-existing fault system is surrounded by the non-fault systems. When the slab dives down, the olivine in both systems undergoes a stress-build-up process and can hold very high stress in both cases. However, as it keeps diving to the transition zone, the slab is heated and its temperature arrives at the boundary temperature from the temperature insensitive regime to the temperature sensitive regime for the olivine in pre-existing fault system. As a result, while the olivine in non-fault system is still in regime of temperature insensitive and can still hold the built-up high stress, the olivine in pre-existing fault system can not hold the built-up stress any more and gives out a stress release. The pre-existing fault is re-activated and heat from the re-activated fault accelerates the ongoing process. Earthquake happens.

We state above that the existence of water shifts down the transition temperature of the boundary between low temperature plasticity and the power-law creep as much as 190°C. As the slab dives down to the deep earth, the temperature goes up. Thus the

olivine in the hydrous environment reaches the boundary and goes into the power-law creep earlier than the olivine in the anhydrous environment during the slab diving process. The maximum stress becomes temperature dependent in the hydrous environment and the hydrous olivine weakens quickly thereafter. We already state that with the strain rate of 10^{-15} s^{-1} in the natural slab (Holts, 1995) olivine in the undamaged zone reaches the boundary at 550-600°C (See Chapter 2). We therefore suggest that in a hydrous slab, olivine could cross the transition boundary earlier than 550-600°C as the slab continuously dives down. As a result it could have a quick stress release and the produced heat can heat the system up. The deep earthquake may happen by such a mechanism of olivine instability too (**Fig 4-5**).

4.7 Conclusions

We present experimental study results of effects of annealing process, grain size, water existence on deformation of polycrystalline olivine based on a D-DIA facility, SAM85, at X17B2, NSLS.

Olivine in the annealed/unannealed system shows similar properties during the deformation. However, the annealing process can shift the transition temperature between regimes of temperature insensitive and sensitive to the higher value side as much as 370°C. Grain size affects the rheological properties of olivine in the low temperature dislocation regime. Existence of water obviously decreases the transition temperature of boundary between the regimes of low temperature plasticity and power-law creep.

The instability of olivine could be the mechanism for the deep-focus earthquake happened in the subduction zone slab.

References

Benioff, H., 1963. Source wave forms of three earthquakes. *Bulletin of Seismological Society of America* **53**, 893-903.

Bridgman, P. W., 1936. Shearing phenomena at high pressure of possible importance for geology. *Journal of Geology* **44**, 653-669.

Bridgman, P. W., 1945. Polymorphic Transitions and Geological Phenomena. *American Journal of Science* **243A**, 90-97.

Carter, N. C. and Ave Lallemant, H. G., 1970. High temperature flow of dunite and peridotite. *Geological Society of America Bulletin* **81**, 2181-2202.

Chai, M., Brown, M., and Wang, Y., 1998. Yield strength, slip systems and deformation induced phase transition of San-Carlos olivine up to the transition zone pressure at room temperature. In: Manghnani, M. H., Yagi, T. (Ed.), *Properties of Earth and Planetary Materials*. American Geophysical Union.

Chen, J., Inoue, T., Weidner, D. J., Wu, Y. J., and Vaughan, M. T., 1998. Strength and water weakening of mantle minerals, olivine, wadsleyite and ringwoodite. *Geophysical Research Letters* **25**, 575-578.

Chen, J., Li, L., Weidner, D. J., and Vaughan, M. T., 2004. Deformation experiments using synchrontron X-rays: in situ stress and strain measurements at high pressure and temperature. *Physics of the Earth and Planetary Interiors* **143-144**, 347-356.

Chopra, P. N. and Paterson, M. S., 1984. The role of water in the deformation of dunite. *Journal of Geophysical Research* **89**, 7861-7876.

Dobson, D. P., Meredith, P. G., and Boon, S. A., 2002. Simulation of subduction zone seismicity by dehydration of serpentine. *Science* **298**, 1407-1410.

Durham, W. B., Weidner, D. J., Karato, S.-I., and Wang, Y., 2002. New developments in deformation experiments at high pressure. In: Karato, S.-I., Wenk, H.R. (Ed.), *Plastic Deformation of Minerals and Rocks, Reviews in Mineralogy and Geochemistry*. Mineralogy Society of America, Chantilly, Virginia.

Evans, B. and Geotze, C., 1979. The temperature variation of hardness of olivine and its implication for polycrystalline yield stress. *Journal of Geophysical Research* **84**, 5505-5524.

Green II, H. W. and Houston, H., 1995. The Mechanics of deep earthquakes. *Annual Review of Earth and Planetary Sciences* **23**, 169-213.

Griggs, D. T., 1954. High-pressure phenomena with applications to geophysics. In: Ridenour, L. N. (Ed.), *Modern Physics for the Engineer*. McGraw Hill, New York.

Griggs, D. T., 1972. The sinking lithophere and the focal mechanism of deep earthquakes. In: Robertson, E. C. (Ed.), *The Nature of Solid Earth*. McGraw Hill, New York.

Griggs, D. T. and Baker, D. W., 1969. The origin of deep-focus earthquakes. In: Mark, H., Fernbach, S. (Ed.), *Properties of matter under unusual conditions*. Interscience Publishers New York/London/Sydney/Toronto.

Griggs, D. T. and Handlin, J., 1960. Observations on fracture and a hyphothesis of earthquakes. In: Griggs, D. T., Handlin, J. (Ed.), *Rock Deformation*. Memoir of Geological Society of America.

Hirth, G. and Kohlstedt, D. L., 1996. Water in the oceanic upper mantle: Implications for rheology, melt extraction and the evolution of the lithosphere. *Earth and Planetary Science Letters* **144**, 93-108.

Hobbs, B. E. and Ord, A., 1988. Plastic instabilities: implications for the origin of intermediate and deep focus earthquakes. *Journal of Geophysical Research* **93**, 10521-10540.

Holt, W. E., 1995. Flow-Fields within the Tonga Slab Determined from the Moment Tensors of Deep Earthquakes. *Geophysical Research Letters* **22**, 989-992.

Isaak, D. G., 1992. High-temperature elasticity of iron-bearing olivines. *Journal of Geophysical Research-Solid Earth* **97**, 1871-1885.

Jung, H., Green, H. W., and Dobrzhinetskaya, L. F., 2004. Intermediate-depth earthquake faulting by dehydration embrittlement with negative volume change. *Nature* **428**, 545-549.

Kao, H. and Chen, W. P., 1995. Transition from interplate slip to double seimic zone along the Kuril-Kamchatka arc. *Journal of Geophysical Research* **100**, 9881-9904.

Karato, S.-I., Paterson, M. S., and FitzGerald, J. D., 1986. Rheology of synthetic olivine aggregates: influence of grain size and water. *Journal of Geophysical Research* **91**, 8151-8176.

Kohlstedt, D. L., Evan, B., and Mackwell, S. J., 1995. Strength of the lithosphere: Constraints imposed by laboratory experiments. *Journal of Geophysical Research* **100**, 17587-17602.

Li, L., Weidner, D. J., Raterron, P., Chen, J., and Vaughan, M. T., 2004. Stress measurement of deforming olivine at high pressure. *Physics of the Earth and Planetary Interiors* **143-144**, 357-367.

Li, L. L., Weidner, D., Raterron, P., Chen, J. H., Vaughan, M., Me, S. H., and Durham, B., 2006. Deformation of olivine at mantle pressure using the D-DIA. *European Journal of Mineralogy* **18**, 7-19.

Liu, W., Kung, J., and Li, B. S., 2005. Elasticity of San Carlos olivine to 8 GPa and 1073 K. *Geophysical Research Letters* **32**.

Mackwell, S. J., Kohlstedt, D. L., and Paterson, M. S., 1985. The role of water in the deformation of olivine single crystals. *Journal of Geophysical Research* **90**, 11319-11333.

Meade, C. and Jeanloz, R., 1989. Acoustic emissions and shear instabilities during phase transformation in Si and Ge at ultrahigh pressure. *Nature* **339**, 616-618.

Meade, C. and Jeanloz, R., 1990. the strength of mantle silicates at high pressure and room temperature: implications for the viscosity of the mantle. *Nature* **348**, 533-535.

Meade, C. and Jeanloz, R., 1991. Deep focus earthquakes and recycling of water into the Earth's mantle. *Science* **252**, 68-72.

Mei, S. and Kohlstedt, D. L., 2000a. Influence of water on plastic deformation of olivine aggregates 1: diffusion creep regime. *Journal of Geophysical Research* **105**, 21457-21469.

Mei, S. and Kohlstedt, D. L., 2000b. Influence of water on plastic deformation of olivine aggregates 2: dislocation creep regime. *Journal of Geophysical Research* **105**, 21471-21481.

Ogawa, M., 1987. Shear instability in a viscoelastic material as the cause of deep focus earthquake. *Journal of Geophysical Research* **92**, 13801-13810.

Orowan, E., 1960. Mechanism of seismic faulting. In: Griggs, D. T., Handlin, J. (Ed.), *Deformation*. Geological Society Memoir, London.

Peacock, S. M., 2001. Are the lower planes of double seismic zones caused by serpentine dehydration in subducting oceanic mantle? *Geology* **29**, 299-302.

Post, J. P. J., 1977. High temperature creep of Mt. Burnet dunite. *Tectonics* **7**, 1243-1256.

Raleigh, C. B. and Paterson, M. S., 1965. Experimental Deformation of Serpentinite and Its Tectionic Implications. *Journal of Geophysical Research* **70**, 3965-&.

Raterron, P., Wu, Y. J., Weidner, D. J., and Chen, J. H., 2004. Low-temperature olivine rheology at high pressure. *Physics of the Earth and Planetary Interiors* **145**, 149-159.

Singh, A. K., Balasingh, C., Mao, H. K., Hemley, R. J., and Shu, J. F., 1998. Analysis of lattice strains measured under nonhydrostatic pressure. *Journal of Applied Physics* **83**, 7567-7575.

Wang, Y., Durham, W. B., Getting, I. C., and D.J., W., 2003. The deformation DIA: a new apparatus for high temperature trialxial deformation for pressure up to 15 GPa. *Review of Scientific Instruments* **74**, 3002-3011.

Zha, C. S., Duffy, T. S., Downs, R. T., Mao, H. K., and Hemley, R. J., 1996. Sound velocity and elasticity of single-crystal forsterite to 16 GPa. *Journal of Geophysical Research-Solid Earth* **101**, 17535-17545.

Zhang, J. F., Green, H. W., Bozhilov, K., and Jin, Z. M., 2004. Faulting induced by precipitation of water at grain boundaries in hot subducting oceanic crust. *Nature* **428**, 633-636.

Figure Captions:

Fig. 4-1a Diagram of absorbance vs. wavenumber of recovered San Carlos olivine polycrystalline sample, San 122. Sample is deformed at 5 GPa.

Fig. 4-1b Diagram of absorbance vs. wavenumber of recovered San Carlos olivine polycrystalline sample, San 123. Sample is deformed at 5 GPa.

Fig. 4-1c Diagram of absorbance vs. wavenumber of recovered San Carlos olivine polycrystalline sample, San 131. Sample is deformed at 5 GPa.

Fig 4-2a SEM image of San Carlos olivine powder, used as "coarse grain" starting material in this study. The majority of grain size is 10-20 um level

Fig 4-2b SEM image of San Carlos olivine powder, used as "fine grain" starting material in this study. The majority grain size is submicron level

Fig. 4-3a Stress vs. temperature for San Carlos olivine during the deformation of olivine in increase and decrease temperature cycles at 5 GPa, unannealed sample, San 122. The temperature is measured by the W3%Re-W25%Re thermalcouple. The stress is the average of the values deduced from five peaks (021), (101), (130), (131) and (112). Blue diamond, temperature increase cycle, coarse sample; open square, temperature decrease cycle, coarse sample; open triangle, temperature increase cycle, fine sample. Solid line: flow law from Raterron et al. (2004)

Fig. 4-3b Stress vs. temperature for San Carlos olivine during the deformation of olivine in increase and decrease temperature cycles at 5 GPa, annealed sample, San 123. The temperature is measured by the W3%Re-W25%Re thermalcouple. The stress is the average of the values deduced from five peaks (021), (101), (130), (131) and (112). Blue diamond, temperature increase cycle; open square, temperature decrease cycle.

Fig. 4-3c Stress vs. temperature for San Carlos olivine during the deformation of olivine in increase and decrease temperature cycles at 5 GPa, annealed sample, San 131. The temperature is measured by the W3%Re-W25%Re thermalcouple. The stress is the average of the values deduced from five peaks (021), (101), (130), (131) and (112). Blue diamond, temperature increase cycle; open square, temperature decrease cycle.

Fig. 4-4a Strain as a function of time for the deformation experiment of run San122 at 5 GPa, unannealed polycrystal San Carlos olivine. Open square, coarse grain; diamond black, fine grain. The strain rate is about 2.3×10^{-5} s^{-1} for coarse sample and 5.0×10^{-5} s^{-1} for fine sample. A little fluctuation is found during the experiment

Fig. 4-4b Strain as a function of time for the deformation experiment of run San123 at 5 GPa, annealed polycrystal San Carlos olivine, "normal".

Fig. 4-4c Strain as a function of time for the deformation experiment of run San131 at 5 GPa, annealed polycrystal San Carlos olivine, "wet"

Fig 4-5 Sketch map for the olivine instability models: "Sandwich" and water weakening.

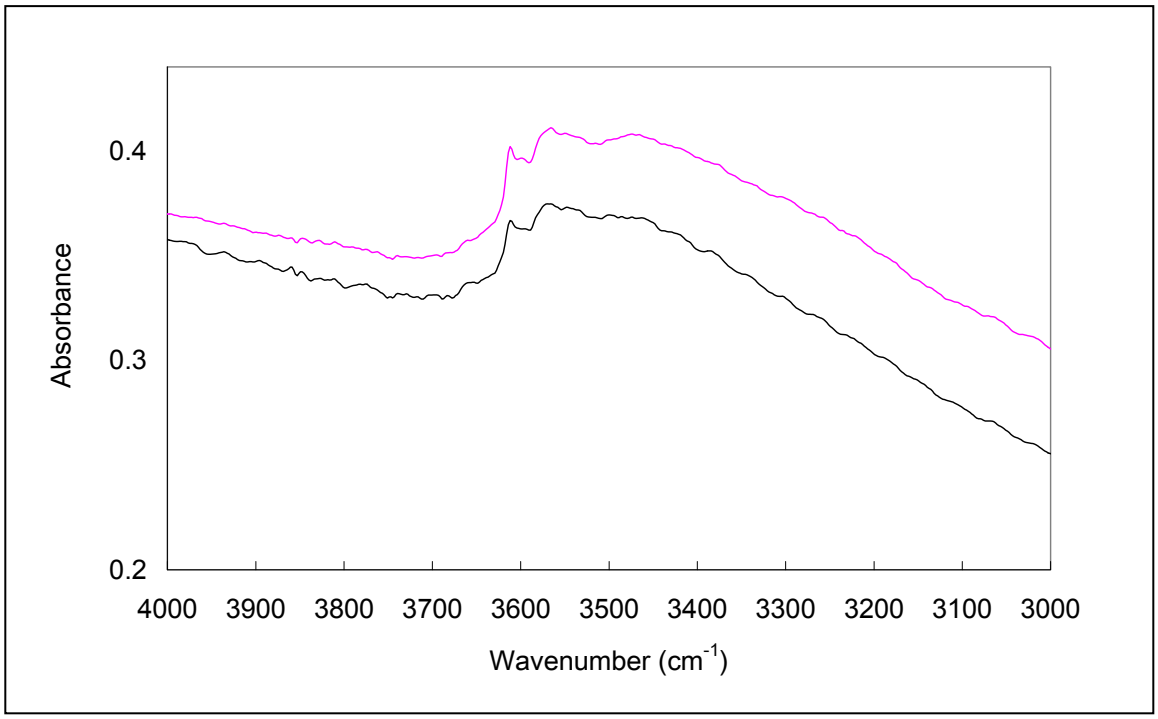

Fig. 4-1a Diagram of absorbance vs. wavenumber of recovered San Carlos olivine polycrystalline sample, San 122. Sample is deformed at 5 GPa.

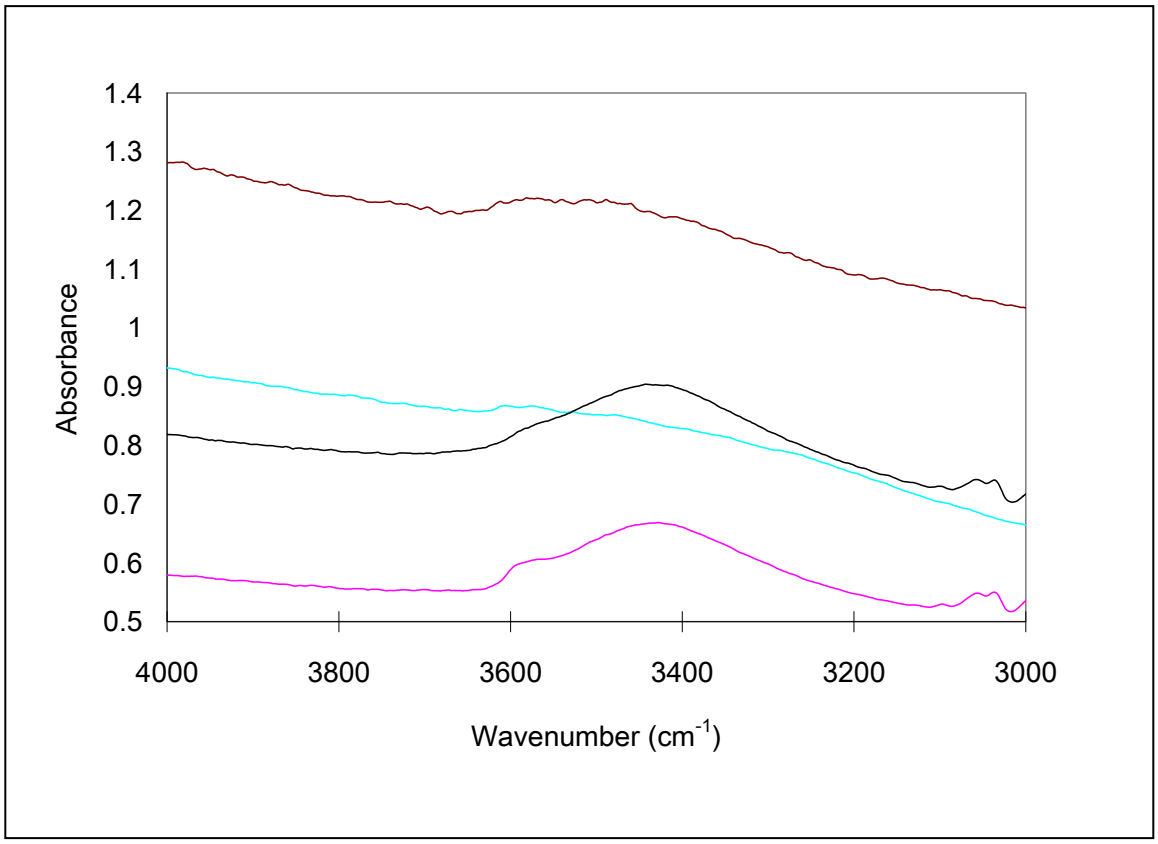

Fig. 4-1b Diagram of absorbance vs. wavenumber of recovered San Carlos olivine polycrystalline sample, San 123. Sample is deformed at 5 GPa.

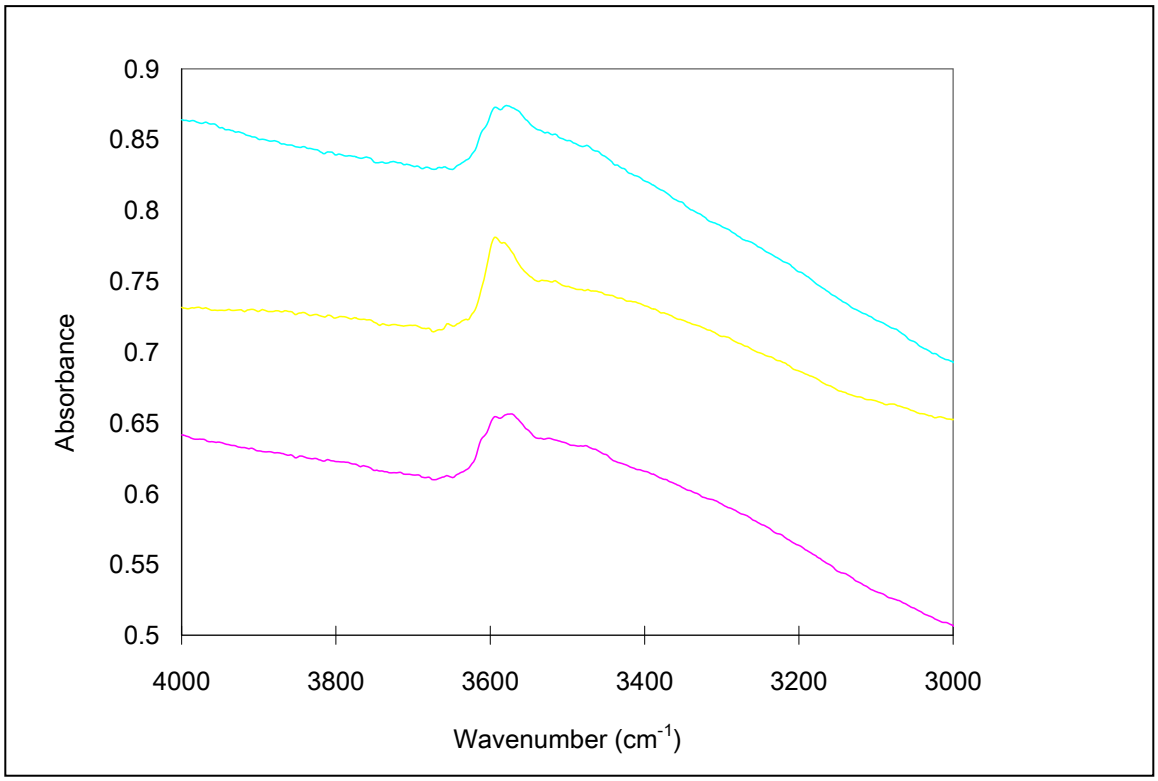

Fig. 4-1c Diagram of absorbance vs. wavenumber of recovered San Carlos olivine polycrystalline sample, San 131. Sample is deformed at 5 GPa.

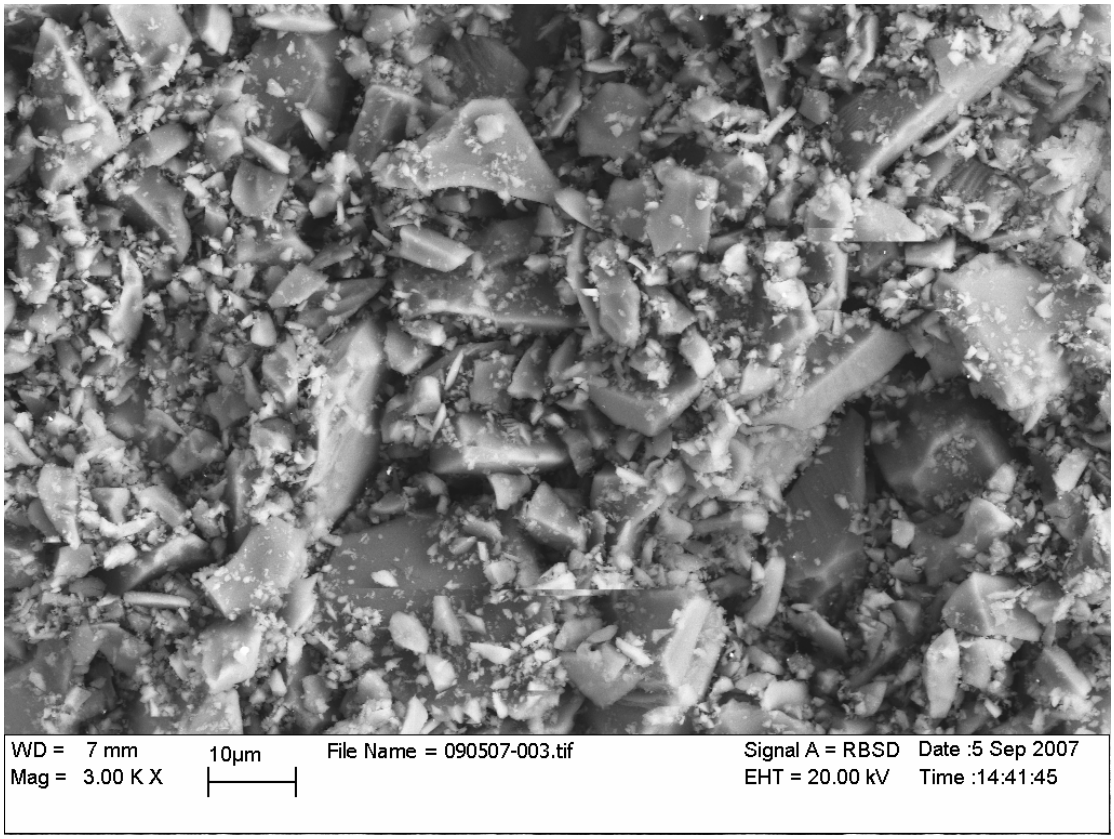

Fig 4-2a SEM image of San Carlos olivine powder, used as "coarse grain" starting material in this study. The majority of grain size is 10-20 um.

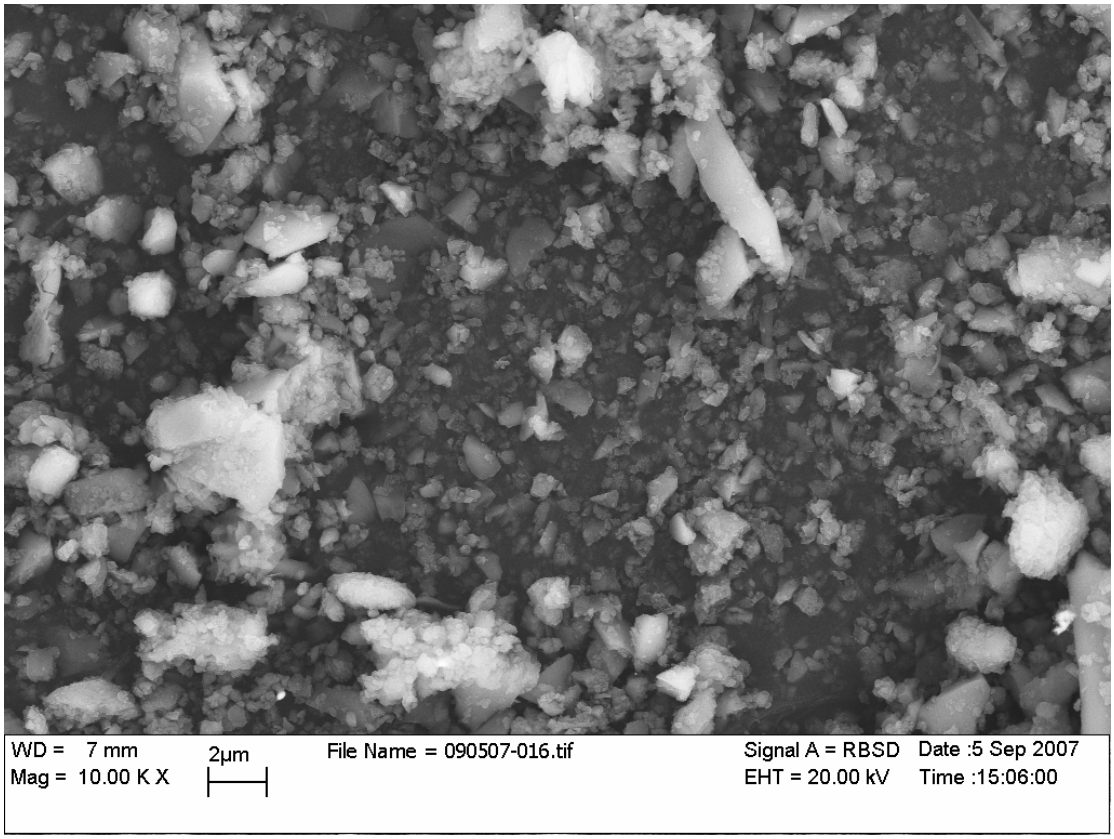

Fig 4-2b SEM image of San Carlos olivine powder, used as "fine grain" starting material in this study. The majority grain is submicron level.

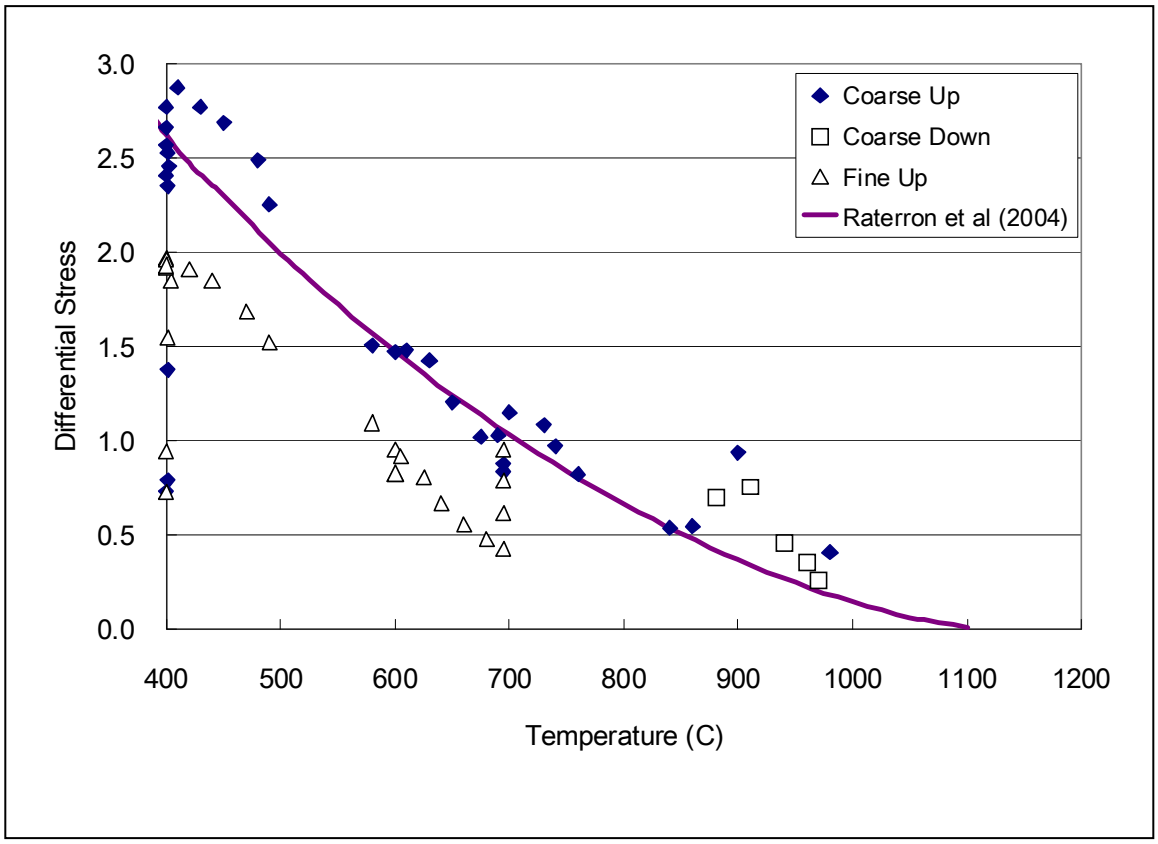

Fig. 4-3a Stress vs. temperature for San Carlos olivine during the deformation of olivine in increase and decrease temperature cycles at 5 GPa, unannealed sample, San 122. The temperature is measured by the W3%Re-W25%Re thermalcouple. The stress is the average of the values deduced from five peaks (021), (101), (130), (131) and (112). Blue diamond, temperature increase cycle, coarse sample; open square, temperature decrease cycle, coarse sample; open triangle, temperature increase cycle, fine sample. Solid line: flow law from Raterron et al. (2004)

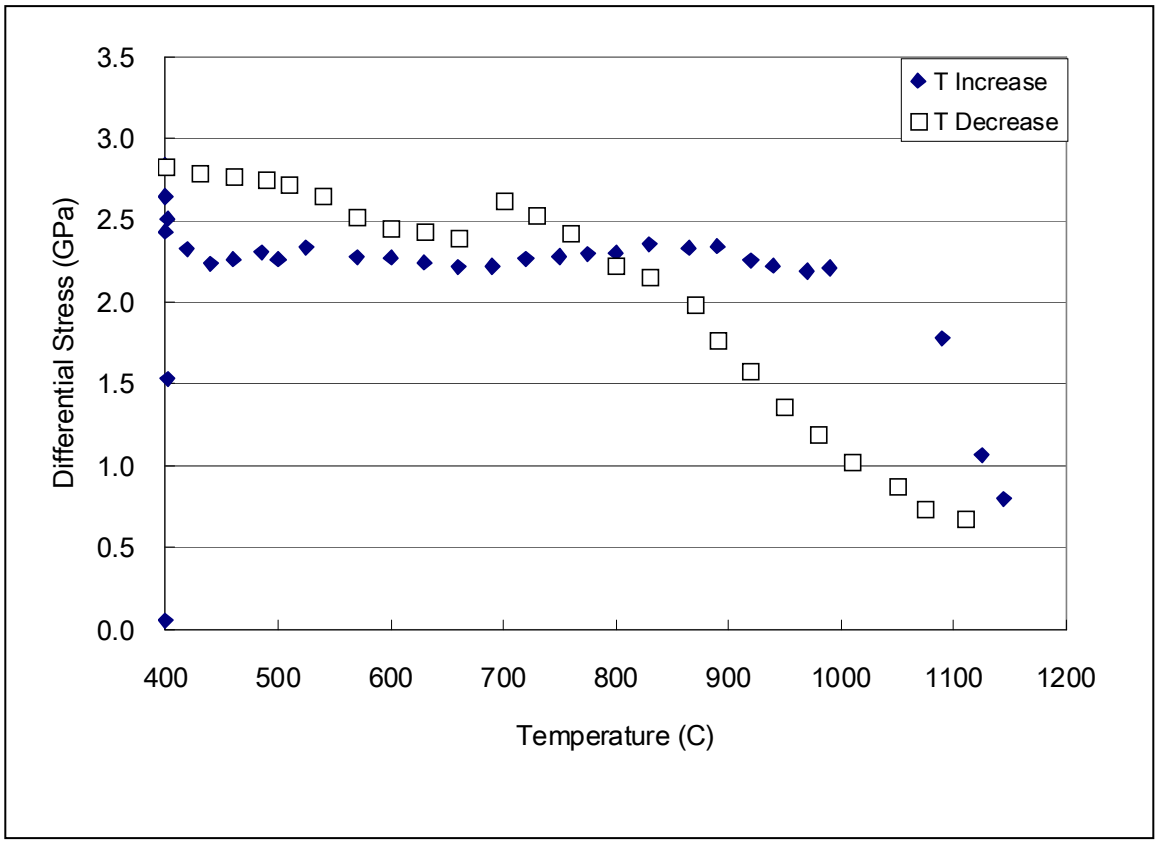

Fig. 4-3b Stress vs. temperature for San Carlos olivine during the deformation of olivine in increase and decrease temperature cycles at 5 GPa, annealed sample, San 123. The temperature is measured by the W3%Re-W25%Re thermalcouple. The stress is the average of the values deduced from five peaks (021), (101), (130), (131) and (112). Blue diamond, temperature increase cycle; open square, temperature decrease cycle.

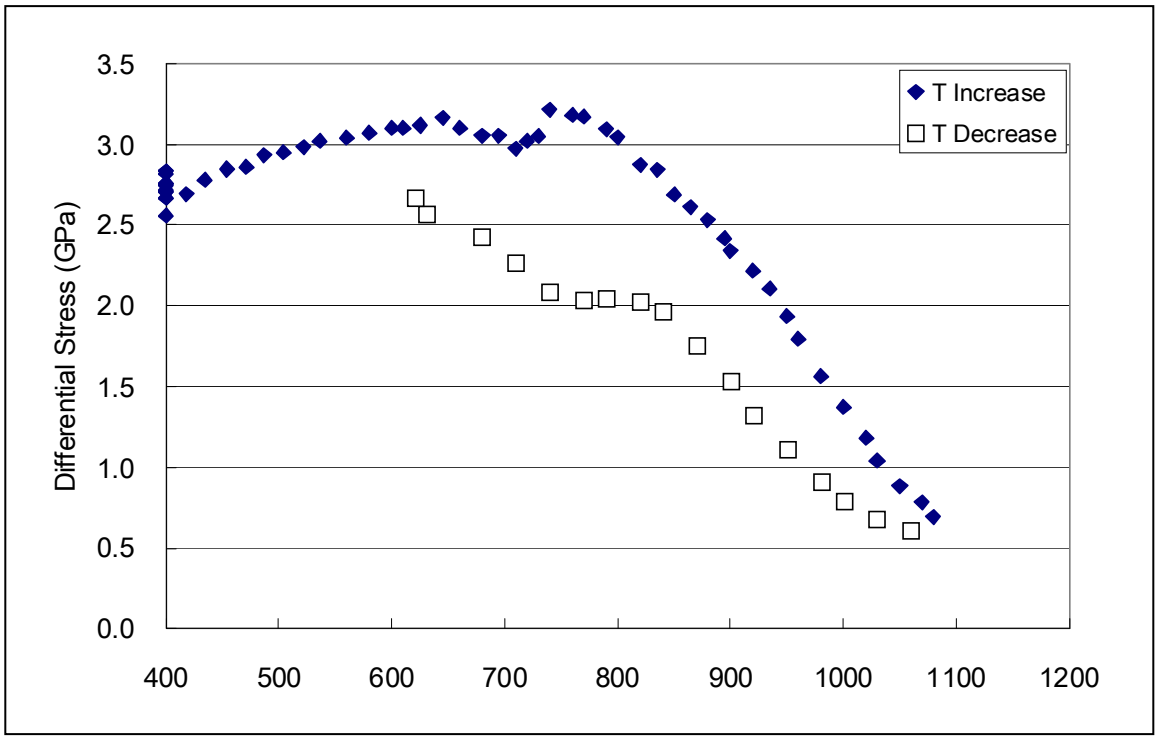

Fig. 4-3c Stress vs. temperature for San Carlos olivine during the deformation of olivine in increase and decrease temperature cycles at 5 GPa, annealed sample, San 131. The temperature is measured by the W3%Re-W25%Re thermalcouple. The stress is the average of the values deduced from five peaks (021), (101), (130), (131) and (112). Blue diamond, temperature increase cycle; open square, temperature decrease cycle.

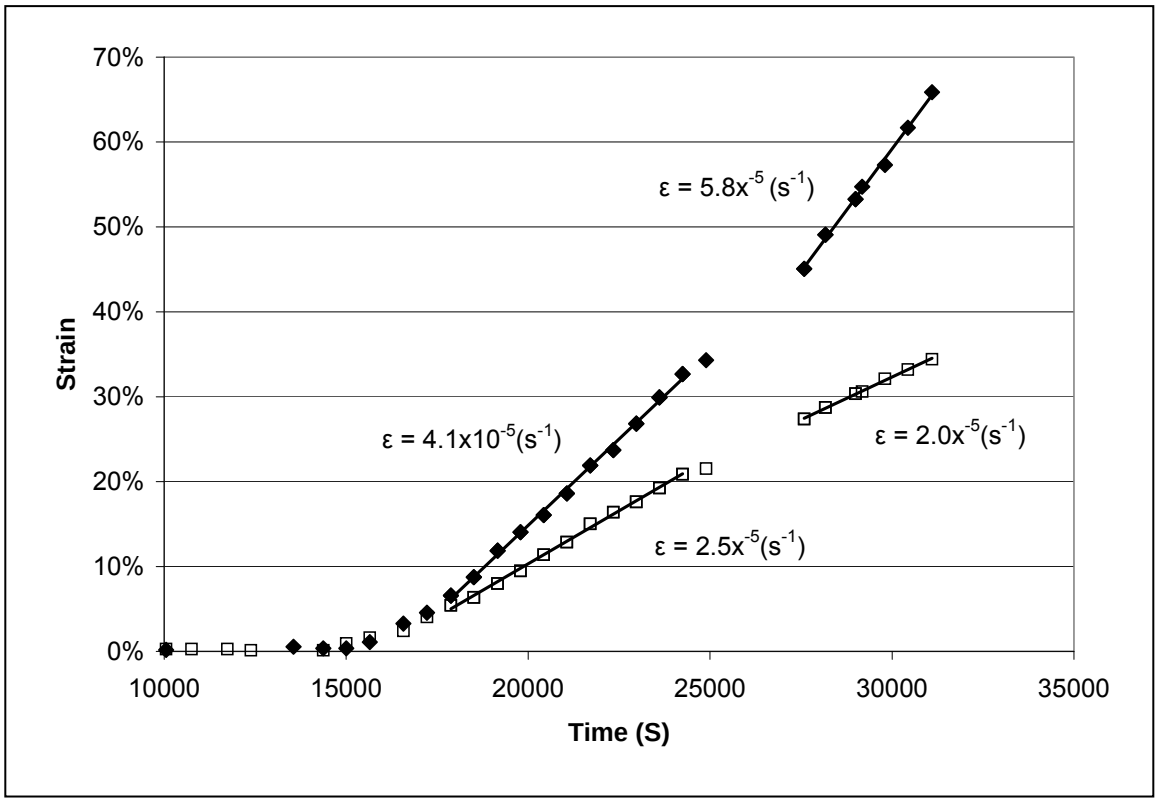

Fig. 4-4a Strain as a function of time for the deformation experiment of run San122 at 5 GPa, unannealed polycrystal San Carlos olivine. Open square, coarse grain; diamond black, fine grain. The strain rate is about 2.3 x 10^{-5} s^{-1} for coarse sample and 5.0 x 10^{-5} s^{-1} for fine sample. A little fluctuation is found during the experiment.

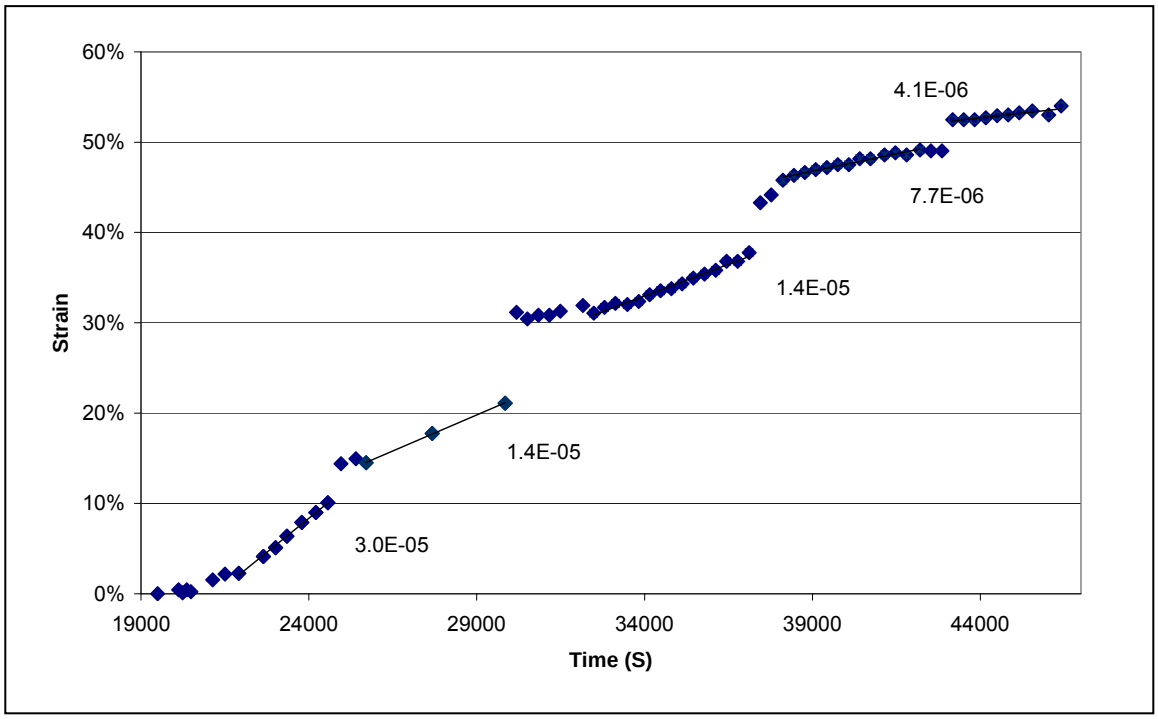

Fig. 4-4b Strain as a function of time for the deformation experiment of run San123 at 5 GPa, annealed polycrystal San Carlos olivine, "normal".

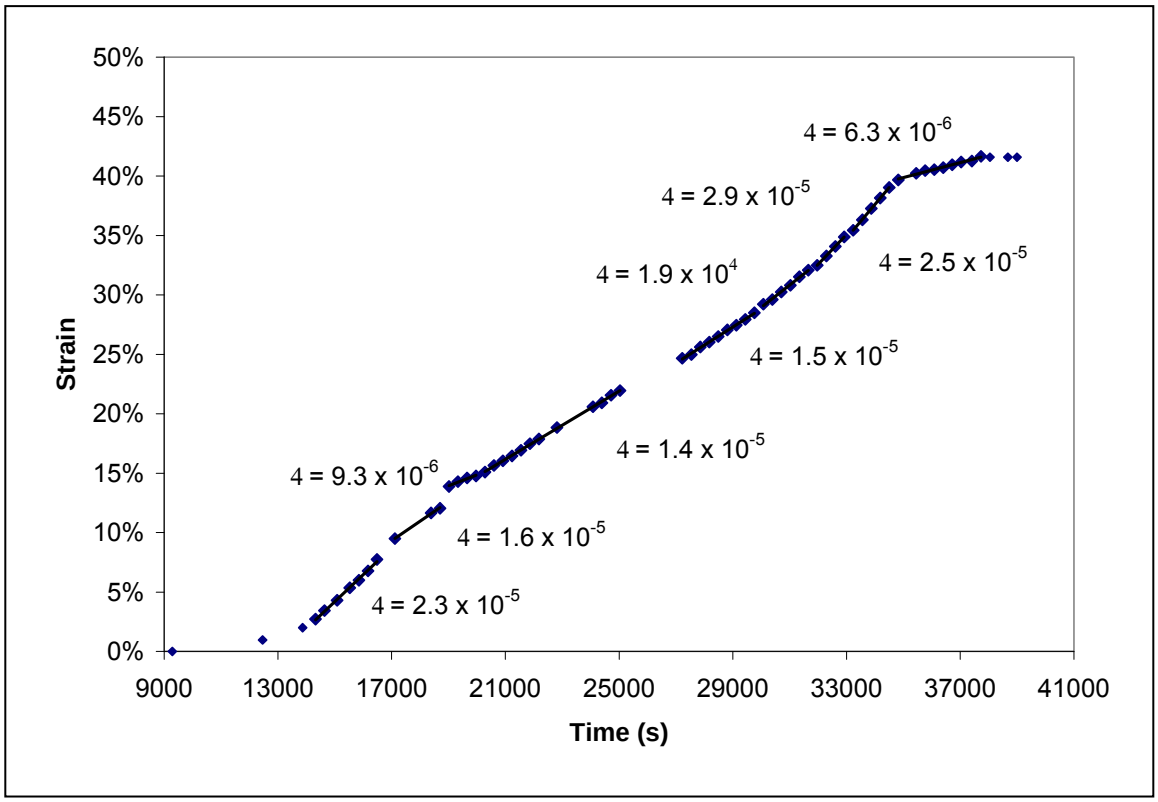

Fig. 4-4c Strain as a function of time for the deformation experiment of run San131 at 5 GPa, annealed polycrystal San Carlos olivine, "wet".

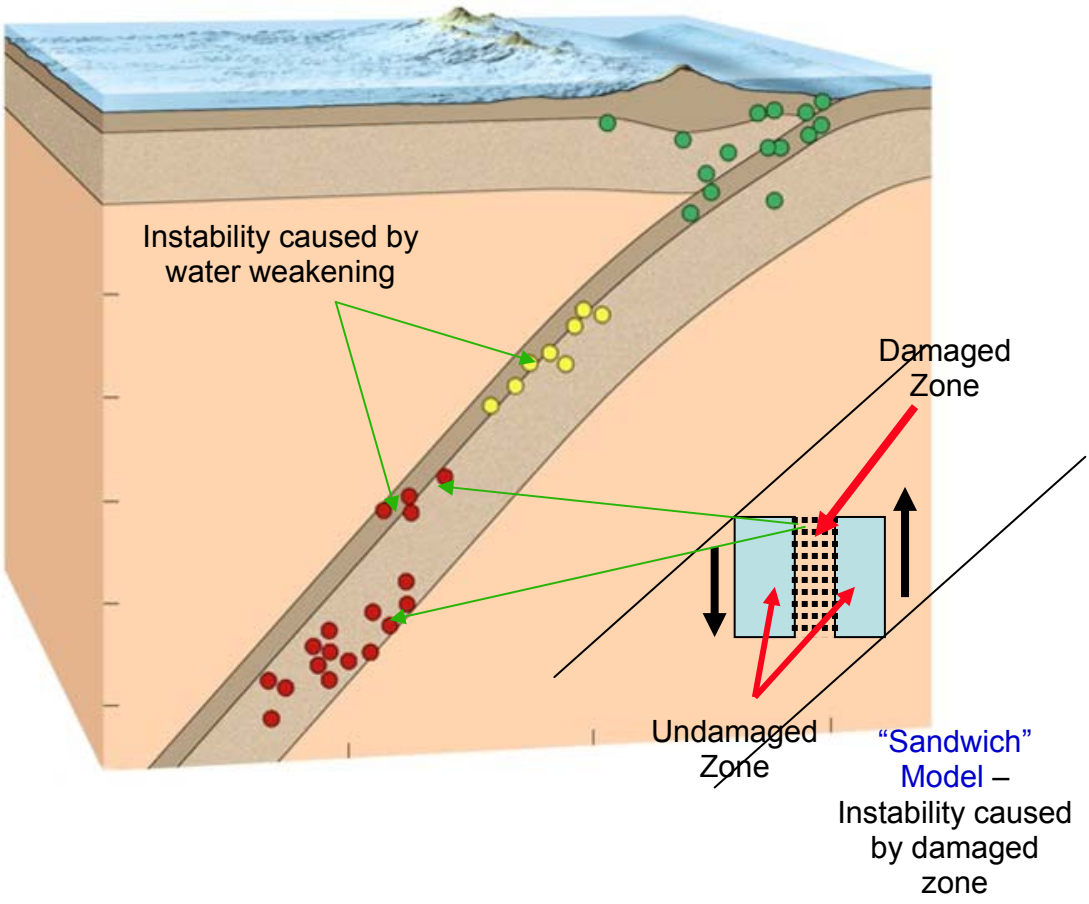

Fig 4-5 Sketch map for the olivine instability models: "Sandwich" and water weakening.

Chapter 5

Summary

The deformation of San Carlos olivine at subduction zone condition (high pressure and low temperature) has been performed on a deformation DIA apparatus, SAM85, at X17B2, NSLS. Powder samples are used in these experiments. Enstatite ($MgSiO_3$) (3-5% total quality of sample) is used as a buffer to control the activity of silica. Ni foil is used in some experiments to buffer the oxygen fugacity. Samples are compressed at room temperature and are then annealed at 1200°C for at least 2 hours before deformation. The total (plastic and elastic) strains (macroscopic) are derived from the direct measurements of the images taken by X-ray radiograph technique. The differential stresses are deduced from elastic strains, which are calculated from olivine elastic. Respecting to the incident synchrotron X-ray beam, the elastic constraints are *in situ* measured in different directions and are collected as a function of time by the X-ray multi-detector EDS. At constant strain rates ($\sim 10^{-5}$-$10^{-7} s^{-1}$) the experiments are preformed at different pressures and temperatures. Water content is confirmed by IR spectra of the recovered samples on a synchrotron IR facility at U2A, NSLS. The microscopic structures of the recovered samples are analyzed by SEM and EBSD. The effects of

annealing/unannealing process, grain size, water, and oxygen fugacity during deformation are discussed.

I conduct six runs for the purpose of studying the deformation of olivine at steady state. It can be concluded that in the regime of 25-400°C, there is a small increase of stress at steady state along with the temperature drop; in the regime of 400°C to transition temperature, the differential stress at steady state is a constant (~3 GPa) and is relatively insensitive to the changes of temperature and strain rate; however, it drastically decreases to about 1 GPa and becomes temperature-dependent above the transition temperature and thereafter. The transition temperature is between 700°C and 900°C. No significant difference of differential stress and strain is observed between the samples with/without Ni foil buffered below 700°C. Two regimes with different deformation mechanisms for olivine have been determined in this study: regime of low temperature plasticity at low temperature (below transition temperature) and regime of power law creep at high temperature (above the transition temperature).

I analyze three recovered samples by SEM and two by EBSD program. All of them are deformed and reach steady state from the single temperature experiments at 25°C, 500°C and 700°C, respectively. The SEM results show that compression and deformation make the grain size of olivine into sub-micron level. The pseudo grains in the recovered sample may be the relics developed from the starting olivine grains and become foliations vertical to the deforming axis undergoing the deformation. In the EBSD study, The LPO shows that the predominant active slip systems of olivine at subduction zone condition and mantle pressure evolve from $\{hk0\}[001]$ ($h > k$) and $\{110\}[001]$ at 500°C to $\{hk0\}[001]$ ($h > k$) and $(100)[001]$ at 700°C.

The annealing process can significantly shift up the transition temperature between regimes of temperature insensitive and sensitive. Grain size affects the rheological properties of olivine in the low temperature dislocation regime. Existence of water significantly decreases the transition temperature of the boundary between the regimes of low temperature plasticity and power-law creep.

The annealed and unannealed olivine can represent the natural olivine in non-fault systems and that in pre-existing fault systems in subduction zone, respectively. I therefore propose a new olivine instability model with a "sandwich" formation for the deep focus earthquakes. In this model the pre-existing fault system is surrounded by the non-fault systems. When the slab dives down, the olivine in both systems undergoes a stress-build-up process and can hold very high stress in both cases. However, as it keeps diving to the transition zone, the slab is heated and its temperature arrives at the boundary temperature from the temperature insensitive regime to the temperature sensitive regime for the olivine in pre-existing fault system. As a result, while the olivine in non-fault system is still in regime of temperature insensitive and can still hold the built-up high stress, the olivine in pre-existing fault system can not hold the built-up stress any more and gives out a stress release. The pre-existing fault is re-activated and heat from the re-activated fault accelerates the ongoing process. Earthquake happens.

The existence of water significantly shifts down the transition temperature of the boundary between low temperature plasticity and the power-law creep. As the slab dives down to the deep earth, the temperature goes up. Thus the olivine in the hydrous environment reaches the boundary and goes into the power-law creep earlier than the

olivine in the anhydrous environment during the slab diving process. The maximum stress becomes temperature dependent in the hydrous environment and the hydrous olivine weakens quickly thereafter. Comparing to the natural system, the transition temperature for the olivine in slab is most likely in the range of 550-600°C. Therefore in a hydrous slab, olivine could cross the transition boundary earlier than 550-600°C as the slab continuously dives down. As a result it could have a quick stress release and the produced heat can heat the system up. The deep earthquake may happen by such a mechanism of olivine instability too.

Bibliography

Bai, Q. and Kohlstedt, D.L., 1992a. High-temperature creep of olivine single crystals, 2. dislocation structures. Tectonophysics, 206(1-2): 1-29.

Bai, Q. and Kohlstedt, D.L., 1992b. High-temperature creep of olivine single-crystals. 3. Mechanical results for unbuffered sample and creep mechanisms. Philosophical Magazine A-Physics of Condensed Matter Structure Defects and Mechanical Properties, 66(6): 1149-1181.

Bai, Q., Mackwell, S.J. and Kohlstedt, D.L., 1991. High-temperature creep of olivine single crystal, 1. Mechanical results for buffered sample. Journal of Geophysical Research, 96(B2): 2441-2463.

Bejina, F., Raterron, P., Zhang, J.Z., Jaoul, O. and Libermann, R.C., 1997. The Activation volume of silicon diffusion in San Carlos olivine. Geophysical Research Letters, 24(21): 2597-2600.

Bell, D.R. and Rossman, G.R., 1992. Water in Earth's mantle: The role of nominally anhydrous minerals. Science, 255(5050): 1391-1397.

Bell, D.R., Rossman, G.R., Maldener, J., Endisch, D. and Rauch, F., 2003. Hydroxide in olivine: A quantitative determination of the absolute amount and calibration of the IR spectrum. Journal of Geophysical Research-Solid Earth, 108(B2): 2105, doi: 10.1029/2001 JB000679.

Benioff, H., 1963. Source wave forms of three earthquakes. Bulletin of Seismological Society of America, 53(5): 893-903.

Borch, R.S. and Green, H.W.I., 1987. Dependence of greep in olivine on homologous temperature and its implications for flow in the mantle. Nature, 330(6146): 345-348.

Brearley, A.J., Rubie, D.C. and Ito, E., 1992. Mechanisms of the transformations between the alpha-polymorphs, beta-polymorphs and gamma polymorphs of Mg2SiO4 at 15 GPa. Physics and Chemistry of Minerals, 18(6): 343-358.

Bridgman, P.W., 1936. Shearing phenomena at high pressure of possible importance for geology. Journal of Geology, 44: 653-669.

Bridgman, P.W., 1945. Polymorphic transitions and geological phenomena. American Journal of Science, 243A: 90-97.

Carter, N.C. and Ave Lallemant, H.G., 1970. High temperature flow of dunite and peridotite. Geological Society of America Bulletin, 81: 2181-2202.

Chai, M., Brown, M. and Wang, Y., 1998. Yield strength, slip systems and deformation induced phase transition of San-Carlos olivine up to the transition zone pressure at room temperature. In: M.H. Manghnani, Yagi, T. (Editor), Properties of Earth and Planetary Materials. American Geophysical Union, pp. 483-493.

Chen, J., Inoue, T., Weidner, D.J., Wu, Y.J. and Vaughan, M.T., 1998. Strength and water weakening of mantle minerals, olivine, wadsleyite and ringwoodite. Geophysical Research Letters, 25(4): 575-578.

Chen, J., Li, L., Weidner, D.J. and Vaughan, M.T., 2004. Deformation experiments using synchrontron X-rays: in situ stress and strain measurements at high pressure and temperature. Physics of the Earth and Planetary Interiors, 143-144: 347-356.

Chopra, P.N. and Paterson, M.S., 1981. The experimental deformation of dunite. Tectonophysics, 78: 453-473.

Chopra, P.N. and Paterson, M.S., 1984. The role of water in the deformation of dunite. Journal of Geophysical Research, 89(NB9): 7861-7876.

Couvy, H. et al., 2004. Shear deformation experiments of forsterite at 11GPa-1400 degrees C in the multianvil apparatus. European Journal of Mineralogy, 16(6): 877-889.

Dobson, D.P., Meredith, P.G. and Boon, S.A., 2002. Simulation of subduction zone seismicity by dehydration of serpentine. Science, 298(5597): 1407-1410.

Durham, W.B. and Goetze, C., 1977. A comparison of creep properties of pure forsterite and iron-bearing olivine. Tectonophysics, 40: 15-18.

Durham, W.B. and Rubie, D.C., 1998. Can the multianvil apparatus really be used for high-pressure deformation experiments. In: M.H. Manghnani, Yagi, T. (Editor), Properties of Earth and Planetary Materials at High Pressure and Temperature. American Geophysical Union, pp. 63-70.

Durham, W.B., Weidner, D.J., Karato, S.-I. and Wang, Y., 2002. New developments in deformation experiments at high pressure. In: S.-I. Karato, Wenk, H.R. (Editor), Plastic Deformation of Minerals and Rocks, Reviews in Mineralogy and Geochemistry. Mineralogy Society of America, Chantilly, Virginia, pp. 21-50.

Evans, B. and Geotze, C., 1979. The temperature variation of hardness of olivine and its implication for polycrystalline yield stress. Journal of Geophysical Research, 84(NB10): 5505-5524.

Evans, B. and Kohlstedt, D., 1995. Rheology of Rocks. In: T. Ahren (Editor), Rock Physics and Phase Relations: a Handbook of Physical Constants. The american Geophysical Union, Washington DC, pp. 148-165.

Frese, K., Trommsdorff, V. and Kunze, K., 2003. Olivine [100] normal to foliation: lattice preferred orientation in prograde garnet peridotite formed at high H2O activity, Cima di Gagnone (Central Alps). Contributions to Mineralogy and Petrology, 145(1): 75-86.

Frost, H.J. and Ashby, M.F., 1982. Deformation-Mechanism Maps The Plasticity and Creep of Metals and Ceramics. Pergamon Press, Oxford, New York, Toronto, Sydney, Paris, Frankfurt.

Green II, H.W., 2007. Shearing instabilities accompanying high-pressure phase transformations and the mechanics of deep earthquakes. Proceedings of the

National Academy of Sciences of the United States of America, 104(22): 9133-9138.

Green II, H.W. and Borch, R.S., 1987. The pressure-dependence of creep. Acta Metallurgica, 35(6): 1301-1305.

Green II, H.W. and Houston, H., 1995. The Mechanics of deep earthquakes. Annual Review of Earth and Planetary Sciences, 23: 169-213.

Griggs, D.T., 1954. High-pressure phenomena with applications to geophysics. In: L.N. Ridenour (Editor), Modern Physics for the Engineer. McGraw Hill, New York, pp. 272-305.

Griggs, D.T., 1972. The sinking lithophere and the focal mechanism of deep earthquakes. In: E.C. Robertson (Editor), The Nature of Solid Earth. McGraw Hill, New York, pp. 361-384.

Griggs, D.T. and Baker, D.W., 1969. The origin of deep-focus earthquakes. In: H. Mark, Fernbach, S. (Editor), Properties of matter under unusual conditions. Interscience Publishers

New York/London/Sydney/Toronto, pp. 23-42.

Griggs, D.T. and Handlin, J., 1960. Observations on fracture and a hyphothesis of earthquakes. In: D.T. Griggs, Handlin, J. (Editor), Rock Deformation. Memoir of Geological Society of America, pp. 347-373.

Hirth, G. and Kohlstedt, D.L., 1996. Water in the oceanic upper mantle: Implications for rheology, melt extraction and the evolution of the lithosphere. Earth and Planetary Science Letters, 144(1-2): 93-108.

Hobbs, B.E., 1983. Constraints on the mechanism of deformation of olivine imposed by defect chemistry. Tectonophysics, 92(1-3): 35-69.

Hobbs, B.E., 1984. Point-defect chemistry of minerals under a hydrothermal environment. Journal of Geophysical Research, 89(NB6): 4026-4038.

Hobbs, B.E. and Ord, A., 1988. Plastic instabilities: implications for the origin of intermediate and deep focus earthquakes. Journal of Geophysical Research, 93(B9): 10521-10540.

Holt, W.E., 1995. Flow-Fields within the Tonga Slab Determined from the Moment Tensors of Deep Earthquakes. Geophysical Research Letters, 22(8): 989-992.

Isaak, D.G., 1992. High-temperature elasticity of iron-bearing olivines. Journal of Geophysical Research-Solid Earth, 97(B2): 1871-1885.

Jin, Z.M., Bai, Q. and Kohlstedt, D.L., 1994. High-temperature creep of olivine crystal from 4 localities. Physics of the Earth and Planetary Interiors, 82(1): 55-64.

Jung, H., Green, H.W. and Dobrzhinetskaya, L.F., 2004. Intermediate-depth earthquake faulting by dehydration embrittlement with negative volume change. Nature, 428(6982): 545-549.

Jung, H. and Karato, S.-I., 2001. The effect of water on dynamically recrystallized grain-size of olivine. Journal of Structural Geology, 23(9): 1337-1344.

Kao, H. and Chen, W.P., 1995. Transition from interplate slip to double seimic zone along the Kuril-Kamchatka arc. Journal of Geophysical Research, 100(B6): 9881-9904.

Karato, S.-I., 1989. Defect and plastic deformation in olivines. In: S.-I. Karato, Toriumi, M. (Editor), Rheology of Solids and of the Earth. Oxford University Press, New York, pp. 176-208.

Karato, S.-I. and Jung, H., 2003. Effects of pressure on high-temperature dislocation creep in olivine. Philosophical Magazine, 83(3): 401-414.

Karato, S.-I., Paterson, M.S. and FitzGerald, J.D., 1986. Rheology of synthetic olivine aggregates: influence of grain size and water. Journal of Geophysical Research, 91(B8): 8151-8176.

Karato, S.-I. and Rubie, D.C., 1997. Toward an experimental study of deep mantle rheology: A new multianvil sample assembly for deformation studies under high pressures and temperatures Journal of Geophysical Research, 102(B9): 20111-20122.

Karato, S.-I., Rubie, D.C. and Yan, H., 1993. Dislocation recovery in olivine under deep upper mantle conditions - implications for creep and diffusion. Journal of Geophysical Research, 98(B6): 9761-9768.

Karato, S.-I. and Sato, H., 1982. Effect of oxygen partial pressure on the dislocation recovery in olivine: a new constraint on creep mechanisms. Physics of the Earth and Planetary Interiors, 28(4): 312-319.

Karato, S.-I. and Wu, P., 1993. Rheology of the upper mantle: a synthesis. Science, 260(5109): 771-778.

Kohlstedt, D.L., Evan, B. and Mackwell, S.J., 1995. Strength of the lithosphere: Constraints imposed by laboratory experiments. Journal of Geophysical Research, 100(B9): 17587-17602.

Kohlstedt, D.L. and Hornack, P., 1981. The effect of oxygen partial pressure on the creep of olivine. In: F.D. Stacey, Paterson, M,S, Nicolas, A. (Editor), Anelasticity in the Earth, Geodynamics Series. American Geophysical Union, Washington, D.C., pp. 101-107.

Kohlstedt, D.L., Keppler, H. and Rubie, D.C., 1996. Solubility of water in the alpha, beta and gamma phases of (Mg,Fe)2SiO4. Contributions to Mineralogy and Petrology, 123(4): 345-357.

Kohlstedt, D.L., Nicholas, H.P.K. and Hornack, P., 1980. The effect of pressure on the rate of dislocation recovery in olivine. Journal of Geophysical Research, 85(NB6): 3122-3130.

Kohlstedt, D.L. and Wang, Z.Y., 2001. Grain boundary sliding accomodated dislocation creep in dunite. EOS, Transactions, American Geophysical Union, 82(47): F1137.

Li, L., Long, H., Raterron, P. and Weidner, D., 2006a. Plastic flow of pyrope at mantle pressure and temperature. American Mineralogist, 91(4): 517-525.

Li, L., Raterron, P., Weidner, D.J. and Chen, J., 2003. Olivine flow mechanisms at 8 GPa. Physics of the Earth and Planetary Interiors, 97: 121-131.

Li, L., Weidner, D.J., Chen, J., Vaughan, M.T. and Davis, M., 2004a. X-ray strain analysis at high pressure: effect of plastic deformation in MgO. Journal of Applied Physics, 95(12): 8357-8365.

Li, L., Weidner, D.J., Raterron, P., Chen, J. and Vaughan, M.T., 2004b. Stress measurement of deforming olivine at high pressure. Physics of the Earth and Planetary Interiors, 143-144: 357-367.

Li, L.L. et al., 2006b. Deformation of olivine at mantle pressure using the D-DIA. European Journal of Mineralogy, 18(1): 7-19.

Liu, W., Kung, J. and Li, B.S., 2005. Elasticity of San Carlos olivine to 8 GPa and 1073 K. Geophysical Research Letters, 32(16).

Mackwell, S.J., Kohlstedt, D.L. and Paterson, M.S., 1985. The role of water in the deformation of olivine single crystals. Journal of Geophysical Research, 90(NB13): 11319-11333.

Meade, C. and Jeanloz, R., 1989. Acoustic emissions and shear instabilities during phase transformation in Si and Ge at ultrahigh pressure. Nature, 339: 616-618.

Meade, C. and Jeanloz, R., 1990. the strength of mantle silicates at high pressure and room temperature: implications for the viscosity of the mantle. Nature, 348: 533-535.

Meade, C. and Jeanloz, R., 1991. Deep focus earthquakes and recycling of water into the Earth's mantle. Science, 252: 68-72.

Mei, S. and Kohlstedt, D.L., 2000a. Influence of water on plastic deformation of olivine aggregates 1: diffusion creep regime. Journal of Geophysical Research, 105(B9): 21457-21469.

Mei, S. and Kohlstedt, D.L., 2000b. Influence of water on plastic deformation of olivine aggregates 2: dislocation creep regime. Journal of Geophysical Research, 105(B9): 21471-21481.

Mercier, J.C., 1985. Olivine and pyroxenes. In: H.R. Wenk (Editor), Preferred Orientation in Deformed Metals and Rocks:

An Introduction to Modern Texture Analysis. Academic Press, Orlando, FL, pp. 407-430.

Mockel, J.R., 1969. Structural petrology of the garnet-peridotite of Alpe Arami (Ticino, Switzerland). Leidse Geol Meded, 42: 61-130.

Nicolas, A., Boudier, F. and Boullier, A.M., 1973. Mechanisms of Flow in Naturally Deformed Peridotites. American Journal of Science, 273(10): 853-876.

Ogawa, M., 1987. Shear instability in a viscoelastic material as the cause of deep focus earthquake. Journal of Geophysical Research, 92(B13): 13801-13810.

Orowan, E., 1960. Mechanism of seismic faulting. In: D.T. Griggs, Handlin, J. (Editor), Deformation. Geological Society Memoir, London, pp. 323-345.

Paterson, M.S., 1982. The determination of hydroxyl by infrared absorption in quartz, silicate glass and similar materials. Bulletin Mineralogie, 105: 20-29.

Peacock, S.M., 2001. Are the lower planes of double seismic zones caused by serpentine dehydration in subducting oceanic mantle? Geology, 29(4): 299-302.

Post, J.P.J., 1977. High temperature creep of Mt. Burnet dunite. Tectonics, 7: 1243-1256.

Poumellec, B. and Jaoul, O., 1984. Influence of P_{O2} and P_{H2O} on the high temperature plasticity of olivine. In: R.E. Tressler, Bradt, R.C. (Editor), Deformation of Ceramic Materials II. Plenum, New York, pp. 281-305.

Raleigh, C.B., 1968. Mechanisms of Plastic Deformation of Olivine. Journal of Geophysical Research, 73(16): 5391-&.

Raleigh, C.B. and Paterson, M.S., 1965. Experimental Deformation of Serpentinite and Its Tectionic Implications. Journal of Geophysical Research, 70(16): 3965-&.

Raterron, P., Chen, J., Li, L., Weidner, D. and Cordier, P., 2007. Pressure-induced slip-system transition in forsterite: Single-crystal rheological properties at mantle pressure and temperature. American Mineralogist, 92: 1436-1445.

Raterron, P., Wu, Y.J., Weidner, D.J. and Chen, J.H., 2004. Low-temperature olivine rheology at high pressure. Physics of the Earth and Planetary Interiors, 145: 149-159.

Ross, J.V., Avelallemant, H.G. and Carter, N.L., 1979. Activation volume for creep in the upper mantle. Science, 203(4377): 261-263.

Singh, A.K., Balasingh, C., Mao, H.K., Hemley, R.J. and Shu, J.F., 1998. Analysis of lattice strains measured under nonhydrostatic pressure. Journal of Applied Physics, 83(12): 7567-7575.

Uchida, T., Wang, Y., Rivers, M.L. and Sutton, S.R., 2004. Yield strength and strain hardening of MgO up to 8 GPa measured in deformation DIA with monochromatic X-ray diffraction. Earth and Planetary Science Letters, 226: 117-126.

Wang, Y., Durham, W.B., Getting, I.C. and D.J., W., 2003. The deformation DIA: a new apparatus for high temperature trialxial deformation for pressure up to 15 GPa. Review of Scientific Instruments, 74: 3002-3011.

Weidner, D.J., 1998. Rheological studies at high pressure. In: R.J. Hemley (Editor), Ultrahigh-Pressure Mineralogy: Physics and Chemistry of the Earth's Deep Inerior. Mineralogical Society of America, Washington, DC, pp. 493-524.

Weidner, D. J., Chen, J., Xu, Y., Wu, Y., Vaughan, M. T., and Li, L., 2001. Subduction zone rheology. Physics of the Earth and Planetary Interiors **127**, 67-81.

Weidner, D. J., Vaughan, M.T., Ko, J., Wang, Y., Leinenweber, K., Liu, X., Yeganeh-Haeri, A., Pacalo, R.E., Zhao, Y.S. 1992a. Large volumn high pressure research using the wigger port at NSLS. High Pressure Research 8: 617-623.

Weidner, D. J., Vaughan, M.T., Ko, J., Wang, Y., Liu, X., Yeganeh-Haeri, A., Pacalo, R.E., Zhao, Y.S. 1992b. Characterization of stress, pressure, and temperature in SAM-85, a DIA type high pressure apparatus. High-Pressure Research: Application to Earth and Planetary Sciences. Y. Syono, Manghnani, H. Tokyo / American Geophysical Union, Washington, D.C., Terra Scientific Publishing Company: 13-17.

Weidner, D.J., Wang, Y., Ando, J. and Vaughan, M.T., 1994. yield stress at high pressure and temperature. Geophysical Research Letters, 21: 753-756.

Weidner, D.J., Wang, Y., Chen, J., Ando, J. and Vaughan, M.T., 1998. Rheology measurements at high pressure and temperature. In: M.H. Manghnani, Yagi, T. (Editor), Properties of the Earth and Planetary Materials at High Pressure and Temperature. American Geophysical Union, pp. 473-482.

Wenk, H.R., 2002. Texture and Anisotropy. In: S.-I. Karato and H.R. Wenk (Editors), Plastic Deformation of Minerals and Rocks, Reviews in Mineralogy and Geochemistry. Mineralogical Society of America and Geochemical Society, Chantilly, Virginia, pp. 291-329.

Wu, Y., 2000. Rheological Studies of Olivine under high pressure and high temperature, Ph.D Thesis, State University of New York at Stony Brook, Stony Brook.

Xu, Z.Q., Wang, Q., Ji, S.C., Chen, J., Zeng, L.S., Yang, J.S., Chen, F.Y., Liang, F.H. and Wenk, H.R., 2006. Petrofabrics and seismic properties of garnet peridotite from the UHP Sulu terrane (China): Implications for olivine deformation mechanism in a cold and dry subducting continental slab. Tectonophysics, 421(1-2): 111-127.

Zha, C.S., Duffy, T.S., Downs, R.T., Mao, H.K. and Hemley, R.J., 1996. Sound velocity and elasticity of single-crystal forsterite to 16 GPa. Journal of Geophysical Research-Solid Earth, 101(B8): 17535-17545.

Zhang, J.F., Green, H.W., Bozhilov, K. and Jin, Z.M., 2004. Faulting induced by precipitation of water at grain boundaries in hot subducting oceanic crust. Nature, 428(6983): 633-636.

Appendix A

Starting Materials and Vocabulary.

San Carlos olivine, $(Mg_{0.9}Fe_{0.1})_2SiO_4$, is used as the sample in the deformation experiments. Optically clear (gem quality) grains of San Carlos olivine with maximum dimension of 3-10 mm are well ground into powder in an agate mortar. Powdered San Carlos Olivine samples are used in these experiments. Powdered enstatite ($MgSiO_3$) (3-5% total quality of sample) is mixed into the olivine samples as a buffer to control the activity of silica. To determine the effect of oxygen fugacity, two samples, one with Ni-NiO foil buffered and another without buffered, are put in one cell assembly during the deformation experiment. In order to explore the effect of water fugacity on deformation of olivine, both "normal" and "wet" samples are investigated. Amorphous boron epoxy (BE) cells are used in this study. To keep away from the moisture, "normal" samples are placed in a vacuum oven at 135°C for at least 2 hours before experiments. In "wet" samples, talc instead of enstatite is used as both water source and the buffer of controlling the activity of silica. Samples are compressed at room temperature and are then annealed at 1200°C for at least 2 hours before dropping to the designed temperature and deformation.

Vocabulary used in the thesis:

"Coarse" grain: polycrystalline olivine specimen with the similar grain size of "normal" Sample, which is about 20 μm, referring to Chapter 4.

"Fine" grain: olivine specimen with the grain size of sub-micron level, referring to Chapter 4.

Grain size: The grain size of polycrystalline olivine specimen.

Macroscopic strain: the total length change of the specimen along the compression axis.

Microscopic strain: the elastic strain from the crystal lattice resistance.

"Normal" sample: olivine powder buffered by enstatite powder, referring to Chapter 4.

Water content: the content of water in the olivine specimen.

"Wet" sample: olivine powder buffered by talc powder and therefore with large amount of water in it after heating comparing to the "normal" sample, referring to Chapter 4.

Appendix B

Experimental Protocol

The deformation experiments are carried out on a D-DIA facility, SAM85, at X17B2 beamline, NSLS. Sample in each experiment is placed in a boron nitride tube, which is used as a capsule to separate the sample from the graphite furnace. Sample(s) is (are) separated from each other or from alumina pistons by Ni/Pt foils, which are also used as strain markers. Surrounded by a machinable alumina sleeve, the furnace is inserted inside a pressure media cube, which is made from amorphous boron powder and expoxy (BE) or mullite. Differential stress is produced by the hard alumina pistons on the top and the bottom in the cell assembly (**Fig. 2-4**). Each of the hard alumina pistons is driven by an independent vertical anvil of the D-DIA, which is driven by an independent ram. The W3%Re-W25%Re thermal couple is used in the experiments. To measure the elastic strain of deformed samples, a solid-state multi-detectors (energy dispersive spectrometer, EDS) is used with a conical slit. Transparent to the X-ray, sintered diamond anvils or cubic boron nitride anvils are used so that the X-ray diffraction data of sample can be properly collected with a two theta angle of about 6.5 degree.

The data of macroscopic strain along the uniaxial direction is measured from the X-ray radiograph of the sample. Using a white incident X-ray beam with 2 x 2 mm^2 in size, the image of the experimental sample is *in situ* captured and magnified by a CCD camera with the X-ray radiographic technique (**Fig.2-5**). The length of the specimen is measured and plotted as a function of time in a diagram, which is used as a strain indicator.

The differential stresses are deduced from elastic strains, which are calculated from olivine elastic constraints which are *in situ* collected as a function of time by the X-ray multi-detector EDS. With a white X-ray beam of 50 x 50 μm^2 in size going through the samples, the samples' elastic constraints are *in situ* measured in different directions respecting to the incident X-ray beam (**Fig. 2-6**).

In this study, the D-DIA apparatus gives the capacity to drive the top and bottom rams at a certain speed to maintain a constant strain rate while the main ram is also driven at a related certain speed to keep the pressure constant (Durham et al., 2002; Wang et al., 2003). During the experiments, the equation of state for the olivine is used as the pressure standard. The experimenter has the capability to control the speeds of differential rams and the directions of the rams, either advance or retreat (**Fig 2-7**).

In the experiments, samples are compressed at room temperature. For the deformation experiments with annealed samples, which are the most of the experiment applied in this thesis, samples are then annealed at 1200°C for at least 2 hours before dropping to the designed temperature and deformation. On the other hand, no annealing process is applied in the deformation experiments with non-annealed sample.

Two kinds of deformation experiments are carried out in this study. The first kind of experiment is a "steady state" experiment. In this kind of experiment, the specimen is deformed at a constant strain rate at a certain temperature until steady state has been reached and confirmed. Another type of experiment is designed to observe the boundary between regimes of temperature independent at low temperature and temperature dependent at high temperature. It is not a steady state experiment but the boundary of steady state is bounded in the run. In such kind of experiment, specimen is at first deformed at 400°C until steady state has been reached. Then a temperature increase cycle is performed until the deformation goes into the temperature-sensitive regime. After that a temperature decrease cycle is performed. The strategy of these investigations is that the observed stress should be higher than or equal to the stress at steady state along increase cycle whereas it should be equal to or lower than that at steady state along decrease cycle at the same temperature. Thus the upper and lower margins of the stress at steady state are bounded by the observed values in the increase and decrease cycles, respectively.

The pressure-power-temperature-time (P-P-T-t) relationships for all the runs for this thesis purpose are shown here (See **Fig** B-1 to **Fig** B-9).

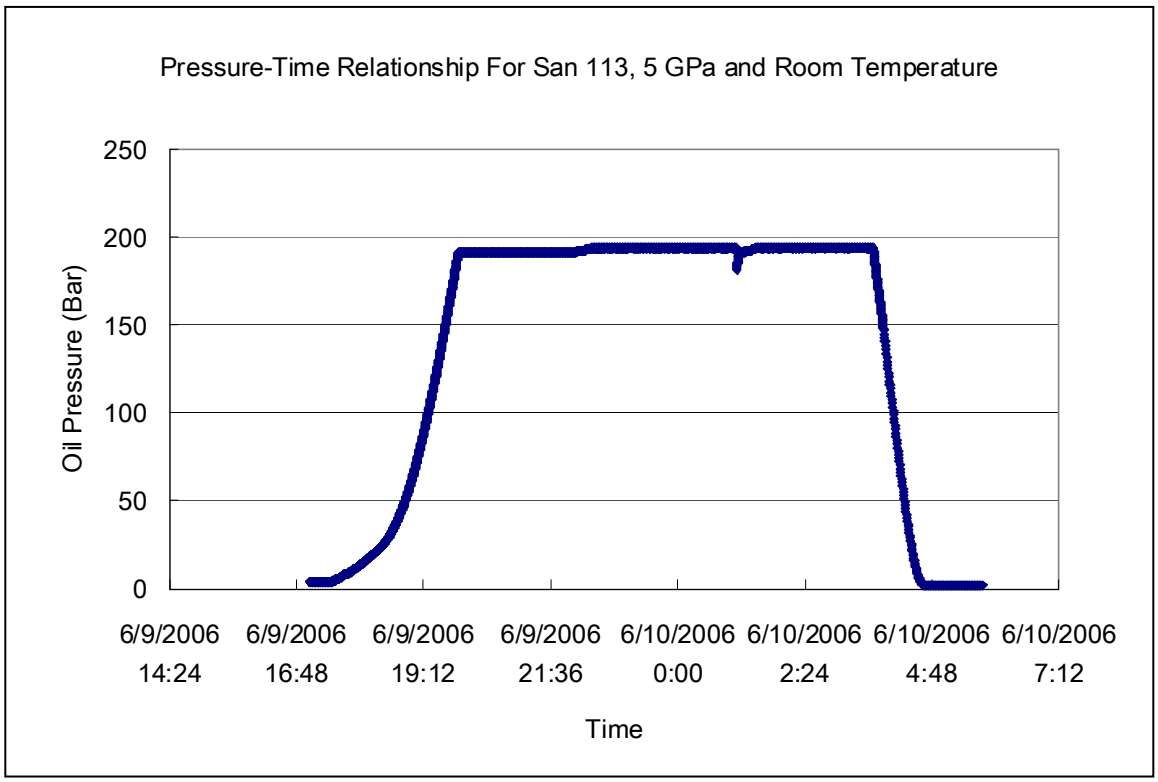

Fig B-1 Pressure - Time Relationship for the deformation experiment of San 113, 5 GPa and 25°C.

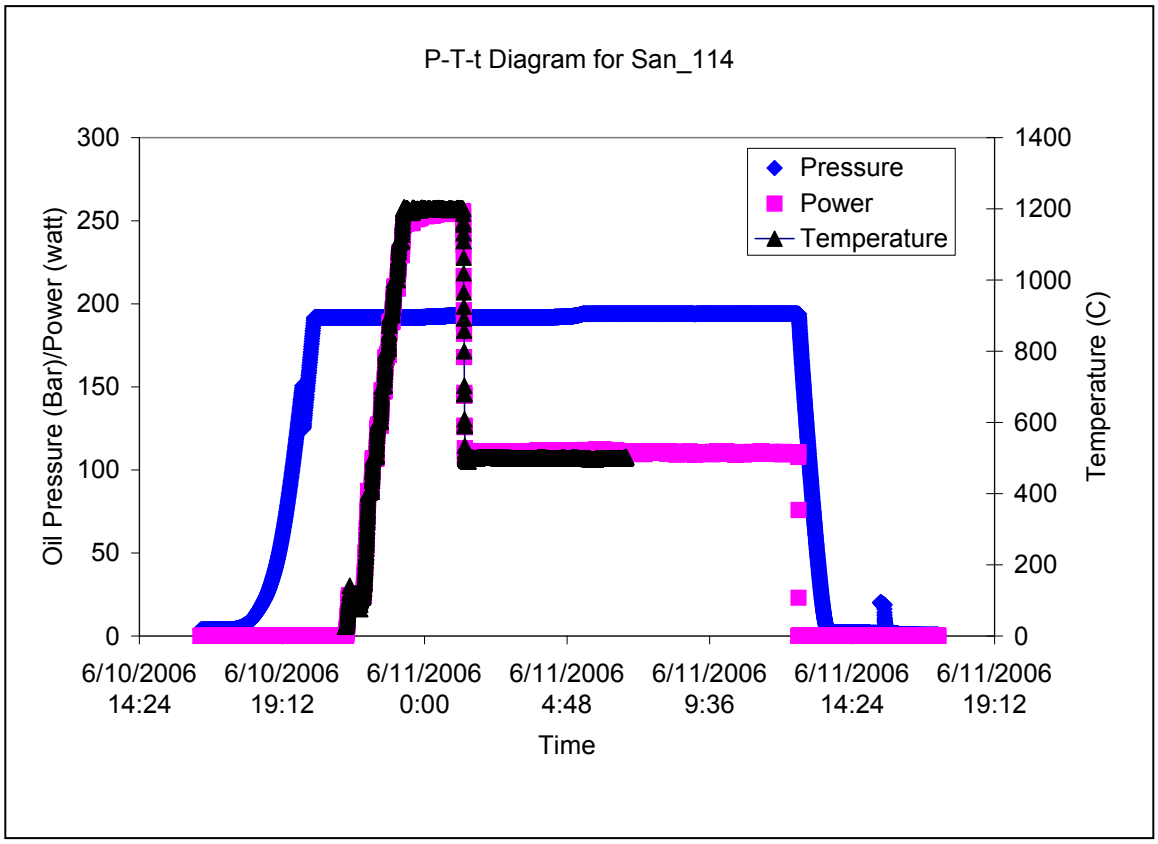

Fig B-2 Pressure-Power-Temperature-Time Relationship for the deformation experiment of San 114, 5 GPa and 500°C. Diamond blue, oil pressure; pink square, power; black triangle, temperature.

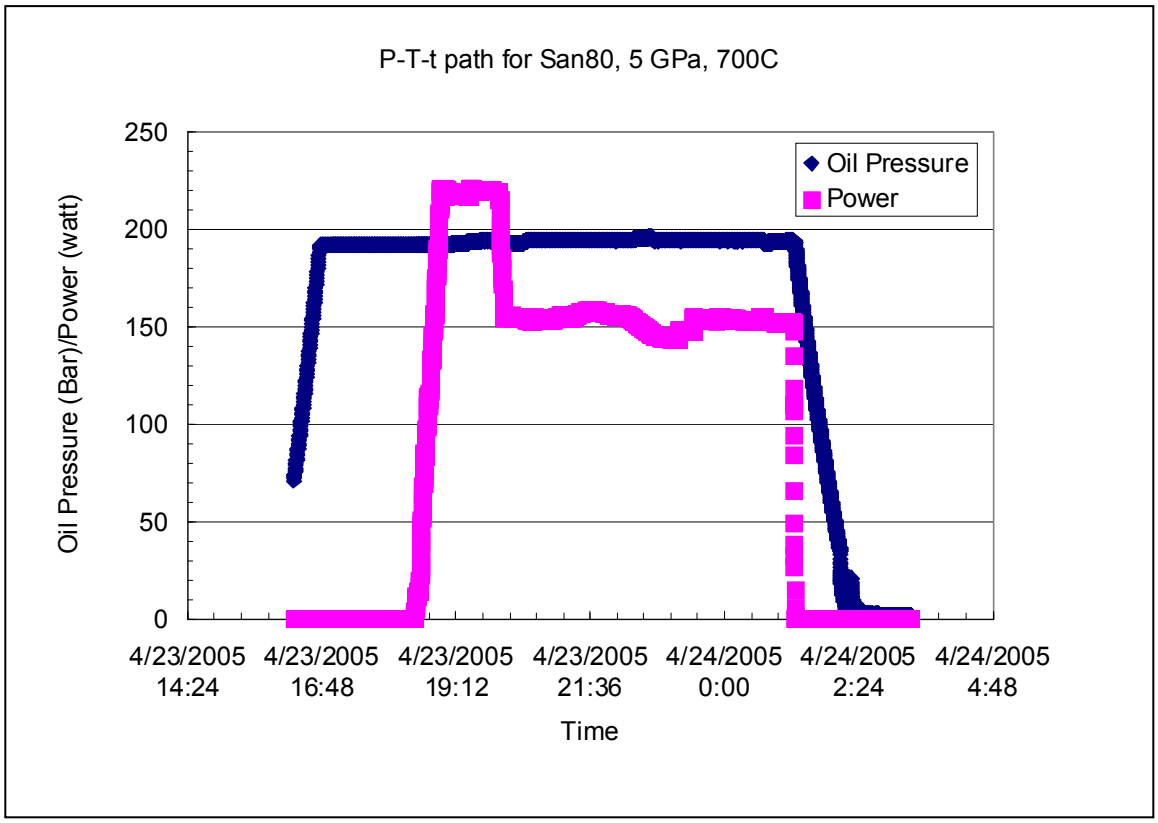

Fig B-3 Pressure-Power-Time Relationship for the deformation experiment of San 80, 5 GPa and 700°C. Diamond blue, oil pressure; pink square, power. There is no thermal couple in the cell assemblage of San 80. The temperature is estimated from the existing power-temperature relationship of previous experiments with similar cell assemblies. Our experiments show that the power-temperature relationship is quite consistent for the similar cell assemblies.

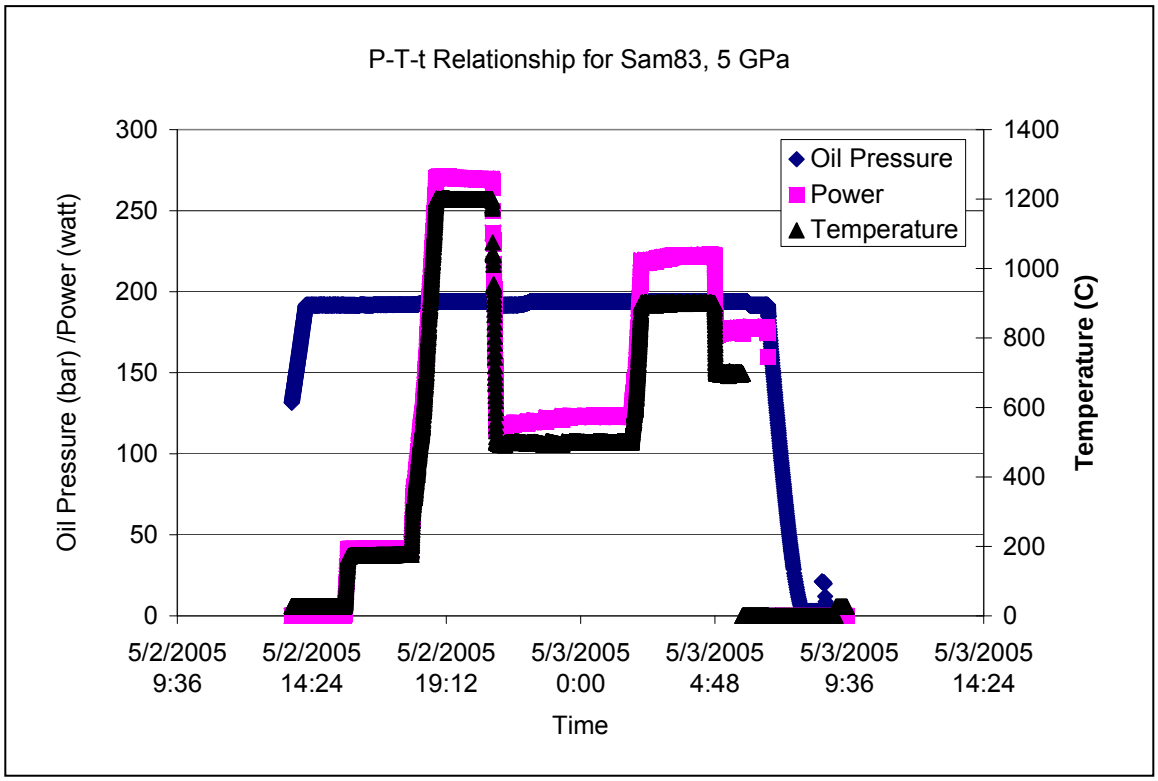

Fig B-4 Pressure-Power-Temperature-time Relationship for the deformation experiment of San 83, 5 GPa. Diamond blue, oil pressure; pink square, power; black triangle, temperature

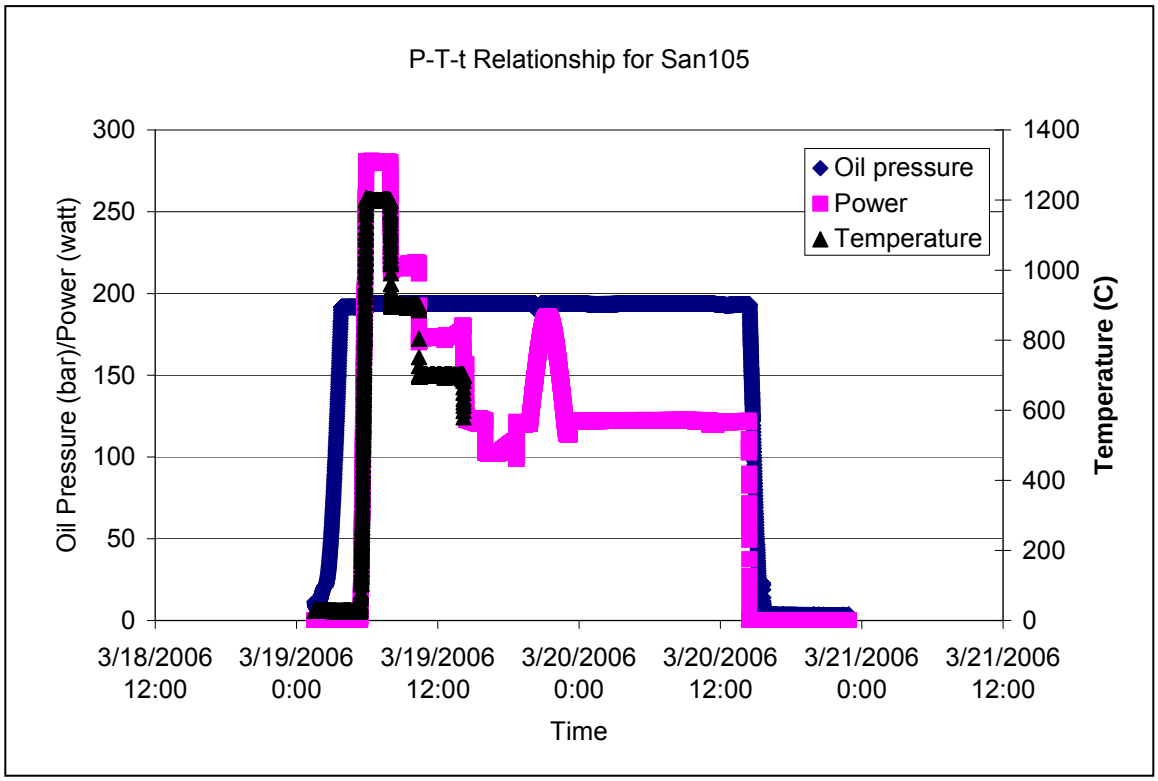

Fig B-5 Pressure- Power-Temperature-time Relationship for the deformation experiment of San 105, 5 GPa. Diamond blue, oil pressure; pink square, power; black triangle, temperature

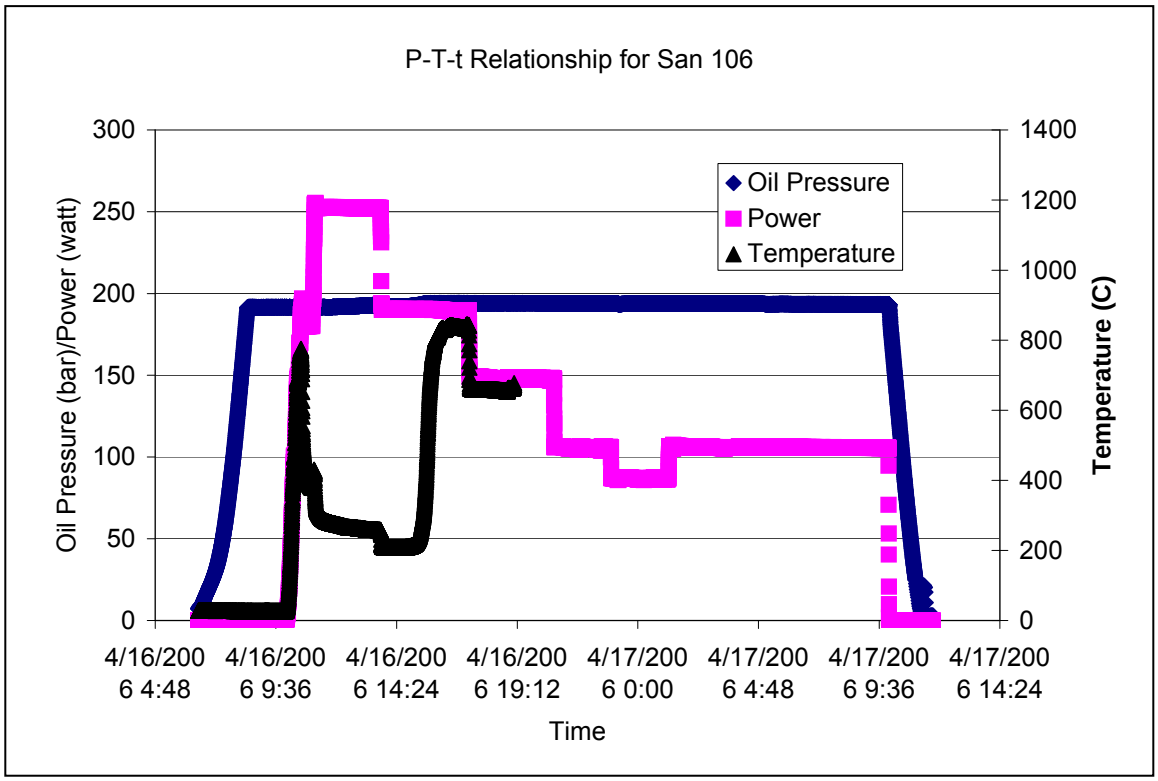

Fig B-6 Pressure-Power-Temperature-time Relationship for the deformation experiment of San 106, 5 GPa. Diamond blue, oil pressure; pink square, power; black triangle, temperature.

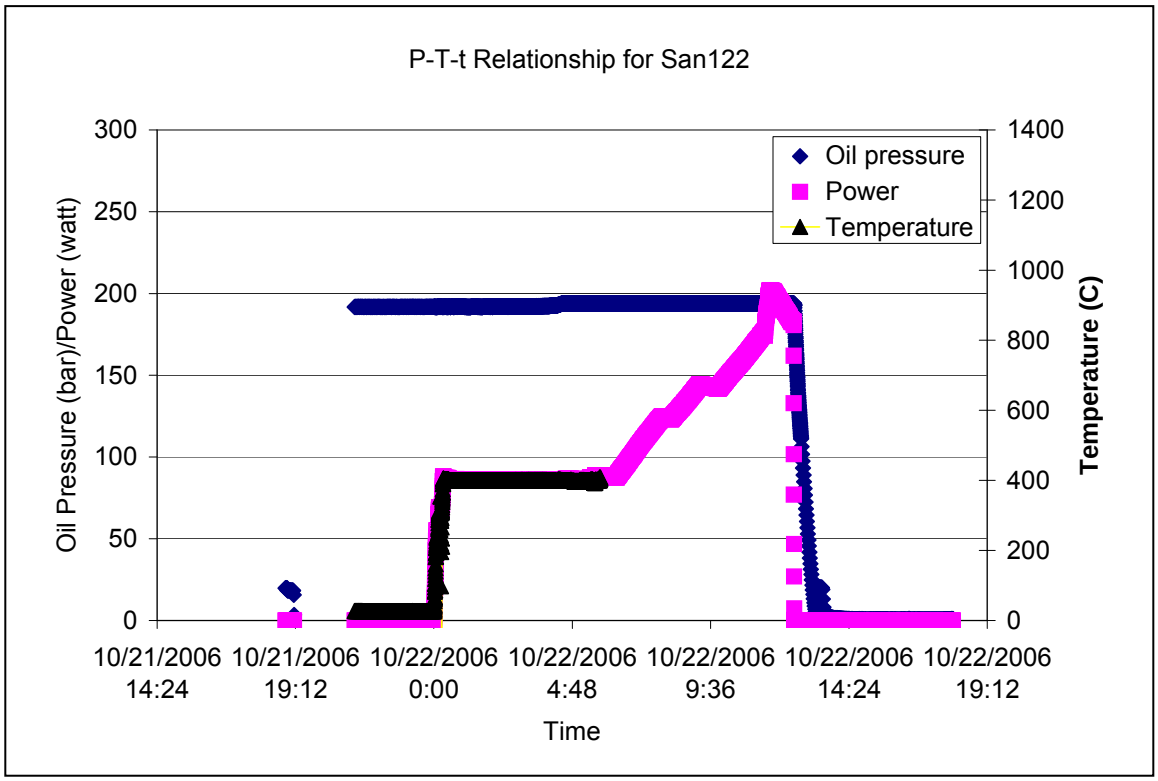

Fig B-7 Pressure-Power-Temperature-time Relationship for the deformation experiment of San 122, 5 GPa. Diamond blue, oil pressure; pink square, power; black triangle, temperature

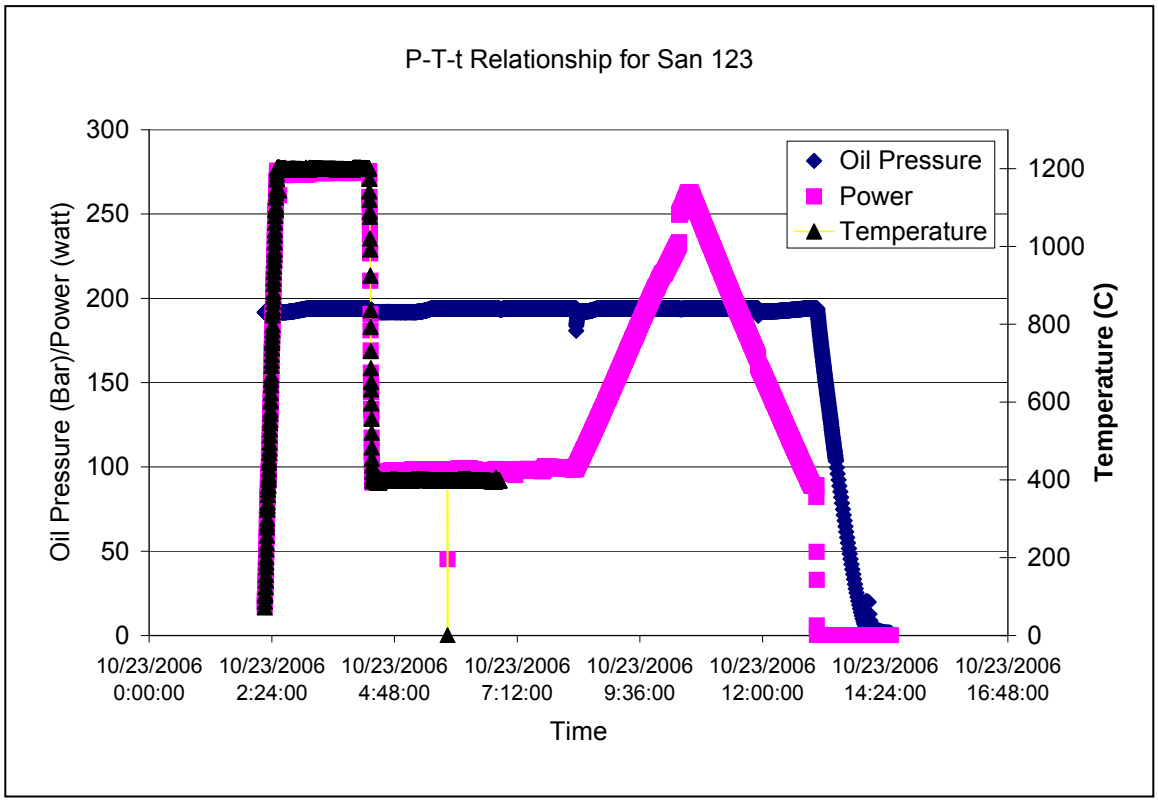

Fig B-8 Pressure- Power-Temperature-time Relationship for the deformation experiment of San 123, 5 GPa. Diamond blue, oil pressure; pink square, power; black triangle, temperature.

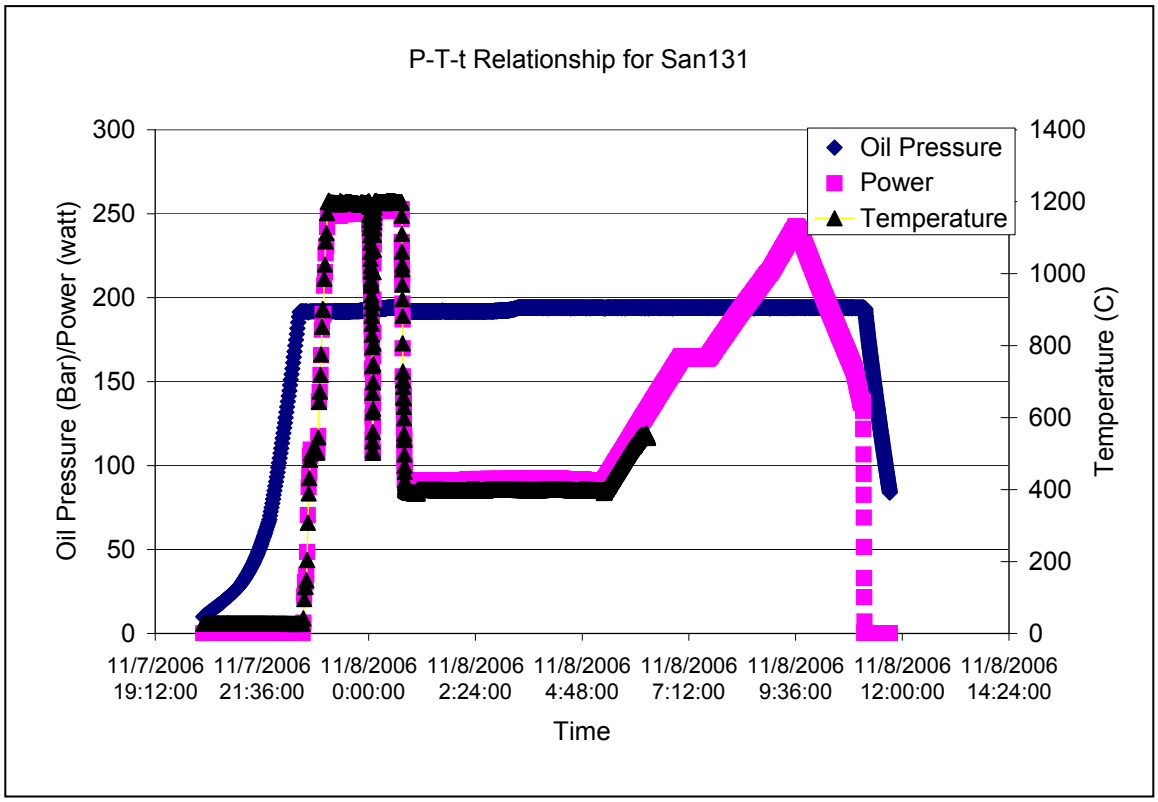

Fig B-9 Pressure- Power-Temperature-time Relationship for the deformation experiment of San 131, 5 GPa. Diamond blue, oil pressure; pink square, power; black triangle, temperature.

Appendix C

Results of IR Test for the Recovered Samples

IR test of the recovered samples is performed at U2A, NSLS. The recovered samples are cut along the deformation axis. Thin sections are prepared and double-side polished. The thickness of thin section is measured by micrometer probe. Please see "water content" section of Chapter 2 for the description and discussion. Here we just give the results.

IR Analytical Results for Recovered Samples

Sample	Thickness (μm)	C_{H2O} (ppm by weight)
San80	140	69
San83	160	59
San105	96	15
San106	98	11
San113	58	67
San114	105	11
San122	90	35
San123	125	9
San131	149	30

$C_{H_2O} = \frac{M_{H_2O} \bullet C_{OH}}{2 \bullet M_{olivine}}$, in which M_{H2O}, $M_{olivine}$ are molar mass of H_2O and olivine, respectively. C_{OH} is molar concentration of hydroxyl ($H/10^6Si$), Paterson (1982), $C_{OH} = \frac{B_i}{150\gamma}\int \frac{H(\upsilon)}{(3780-\upsilon)}$, in which $B_i = 4.39 \times 10^4$, $\gamma = 0.5$, $H(\nu)$ is absorption coefficient in mm^{-1} at wavenumber ν in cm^{-1}.

Appendix D Data for the Deformation Experiments

Table D-1A Data table for experiment San80, unbuffered sample

No.	Time (sec)	d value (Detector 1)			d value (Detector 2)			d value (Detector 3)		
Peak		130	131	112	130	131	112	130	131	112
san80.003	51697	2.76991	2.51885	2.4591	2.76756	2.51403	2.45988	2.76822	2.51243	2.45724
san80.005	64943	2.69254	2.43158	2.39158	2.69683	2.4346	2.39095	2.74726	2.50763	2.44588
san80.007	68536	2.76066	2.50863	2.45803	2.76098	2.50671	2.45761	2.76142	2.51203	2.45932
san80.009	72421	2.76129	2.50856	2.45785	2.76132	2.50585	2.45679	2.75375	2.50411	2.45065
san80.011	74057	2.73113	2.478	2.43283	2.73008	2.4749	2.43811	2.76002	2.51095	2.45493
san80.012	75140	2.71465	2.46209	2.42087	2.71221	2.46174	2.41979	2.76503	2.51335	2.45839
san80.014	76017	2.71081	2.45821	2.41557	2.70943	2.46001	2.41836	2.76664	2.51332	2.46146
san80.016	76749	2.71091	2.45834	2.4165	2.70844	2.45645	2.41534	2.76771	2.5193	2.46291
san80.018	77467	2.71427	2.4609	2.42182	2.71121	2.45493	2.41529	2.77471	2.52374	2.46054
san80.020	79113	2.72052	2.46822	2.42907	2.71815	2.46265	2.42026	2.77621	2.5265	2.47153
san80.022	80039	2.71951	2.46563	2.42473	2.71727	2.46246	2.42097	2.77503	2.50989	2.46037
san80.024	80782	2.7209	2.46646	2.42852	2.72319	2.46086	2.41728	2.77701	2.51126	2.46366
san80.026	81648	2.72752	2.46883	2.42169	2.71678	2.46578	2.42224	2.78038	2.52036	2.46556
san80.028	82515	2.72937	2.46983	2.42465	2.72374	2.46856	2.42314	2.78349	2.51213	2.46225
san80.030	83377	2.7267	2.46981	2.42585	2.72367	2.46844	2.42367	2.78442	2.51345	2.46272
san80.032	84711	2.72906	2.47113	2.42564	2.72724	2.47129	2.42622	2.78351	2.52103	2.46925
san80.034	85464	2.73011	2.47166	2.42675	2.72698	2.47082	2.42237	2.78517	2.5231	2.46718
san80.036	86207	2.73037	2.47111	2.42188	2.72738	2.46835	2.41902	2.78492	2.5238	2.46677
san80.038	87043	2.7305	2.47276	2.42749	2.72788	2.47207	2.42592	2.7862	2.52113	2.46679
san80.040	87921	2.73076	2.47344	2.42333	2.72902	2.47013	2.42325	2.78998	2.52811	2.47047
san80.042	88816	2.7315	2.47343	2.4245	2.73059	2.47113	2.42488	2.79039	2.5356	2.4722
san80.044	90138	2.73027	2.47154	2.42424	2.72769	2.46941	2.42058	2.7885	2.53232	2.47105

1. Differential stress.

Table D-1A data table for experiment San80, unbuffered sample (continued)

No. Peak	Time (sec)	d value (Detector 4)			τ [1] (GPa)			τ (GPa) (average)	Pressure (GPa)	Strain	T(K)
		130	131	112	130	131	112				
san80.003	51697	2.76839	2.51618	2.45691	-0.09	-0.37	-0.12	-0.19	0.00		298
san80.005	64943	2.7447	2.48871	2.43685	3.16	4.65	3.69	3.83			298
san80.007	68536	2.76209	2.5084	2.45835	0.04	0.20	0.08	0.11	7.28		1473
san80.009	72421	2.75584	2.50203	2.45234	-0.41	-0.26	-0.46	-0.38	4.98		973
san80.011	74057	2.76233	2.50682	2.45677	1.60	1.95	1.44	1.66	5.97	3.54%	973
san80.012	75140	2.76797	2.50942	2.45714	2.81	3.05	2.46	2.77	6.12	10.27%	973
san80.014	76017	2.77142	2.51355	2.46124	3.11	3.29	3.00	3.14	5.94	14.69%	973
san80.016	76749	2.77116	2.51799	2.46277	3.16	3.61	3.03	3.27	6.13	18.05%	973
san80.018	77467	2.77418	2.52293	2.46239	3.33	3.69	2.53	3.18	5.61	25.13%	973
san80.020	79113	2.7802	2.52299	2.46489	3.05	3.40	2.72	3.06	4.42	29.91%	973
san80.022	80039	2.78414	2.52881	2.46855	3.05	2.64	2.32	2.67	3.78	30.80%	973
san80.024	80782	2.78655	2.52988	2.47091	3.07	2.67	2.27	2.67	3.10	36.11%	973
san80.026	81648	2.7855	2.52847	2.46977	2.87	3.03	2.84	2.91	3.77	38.23%	973
san80.028	82515	2.78572	2.52759	2.46609	2.93	2.51	2.44	2.63	2.00	39.29%	973
san80.030	83377	2.78469	2.52567	2.46495	3.12	2.58	2.39	2.70	2.22	39.82%	973
san80.032	84711	2.78446	2.52887	2.46816	2.94	2.92	2.81	2.89	2.93	40.88%	973
san80.034	85464	2.78644	2.52996	2.46804	2.97	3.00	2.61	2.86	3.07	41.42%	973
san80.036	86207	2.78737	2.53045	2.46749	2.94	3.08	2.91	2.97	3.41	41.77%	973
san80.038	87043	2.78679	2.52974	2.4682	3.00	2.83	2.53	2.79	2.69	42.83%	973
san80.040	87921	2.78987	2.53365	2.46971	3.17	3.17	3.03	3.13	2.97	43.19%	973
san80.042	88816	2.78913	2.53242	2.46871	3.15	3.57	3.06	3.26	3.39	42.65%	973
san80.044	90138	2.78873	2.53175	2.46932	3.13	3.51	3.01	3.21	3.43	45.49%	973

Table D-1B data table for experiment San80, buffered sample

No. Peak	Time (Sec)	d value (Detector 1)			d value (Detector 2)			d value (Detector 3)		
		130	131	112	130	131	112	130	131	112
san80.004	52092	2.76946	2.51068	2.45937	2.76518	2.51589	2.45201	2.76819	2.52292	2.464
san80.006	65842	2.69364	2.43647	2.40488	2.68482	2.42167	2.39097	2.73586	2.47778	2.44403
san80.008	71548	2.76393	2.51017	2.46004	2.76129	2.50744	2.45768	2.76351	2.51115	2.45878
san80.010	72767	2.76184	2.5083	2.45773	2.76054	2.5056	2.45627	2.75684	2.50591	2.45143
san80.013	75576	2.71624	2.46155	2.42152	2.71258	2.46033	2.41915	2.76536	2.51174	2.45423
san80.015	76335	2.71379	2.45873	2.41828	2.71036	2.45774	2.41704	2.76668	2.5131	2.45619
san80.017	77062	2.71192	2.45684	2.41556	2.71012	2.45656	2.41721	2.76558	2.5186	2.46043
san80.019	77880	2.71371	2.45809	2.41904	2.71094	2.45605	2.41407	2.7611	2.51932	2.46174
san80.021	79426	2.72299	2.46056	2.4228	2.72225	2.46242	2.42094	2.77235	2.52153	2.46034
san80.023	80354	2.7224	2.46259	2.42083	2.71913	2.46598	2.42933	2.77789	2.51281	2.45908
san80.025	81152	2.72254	2.47355	2.43803	2.72172	2.46505	2.42192	2.77945	2.52354	2.46407
san80.027	82000	2.72706	2.47342	2.42636	2.72052	2.47004	2.4254	2.77878	2.52182	2.46353
san80.029	82899	2.7259	2.46776	2.42435	2.72482	2.46567	2.42174	2.78112	2.52112	2.46362
san80.031	84145	2.72663	2.47116	2.42897	2.72622	2.46714	2.42346	2.78288	2.52186	2.46339
san80.033	85026	2.72894	2.4715	2.4286	2.72773	2.47094	2.42969	2.78305	2.52106	2.46458
san80.035	85778	2.73058	2.47366	2.4294	2.72921	2.46895	2.42257	2.78231	2.52487	2.46557
san80.037	86533	2.73093	2.47291	2.42816	2.72867	2.47018	2.42414	2.78168	2.51706	2.46397
san80.039	87378	2.73144	2.47442	2.42833	2.72805	2.47031	2.42465	2.7836	2.52146	2.46529
san80.041	88257	2.731	2.47264	2.42718	2.72936	2.4724	2.42615	2.78672	2.52906	2.46633
san80.043	89215	2.72867	2.4742	2.42689	2.72777	2.47163	2.42459	2.78483	2.52759	2.46764

Table D-1B data table for experiment San80, buffered sample (continued)

No.	Time (Sec)	d value (Detector 4)			τ (GPa)			τ (GPa) (average)	P (GPa)	Strain	T(K)
Peak		130	131	112	130	131	112				
san80.004	52092	2.77009	2.51135	2.46126	-0.07	0.70	0.29	0.31			
san80.006	65842	2.74922	2.47785	2.43319	2.47	2.62	2.64	2.58			
san80.008	71548	2.76335	2.50923	2.45874	-0.02	0.06	-0.08	-0.02			
san80.010	72767	2.75865	2.50477	2.45348	-0.27	-0.14	-0.41	-0.27	4.88	3.54%	973
san80.013	75576	2.76632	2.51079	2.45623	2.73	2.99	2.15	2.63	6.33	10.27%	973
san80.015	76335	2.76663	2.51149	2.45618	2.94	3.24	2.49	2.89	6.29	14.69%	973
san80.017	77062	2.77074	2.51322	2.45846	2.99	3.66	2.94	3.20	6.63	18.05%	973
san80.019	77880	2.77467	2.51119	2.45719	2.66	3.63	2.79	3.02	6.77	25.13%	973
san80.021	79426	2.77681	2.51584	2.45901	2.71	3.59	2.45	2.92	5.37	29.91%	973
san80.023	80354	2.7753	2.51651	2.4595	3.03	2.99	2.50	2.84	3.79	30.80%	973
san80.025	81152	2.77964	2.51589	2.4609	3.10	2.91	1.67	2.56	4.37	36.11%	973
san80.027	82000	2.77878	2.51604	2.46042	2.82	2.83	2.41	2.68	4.57	38.23%	973
san80.029	82899	2.78662	2.52295	2.46697	3.00	3.13	2.55	2.89	4.04	39.29%	973
san80.031	84145	2.78619	2.521	2.46573	3.05	2.97	2.23	2.75	3.86	39.82%	973
san80.033	85026	2.78934	2.52321	2.46725	2.93	2.90	2.33	2.72	3.50	40.88%	973
san80.035	85778	2.78639	2.5226	2.46568	2.80	2.98	2.33	2.70	3.94	41.42%	973
san80.037	86533	2.77984	2.52185	2.46447	2.75	2.60	2.32	2.55	3.16	41.77%	973
san80.039	87378	2.77883	2.52188	2.46449	2.82	2.75	2.39	2.65	3.44	42.83%	973
san80.041	88257	2.78118	2.52648	2.46592	3.00	3.27	2.53	2.93	3.78	43.19%	973
san80.043	89215	2.77929	2.5257	2.46745	3.03	3.09	2.63	2.92	3.97	42.65%	973

Table D-2A data table for experiment San83, buffered sample

No.	Time (sec)	d value (Detector 1)			d value (Detector 2)			d value (Detector 3)		
Peak		130	131	112	130	131	112	130	131	112
san83.003	33585	2.76605	2.51742	2.45941	2.76816	2.51798	2.4587	2.76786	2.53068	2.45724
san83.006	55490	2.71358	2.46164	2.42018	2.71659	2.46645	2.423	2.74959	2.51164	2.44764
san83.010	74446	2.79134	2.53096	2.48652	2.78855	2.53366	2.47559	2.79556	2.56283	2.49841
san83.012	76341	2.77357	2.53336	2.47229	2.77333	2.51791	2.46043	2.7726	2.53846	2.46685
san83.014	77877	2.77235	2.52627	2.46984	2.77439	2.51758	2.46087	2.77413	2.53798	2.46704
san83.016	79029	2.77071	2.52713	2.46247	2.76817	2.51355	2.45848	2.77113	2.54249	2.46711
san83.018	79932	2.74848	2.50015	2.44609	2.74297	2.49233	2.44481	2.77469	2.53596	2.4699
san83.020	80681	2.73334	2.49679	2.44026	2.73951	2.48886	2.43744	2.77652	2.51417	2.45331
san83.022	81593	2.7303	2.49805	2.43659	2.72764	2.4794	2.4322	2.77659	2.51693	2.4521
san83.024	82334	2.72946	2.49421	2.43235	2.72995	2.47057	2.42964	2.7699	2.51691	2.45297
san83.026	83055	2.7273	2.48758	2.43578	2.72635	2.47852	2.43091	2.76757	2.51205	2.45588
san83.028	83857	2.72478	2.47936	2.43617	2.72492	2.4583	2.42942	2.77038	2.53304	2.4632
san83.030	84608	2.72315	2.47609	2.43377	2.72504	2.47322	2.43185	2.76941	2.535	2.46409
san83.032	85397	2.72211	2.46274	2.4286	2.72325	2.46825	2.42982	2.77152	2.53232	2.46269
san83.034	86280	2.72126	2.46835	2.42699	2.7227	2.46792	2.42951	2.76997	2.53658	2.46412
san83.036	87183	2.72015	2.46845	2.42857	2.72155	2.46757	2.42697	2.77023	2.5354	2.46496
san83.038	87934	2.72013	2.46939	2.42832	2.72108	2.46968	2.42833	2.77276	2.53341	2.46572
san83.040	88722	2.72004	2.46779	2.42586	2.72107	2.47182	2.42919	2.77413	2.53635	2.46704
san83.045	90508	2.71925	2.47104	2.42555	2.72259	2.47143	2.42855	2.77497	2.53909	2.46791
san83.046	90822	2.72385	2.46344	2.42612	2.72177	2.46899	2.42749	2.78241	2.52695	2.46014
san83.047	91131	2.72112	2.4722	2.42922	2.71859	2.46876	2.42824	2.77189	2.51735	2.46192
san83.048	91679	2.7257	2.46768	2.42548	2.72257	2.46466	2.42873	2.77316	2.52272	2.46359
san83.050	92305	2.71985	2.46863	2.42617	2.72254	2.47046	2.42812	2.78031	2.53347	2.46523

No.	Time (sec)	d value (Detector 1)			d value (Detector 2)			d value (Detector 3)		
Peak		130	131	112	130	131	112	130	131	112
san83.052	94669	2.75596	2.50374	2.45269	2.75295	2.50414	2.45426	2.78411	2.53226	2.47128
san83.054	95382	2.75691	2.50405	2.45393	2.75502	2.50604	2.45639	2.78341	2.53733	2.47226
san83.056	96136	2.76129	2.50823	2.45923	2.76091	2.50791	2.45707	2.78129	2.53998	2.47312
san83.058	96888	2.76202	2.5105	2.45915	2.76174	2.50897	2.46046	2.77983	2.53546	2.47314
san83.060	97619	2.76322	2.51095	2.46002	2.76289	2.51091	2.4635	2.78063	2.53494	2.4742
san83.062	98446	2.76859	2.51545	2.46301	2.76804	2.51426	2.46241	2.77924	2.53389	2.47332
san83.064	99199	2.76891	2.51582	2.46308	2.76846	2.51477	2.46259	2.77923	2.53341	2.47325
san83.066	99937	2.76836	2.516	2.46182	2.76839	2.51472	2.4626	2.77934	2.53256	2.4734
san83.068	100698	2.76841	2.51579	2.46243	2.76804	2.51514	2.46226	2.78152	2.53199	2.47365
san83.070	101501	2.77096	2.51497	2.46522	2.76803	2.51361	2.46205	2.78419	2.53293	2.47552
san83.072	102254	2.7704	2.51513	2.46473	2.76831	2.51334	2.46204	2.7851	2.53435	2.47516
san83.074	102978	2.77	2.51574	2.46551	2.76859	2.51379	2.46255	2.78418	2.5344	2.47568
san83.076	104094	2.75043	2.49979	2.45331	2.74973	2.49714	2.44919	2.78657	2.53647	2.47532
san83.078	104819	2.7502	2.4996	2.456	2.74789	2.50095	2.45569	2.78873	2.53902	2.47645
san83.080	105532	2.75242	2.50424	2.46111	2.7486	2.50201	2.45664	2.79069	2.5389	2.47753
san83.082	106261	2.75269	2.51167	2.46884	2.74755	2.50849	2.46796	2.78886	2.54016	2.47839
san83.084	107047	2.75254	2.51121	2.46627	2.75033	2.5075	2.46354	2.78772	2.53794	2.47638
san83.086	108009	2.7637	2.51532	2.46843	2.76126	2.51317	2.46635	2.78374	2.53252	2.47186
san83.088	108845	2.77402	2.52183	2.47076	2.7721	2.51877	2.4696	2.77676	2.52696	2.46479
san83.090	109665	2.77903	2.52552	2.46911	2.77557	2.52032	2.46505	2.78101	2.52307	2.4662

Table D-2A data table for experiment San83, unbuffered sample (continued)

No.	Time (sec)	d value (Detector 4)			τ (GPa)			τ (GPa) (average)	P (GPa)	T(K)
Peak		130	131	112	130	131	112			
san83.003	33585	2.77003	2.51799	2.45913	0.10	0.74	-0.14	0.23	0.00	298
san83.006	55490	2.7465	2.50202	2.44084	2.05	2.98	1.82	2.28	4.15	298
san83.010	74446	2.78953	2.53758	2.48317	0.22	1.70	0.71	0.87	1.67	1473
san83.012	76341	2.76834	2.51457	2.46209	-0.05	0.28	-0.34	-0.04	0.54	773
san83.014	77877	2.76826	2.51649	2.46235	0.09	0.65	-0.18	0.19	0.89	773
san83.016	79029	2.76899	2.51829	2.4621	0.02	0.84	0.29	0.39	0.54	773
san83.018	79932	2.77403	2.52302	2.46703	1.42	2.02	1.51	1.65	2.20	773
san83.020	80681	2.7734	2.52643	2.46555	2.35	1.01	0.85	1.40	3.52	773
san83.022	81593	2.77065	2.51951	2.46091	2.52	1.09	1.01	1.54	3.99	773
san83.024	82334	2.76775	2.52046	2.46009	2.22	1.32	1.35	1.63	4.48	773
san83.026	83055	2.76781	2.51892	2.46169	2.22	1.43	1.31	1.65	4.20	773
san83.028	83857	2.76852	2.51865	2.45998	2.51	3.08	1.74	2.44	3.67	773
san83.030	84608	2.76904	2.52096	2.46016	2.55	3.38	1.95	2.63	3.70	773
san83.032	85397	2.76935	2.51917	2.45931	2.72	4.04	2.21	2.99	4.10	773
san83.034	86280	2.7693	2.51881	2.4595	2.69	3.92	2.40	3.01	3.99	773
san83.036	87183	2.76961	2.51846	2.45887	2.77	3.86	2.35	2.99	3.96	773
san83.038	87934	2.7705	2.51843	2.45775	2.90	3.69	2.41	3.00	3.89	773
san83.040	88722	2.77162	2.51779	2.45711	2.97	3.94	2.66	3.19	3.79	773
san83.045	90508	2.77191	2.5181	2.4569	3.06	3.89	2.73	3.23	3.58	773
san83.046	90822	2.77396	2.51887	2.45913	3.18	3.71	2.22	3.04	3.13	773
san83.047	91131	2.77066	2.52434	2.46149	2.80	2.66	2.12	2.52	3.73	773
san83.048	91679	2.76757	2.51499	2.45903	2.60	3.22	2.47	2.77	3.60	773
san83.050	92305	2.77338	2.51693	2.45586	3.30	3.74	2.53	3.19	3.60	773

No.	Time (sec)	d value (Detector 4)			τ (GPa)			τ (GPa) (average)	P (GPa)	T(K)
Peak		130	131	112	130	131	112			
san83.052	94669	2.77822	2.52309	2.46941	1.50	1.61	1.17	1.43	3.72	1173
san83.054	95382	2.77909	2.52481	2.4706	1.41	1.87	1.15	1.48	3.75	1173
san83.056	96136	2.77767	2.52472	2.46916	1.06	1.77	0.87	1.23	3.51	1173
san83.058	96888	2.77754	2.52302	2.46867	0.95	1.40	0.88	1.07	3.59	1173
san83.060	97619	2.77669	2.52267	2.46926	0.93	1.34	0.89	1.05	3.42	1173
san83.062	98446	2.77471	2.52024	2.46761	0.57	1.03	0.64	0.75	3.32	1173
san83.064	99199	2.77371	2.52013	2.46811	0.55	0.98	0.64	0.72	3.31	1173
san83.066	99937	2.77381	2.51958	2.4681	0.58	0.93	0.72	0.74	3.34	1173
san83.068	100698	2.77428	2.51948	2.46791	0.69	0.91	0.70	0.77	3.15	1173
san83.070	101501	2.78197	2.52282	2.47209	0.70	1.01	0.64	0.78	2.64	1173
san83.072	102254	2.78194	2.5229	2.47164	0.77	1.08	0.65	0.83	2.70	1173
san83.074	102978	2.78177	2.5243	2.47164	0.75	1.04	0.63	0.81	2.74	1173
san83.076	104094	2.78474	2.52674	2.47118	1.92	2.07	1.38	1.79	2.26	973
san83.078	104819	2.78826	2.52781	2.47161	2.04	2.21	1.28	1.85	2.03	973
san83.080	105532	2.78982	2.52824	2.4714	2.02	1.94	1.02	1.66	1.65	973
san83.082	106261	2.7924	2.53015	2.47363	1.92	1.59	0.59	1.36	1.54	973
san83.084	107047	2.78703	2.53022	2.47176	1.87	1.49	0.63	1.33	1.79	973
san83.086	108009	2.78111	2.52492	2.4672	1.06	0.96	0.21	0.75	1.85	973
san83.088	108845	2.77101	2.51752	2.45985	0.15	0.29	-0.38	0.02	2.28	973
san83.090	109665	2.76541	2.51384	2.45972	0.10	-0.14	-0.18	-0.07	1.60	973

Table D-2B data table for experiment San83, unbuffered sample

No.	Time (sec)	d value (Detector 1)			d value (Detector 2)			d value (Detector 3)		
Peak		130	131	112	130	131	112	130	131	112
san83.002	32798	2.76908	2.51665	2.46457	2.76913	2.51777	2.4594	2.76887	2.51868	2.45906
san83.005	55040	2.70721	2.46343	2.42403	2.70579	2.44949	2.41243	2.7517	2.517	2.45179
san83.007	63312	2.71467	2.47589	2.4265	2.70454	2.45717	2.41295	2.75042	2.5234	2.45193
san83.009	73835	2.78616	2.53745	2.48397	2.78468	2.52756	2.48168	2.78614	2.54165	2.48206
san83.011	75635	2.77404	2.52662	2.46951	2.77333	2.51546	2.46868	2.76877	2.52515	2.46007
san83.013	77520	2.77571	2.52046	2.46819	2.77285	2.51551	2.46256	2.77494	2.52315	2.45874
san83.015	78705	2.76997	2.51584	2.4636	2.77903	2.51691	2.45949	2.7725	2.52382	2.46787
san83.017	79586	2.75923	2.50836	2.45568	2.7536	2.50329	2.44472	2.76904	2.52319	2.46193
san83.019	80360	2.743	2.48521	2.44246	2.73913	2.48483	2.44142	2.77321	2.52349	2.46454
san83.021	81282	2.73511	2.48026	2.43486	2.73273	2.48106	2.44011	2.77071	2.52215	2.46609
san83.023	82022	2.72774	2.47766	2.43249	2.7272	2.47998	2.43152	2.77802	2.52367	2.46336
san83.025	82740	2.72236	2.47851	2.43034	2.72454	2.48136	2.42921	2.77293	2.52272	2.46237
san83.027	83522	2.7228	2.47568	2.43169	2.72628	2.46791	2.42769	2.77074	2.51914	2.46122
san83.029	84292	2.72344	2.47569	2.43323	2.72571	2.47129	2.42841	2.77163	2.51471	2.46177
san83.031	85083	2.724	2.47529	2.43274	2.72403	2.47169	2.43033	2.77244	2.50917	2.46173
san83.033	85959	2.72503	2.47456	2.43167	2.72038	2.46766	2.42964	2.77296	2.52065	2.46741
san83.035	86765	2.72582	2.47429	2.4324	2.71607	2.46702	2.42895	2.77309	2.51843	2.46385
san83.037	87620	2.72517	2.47357	2.43304	2.71421	2.46876	2.42948	2.77363	2.52288	2.46446
san83.039	88406	2.72552	2.47263	2.43419	2.71321	2.46729	2.4286	2.77425	2.52324	2.4633
san83.041	89204	2.72049	2.47099	2.42457	2.72265	2.46795	2.42965	2.77536	2.52432	2.46594
san83.042	89521	2.72074	2.47264	2.42763	2.71668	2.47005	2.42369	2.78631	2.51367	2.46041
san83.043	89841	2.72291	2.4721	2.43348	2.71887	2.464	2.42761	2.77496	2.52089	2.46396
san83.044	90155	2.72058	2.48064	2.43187	2.72123	2.47635	2.42467	2.767	2.52041	2.47364

No.	Time (sec)	d value (Detector 1)			d value (Detector 2)			d value (Detector 3)		
Peak		130	131	112	130	131	112	130	131	112
san83.049	91994	2.72489	2.47112	2.42785	2.71893	2.46691	2.42823	2.77186	2.52859	2.46889
san83.051	94359	2.75426	2.50307	2.45322	2.75139	2.50069	2.45396	2.7797	2.52956	2.47052
san83.053	95069	2.75369	2.50255	2.45377	2.75057	2.49792	2.45203	2.77863	2.53575	2.47289
san83.055	95825	2.754	2.5032	2.4541	2.75174	2.49786	2.4505	2.77857	2.53728	2.47397
san83.057	96571	2.75483	2.50571	2.45655	2.75314	2.49887	2.45107	2.78302	2.53576	2.47447
san83.059	97303	2.75486	2.50663	2.45797	2.75384	2.49904	2.45175	2.79133	2.53964	2.47585
san83.061	98134	2.75914	2.51051	2.45984	2.75656	2.5045	2.45581	2.78719	2.53763	2.47478
san83.063	98851	2.76102	2.5108	2.46069	2.75833	2.50657	2.45717	2.78591	2.53627	2.47499
san83.065	99617	2.7605	2.51077	2.46074	2.7583	2.50697	2.45741	2.78675	2.53613	2.47523
san83.067	100385	2.76068	2.51135	2.46035	2.75849	2.50784	2.45699	2.78639	2.53472	2.47433
san83.069	101128	2.76478	2.51249	2.46589	2.76043	2.50985	2.459	2.78892	2.53348	2.47802
san83.071	101938	2.76357	2.51241	2.46565	2.76061	2.50976	2.45911	2.79024	2.5347	2.4781
san83.073	102662	2.76481	2.51176	2.46561	2.76172	2.50941	2.45967	2.78809	2.5336	2.47775
san83.075	103776	2.75586	2.50642	2.45907	2.75288	2.49957	2.45269	2.78291	2.53192	2.47476
san83.077	104508	2.74266	2.49423	2.45322	2.73976	2.4823	2.44338	2.78704	2.53487	2.47516
san83.079	105222	2.744	2.49264	2.45124	2.74111	2.48625	2.4436	2.78449	2.53153	2.47287
san83.081	105945	2.74402	2.49195	2.4506	2.73968	2.48518	2.44209	2.78602	2.53427	2.47463
san83.083	106687	2.74321	2.49009	2.44662	2.7377	2.48878	2.44393	2.78763	2.53572	2.47448
san83.085	107670	2.75168	2.49547	2.44866	2.7486	2.49835	2.45445	2.78653	2.53408	2.47094
san83.087	108528	2.76295	2.51179	2.46042	2.76024	2.51087	2.46201	2.78076	2.5296	2.46914
san83.089	109324	2.77265	2.52047	2.46697	2.77098	2.5188	2.46662	2.77611	2.52637	2.46823

(Continued)

No.	Time (sec)	d value (Detector 4)			τ (GPa)			τ (GPa) (average)	P (GPa)	T(K)
Peak		130	131	112	130	131	112			
san83.002	32798	2.77254	2.51602	2.46009	-0.01128	0.115777	-0.3503	-0.08193	0	298
san83.005	55040	2.7495	2.47964	2.43413	2.531282	3.170594	1.82995	2.510609	3.902255	298
san83.007	63312	2.74712	2.49211	2.4421	2.028057	2.765734	1.673321	2.155704	2.921217	298
san83.009	73835	2.78581	2.53049	2.47872	-0.00104	0.229342	-0.11634	0.037321	3.63042	1473
san83.011	75635	2.76888	2.51241	2.45615	-0.28231	-0.08259	-0.59741	-0.32077	2.030192	773
san83.013	77520	2.76942	2.49848	2.45564	-0.04091	0.152146	-0.59961	-0.16279	1.725901	773
san83.015	78705	2.75963	2.51133	2.46124	0.135256	0.452316	0.268517	0.285363	1.607248	773
san83.017	79586	2.76769	2.48622	2.45678	0.529989	0.845394	0.398167	0.591183	2.705007	773
san83.019	80360	2.77106	2.48177	2.45969	1.639792	2.214601	1.414055	1.756149	2.876746	773
san83.021	81282	2.77294	2.5093	2.46359	1.947259	2.435587	2.005965	2.129603	3.405712	773
san83.023	82022	2.77333	2.5056	2.4595	2.738372	2.674363	1.993073	2.468603	3.378553	773
san83.025	82740	2.76595	2.50588	2.45944	2.779832	2.571505	2.073591	2.474976	4.144365	773
san83.027	83522	2.76417	2.50271	2.45563	2.641462	2.544483	1.912938	2.366295	4.142613	773
san83.029	84292	2.76335	2.50284	2.45562	2.651406	2.297828	1.845599	2.264945	3.604424	773
san83.031	85083	2.76281	2.50287	2.45586	2.661698	2.01023	1.875402	2.182443	2.830293	773
san83.033	85959	2.76113	2.50062	2.45592	2.630425	2.695105	2.296481	2.54067	3.420541	773
san83.035	86765	2.76008	2.50304	2.45627	2.59258	2.589061	2.029332	2.403658	3.436071	773
san83.037	87620	2.76051	2.49977	2.4535	2.657166	2.876844	2.024919	2.519643	3.632455	773
san83.039	88406	2.75988	2.49711	2.45097	2.669438	2.953115	1.87749	2.500014	3.596137	773
san83.041	89204	2.76709	2.51254	2.45721	3.010829	3.110768	2.675841	2.932479	3.898242	773
san83.042	89521	2.76438	2.5189	2.45654	3.550784	2.42434	2.131421	2.702182	1.785446	773
san83.043	89841	2.76858	2.49941	2.45002	2.853333	2.856692	1.965062	2.558362	3.450156	773
san83.044	90155	2.76619	2.51193	2.44777	2.572561	2.317026	2.661712	2.5171	3.772867	773
san83.049	91994	2.76135	2.49948	2.4473	2.58134	3.333272	2.638524	2.851045	3.827513	773
san83.051	94359	2.77219	2.51777	2.46061	1.361101	1.502749	1.091531	1.318461	4.251477	1173
san83.053	95069	2.77469	2.51928	2.46362	1.336502	1.868875	1.202185	1.469187	4.247296	1173

No.	Time (sec)	d value (Detector 4)			τ (GPa)			τ (GPa) (average)	P (GPa)	T(K)
Peak		130	131	112	130	131	112			
san83.055	95825	2.77775	2.52123	2.47046	1.316526	1.913774	1.247304	1.492535	4.14838	1173
san83.057	96571	2.78004	2.52275	2.47295	1.501783	1.688051	1.122355	1.437397	3.804389	1173
san83.059	97303	2.77969	2.52319	2.47208	1.92377	1.843863	1.116787	1.62814	3.222639	1173
san83.061	98134	2.7775	2.52338	2.47083	1.483138	1.514999	0.933319	1.310485	3.356754	1173
san83.063	98851	2.77761	2.52276	2.46971	1.316585	1.425081	0.892595	1.21142	3.315771	1173
san83.065	99617	2.77725	2.52274	2.46984	1.387568	1.419213	0.90414	1.236974	3.255984	1173
san83.067	100385	2.77744	2.52256	2.47013	1.359459	1.309759	0.87357	1.18093	3.316412	1173
san83.069	101128	2.77891	2.52671	2.47088	1.269522	1.177402	0.751582	1.066169	2.447925	1173
san83.071	101938	2.77997	2.5271	2.47151	1.401385	1.248401	0.77145	1.140412	2.458959	1173
san83.073	102662	2.78066	2.52808	2.47131	1.225479	1.225473	0.752606	1.067853	2.538864	1173
san83.075	103776	2.77699	2.51759	2.46755	1.440357	1.438986	0.980693	1.286679	2.330405	973
san83.077	104508	2.78075	2.52752	2.47142	2.370093	2.302785	1.375891	2.016256	2.566775	973
san83.079	105222	2.77593	2.52121	2.46953	2.167189	2.215561	1.362297	1.915016	2.751706	973
san83.081	105945	2.77754	2.52314	2.47023	2.243897	2.403435	1.510598	2.052643	2.642569	973
san83.083	106687	2.77989	2.52431	2.47038	2.369791	2.589657	1.756286	2.238578	2.718123	973
san83.085	107670	2.77193	2.51964	2.46689	1.852321	2.188245	1.409175	1.81658	2.68439	973
san83.087	108528	2.76856	2.51728	2.46287	0.946775	1.004554	0.548582	0.833304	2.570207	973
san83.089	109324	2.76532	2.51481	2.46145	0.183889	0.332301	0.079022	0.198404	2.43498	973

Table D-3 data table for experiment San105

No.	time(s)	d (Detector 1)					d (Detector 2)				
Peak		(021)	(101)	(130)	(131)	(112)	(021)	(101)	(130)	(131)	(112)
AN105.003	4207	3.88252	3.72371	2.77164	2.51536	2.46137	3.88143	3.71839	2.77135	2.51393	2.45695
AN105.005	19006	3.77958	3.65853	2.69776	2.44722	2.40156	3.76803	3.65121	2.69358	2.44306	2.39994
AN105.006	21619	3.89635	3.72741	2.77545	2.52577	2.47386	3.89131	3.74029	2.77066	2.51473	2.46732
AN105.007	30525	3.86423	3.70788	2.77161	2.5154	2.46765	3.86423	3.70788	2.78223	2.53173	2.46824
AN105.008	31126	3.8974	3.6979	2.7706	2.5313	2.4709	3.90066	3.7455	2.76902	2.5068	2.46947
AN105.009	33122	3.87992	3.7254	2.76282	2.51271	2.4558	3.87694	3.70511	2.75766	2.50578	2.46044
AN105.010	33620	3.87194	3.72708	2.75162	2.50615	2.45406	3.87034	3.70695	2.75244	2.50611	2.45745
AN105.011	34107	3.86968	3.69332	2.75291	2.50858	2.45335	3.86532	3.71665	2.74706	2.5014	2.44966
AN105.012	34548	3.86317	3.68399	2.75052	2.50654	2.45345	3.86042	3.71527	2.74512	2.5014	2.44968
AN105.013	34986	3.86088	3.67687	2.74917	2.50353	2.45232	3.85946	3.72653	2.7445	2.4989	2.44848
AN105.014	35495	3.85947	3.6919	2.74745	2.5008	2.45226	3.85731	3.72693	2.74161	2.49617	2.44566
AN105.015	36017	3.85775	3.70365	2.74833	2.5	2.45177	3.85834	3.71589	2.74362	2.49071	2.44014
AN105.016	36479	3.85616	3.7067	2.74693	2.49675	2.45209	3.85628	3.71309	2.7419	2.48828	2.44274
AN105.017	37135	3.85351	3.70117	2.74468	2.49693	2.45388	3.84977	3.71127	2.74053	2.48645	2.44426
AN105.018	37709	3.8471	3.6958	2.73835	2.48985	2.44905	3.83716	3.6997	2.73427	2.48087	2.44002
AN105.019	37709	3.84647	3.69556	2.73831	2.48983	2.44899	3.83692	3.70014	2.73415	2.48085	2.4397
AN105.020	38362	3.83724	3.69234	2.73243	2.48527	2.44547	3.8276	3.69969	2.72862	2.47857	2.43697
AN105.021	38778	3.83337	3.68892	2.72938	2.48246	2.44309	3.82231	3.69587	2.72471	2.47699	2.4349
AN105.022	39193	3.82943	3.68569	2.72677	2.48055	2.44055	3.82008	3.69392	2.72366	2.4756	2.43531
AN105.023	39609	3.8236	3.68506	2.72514	2.47902	2.43772	3.81672	3.68833	2.72212	2.47511	2.43473
AN105.024	40058	3.82008	3.68289	2.72459	2.47647	2.43528	3.8143	3.69088	2.72003	2.47378	2.4319
AN105.025	40496	3.81765	3.68503	2.72457	2.47498	2.43368	3.81191	3.69125	2.71861	2.47218	2.43038
AN105.026	40940	3.81562	3.68233	2.72386	2.47366	2.43272	3.80841	3.68972	2.71686	2.47072	2.43086

No.	time(s)	d (Detector 1)					d (Detector 2)				
Peak		(021)	(101)	(130)	(131)	(112)	(021)	(101)	(130)	(131)	(112)
AN105.027	41494	3.81524	3.68631	2.72302	2.47475	2.42967	3.81283	3.68925	2.71795	2.47389	2.43429
AN105.028	42099	3.81542	3.68918	2.72283	2.4724	2.42942	3.80974	3.68968	2.71472	2.47037	2.43559
AN105.029	42565	3.81171	3.69104	2.72185	2.47264	2.42999	3.80807	3.68516	2.71376	2.46904	2.43453
AN105.030	43112	3.80956	3.68756	2.7202	2.47397	2.43017	3.80622	3.67794	2.71598	2.46727	2.42866
AN105.031	43522	3.80671	3.68538	2.71954	2.47353	2.42986	3.80494	3.6763	2.7157	2.46683	2.42581
AN105.032	44021	3.80781	3.68427	2.7189	2.47067	2.4291	3.8053	3.67528	2.71295	2.46734	2.42463
AN105.033	44438	3.80532	3.68422	2.71822	2.47007	2.42824	3.80351	3.67479	2.71342	2.46654	2.4245
AN105.034	45178	3.81232	3.68498	2.71755	2.46796	2.42479	3.79921	3.67634	2.71089	2.46354	2.42462
AN105.035	45702	3.80914	3.68275	2.71552	2.46618	2.42263	3.79674	3.67109	2.71028	2.4641	2.42382
AN105.036	46194	3.80532	3.68273	2.71664	2.46576	2.42457	3.79713	3.67192	2.71026	2.46306	2.42293
AN105.037	46709	3.80593	3.67817	2.71388	2.46459	2.42458	3.79929	3.67292	2.70938	2.45976	2.41837
AN105.038	47121	3.80139	3.68074	2.71387	2.46577	2.42526	3.79652	3.67565	2.70968	2.4602	2.41796
AN105.039	47543	3.80097	3.6784	2.71351	2.46486	2.42444	3.79863	3.67341	2.70957	2.46009	2.41922
AN105.040	47948	3.80232	3.67912	2.71342	2.46418	2.42524	3.79781	3.6719	2.70946	2.45996	2.42016
AN105.041	48425	3.8068	3.68246	2.71575	2.4682	2.42432	3.7983	3.6754	2.71162	2.4622	2.42128
AN105.042	48642	3.80214	3.68683	2.71493	2.46446	2.42473	3.79587	3.67871	2.71155	2.46091	2.42086
AN105.043	48854	3.80297	3.6808	2.71583	2.46705	2.42398	3.79195	3.68061	2.71109	2.4604	2.41885
AN105.044	49212	3.80005	3.68081	2.71526	2.46457	2.42695	3.79323	3.66973	2.70657	2.45879	2.42418
AN105.045	49430	3.80212	3.67813	2.71351	2.46351	2.42489	3.79595	3.67166	2.70881	2.45914	2.42197
AN105.046	49837	3.81109	3.68643	2.71611	2.47858	2.43869	3.79009	3.67101	2.70872	2.45939	2.42516
AN105.047	50140	3.80634	3.68601	2.71439	2.46559	2.42198	3.79444	3.67461	2.71003	2.46081	2.41924
AN105.048	50357	3.80095	3.6808	2.71494	2.4639	2.42272	3.79242	3.673	2.70695	2.45902	2.41549
AN105.049	50641	3.80105	3.67777	2.71412	2.46366	2.42481	3.79451	3.67046	2.70815	2.45735	2.42481
AN105.051	52946	3.78384	3.66891	2.70607	2.45441	2.41642	3.7745	3.65665	2.69929	2.44944	2.41717
AN105.052	53375	3.78415	3.6684	2.7055	2.45404	2.41612	3.77351	3.65751	2.69898	2.44949	2.41678

No.	time(s)	d (Detector 1)					d (Detector 2)				
Peak		(021)	(101)	(130)	(131)	(112)	(021)	(101)	(130)	(131)	(112)
AN105.053	53806	3.78318	3.66644	2.70531	2.45375	2.4171	3.77513	3.66006	2.69843	2.44922	2.41933
AN105.054	54490	3.78116	3.67195	2.70405	2.4531	2.41631	3.77315	3.66018	2.69832	2.44756	2.41468
AN105.055	54997	3.77739	3.66888	2.70262	2.45317	2.41679	3.77312	3.66045	2.69858	2.44731	2.41396
AN105.056	55542	3.77841	3.67195	2.70251	2.45314	2.41765	3.77314	3.66249	2.69759	2.4472	2.4161
AN105.057	56016	3.77772	3.6724	2.70205	2.45334	2.41815	3.77297	3.66251	2.69683	2.44762	2.41609
AN105.058	56526	3.7787	3.67244	2.70168	2.45305	2.41686	3.77308	3.66103	2.69684	2.44714	2.41762
AN105.059	56970	3.77542	3.66671	2.7019	2.45308	2.41705	3.77235	3.65952	2.69735	2.44674	2.41637
AN105.060	57378	3.77535	3.66396	2.70248	2.45281	2.41678	3.76915	3.65707	2.69851	2.44699	2.41601
AN105.061	58012	3.7694	3.66149	2.70014	2.45082	2.4146	3.76493	3.65619	2.69586	2.44362	2.41103
AN105.062	58505	3.76648	3.65763	2.70024	2.45028	2.41477	3.7631	3.65427	2.69635	2.44513	2.41616
AN105.063	58920	3.76719	3.6591	2.7006	2.44999	2.41552	3.76366	3.65671	2.69595	2.44614	2.41839
AN105.064	59388	3.76783	3.65644	2.70009	2.45025	2.41681	3.76181	3.65677	2.69511	2.44255	2.39664
AN105.065	59811	3.76782	3.65772	2.69942	2.44926	2.41539	3.76263	3.65566	2.69529	2.44179	2.39318
AN105.066	60242	3.765	3.65745	2.69898	2.44789	2.41294	3.75855	3.6581	2.69475	2.44174	2.39376
AN105.067	60659	3.76687	3.66396	2.69897	2.44891	2.41634	3.76109	3.66099	2.69517	2.44393	2.41287
AN105.068	61103	3.76818	3.66686	2.6986	2.44792	2.41558	3.75977	3.66273	2.69432	2.44199	2.39792
AN105.069	61591	3.76715	3.66485	2.69882	2.44731	2.41554	3.76102	3.66165	2.69329	2.44375	2.40996
AN105.070	62053	3.76593	3.66645	2.69831	2.44721	2.41672	3.7588	3.65828	2.69395	2.4437	2.41319

(Continued)

No.	time(s)	Detector 3					Detector 4				
Peak		(021)	(101)	(130)	(131)	(112)	(021)	(101)	(130)	(131)	(112)
AN105.003	4207	3.90366	3.71986	2.77058	2.51975	2.45684	3.88637	3.71882	2.7718	2.51784	2.46065
AN105.005	19006	3.82736	3.68209	2.7302	2.47657	2.4301	3.81782	3.68285	2.71813	2.47943	2.43031
AN105.006	21619	3.91535	3.75099	2.77385	2.52412	2.47253	3.89113	3.72708	2.77282	2.51505	2.46693
AN105.007	30525	3.88174	3.72153	2.77216	2.54851	2.46609	3.86844	3.6842	2.76417	2.52242	2.46652
AN105.008	31126	3.89315	3.70024	2.77344	2.5455	2.47275	3.85017	3.68115	2.7649	2.52251	2.47146
AN105.009	33122	3.81133	3.69904	2.76868	2.54483	2.47542	3.89875	3.73838	2.69604	2.5414	2.4594
AN105.010	33620	3.90127	3.74677	2.82266	2.52911	2.46879	3.88287	3.71543	2.77162	2.51463	2.46567
AN105.011	34107	3.88404	3.73699	2.76875	2.52128	2.46681	3.89888	3.74846	2.77828	2.51444	2.46043
AN105.012	34548	3.88394	3.73439	2.7731	2.52069	2.46857	3.89604	3.72944	2.77669	2.51291	2.46917
AN105.013	34986	3.88701	3.7211	2.77432	2.51808	2.46642	3.89721	3.73434	2.77609	2.51368	2.47175
AN105.014	35495	3.88009	3.72404	2.7735	2.51746	2.46374	3.89366	3.73292	2.77762	2.51691	2.47402
AN105.015	36017	3.88716	3.73331	2.76943	2.51266	2.45933	3.88192	3.72759	2.77234	2.5215	2.4631
AN105.016	36479	3.8891	3.73175	2.77093	2.51183	2.45817	3.87939	3.72533	2.77257	2.52214	2.46095
AN105.017	37135	3.88834	3.72903	2.77215	2.51154	2.45841	3.88234	3.72523	2.77424	2.52297	2.45937
AN105.018	37709	3.88402	3.73729	2.76982	2.50822	2.45513	3.87955	3.71418	2.77064	2.52049	2.45655
AN105.019	37709	3.88396	3.7364	2.76961	2.50824	2.45508	3.87955	3.71426	2.77064	2.52049	2.45653
AN105.020	38362	3.88329	3.72885	2.77186	2.50772	2.455	3.87858	3.72019	2.77096	2.52162	2.45604
AN105.021	38778	3.88274	3.72785	2.774	2.50658	2.4561	3.87845	3.71691	2.77001	2.52245	2.45597
AN105.022	39193	3.88202	3.73478	2.7746	2.50502	2.45793	3.87646	3.71625	2.76985	2.52354	2.45822
AN105.023	39609	3.88208	3.72348	2.77211	2.50502	2.4621	3.87543	3.71866	2.7692	2.5249	2.45924
AN105.024	40058	3.88108	3.72071	2.77195	2.50421	2.46149	3.87525	3.71607	2.76753	2.52432	2.45914
AN105.025	40496	3.8848	3.73491	2.77036	2.50598	2.46336	3.87278	3.71454	2.76532	2.52362	2.46017
AN105.026	40940	3.88528	3.72812	2.76979	2.50491	2.46377	3.87459	3.7095	2.76327	2.52385	2.462

No.	time(s)	Detector 3					Detector 4				
Peak		(021)	(101)	(130)	(131)	(112)	(021)	(101)	(130)	(131)	(112)
AN105.027	41494	3.88445	3.72986	2.76475	2.51012	2.4554	3.86986	3.7168	2.77138	2.51591	2.46431
AN105.028	42099	3.89234	3.71408	2.76727	2.50909	2.45638	3.87505	3.70701	2.76938	2.51802	2.46314
AN105.029	42565	3.9006	3.70879	2.76734	2.51332	2.45705	3.87469	3.71034	2.77006	2.51819	2.46244
AN105.030	43112	3.89367	3.71947	2.76846	2.51518	2.46258	3.88393	3.72457	2.77881	2.51799	2.46154
AN105.031	43522	3.89355	3.71336	2.76827	2.51364	2.46226	3.88232	3.72358	2.77899	2.51903	2.46115
AN105.032	44021	3.89499	3.71827	2.77025	2.50829	2.45985	3.88176	3.72238	2.77851	2.51934	2.46276
AN105.033	44438	3.89846	3.7167	2.7695	2.51207	2.45975	3.88381	3.72141	2.77874	2.5192	2.46253
AN105.034	45178	3.89669	3.7226	2.77758	2.51472	2.46463	3.88261	3.71855	2.77429	2.52144	2.4605
AN105.035	45702	3.88751	3.715	2.77087	2.5144	2.46224	3.87969	3.70816	2.76566	2.51875	2.45794
AN105.036	46194	3.88707	3.70975	2.77162	2.51196	2.46517	3.8815	3.71867	2.76555	2.5197	2.45848
AN105.037	46709	3.8903	3.71765	2.76579	2.52303	2.45965	3.89163	3.71986	2.77097	2.51439	2.45658
AN105.038	47121	3.88969	3.7195	2.76459	2.52349	2.45992	3.8887	3.71953	2.77298	2.5139	2.45541
AN105.039	47543	3.88799	3.72229	2.76407	2.52348	2.46	3.89198	3.72084	2.77126	2.51549	2.45639
AN105.040	47948	3.89029	3.7187	2.76495	2.52319	2.45999	3.89309	3.7206	2.77132	2.51559	2.45641
AN105.041	48425	3.87564	3.71898	2.76509	2.51301	2.45632	3.87153	3.71745	2.76016	2.50608	2.45385
AN105.042	48642	3.88573	3.72846	2.77362	2.51794	2.46159	3.8873	3.72261	2.77378	2.51061	2.45836
AN105.043	48854	3.89653	3.72711	2.7724	2.52316	2.45652	3.88199	3.72527	2.76896	2.51649	2.45813
AN105.044	49212	3.90111	3.72334	2.77869	2.5184	2.45589	3.89062	3.72062	2.77167	2.5174	2.45547
AN105.045	49430	3.89206	3.71805	2.76712	2.52366	2.45987	3.89328	3.72135	2.77341	2.51524	2.45559
AN105.046	49837	3.89858	3.72657	2.77957	2.51819	2.45726	3.88966	3.71054	2.76585	2.50672	2.45163
AN105.047	50140	3.88066	3.71363	2.76789	2.51664	2.45602	3.87694	3.70737	2.76502	2.51097	2.45742
AN105.048	50357	3.87977	3.71602	2.76477	2.52161	2.46123	3.87334	3.71199	2.76559	2.50465	2.45583
AN105.049	50641	3.89261	3.72162	2.76712	2.5248	2.46043	3.89318	3.72357	2.76979	2.51774	2.45502
AN105.051	52946	3.88115	3.71811	2.76031	2.51559	2.45694	3.88028	3.71719	2.76124	2.51176	2.45219
AN105.052	53375	3.87973	3.71781	2.76132	2.51432	2.45607	3.87917	3.71584	2.76058	2.51182	2.45256

No.	time(s)	Detector 3					Detector 4				
Peak		(021)	(101)	(130)	(131)	(112)	(021)	(101)	(130)	(131)	(112)
AN105.053	53806	3.88404	3.71437	2.76136	2.51413	2.45696	3.87991	3.71795	2.76046	2.51105	2.45221
AN105.054	54490	3.88233	3.71298	2.76028	2.51399	2.45837	3.88206	3.71385	2.76172	2.50962	2.45506
AN105.055	54997	3.88172	3.71539	2.76039	2.51523	2.46006	3.88229	3.71344	2.762	2.50985	2.45573
AN105.056	55542	3.88124	3.71676	2.76004	2.51588	2.46025	3.88235	3.71059	2.76209	2.5103	2.45616
AN105.057	56016	3.8821	3.7157	2.76082	2.51698	2.46071	3.88262	3.71127	2.7624	2.51055	2.45575
AN105.058	56526	3.88132	3.71944	2.76166	2.51687	2.45994	3.88062	3.71643	2.76324	2.51091	2.45538
AN105.059	56970	3.88365	3.72329	2.76229	2.51663	2.4591	3.8828	3.72073	2.76345	2.511	2.45489
AN105.060	57378	3.88575	3.72605	2.76427	2.51705	2.45797	3.88157	3.71924	2.764	2.51121	2.45472
AN105.061	58012	3.88234	3.719	2.76274	2.51476	2.45601	3.88015	3.71448	2.76273	2.50935	2.45414
AN105.062	58505	3.88156	3.71785	2.76347	2.51421	2.45617	3.8795	3.71001	2.76167	2.50878	2.45367
AN105.063	58920	3.87859	3.71662	2.76412	2.51482	2.45667	3.88038	3.70953	2.76201	2.50826	2.45344
AN105.064	59388	3.88202	3.71687	2.76498	2.51633	2.45759	3.87821	3.71187	2.7622	2.50801	2.45334
AN105.065	59811	3.88084	3.72129	2.7645	2.51553	2.45748	3.87907	3.71188	2.76258	2.50793	2.45358
AN105.066	60242	3.88326	3.72402	2.76534	2.5153	2.45729	3.87858	3.7106	2.76218	2.50789	2.45308
AN105.067	60659	3.88227	3.72351	2.76541	2.5157	2.45719	3.88028	3.71169	2.76315	2.50829	2.45329
AN105.068	61103	3.88239	3.7215	2.76547	2.51579	2.4566	3.87927	3.71267	2.76328	2.5082	2.45235
AN105.069	61591	3.88275	3.72419	2.76769	2.51503	2.45586	3.87998	3.71141	2.76328	2.50797	2.4521
AN105.070	62053	3.88349	3.72156	2.76601	2.51659	2.45709	3.87948	3.71838	2.76341	2.50753	2.45211

(Continued)

No. Peak	time(s)	τ (GPa) (021)	(101)	(130)	(131)	(112)	τ (GPa) (average)	P(GPa)	Strain	T(K)
AN105.003	4207	0.46	-0.08	-0.02	0.24	-0.03	0.11	0.00		298
AN105.005	19006	1.90	1.38	1.69	2.07	2.03	1.81	7.77		298
AN105.006	21619	0.33	0.24	0.01	-0.04	-0.05	0.10	5.61		1473
AN105.007	30525	0.39	-0.24	-0.47	0.66	-0.10	0.05	3.95		1173
AN105.008	31126	-0.97	-1.50	-0.03	0.83	0.12	-0.31	3.85	-0.08%	1173
AN105.009	33122	-0.85	0.16	-1.57	1.88	0.59	0.04	1.42	0.66%	1173
AN105.010	33620	0.74	0.66	2.37	0.90	0.73	1.08	2.06	1.07%	1173
AN105.011	34107	0.85	1.76	1.27	0.74	0.77	1.08	5.17	1.48%	1173
AN105.012	34548	1.00	1.52	1.46	0.74	1.10	1.16	4.61	1.73%	1173
AN105.013	34986	1.13	1.23	1.53	0.85	1.18	1.18	4.45	2.14%	1173
AN105.014	35495	1.01	0.90	1.68	1.08	1.26	1.19	4.62	2.64%	1173
AN105.015	36017	0.94	0.97	1.35	1.26	0.98	1.10	5.68	3.05%	1173
AN105.016	36479	1.00	0.88	1.49	1.42	0.78	1.11	5.63	3.46%	1173
AN105.017	37135	1.20	0.99	1.66	1.48	0.63	1.19	5.55	4.20%	1173
AN105.018	37709	1.43	1.33	1.86	1.70	0.73	1.41	4.81	4.04%	973
AN105.019	37709	1.44	1.30	1.85	1.70	0.74	1.41	4.84	4.28%	973
AN105.020	38362	1.75	1.35	2.24	1.92	0.93	1.64	5.05	4.61%	973
AN105.021	38778	1.91	1.43	2.47	2.04	1.11	1.79	5.12	4.70%	973
AN105.022	39193	1.98	1.70	2.58	2.13	1.31	1.94	4.98	5.27%	973
AN105.023	39609	2.13	1.64	2.59	2.23	1.58	2.04	5.12	5.77%	973
AN105.024	40058	2.22	1.51	2.62	2.31	1.73	2.08	5.29	6.51%	973
AN105.025	40496	2.34	1.74	2.56	2.43	1.92	2.20	5.47	6.75%	973
AN105.026	40940	2.48	1.57	2.56	2.49	2.01	2.22	5.51	6.92%	973
AN105.027	41494	2.31	1.69	2.63	2.29	1.81	2.15	5.55	7.50%	973

No. Peak	time(s)	τ (GPa) (021)	(101)	(130)	(131)	(112)	τ(GPa) (average)	P(GPa)	Strain	T(K)
AN105.028	42099	2.59	1.02	2.74	2.49	1.77	2.12	5.53	8.40%	973
AN105.027	41494	2.31	1.69	2.63	2.29	1.81	2.15	5.55	7.50%	973
AN105.028	42099	2.59	1.02	2.74	2.49	1.77	2.12	5.53	8.40%	973
AN105.029	42565	2.82	1.04	2.82	2.65	1.78	2.22	5.70	8.98%	973
AN105.030	43112	2.94	1.88	3.06	2.71	2.12	2.54	5.12	9.72%	973
AN105.031	43522	2.98	1.81	3.09	2.72	2.20	2.56	5.20	9.97%	973
AN105.032	44021	2.97	1.94	3.22	2.65	2.24	2.61	4.97	10.46%	973
AN105.033	44438	3.15	1.90	3.21	2.80	2.26	2.66	5.21	10.96%	973
AN105.034	45178	3.04	1.91	3.40	3.09	2.46	2.78	5.15	14.17%	973
AN105.035	45702	2.95	1.68	3.08	3.04	2.41	2.63	6.20	14.25%	973
AN105.036	46194	3.03	1.78	3.06	3.05	2.48	2.68	5.89	14.42%	973
AN105.037	46709	3.21	2.08	3.16	3.34	2.40	2.84	6.52	14.91%	973
AN105.038	47121	3.29	1.98	3.17	3.29	2.36	2.82	6.52	15.32%	973
AN105.039	47543	3.28	2.19	3.12	3.37	2.38	2.87	6.61	15.57%	973
AN105.036	46194	3.03	1.78	3.06	3.05	2.48	2.68	5.89	14.42%	973
AN105.037	46709	3.21	2.08	3.16	3.34	2.40	2.84	6.52	14.91%	973
AN105.038	47121	3.29	1.98	3.17	3.29	2.36	2.82	6.52	15.32%	973
AN105.039	47543	3.28	2.19	3.12	3.37	2.38	2.87	6.61	15.57%	973
AN105.040	47948	3.33	2.12	3.15	3.38	2.32	2.86	6.52		973
AN105.041	48425	2.62	1.89	2.74	2.65	2.12	2.40	6.69		973
AN105.042	48642	3.19	2.04	3.34	3.07	2.43	2.81	5.23		973
AN105.043	48854	3.34	2.17	3.17	3.31	2.35	2.87	6.38		973
AN105.044	49212	3.60	2.24	3.55	3.33	1.97	2.94	5.79		973
AN105.045	49430	3.40	2.15	3.28	3.43	2.24	2.90	6.33		973
AN105.046	49837	3.39	1.91	3.34	2.58	1.47	2.54	5.65	17.46%	973

No. Peak	time(s)	τ (GPa) (021)	(101)	(130)	(131)	(112)	τ (GPa) (average)	P(GPa)	Strain	T(K)
AN105.047	50140	2.88	1.46	3.02	3.01	2.37	2.55	6.55		973
AN105.048	50357	2.94	1.79	3.03	3.08	2.58	2.69	6.55		973
AN105.049	50641	3.45	2.33	3.19	3.58	2.15	2.94	6.51	19.11%	973
AN105.051	52946	3.76	2.66	3.28	3.70	2.49	3.18	6.25	21.58%	773
AN105.052	53375	3.73	2.61	3.31	3.68	2.50	3.17	6.25	21.99%	773
AN105.053	53806	3.80	2.56	3.33	3.67	2.40	3.15	6.14		773
AN105.054	54490	3.88	2.30	3.38	3.70	2.71	3.19	6.01	23.64%	773
AN105.055	54997	3.95	2.41	3.42	3.74	2.80	3.26	5.98	24.38%	773
AN105.056	55542	3.92	2.25	3.45	3.78	2.71	3.22	5.97	25.21%	773
AN105.057	56016	3.96	2.23	3.51	3.79	2.70	3.24	5.99	26.11%	773
AN105.058	56526	3.89	2.47	3.57	3.82	2.66	3.28	5.95	26.36%	773
AN105.059	56970	4.05	2.84	3.57	3.83	2.65	3.39	5.95	26.94%	773
AN105.060	57378	4.12	3.00	3.58	3.85	2.63	3.44	5.86	27.68%	773
AN105.061	58012	4.24	2.81	3.65	3.90	2.79	3.48	5.53	28.24%	673
AN105.062	58505	4.31	2.82	3.63	3.84	2.60	3.44	5.41	29.00%	673
AN105.063	58920	4.25	2.69	3.66	3.82	2.51	3.39	5.30	29.74%	673
AN105.064	59388	4.29	2.81	3.72	3.96	3.23	3.60	5.66	30.31%	673
AN105.065	59811	4.27	2.91	3.73	3.99	3.41	3.66	5.70	30.97%	673
AN105.066	60242	4.44	2.89	3.77	4.03	3.45	3.72	5.73	31.47%	673
AN105.067	60659	4.37	2.67	3.79	3.95	2.68	3.49	5.28	32.21%	673
AN105.068	61103	4.35	2.53	3.83	4.04	3.17	3.59	5.64	32.70%	673
AN105.069	61591	4.36	2.64	3.91	3.98	2.73	3.53	5.30	33.44%	673
AN105.070	62053	4.44	2.78	3.87	4.01	2.62	3.54	5.84	34.18%	673

Table D-4 Data table for San106

No.		Detector 1					Detector 2				
	time(s)	(021)	(101)	(130)	(131)	(112)	(021)	(101)	(130)	(131)	(112)
3		3.88999	3.72169	2.77011	2.51295	2.46217	3.88622	3.73013	2.77128	2.5154	2.4607
4	7454	3.76509	3.646	2.68905	2.44149	2.39613	3.76051	3.64418	2.68611	2.43713	2.39155
5	21084	3.89345	3.74145	2.77615	2.52128	2.46577	3.88197	3.72783	2.76962	2.51155	2.46453
6	23020	3.89267	3.7308	2.77101	2.5154	2.4671	3.88598	3.72755	2.76916	2.51279	2.4682
7	24018	3.89531	3.7296	2.76664	2.51359	2.46446	3.88722	3.72933	2.77059	2.51342	2.46358
8	24670	3.89535	3.73179	2.76575	2.51179	2.46347	3.88741	3.72994	2.76925	2.51367	2.46313
9	25241	3.89407	3.73058	2.76491	2.51076	2.46246	3.88589	3.72872	2.76935	2.51287	2.46185
10	25702	3.89226	3.72925	2.76378	2.50966	2.4614	3.88429	3.72736	2.76817	2.51179	2.45963
11	26279	3.88989	3.72575	2.76183	2.50778	2.45988	3.88237	3.72579	2.76662	2.5097	2.45686
12	26939	3.88394	3.72073	2.75864	2.50404	2.45617	3.87768	3.71917	2.76132	2.50571	2.4536
13	27621	3.87502	3.71467	2.75613	2.50057	2.45176	3.86905	3.71253	2.75539	2.50074	2.45032
14	28071	3.87041	3.70995	2.75037	2.49764	2.44907	3.86371	3.71026	2.75311	2.49734	2.45534
15	28581	3.86599	3.70637	2.74589	2.49488	2.44545	3.8564	3.70469	2.74917	2.49435	2.45769
16	29054	3.86043	3.7049	2.74396	2.493	2.44348	3.85064	3.69745	2.74455	2.49173	2.45511
17	29537	3.85383	3.70706	2.74154	2.48964	2.44485	3.84696	3.69783	2.74154	2.48927	2.45409
18	30048	3.85093	3.70361	2.7396	2.49022	2.4477	3.84616	3.70551	2.73769	2.48843	2.45113
19	30608	3.84961	3.70461	2.7368	2.48913	2.44716	3.84503	3.70437	2.73509	2.48855	2.44679
20	31109	3.84627	3.70327	2.73668	2.48689	2.44637	3.84271	3.70026	2.73082	2.48695	2.444
21	31659	3.84556	3.7028	2.7356	2.48616	2.4465	3.83927	3.69957	2.72985	2.48526	2.44057
22	32353	3.84238	3.70048	2.73509	2.48476	2.44494	3.83484	3.70048	2.73062	2.48338	2.4417
23	32932	3.83973	3.69978	2.73505	2.48297	2.44373	3.8347	3.69912	2.72923	2.48236	2.44015
24	33602	3.83869	3.69834	2.73345	2.4822	2.44183	3.83368	3.69777	2.72845	2.48199	2.43775
25	34446	3.8285	3.69196	2.72687	2.47589	2.43725	3.82222	3.68915	2.72201	2.47599	2.43184
26	35046	3.82235	3.69032	2.72371	2.47248	2.4346	3.81541	3.68545	2.71848	2.47252	2.42901
27	35720	3.82019	3.68635	2.72298	2.47122	2.4328	3.81073	3.68228	2.71852	2.47154	2.42639
28	36209	3.81724	3.68468	2.72203	2.47025	2.42778	3.81001	3.68054	2.71723	2.47071	2.42473
29	39012	3.80254	3.69267	2.71854	2.46845	2.4299	3.8085	3.68524	2.71976	2.46805	2.42908

No.		Detector 1					Detector 2				
	time(s)	(021)	(101)	(130)	(131)	(112)	(021)	(101)	(130)	(131)	(112)
30	39999	3.8043	3.69204	2.71845	2.46796	2.43056	3.80822	3.68566	2.71939	2.46767	2.42959
31	41890	3.80081	3.68652	2.71687	2.46582	2.42906	3.8053	3.68321	2.71563	2.46593	2.43105
32	42494	3.80033	3.68407	2.71659	2.46604	2.43187	3.80712	3.68299	2.71479	2.46569	2.43185
33	43108	3.79787	3.68408	2.71604	2.46558	2.43131	3.80397	3.68161	2.71422	2.46579	2.43137
34	43652	3.79758	3.68361	2.71553	2.46523	2.43206	3.80255	3.68127	2.71406	2.46567	2.43116
35	44299	3.79724	3.68288	2.71499	2.4645	2.4333	3.80187	3.68151	2.71374	2.46458	2.42948
36	45766	3.79586	3.68353	2.71427	2.46173	2.42944	3.7982	3.68205	2.71363	2.46386	2.43134
37	46461	3.78898	3.67743	2.71022	2.45779	2.42348	3.79102	3.67719	2.70871	2.45935	2.42466
38	46954	3.78507	3.67518	2.70913	2.45599	2.4211	3.78725	3.67418	2.70758	2.45778	2.42252
39	47685	3.78441	3.67408	2.70796	2.45541	2.4206	3.78524	3.67432	2.70768	2.45781	2.42093
40	48348	3.78169	3.67197	2.70715	2.45437	2.41921	3.78396	3.67576	2.7057	2.45736	2.42152
41	49751	3.77792	3.67363	2.70469	2.45382	2.42102	3.7798	3.67586	2.7038	2.45621	2.41993
42	51609	3.77488	3.67971	2.70423	2.45301	2.41807	3.77891	3.67559	2.70357	2.45467	2.41891
43	52681	3.77356	3.67884	2.70348	2.45351	2.41693	3.77569	3.67094	2.70304	2.45305	2.41812
44	54036	3.77232	3.67407	2.70228	2.45286	2.41862	3.77699	3.66773	2.70305	2.45274	2.41852
45	54559	3.77071	3.67513	2.70017	2.4498	2.41294	3.77346	3.66822	2.70127	2.45019	2.41695
46	55173	3.77101	3.68113	2.70106	2.45005	2.41229	3.7744	3.6671	2.70071	2.44971	2.41612
47	55639	3.77685	3.67985	2.70501	2.45381	2.41838	3.77695	3.66857	2.70438	2.45373	2.41632
48	56104	3.77343	3.67635	2.70359	2.45248	2.4156	3.77574	3.66624	2.70274	2.45293	2.41498
49	56549	3.77045	3.67315	2.7022	2.45104	2.41432	3.77209	3.66248	2.70076	2.45167	2.41428
50	57021	3.77174	3.67455	2.70144	2.45095	2.41419	3.77017	3.66417	2.7002	2.45023	2.41348
51	57455	3.77166	3.6711	2.70033	2.45165	2.42134	3.77125	3.66258	2.70025	2.45031	2.41781
52	58300	3.77368	3.67647	2.70108	2.44864	2.40883	3.77311	3.66361	2.70116	2.45055	2.42205
53	58705	3.76963	3.67205	2.70146	2.44936	2.42114	3.77447	3.66815	2.70125	2.45123	2.42338
54	59120	3.76752	3.6704	2.70168	2.45012	2.42924	3.77335	3.66999	2.70138	2.45097	2.42347
55	59709	3.77496	3.67111	2.70128	2.44808	2.41645	3.76669	3.66214	2.69828	2.44987	2.41645
56	60347	3.77263	3.66978	2.70093	2.44782	2.42681	3.76662	3.65826	2.69767	2.45119	2.42681
57	62327	3.7702	3.66932	2.70077	2.44804	2.41093	3.76168	3.65755	2.69798	2.44897	2.41093
58	62892	3.77643	3.67628	2.70633	2.45339	2.4171	3.76916	3.66479	2.70318	2.45356	2.4171

No.	Detector 1						Detector 2				
	time(s)	(021)	(101)	(130)	(131)	(112)	(021)	(101)	(130)	(131)	(112)
59	63395	3.77726	3.66853	2.70603	2.45255	2.41896	3.7728	3.66376	2.70344	2.45285	2.41896
60	63795	3.77998	3.67705	2.70578	2.45355	2.41948	3.77117	3.663	2.70229	2.45297	2.41948
61	64213	3.78288	3.68061	2.70558	2.45254	2.41263	3.76997	3.65763	2.70192	2.45203	2.41839
62	64613	3.77613	3.66183	2.70513	2.4516	2.41414	3.76876	3.65942	2.70146	2.45186	2.41549
63	65051	3.77714	3.67316	2.70511	2.45174	2.41065	3.76897	3.65763	2.70148	2.45213	2.41759
64	65499	3.77607	3.65892	2.70524	2.45246	2.41421	3.76793	3.65974	2.70135	2.45167	2.41399
65	65930	3.77518	3.66124	2.70536	2.4522	2.41304	3.76612	3.65859	2.70098	2.45252	2.41619
66	66689	3.77773	3.67068	2.70485	2.45325	2.41502	3.76621	3.66144	2.70137	2.45256	2.41774
67	67257	3.77746	3.67652	2.70654	2.45088	2.41983	3.77191	3.66587	2.70313	2.4514	2.41983
68	68126	3.77523	3.66661	2.70426	2.45144	2.41412	3.76937	3.66084	2.70187	2.45096	2.41471
69	68900	3.77927	3.68442	2.70407	2.45192	2.41363	3.76985	3.66846	2.7014	2.45137	2.41567
70	69353	3.77814	3.66414	2.70446	2.45119	2.41562	3.76827	3.65814	2.70172	2.45105	2.41562
71	70316	3.77798	3.66598	2.70433	2.45279	2.41935	3.77056	3.66446	2.70105	2.4512	2.41841
72	70792	3.77792	3.6719	2.70512	2.45337	2.41717	3.77011	3.66371	2.70171	2.45036	2.41717
73	71427	3.77909	3.67341	2.70585	2.45292	2.41657	3.77165	3.66001	2.70207	2.4526	2.41657
74	72426	3.77974	3.67354	2.70688	2.45424	2.42028	3.77243	3.65744	2.70329	2.45351	2.42028
75	75292	3.78342	3.67837	2.70756	2.45375	2.41532	3.77467	3.66479	2.70422	2.45349	2.41532
76	78050	3.7835	3.67804	2.70772	2.45525	2.41539	3.77341	3.67085	2.70447	2.45306	2.41221
77	81644	3.78051	3.67354	2.70683	2.45208	2.41858	3.77555	3.66283	2.70436	2.45365	2.41858
78	91583	3.78383	3.66525	2.70664	2.45366	2.41063	3.77506	3.65416	2.70393	2.45341	2.42035
79	93306	3.78557	3.67308	2.70687	2.45301	2.41607	3.77545	3.66579	2.70445	2.45337	2.41607
80	99964	3.88091	3.72337	2.76833	2.5124	2.46473	3.87494	3.71841	2.76765	2.51202	2.46796

(Continued)

No. Peak	time(s)	Detector 3					Detector 4				
		(021)	(101)	(130)	(131)	(112)	(021)	(101)	(130)	(131)	(112)
3		3.88494	3.72872	2.76901	2.52284	2.4652	3.88876	3.72617	2.77028	2.52477	2.46176
4	7454	3.84497	3.69322	2.74796	2.49457	2.44577	3.85332	3.69398	2.7456	2.4927	2.44041
5	21084	3.89779	3.73152	2.77804	2.53516	2.47201	3.89279	3.72954	2.77436	2.51979	2.47105
6	23020	3.88267	3.72325	2.7674	2.51818	2.4646	3.88037	3.68894	2.7616	2.51462	2.46254
7	24018	3.88757	3.73326	2.76364	2.51943	2.46569	3.88487	3.69352	2.76277	2.51252	2.46172
8	24670	3.89009	3.73515	2.76406	2.52041	2.46481	3.89184	3.70328	2.76475	2.51229	2.4607
9	25241	3.88783	3.73635	2.76749	2.52117	2.46617	3.8949	3.71045	2.76806	2.51299	2.46152
10	25702	3.88873	3.73861	2.77074	2.52141	2.46566	3.89593	3.71507	2.77016	2.51326	2.46175
11	26279	3.88809	3.73781	2.77409	2.52169	2.46618	3.89198	3.71538	2.77243	2.51355	2.46189
12	26939	3.89185	3.73812	2.77727	2.52291	2.46624	3.89159	3.7151	2.77368	2.51434	2.46211
13	27621	3.89081	3.74292	2.77173	2.52467	2.46795	3.89125	3.71155	2.77066	2.51514	2.46445
14	28071	3.89049	3.73848	2.76843	2.52447	2.46775	3.89387	3.70845	2.77065	2.51613	2.46655
15	28581	3.88931	3.73814	2.76905	2.52586	2.46844	3.89245	3.72251	2.77339	2.51641	2.46693
16	29054	3.89049	3.73461	2.76994	2.52619	2.46912	3.88342	3.72429	2.77341	2.51671	2.46756
17	29537	3.89415	3.7365	2.77215	2.52828	2.47097	3.88463	3.7302	2.77489	2.52034	2.46681
18	30048	3.89175	3.73265	2.77378	2.5235	2.47028	3.8868	3.73146	2.77286	2.51941	2.46604
19	30608	3.89179	3.72638	2.77385	2.52154	2.4701	3.88948	3.73016	2.77488	2.51661	2.46423
20	31109	3.89026	3.72625	2.77269	2.51975	2.46803	3.88923	3.72981	2.77519	2.51663	2.46358
21	31659	3.88979	3.72656	2.7757	2.52056	2.46734	3.88833	3.73063	2.77559	2.51798	2.46321
22	32353	3.88909	3.73078	2.77831	2.52227	2.46675	3.88931	3.73024	2.77753	2.51887	2.46164
23	32932	3.89142	3.72985	2.7788	2.52136	2.46683	3.89146	3.72902	2.77629	2.51958	2.46364
24	33602	3.89028	3.72984	2.78266	2.52162	2.46636	3.88804	3.72744	2.7739	2.52009	2.46515
25	34446	3.88366	3.72218	2.78025	2.51878	2.46293	3.88423	3.72266	2.77182	2.51699	2.46175
26	35046	3.88256	3.72264	2.78109	2.5195	2.46402	3.8858	3.7234	2.77411	2.51626	2.46173
27	35720	3.88117	3.72406	2.78012	2.51989	2.46464	3.88673	3.72157	2.77596	2.51389	2.46074
28	36209	3.88174	3.72456	2.77861	2.52189	2.46388	3.88896	3.72135	2.77288	2.51409	2.46057
29	39012	3.8921	3.7142	2.77794	2.51883	2.46256	3.90548	3.71934	2.77221	2.5249	2.4721

No.	time(s)			Detector 3					Detector 4		
Peak		(021)	(101)	(130)	(131)	(112)	(021)	(101)	(130)	(131)	(112)
30	39999	3.89504	3.71286	2.77872	2.51835	2.46244	3.90679	3.71987	2.77258	2.52553	2.47267
31	41890	3.89292	3.71916	2.78389	2.51893	2.46302	3.90622	3.72157	2.77538	2.52528	2.47094
32	42494	3.89271	3.72075	2.78171	2.51942	2.46195	3.90719	3.72327	2.77754	2.52601	2.47053
33	43108	3.89443	3.72654	2.78186	2.52026	2.46189	3.90767	3.72325	2.778	2.5267	2.47019
34	43652	3.89642	3.72692	2.78041	2.52043	2.46177	3.90828	3.72383	2.7787	2.52697	2.4699
35	44299	3.89785	3.72819	2.77838	2.52262	2.46172	3.90768	3.72393	2.77989	2.52732	2.46944
36	45766	3.89687	3.72602	2.7781	2.52474	2.46401	3.90351	3.72567	2.78101	2.52644	2.47072
37	46461	3.89317	3.72291	2.77458	2.52239	2.46135	3.89602	3.72156	2.77714	2.52259	2.46707
38	46954	3.89192	3.71945	2.77184	2.521	2.4602	3.89335	3.71751	2.77517	2.52081	2.46672
39	47685	3.88746	3.72016	2.77006	2.51897	2.46005	3.8914	3.71917	2.77487	2.52072	2.46716
40	48348	3.88742	3.72146	2.77045	2.51957	2.46074	3.89224	3.71906	2.77504	2.51948	2.46561
41	49751	3.88705	3.72175	2.77129	2.51731	2.45937	3.8911	3.72029	2.77385	2.51953	2.46371
42	51609	3.88617	3.72197	2.7694	2.51428	2.45918	3.89147	3.72186	2.7758	2.51646	2.46037
43	52681	3.88577	3.72381	2.77004	2.51386	2.45913	3.89212	3.72568	2.77546	2.51527	2.46008
44	54036	3.88504	3.72404	2.76909	2.51422	2.45857	3.89171	3.72573	2.77281	2.51453	2.45939
45	54559	3.88255	3.72153	2.76754	2.51419	2.45741	3.88919	3.72619	2.77141	2.51397	2.45855
46	55173	3.88124	3.72186	2.76821	2.51365	2.45767	3.8868	3.72334	2.77	2.51257	2.45838
47	55639	3.87598	3.71733	2.76697	2.50669	2.45502	3.88203	3.71933	2.76537	2.50797	2.45603
48	56104	3.8783	3.71927	2.76815	2.50883	2.45609	3.88453	3.72028	2.76634	2.50907	2.45672
49	56549	3.87895	3.71176	2.76815	2.50979	2.45627	3.88655	3.71959	2.76701	2.50975	2.45754
50	57021	3.88035	3.7266	2.76855	2.51013	2.45711	3.88546	3.72199	2.76654	2.50967	2.4587
51	57455	3.88213	3.72639	2.7694	2.5107	2.45754	3.88646	3.72587	2.76643	2.50924	2.45799
52	58300	3.88318	3.73029	2.76876	2.51372	2.46027	3.88469	3.72977	2.76709	2.51051	2.45669
53	58705	3.88415	3.72704	2.76947	2.51788	2.46224	3.88441	3.72422	2.76724	2.51156	2.45848
54	59120	3.88487	3.72962	2.76779	2.51808	2.46152	3.88528	3.7246	2.76747	2.5113	2.45844
55	59709	3.88431	3.7269	2.77149	2.51403	2.45805	3.88729	3.7279	2.7713	2.51373	2.46006
56	60347	3.88514	3.72992	2.77165	2.50846	2.45482	3.888	3.73005	2.77174	2.51362	2.45975
57	62327	3.88802	3.727	2.77597	2.51163	2.45706	3.89051	3.72811	2.77321	2.51497	2.45968
58	62892	3.89276	3.73143	2.77916	2.51638	2.46005	3.89567	3.73101	2.77631	2.51698	2.4601

No. Peak	time(s)	Detector 3					Detector 4				
		(021)	(101)	(130)	(131)	(112)	(021)	(101)	(130)	(131)	(112)
59	63395	3.88887	3.73601	2.77692	2.51675	2.45934	3.89383	3.72789	2.77517	2.57952	2.51609
60	63795	3.88956	3.73111	2.77791	2.51683	2.45963	3.89564	3.72973	2.77598	2.51671	2.46069
61	64213	3.8904	3.73382	2.77853	2.51695	2.45978	3.8953	3.7276	2.77665	2.51735	2.4613
62	64613	3.89054	3.73283	2.77954	2.51831	2.46032	3.89657	3.73452	2.77703	2.51802	2.46127
63	65051	3.89154	3.73292	2.77972	2.51834	2.46005	3.89726	3.73193	2.77742	2.51769	2.46125
64	65499	3.89275	3.73302	2.78084	2.51683	2.4597	3.89651	3.73075	2.77786	2.51786	2.46098
65	65930	3.89262	3.73278	2.78013	2.51801	2.45989	3.8981	3.73285	2.77783	2.51743	2.46029
66	66689	3.89336	3.72748	2.78083	2.51613	2.45959	3.89823	3.73239	2.77819	2.5177	2.4608
67	67257	3.89627	3.73511	2.78067	2.52393	2.46415	3.89786	3.73433	2.77632	2.51662	2.45995
68	68126	3.89357	3.74297	2.7807	2.52021	2.46323	3.89847	3.73012	2.77885	2.51879	2.46321
69	68900	3.8936	3.73955	2.78121	2.51921	2.46297	3.89827	3.73265	2.77927	2.58442	2.51899
70	69353	3.89449	3.73962	2.7808	2.51985	2.46327	3.89906	3.73168	2.77888	2.51898	2.46315
71	70316	3.89575	3.74059	2.7807	2.51764	2.4624	3.8997	3.73019	2.77969	2.51931	2.46337
72	70792	3.89479	3.73501	2.78106	2.51807	2.46259	3.90021	3.73531	2.77996	2.58408	2.46334
73	71427	3.89552	3.73767	2.78027	2.51895	2.4627	3.8997	3.73839	2.7795	2.51912	2.46288
74	72426	3.89636	3.73886	2.78104	2.51797	2.46239	3.89973	3.74006	2.77991	2.51924	2.46267
75	75292	3.89618	3.74131	2.78053	2.51785	2.46232	3.89951	3.73798	2.77955	2.51929	2.4626
76	78050	3.89493	3.74344	2.78132	2.52001	2.4638	3.8993	3.7383	2.77948	2.51908	2.46414
77	81644	3.89744	3.73794	2.78002	2.51786	2.46217	3.90104	3.73855	2.77973	2.52033	2.46348
78	91583	3.89613	3.73663	2.77874	2.51531	2.46128	3.90216	3.73441	2.77975	2.52169	2.46487
79	93306	3.89587	3.73431	2.77899	2.51497	2.461	3.90125	3.73338	2.77923	2.52105	2.46432
80	99964	3.87268	3.71461	2.76338	2.50699	2.45509	3.88509	3.72584	2.76966	2.51195	2.45973

(Continued)

No. Peak	time(s)	τ (GPa) (021)	(101)	(130)	(131)	(112)	τ (GPa) (average)	P(GPa)	Strain	T(K)
3		-0.04	0.07	-0.06	0.55	0.13	0.13	0.00		298
4	7454	3.31	2.42	3.43	3.37	3.35	3.17	5.92		298
5	21084	0.26	-0.19	0.18	0.62	0.40	0.25	5.85		1473
6	23020	-0.28	-1.10	-0.30	0.13	-0.26	-0.36	4.71		1173
7	24018	-0.18	-0.76	-0.29	0.14	-0.02	-0.22	4.98		1173
8	24670	-0.01	-0.55	-0.17	0.21	-0.03	-0.11	5.02	0.16%	1173
9	25241	0.05	-0.29	0.03	0.30	0.11	0.04	4.70	0.16%	1173
10	25702	0.14	-0.07	0.24	0.38	0.20	0.18	4.55	0.31%	1173
11	26279	0.14	0.04	0.48	0.51	0.36	0.31	4.34	0.55%	1173
12	26939	0.38	0.31	0.83	0.79	0.59	0.58	4.38	0.63%	1173
13	27621	0.67	0.64	0.83	1.11	0.96	0.84	5.00	1.10%	1173
14	28071	0.89	0.63	0.97	1.31	0.95	0.95	5.16	1.18%	1173
15	28581	1.05	1.17	1.29	1.53	1.02	1.21	5.14	1.73%	1173
16	29054	1.12	1.33	1.49	1.68	1.21	1.37	5.25	1.97%	1173
17	29537	1.39	1.45	1.74	2.01	1.23	1.56	5.23	2.36%	1173
18	30048	1.45	1.29	1.89	1.86	1.19	1.54	5.27	2.68%	1173
19	30608	1.54	1.12	2.09	1.76	1.28	1.56	3.95	2.99%	973
20	31109	1.62	1.24	2.19	1.82	1.32	1.64	4.15	3.78%	973
21	31659	1.67	1.29	2.34	1.95	1.39	1.73	4.17	4.65%	973
22	32353	1.81	1.42	2.45	2.12	1.34	1.83	4.05	4.96%	973
23	32932	1.94	1.42	2.47	2.20	1.49	1.90	4.03	5.83%	973
24	33602	1.90	1.45	2.57	2.25	1.66	1.97	4.07	6.14%	973
25	34446	2.12	1.52	2.82	2.46	1.79	2.14	4.66	7.01%	973
26	35046	2.37	1.68	3.09	2.67	2.01	2.36	4.57	7.80%	973
27	35720	2.49	1.84	3.13	2.68	2.14	2.46	4.48	8.11%	973
28	36209	2.60	1.93	3.08	2.80	2.34	2.55	5.10	9.13%	973
29	39012	3.36	1.33	3.07	3.14	2.44	2.67	4.88	12.83%	973

No. Peak	time(s)	τ (GPa) (021)	(101)	(130)	(131)	(112)	τ (GPa) (average)	P(GPa)	Strain	T(K)
30	39999	3.40	1.32	3.11	3.17	2.41	2.68	4.78	13.46%	973
31	41890	3.48	1.70	3.47	3.30	2.38	2.86	4.43	16.54%	973
32	42494	3.46	1.84	3.50	3.33	2.21	2.87	4.52	17.72%	973
33	43108	3.61	2.01	3.55	3.39	2.23	2.96	4.62	18.11%	973
34	43652	3.68	2.05	3.55	3.41	2.20	2.98	4.70	18.82%	973
35	44299	3.71	2.09	3.55	3.54	2.20	3.02	4.87	19.76%	973
36	45766	3.72	2.05	3.60	3.68	2.38	3.09	4.72	21.97%	973
37	46461	3.81	2.15	3.67	3.77	2.60	3.20	4.22	22.20%	773
38	46954	3.89	2.11	3.61	3.79	2.71	3.22	4.49	22.91%	773
39	47685	3.83	2.19	3.59	3.75	2.79	3.23	4.57	23.86%	773
40	48348	3.92	2.23	3.68	3.77	2.79	3.28	4.61	25.04%	773
41	49751	4.05	2.22	3.80	3.77	2.68	3.30	4.75	27.56%	773
42	51609	4.12	2.12	3.82	3.67	2.70	3.29	4.65	30.63%	773
43	52681	4.21	2.39	3.86	3.66	2.76	3.38	4.61	32.05%	773
44	54036	4.19	2.59	3.81	3.68	2.65	3.38	4.85	34.57%	773
45	54559	4.20	2.50	3.84	3.84	2.83	3.44	4.63	35.04%	673
46	55173	4.12	2.33	3.82	3.80	2.88	3.39	4.59	38.98%	673
47	55639	3.79	2.12	3.44	3.23	2.52	3.02	4.35	39.69%	673
48	56104	3.96	2.33	3.59	3.39	2.71	3.20	4.46	39.84%	673
49	56549	4.13	2.32	3.70	3.52	2.81	3.30	4.55	40.08%	673
50	57021	4.15	2.64	3.74	3.57	2.90	3.40	4.50	40.24%	673
51	57455	4.18	2.85	3.79	3.55	2.51	3.37	4.27	40.79%	673
52	58300	4.09	2.87	3.74	3.76	2.83	3.46	4.50	41.73%	673
53	58705	4.15	2.66	3.75	3.86	2.49	3.38	4.28	42.44%	673
54	59120	4.24	2.73	3.70	3.84	2.19	3.34	4.23	42.91%	673
55	59709	4.25	2.91	4.00	3.89	2.80	3.57	4.20	44.25%	673
56	60347	4.32	3.16	4.04	3.70	1.99	3.44	3.54	44.57%	673
57	62327	4.55	3.08	4.18	3.89	3.13	3.77	4.00	47.56%	673
58	62892	4.45	2.90	4.03	3.77	2.81	3.59	4.07	49.61%	773

No. Peak	time(s)	τ (GPa) (021)	(101)	(130)	(131)	(112)	τ (GPa) (average)	P(GPa)	Strain	T(K)
59	63395	4.27	3.14	3.95	5.46	4.34	4.23	3.27	50.08%	773
60	63795	4.29	2.88	4.03	3.79	2.66	3.53	4.11	50.31%	773
61	64213	4.27	2.94	4.08	3.87	2.95	3.62	4.18	50.16%	773
62	64613	4.44	3.49	4.14	3.96	3.01	3.81	4.21	50.16%	773
63	65051	4.45	3.20	4.16	3.94	3.05	3.76	4.21	50.39%	773
64	65499	4.50	3.48	4.20	3.89	3.03	3.82	4.06	50.87%	773
65	65930	4.57	3.49	4.18	3.89	2.98	3.82	4.18	51.34%	773
66	66689	4.54	3.06	4.21	3.82	2.87	3.70	3.95	51.89%	773
67	67257	4.47	3.02	4.06	4.11	2.75	3.68	3.96	52.36%	773
68	68126	4.53	3.47	4.23	4.06	3.19	3.90	3.95	52.52%	773
69	68900	4.44	2.83	4.27	5.71	4.81	4.41	3.01	53.15%	773
70	69353	4.52	3.56	4.23	4.06	3.11	3.90	3.87	53.31%	773
71	70316	4.51	3.34	4.27	3.96	2.87	3.79	3.66	53.94%	773
72	70792	4.51	3.21	4.25	5.66	2.99	4.12	4.23		773
73	71427	4.46	3.39	4.18	3.94	3.02	3.80	3.85	54.33%	773
74	72426	4.45	3.51	4.15	3.85	2.75	3.74	3.56	54.49%	773
75	75292	4.33	3.22	4.08	3.86	3.08	3.72	3.78	54.33%	773
76	78050	4.33	3.14	4.09	3.88	3.28	3.74	3.80	54.49%	773
77	81644	4.42	3.33	4.09	3.94	2.88	3.73	3.66	54.88%	773
78	91583	4.36	3.62	4.08	3.86	3.11	3.81	3.86	54.80%	773
79	93306	4.30	3.07	4.05	3.86	3.04	3.66	3.77	55.43%	773
80	99964	0.03	-0.03	-0.08	-0.16	-0.57	-0.16	2.04	55.67%	773

Table D-5 Data table for San113, Room Temperature.

No. Peak	time(s)	Detector 1 (021)	(101)	(130)	(131)	(112)	Detector 2 (021)	(101)	(130)	(131)	(112)
AN113.003	53550	3.88906	3.73286	2.77198	2.5148	2.46329	3.88851	3.72121	2.77382	2.51709	2.46291
AN113.004	69446	3.75715	3.64149	2.68644	2.44089	2.39823	3.75854	3.63889	2.68646	2.44174	2.39584
AN113.005	70989	3.76174	3.64781	2.68622	2.43726	2.39415	3.75839	3.64666	2.68773	2.43954	2.39553
AN113.006	72135	3.76212	3.64704	2.68651	2.43679	2.39296	3.76052	3.64653	2.68909	2.44172	2.39564
AN113.007	73384	3.75973	3.64905	2.68462	2.43598	2.39429	3.76166	3.64863	2.68434	2.4405	2.39615
AN113.008	74371	3.74894	3.63606	2.68211	2.43815	2.39649	3.75767	3.63583	2.68383	2.44018	2.39668
AN113.009	78110	3.73898	3.63022	2.66914	2.4225	2.39107	3.73671	3.627	2.67058	2.42391	2.38484
AN113.010	79485	3.73677	3.62842	2.66694	2.41509	2.3856	3.73437	3.629	2.66964	2.42178	2.3843
AN113.011	81568	3.73158	3.62463	2.66717	2.41887	2.38078	3.73452	3.62783	2.66971	2.42421	2.38657
AN113.012	83440	3.73189	3.62357	2.66752	2.4218	2.38514	3.73247	3.62853	2.66903	2.42527	2.38539
AN113.013	84480	3.73667	3.63052	2.67351	2.42643	2.38695	3.74034	3.6379	2.67309	2.42906	2.39024
AN113.014	85384	3.73744	3.63045	2.67397	2.42746	2.3873	3.74168	3.64521	2.67533	2.42984	2.39087
AN113.015	86672	3.77418	3.66248	2.69074	2.43563	2.40343	3.77235	3.65294	2.69535	2.43845	2.40523
AN113.016	88161	3.75549	3.64731	2.67991	2.43045	2.39368	3.74796	3.64724	2.68283	2.43073	2.39295
AN113.017	88832	3.74629	3.64265	2.67957	2.43143	2.39486	3.74431	3.64293	2.68112	2.43076	2.39049
AN113.018	89281	3.74408	3.6436	2.6803	2.43191	2.39692	3.74502	3.64014	2.68109	2.43265	2.39411
AN113.019	90211	3.73946	3.64269	2.67817	2.43106	2.4009	3.7426	3.64207	2.6794	2.4299	2.39323
AN113.020	91614	3.7394	3.63312	2.6775	2.43024	2.39174	3.73626	3.63015	2.68119	2.43113	2.40309
AN113.021	92656	3.7402	3.63205	2.67929	2.42989	2.39177	3.73445	3.63208	2.68193	2.43241	2.39869
AN113.022	93746	3.74378	3.63506	2.68161	2.43206	2.39561	3.74123	3.64106	2.68234	2.43249	2.3968
AN113.023	94302	3.74817	3.64582	2.68235	2.43275	2.39434	3.74567	3.63994	2.68343	2.43305	2.39508
AN113.024	95170	3.74604	3.64204	2.6804	2.43438	2.39831	3.74533	3.65735	2.68076	2.43135	2.39831

Detector 4					τ (GPa)				
(021)	(101)	(130)	(131)	(112)	(021)	(101)	(130)	(131)	(112)
3.89124	3.72611	2.7689	2.51546	2.45891	0.09	-0.04	-0.21	-0.03	-0.27
3.83851	3.695	2.739	2.48912	2.43699	3.12	2.73	3.07	2.98	2.73
3.84103	3.69399	2.74119	2.49638	2.43132	3.12	2.33	3.16	3.58	2.52
3.84192	3.6958	2.74253	2.49032	2.43096	3.11	2.43	3.19	3.18	2.53
3.84442	3.69561	2.74299	2.47886	2.42597	3.22	2.32	3.41	2.57	2.14
3.84578	3.69823	2.74025	2.49196	2.43685	3.56	3.10	3.35	3.28	2.76
3.85284	3.70135	2.74562	2.4899	2.44184	4.44	3.62	4.44	4.20	3.69
3.85729	3.70728	2.74958	2.49318	2.44798	4.68	3.89	4.75	4.70	4.29
3.86077	3.70943	2.75344	2.49687	2.45066	4.90	4.12	4.94	4.71	4.54
3.86843	3.71552	2.75813	2.50058	2.45389	5.20	4.41	5.19	4.78	4.63
3.86915	3.71441	2.75785	2.50199	2.45257	4.97	3.94	4.87	4.59	4.31
3.86961	3.71601	2.75756	2.50073	2.45345	4.94	3.83	4.78	4.46	4.33
3.86813	3.71704	2.7532	2.49558	2.44803	3.56	2.88	3.45	3.63	2.93
3.87812	3.72975	2.76055	2.50478	2.45634	4.74	3.98	4.53	4.56	4.21
3.87316	3.7229	2.7593	2.50416	2.45579	4.83	3.89	4.52	4.49	4.23
3.87139	3.72358	2.75829	2.50391	2.45534	4.80	3.97	4.45	4.40	4.00
3.87032	3.72501	2.75856	2.50133	2.45614	4.91	4.01	4.58	4.37	3.94
3.86851	3.72253	2.75833	2.50003	2.45592	4.97	4.44	4.53	4.29	3.90
3.86782	3.72225	2.75612	2.49825	2.45203	4.97	4.41	4.34	4.16	3.81
3.86552	3.71839	2.75586	2.49766	2.45007	4.68	3.93	4.25	4.05	3.62
3.86658	3.71231	2.75395	2.49941	2.44863	4.54	3.41	4.09	4.11	3.64
3.86607	3.71646	2.75454	2.50182	2.45186	4.58	3.25	4.26	4.25	3.59

τ (GPa) (average)	P (Gpa)	Strain	T(K)
-0.09	0.00		298
2.93	7.11		298
2.94	7.74		298
2.89	7.29		298
2.73	6.39	8.22%	298
3.21	7.31	10.77%	298
4.08	6.42	14.92%	298
4.46	5.59	17.80%	298
4.64	5.53	24.58%	298
4.84	5.09	28.57%	298
4.54	5.18	30.65%	298
4.47	4.92	31.68%	298
3.29	3.84	44.05%	298
4.40	4.20	45.89%	298
4.39	4.48	47.73%	298
4.33	4.54	49.00%	298
4.36	4.05	51.80%	298
4.43	3.87	55.79%	298
4.34	4.38	58.34%	298
4.11	4.45	61.29%	298
3.96	5.14	62.73%	298
3.99	5.02	65.20%	298

Table D-6 Data table for San114, 500°C.

No. Peak	time(s)	Detector 1 (021)	(101)	(130)	(131)	(112)	Detector 2 (021)	(101)	(130)	(131)
AN114.003	53502	3.88331	3.72344	2.76937	2.51491	2.45539	3.89246	3.7232	2.7697	2.51221
AN114.004	71663	3.85438	3.69803	2.74884	2.49498	2.44288	3.85994	3.69721	2.74677	2.49377
AN114.005	75445	3.84487	3.69928	2.7453	2.4833	2.43863	3.84433	3.69696	2.74527	2.4848
AN114.006	76071	3.84925	3.69355	2.74941	2.49254	2.44416	3.85011	3.70162	2.74522	2.49494
AN114.007	76616	3.85601	3.69928	2.74981	2.49594	2.44825	3.85438	3.70681	2.74974	2.49753
AN114.008	77070	3.86093	3.70556	2.7532	2.49922	2.45076	3.85776	3.70833	2.75282	2.49989
AN114.009	77559	3.8693	3.71363	2.75893	2.50403	2.45501	3.86379	3.71414	2.75794	2.50435
AN114.010	78021	3.88014	3.72246	2.76528	2.50926	2.45988	3.87236	3.72143	2.76497	2.50975
AN114.011	79154	3.89124	3.73349	2.77781	2.51931	2.4677	3.88874	3.71729	2.78294	2.52038
AN114.012	79677	3.897	3.74209	2.77707	2.52272	2.47295	3.89697	3.73482	2.77905	2.51997
AN114.013	92637	3.88603	3.744	2.77378	2.51806	2.4656	3.88955	3.72615	2.76106	2.52944
AN114.014	95575	3.87843	3.73799	2.7749	2.51858	2.46905	3.89429	3.7187	2.77354	2.51987
AN114.015	96704	3.87764	3.73687	2.77425	2.51973	2.46916	3.8947	3.71763	2.77308	2.51905
AN114.016	97611	3.87736	3.73649	2.77391	2.51982	2.46868	3.89384	3.71778	2.77308	2.51882
AN114.017	98291	3.87694	3.73659	2.77381	2.51842	2.46843	3.89448	3.72047	2.77315	2.52049
AN114.018	99297	3.87667	3.73616	2.77281	2.51642	2.46744	3.8933	3.71885	2.77228	2.52046
AN114.019	100270	3.87149	3.72968	2.76991	2.51351	2.46371	3.88601	3.71197	2.77002	2.51538
AN114.020	101227	3.86685	3.70809	2.75863	2.50131	2.45204	3.86333	3.70106	2.74594	2.50415
AN114.021	102174	3.84011	3.68886	2.73474	2.48493	2.43942	3.83511	3.68224	2.73255	2.48051
AN114.022	103293	3.82118	3.69363	2.72853	2.47688	2.43392	3.81546	3.67538	2.72357	2.47124
AN114.023	103776	3.81932	3.69119	2.72451	2.47643	2.43384	3.80512	3.67689	2.72021	2.46987
AN114.024	104474	3.8158	3.69001	2.71869	2.46803	2.42443	3.807	3.67884	2.71726	2.46926
AN114.025	106013	3.80796	3.68273	2.71653	2.47042	2.42689	3.80258	3.6822	2.71802	2.47271
AN114.026	106441	3.80635	3.67897	2.71776	2.46619	2.42576	3.7994	3.68065	2.71565	2.47182

No. Peak	time(s)	Detector 1					Detector 2			
		(021)	(101)	(130)	(131)	(112)	(021)	(101)	(130)	(131)
AN114.027	106850	3.80614	3.68127	2.7173	2.46532	2.42531	3.79758	3.67967	2.71522	2.47037
AN114.028	107244	3.80285	3.68213	2.71634	2.46704	2.4262	3.79647	3.67699	2.71483	2.46932
AN114.029	109844	3.80041	3.684	2.7137	2.46655	2.42873	3.79179	3.67734	2.71251	2.46194
AN114.030	110296	3.79806	3.68402	2.71366	2.46741	2.43093	3.78961	3.67504	2.71141	2.46149
AN114.031	110790	3.79488	3.68219	2.7132	2.46661	2.43113	3.79146	3.67565	2.7113	2.46075
AN114.032	111272	3.79319	3.68087	2.71385	2.46501	2.4279	3.79025	3.6772	2.7111	2.46047
AN114.033	111932	3.79518	3.67772	2.71254	2.46373	2.42105	3.79084	3.67685	2.71243	2.46218
AN114.034	112804	3.79324	3.68146	2.712	2.46184	2.42359	3.79221	3.67916	2.71189	2.46354
AN114.035	113467	3.79292	3.68179	2.71211	2.46285	2.42461	3.79152	3.67815	2.71139	2.46199
AN114.036	114032	3.79157	3.67931	2.71116	2.46172	2.42467	3.79199	3.6753	2.7105	2.4611
AN114.037	114658	3.79106	3.68152	2.71086	2.46292	2.42635	3.79217	3.67575	2.71031	2.46107
AN114.038	115053	3.79768	3.68907	2.71422	2.46591	2.42903	3.79889	3.6781	2.71315	2.4647
AN114.039	115501	3.79559	3.68646	2.71264	2.46388	2.42972	3.79698	3.68139	2.7119	2.46329
AN114.040	116366	3.79998	3.68794	2.71127	2.4649	2.43093	3.79741	3.68293	2.7112	2.46265
AN114.041	116812	3.79716	3.68679	2.71088	2.46409	2.42871	3.79614	3.68602	2.71074	2.46173
AN114.042	117328	3.79826	3.68691	2.71014	2.46551	2.43357	3.79569	3.68072	2.70949	2.46222
AN114.043	117858	3.79729	3.68213	2.71016	2.46763	2.43497	3.7952	3.68478	2.70838	2.46129
AN114.044	118411	3.78686	3.67662	2.71109	2.46509	2.42496	3.78353	3.67735	2.71082	2.46021
AN114.045	118995	3.78911	3.67344	2.71127	2.46337	2.424	3.78281	3.67832	2.71076	2.45991
AN114.046	119672	3.79025	3.67557	2.71198	2.45837	2.41672	3.78445	3.68151	2.71004	2.46239
AN114.047	120594	3.78818	3.67858	2.71321	2.46439	2.43474	3.79564	3.69326	2.70817	2.46102
AN114.048	121203	3.79391	3.68264	2.71508	2.46575	2.43664	3.79318	3.69605	2.70914	2.46436
AN114.049	122296	3.79847	3.68946	2.71253	2.4738	2.43572	3.80915	3.68965	2.70906	2.45698
AN114.050	122922	3.80249	3.69203	2.71359	2.47321	2.43788	3.81461	3.69426	2.70511	2.459
AN114.051	123512	3.80695	3.69467	2.71417	2.44866	2.42162	3.81746	3.70082	2.71067	2.46191

No. Peak	time(s)	Detector 1					Detector 2			
		(021)	(101)	(130)	(131)	(112)	(021)	(101)	(130)	(131)
AN114.052	124124	3.80792	3.69533	2.71408	2.47261	2.44555	3.81927	3.70184	2.70365	2.46278
AN114.053	124734	3.80812	3.6997	2.71403	2.44925	2.41448	3.81566	3.69854	2.71069	2.44923
AN114.054	125413	3.8043	3.70275	2.71434	2.44313	2.41306	3.79536	3.68295	2.71598	2.45569
AN114.055	126000	3.79986	3.68731	2.70752	2.45097	2.41575	3.79017	3.6787	2.70552	2.4548
AN114.056	126600	3.80828	3.69595	2.70892	2.4494	2.41875	3.79437	3.68318	2.70635	2.45582
AN114.057	127208	3.81855	3.69335	2.71143	2.45863	2.42171	3.79785	3.67641	2.70993	2.45777

(Continued)

Detector 4						τ (GPa)				
(112)	(021)	(101)	(130)	(131)	(112)	(021)	(101)	(130)	(131)	(112)
2.46022	3.88768	3.72608	2.77437	2.51367	2.45871	-0.01	0.13	0.26	0.01	0.06
2.4445	3.82766	3.67565	2.73204	2.47192	2.4251	-1.10	-1.09	-0.90	-1.38	-1.25
2.43816	3.85655	3.7011	2.75115	2.49141	2.4459	0.44	0.14	0.33	0.44	0.49
2.44708	3.8593	3.70343	2.7491	2.50415	2.45089	0.35	0.28	0.10	0.61	0.34
2.44923	3.86157	3.70951	2.7525	2.50199	2.45284	0.23	0.31	0.15	0.31	0.27
2.45161	3.86778	3.7138	2.75642	2.50518	2.45624	0.30	0.33	0.19	0.33	0.33
2.45495	3.87459	3.71917	2.76098	2.50839	2.4594	0.29	0.25	0.14	0.24	0.28
2.45952	3.88075	3.72168	2.7654	2.51221	2.46257	0.16	-0.01	0.01	0.16	0.18
2.46578	3.89481	3.7342	2.77655	2.5207	2.46905	0.17	0.41	-0.20	0.05	0.14
2.47323	3.90106	3.74617	2.7827	2.52412	2.47323	0.14	0.35	0.24	0.16	0.01
2.46596	3.87591	3.70774	2.76191	2.50846	2.45315	-0.42	-1.29	-0.30	-0.88	-0.81
2.46726	3.87629	3.70965	2.76441	2.57389	2.51166	-0.36	-0.89	-0.53	2.90	2.58
2.46739	3.87616	3.70981	2.7643	2.51313	2.4537	-0.36	-0.83	-0.50	-0.36	-0.93
2.46732	3.87591	3.70987	2.76373	2.51337	2.45347	-0.34	-0.82	-0.53	-0.34	-0.93

Detector 4					τ (GPa)					
(112)	(021)	(101)	(130)	(131)	(112)	(021)	(101)	(130)	(131)	(112)
2.46708	3.87599	3.70993	2.76406	2.51151	2.45357	-0.34	-0.88	-0.51	-0.46	-0.91
2.46673	3.87642	3.71019	2.76338	2.51137	2.45395	-0.30	-0.82	-0.49	-0.41	-0.84
2.45631	3.88118	3.71225	2.76592	2.51294	2.45434	0.09	-0.41	-0.22	-0.09	-0.36
2.44212	3.88342	3.71561	2.76972	2.51428	2.46028	0.65	0.53	0.95	0.67	0.85
2.44014	3.88164	3.71946	2.77618	2.51267	2.46563	1.59	1.62	2.31	1.76	1.66
2.43253	3.88186	3.71742	2.77691	2.50653	2.46855	2.31	1.58	2.78	1.93	2.26
2.42998	3.88005	3.72377	2.7792	2.51567	2.46811	2.48	1.90	3.10	2.50	2.32
2.42552	3.88266	3.72579	2.77584	2.5158	2.46706	2.60	1.97	3.18	2.79	2.72
2.42416	3.88221	3.72488	2.77375	2.51345	2.46328	2.81	2.02	3.11	2.48	2.45
2.42418	3.88648	3.72379	2.77221	2.5135	2.46138	3.05	2.10	3.06	2.64	2.37
2.42327	3.88422	3.72395	2.77026	2.51396	2.46153	3.01	2.08	2.99	2.73	2.42
2.42325	3.8851	3.723	2.76921	2.51518	2.46136	3.12	2.08	2.97	2.78	2.38
2.42239	3.88274	3.72348	2.77096	2.51469	2.46022	3.18	2.05	3.21	2.99	2.26
2.42055	3.88417	3.72154	2.77171	2.51405	2.46023	3.31	2.01	3.28	2.95	2.25
2.42037	3.885	3.72033	2.7728	2.51274	2.46063	3.36	1.99	3.35	2.92	2.27
2.41995	3.88528	3.7215	2.77026	2.51113	2.45981	3.43	2.04	3.21	2.89	2.34
2.42378	3.89345	3.71862	2.76552	2.51446	2.46255	3.65	1.99	2.96	3.06	2.61
2.42392	3.88623	3.72223	2.76987	2.51425	2.46154	3.42	2.01	3.22	3.06	2.46
2.4257	3.88671	3.72807	2.77063	2.51502	2.462	3.46	2.29	3.27	3.12	2.39
2.4243	3.88602	3.72435	2.77051	2.51546	2.46166	3.45	2.25	3.31	3.21	2.42
2.42482	3.88628	3.72105	2.76737	2.51556	2.4613	3.47	2.03	3.16	3.18	2.32
2.42938	3.87939	3.72363	2.76502	2.51362	2.45969	2.98	1.91	2.86	2.87	1.98
2.42731	3.88308	3.72057	2.76432	2.51503	2.46177	3.18	1.75	2.91	3.05	2.16
2.42588	3.88843	3.7164	2.75882	2.51395	2.46162	3.27	1.49	2.68	2.98	2.16
2.42233	3.88696	3.71667	2.75906	2.51588	2.46312	3.30	1.45	2.72	3.14	2.44

Detector 4					τ (GPa)					
(112)	(021)	(101)	(130)	(131)	(112)	(021)	(101)	(130)	(131)	(112)
2.42371	3.8897	3.718	2.75908	2.51611	2.46354	3.38	1.64	2.77	3.09	2.26
2.4244	3.89014	3.71954	2.7597	2.51673	2.46439	3.42	1.73	2.84	3.09	2.24
2.4243	3.88634	3.72288	2.7705	2.50951	2.46167	3.71	2.20	3.31	2.80	2.41
2.4212	3.88585	3.72044	2.77125	2.51322	2.46344	3.67	2.14	3.34	3.07	2.65
2.42311	3.88784	3.72299	2.77147	2.51643	2.46514	3.68	2.13	3.35	3.33	2.94
2.42301	3.88823	3.72414	2.77013	2.51603	2.46495	3.52	1.82	3.30	3.16	2.33
2.42793	3.88789	3.73023	2.77151	2.51301	2.46269	3.45	1.94	3.29	2.85	1.97
2.41453	3.89148	3.72581	2.76439	2.5169	2.46358	3.18	1.72	3.00	3.05	2.49
2.42165	3.89161	3.72795	2.763	2.51814	2.46375	3.01	1.65	3.01	3.07	2.20
2.42615	3.891	3.729	2.76019	2.51684	2.46406	2.85	1.48	2.68	3.66	2.61
2.42541	3.8925	3.72961	2.75962	2.51863	2.46505	2.85	1.46	2.86	3.00	1.90
2.41955	3.89498	3.72705	2.7602	2.51721	2.46425	2.99	1.32	2.69	4.06	3.08
2.41981	3.89292	3.7253	2.77216	2.51756	2.46366	3.38	1.54	3.15	4.07	3.08
2.4177	3.89434	3.7298	2.77221	2.51654	2.46162	3.61	2.22	3.65	3.80	2.94
2.41782	3.89458	3.72902	2.77223	2.51731	2.46221	3.38	1.87	3.59	3.86	2.87
2.41916	3.89639	3.73348	2.77448	2.51916	2.46452	3.18	2.30	3.53	3.61	2.86

(Continued)

τ (GPa) (average)	P (GPa)	Strain	T(K)
0.09	0.00		298
-1.14	4.41		298
0.37	9.48		1473
0.34	8.42		1173
0.25	7.60		1173
0.29			
0.24			
0.10			
0.11			
0.18			
-0.74			
0.74			
-0.60	3.27	-0.09%	773
-0.59	3.36	0.09%	773
-0.62	3.25	0.00%	773
-0.57	3.31	0.09%	773
-0.20	3.41	0.28%	773
0.73	3.64	0.37%	773
1.79	2.63	1.21%	773
2.17	1.38	2.52%	773
2.46	2.90	4.01%	773
2.65	3.83	5.50%	773
2.57	4.36	9.70%	773
2.64	4.65	11.10%	773
2.65	4.92	12.31%	773

τ(GPa) (average)	P (GPa)	Strain	T(K)
2.67	5.20	13.62%	773
2.74	4.98	21.27%	773
2.76	4.86	22.67%	773
2.78	4.51	24.07%	773
2.78	4.75	25.47%	773
2.85	5.50	27.71%	773
2.83	5.03	30.04%	773
2.91	4.91	31.81%	773
2.93	5.03	33.30%	773
2.83	5.42	34.98%	773
2.52	5.47	37.78%	773
2.61	5.52	38.15%	773
2.51	6.04	38.99%	773
2.61	6.09	40.95%	773
2.63	6.00	42.07%	773
2.66	5.90	43.28%	773
2.89	4.40	44.96%	773
2.97	4.63	46.46%	773
3.09	4.85	47.57%	773
2.83	4.73	49.53%	773
2.70	4.32	51.21%	773
2.69	5.72	53.64%	773
2.59	5.76	54.57%	773
2.66	5.77	55.78%	773
2.41	5.72	56.90%	773

τ(GPa) (average)	P (GPa)	Strain	T(K)
2.83	5.85	58.12%	773
3.04	4.24	59.14%	773
3.24	5.11	60.45%	773
3.11	4.98	61.75%	773
3.10	4.69	63.43%	773

Table D-7A Data table for San122, Coarse grain.

No.		Detector 1					Detector 2			
Peak	Time(s)	(021)	(101)	(130)	(131)	(112)	(021)	(101)	(130)	(131)
22\mca\SAN122.003		3.89185	3.72243	2.77508	2.5242	2.46421	3.88218	3.72256	2.7705	2.5235
SAN_122_00011.med	12742	3.82407	3.69911	2.73313	2.48097	2.43079	3.83517	3.6924	2.73607	2.48179
SAN_122_00013.med	13888	3.82061	3.69454	2.73627	2.47968	2.43145	3.83475	3.68904	2.73484	2.48266
SAN_122_00015.med	14690	3.81952	3.69394	2.73057	2.47543	2.42985	3.82754	3.68319	2.72826	2.47633
SAN_122_00017.med	15336	3.80829	3.68525	2.72114	2.46825	2.42782	3.81777	3.68009	2.72245	2.47192
SAN_122_00020.med	16898	3.7966	3.6721	2.71226	2.46318	2.41473	3.79971	3.67376	2.71282	2.46232
SAN_122_00022.med	17543	3.79508	3.6717	2.71021	2.46075	2.41621	3.79597	3.67246	2.70962	2.46107
SAN_122_00024.med	18200	3.79216	3.67161	2.7096	2.45783	2.41554	3.79511	3.67314	2.70961	2.45993
SAN_122_00026.med	18834	3.79063	3.66876	2.70813	2.45846	2.4148	3.79043	3.66995	2.70938	2.45984
SAN_122_00028.med	19483	3.78905	3.66942	2.70904	2.45709	2.41431	3.78815	3.66678	2.70883	2.45889
SAN_122_00030.med	20119	3.78712	3.66969	2.70691	2.45627	2.41398	3.7886	3.66379	2.70925	2.46002
SAN_122_00032.med	20754	3.78593	3.67279	2.70486	2.45745	2.41494	3.79206	3.66521	2.70901	2.46053
SAN_122_00034.med	21391	3.78631	3.6722	2.70452	2.45582	2.41413	3.78986	3.66505	2.70723	2.46047
SAN_122_00036.med	22032	3.78524	3.67222	2.70293	2.45548	2.41546	3.78852	3.66418	2.70509	2.45999
SAN_122_00038.med	22662	3.78532	3.67074	2.70239	2.45644	2.41567	3.78573	3.66751	2.70418	2.45944
SAN_122_00040.med	23293	3.7871	3.6721	2.70566	2.45719	2.41697	3.78891	3.67066	2.70715	2.46107

No.	Detector 1					Detector 2				
Peak	Time(s)	(021)	(101)	(130)	(131)	(112)	(021)	(101)	(130)	(131)
SAN_122_00042.med	23933	3.79185	3.67424	2.70855	2.45996	2.42033	3.79379	3.6714	2.70859	2.4631
SAN_122_00044.med	24571	3.79725	3.67922	2.71228	2.46341	2.42374	3.80112	3.67566	2.7135	2.46439
SAN_122_00046.med	25172	3.80647	3.68194	2.71646	2.46686	2.42751	3.80621	3.67835	2.71639	2.46703
SAN_122_00048.med	27898	3.83307	3.70288	2.73571	2.48686	2.44399	3.8236	3.68703	2.72815	2.48375
SAN_122_00052.med	29450	3.83531	3.70002	2.7357	2.48544	2.44119	3.83088	3.69166	2.73275	2.48677
SAN_122_00054.med	30126	3.83857	3.70058	2.73565	2.4854	2.44297	3.83325	3.6908	2.73452	2.48723
SAN_122_00056.med	30783	3.84133	3.70351	2.73708	2.48602	2.44463	3.83753	3.69387	2.73619	2.48883
SAN_122_00058.med	31505	3.8491	3.70422	2.74213	2.49157	2.44803	3.84579	3.69788	2.74142	2.49258
SAN_122_00060.med	32152	3.85488	3.7072	2.74579	2.49511	2.45058	3.85257	3.70174	2.74605	2.49559
SAN_122_00062.med	32820	3.86076	3.70876	2.75012	2.49787	2.45217	3.85721	3.70559	2.7504	2.498
SAN_122_00064.med	33457	3.86248	3.71022	2.75202	2.49877	2.45235	3.85978	3.70795	2.75266	2.49948
SAN_122_00067.med	35106	3.85654	3.71036	2.75037	2.49635	2.45059	3.85316	3.70511	2.75016	2.49721
SAN_122_00069.med	35786	3.85617	3.70919	2.7505	2.49526	2.45073	3.85018	3.70394	2.74849	2.49633
SAN_122_00071.med	36502	3.85949	3.71149	2.75087	2.49792	2.45294	3.8542	3.7057	2.74994	2.49851
SAN_122_00073.med	37147	3.86335	3.71182	2.75363	2.50102	2.4549	3.85874	3.70742	2.75239	2.50114
SAN_122_00075.med	37792	3.86898	3.71494	2.757	2.50375	2.45684	3.86365	3.70963	2.7558	2.50369
SAN_122_00077.med	40435	3.88284	3.72369	2.7666	2.51205	2.46309	3.87852	3.71864	2.76454	2.51144
SAN_122_00079.med	40845	3.88517	3.72662	2.76803	2.51333	2.46429	3.8805	3.71945	2.76542	2.5123
SAN_122_00081.med	41205	3.8941	3.73267	2.77356	2.51852	2.46924	3.88903	3.72783	2.77107	2.5176
SAN_122_00083.med	41560	3.9189	3.74878	2.79054	2.53369	2.48116	3.91224	3.74854	2.78957	2.53258
AN_122_00086.med	42506	3.92319	3.75114	2.79324	2.53706	2.48371	3.91684	3.7511	2.79317	2.53647
AN_122_00088.med	42895	3.92152	3.74846	2.79136	2.53448	2.48103	3.91345	3.74722	2.79098	2.53386
AN_122_00090.med	43260	3.91731	3.74685	2.78835	2.53246	2.48143	3.91025	3.74415	2.78805	2.53159
AN_122_00092.med	44079	3.90792	3.74117	2.7823	2.52528	2.47541	3.89843	3.73509	2.78096	2.52572
AN_122_00094.med	44921	3.90538	3.73472	2.78233	2.52604	2.47463	3.90073	3.73272	2.78316	2.52569

(Continued)

Detector 3					Detector 4					
(112)	(021)	(101)	(130)	(131)	(112)	(021)	(101)	(130)	(131)	(112)
2.46377	3.89449	3.74291	2.77229	2.51829	2.46365	3.89086	3.73105	2.77505	2.52033	2.46433
2.44009	3.85699	3.70106	2.75342	2.49323	2.44376	3.85876	3.7006	2.74605	2.49739	2.44803
2.44161	3.85678	3.70465	2.75177	2.49322	2.44438	3.86039	3.70141	2.74827	2.49715	2.44747
2.43535	3.85612	3.70393	2.74863	2.49332	2.44438	3.8602	3.70232	2.74781	2.49729	2.4475
2.43339	3.86017	3.70759	2.7492	2.49468	2.4457	3.85836	3.701	2.74789	2.49706	2.4469
2.42047	3.85239	3.71472	2.74811	2.49579	2.4484	3.86371	3.71938	2.75367	2.49745	2.44903
2.41745	3.85571	3.72021	2.74964	2.49733	2.44945	3.86291	3.71504	2.75399	2.49933	2.44982
2.41769	3.85747	3.72076	2.75122	2.49821	2.44994	3.86221	3.71319	2.75268	2.50149	2.45074
2.41812	3.85726	3.71711	2.75247	2.49988	2.4475	3.86382	3.71439	2.7504	2.50279	2.45126
2.41622	3.85815	3.71274	2.75304	2.50115	2.44715	3.86466	3.71276	2.75035	2.50278	2.45184
2.4161	3.86162	3.71031	2.75512	2.503	2.44719	3.86955	3.71037	2.7526	2.5035	2.45189
2.417	3.86698	3.71158	2.75646	2.50452	2.449	3.87085	3.71135	2.75541	2.50347	2.45233
2.41712	3.87067	3.71275	2.75368	2.50654	2.45004	3.87237	3.71024	2.75852	2.50545	2.45325
2.41711	3.87275	3.71771	2.75048	2.50719	2.45181	3.87346	3.71748	2.75816	2.50751	2.45376
2.41729	3.87515	3.72072	2.75246	2.50996	2.45372	3.87566	3.71848	2.76041	2.5076	2.45617
2.41901	3.87864	3.72472	2.75462	2.50283	2.45364	3.87709	3.71548	2.76288	2.50744	2.45664
2.42073	3.87914	3.72162	2.75675	2.50537	2.45382	3.87821	3.72075	2.76398	2.50808	2.45764
2.42287	3.87626	3.72219	2.75678	2.5064	2.45391	3.88127	3.71952	2.76426	2.50867	2.458
2.42469	3.86996	3.718	2.7545	2.50816	2.45343	3.87826	3.72222	2.76336	2.50963	2.45854
2.44268	3.88084	3.72349	2.76115	2.50897	2.45757	3.87774	3.72465	2.76844	2.51126	2.46103
2.44349	3.88034	3.72492	2.76258	2.50954	2.45867	3.87803	3.7249	2.76975	2.51079	2.4617
2.44528	3.88399	3.72642	2.76431	2.51052	2.45967	3.88033	3.72631	2.77078	2.51187	2.46111
2.44625	3.8841	3.72594	2.76539	2.51161	2.46115	3.88144	3.72647	2.77207	2.51349	2.46204

Detector 3					Detector 4					
(112)	(021)	(101)	(130)	(131)	(112)	(021)	(101)	(130)	(131)	(112)
2.44875	3.88488	3.72642	2.76474	2.51313	2.46016	3.88176	3.72772	2.7714	2.51433	2.46208
2.45113	3.88477	3.72836	2.76437	2.51391	2.46089	3.88069	3.72768	2.77059	2.51414	2.46272
2.45203	3.8855	3.72775	2.76484	2.51457	2.4612	3.88089	3.72767	2.77098	2.51422	2.46336
2.45285	3.88658	3.73062	2.76498	2.51502	2.4618	3.88224	3.72768	2.77117	2.5146	2.46386
2.45022	3.8832	3.73013	2.76661	2.51379	2.46344	3.887	3.72932	2.7729	2.5162	2.46598
2.44936	3.8871	3.73353	2.76793	2.51492	2.46478	3.8879	3.73111	2.7734	2.51703	2.46666
2.45092	3.88895	3.73259	2.76882	2.5167	2.46575	3.88894	3.73251	2.77371	2.51788	2.46707
2.45308	3.88884	3.7345	2.76914	2.51755	2.46621	3.89002	3.73185	2.77374	2.5175	2.4673
2.45508	3.89051	3.73342	2.76977	2.51792	2.46678	3.89066	3.73021	2.77388	2.51724	2.46751
2.46158	3.89715	3.73646	2.77459	2.52097	2.46936	3.8955	3.73293	2.77723	2.52045	2.4698
2.46232	3.89868	3.73983	2.77523	2.52232	2.47039	3.89796	3.7357	2.77863	2.52163	2.47073
2.46763	3.91861	3.75693	2.78932	2.53503	2.48015	3.91878	3.75052	2.79139	2.53541	2.4827
2.47979	3.92885	3.75948	2.79573	2.54096	2.48577	3.92785	3.75817	2.79932	2.54078	2.48674
2.48334	3.92784	3.76248	2.79649	2.54034	2.48577	3.93066	3.75843	2.79841	2.54146	2.48693
2.481	3.92832	3.75904	2.79712	2.54022	2.48526	3.92908	3.75718	2.79681	2.54074	2.48647
2.47845	3.92712	3.75873	2.79649	2.53892	2.48444	3.9291	3.75893	2.79727	2.54121	2.48612
2.47347	3.92599	3.7562	2.79529	2.53793	2.48568	3.92769	3.75645	2.79797	2.53915	2.48546
2.47217	3.92159	3.74859	2.79259	2.54687	2.48324	3.92087	3.75475	2.79448	2.53676	2.48438

(Continued)

τ(GPa) (021)	(101)	(130)	(131)	(112)	τ(GPa) (average)	P (Gpa)	Strain	T(K)
0.20	0.67	0.05	-0.26	0.00	0.13	0.00		298.15
1.04	0.25	0.85	0.84	0.69	0.73	5.38	-0.14%	673.15
1.14	0.54	0.81	0.84	0.62	0.79	5.20	0.14%	674.15
1.28	0.71	1.06	1.17	0.88	1.02	5.74	0.95%	672.15
1.72	1.05	1.51	1.56	1.04	1.38	6.00	1.63%	674.15
2.24	2.13	2.18	2.06	2.07	2.13	6.36	2.44%	672.15
2.39	2.20	2.38	2.27	2.18	2.28	6.44	4.07%	671.15
2.48	2.15	2.41	2.49	2.24	2.35	6.44	5.42%	674.15
2.62	2.24	2.43	2.56	2.19	2.41	6.79	6.37%	673.15
2.73	2.17	2.43	2.66	2.28	2.45	6.80	7.99%	675.15
2.90	2.12	2.60	2.73	2.29	2.53	6.72	9.49%	674.15
2.97	2.06	2.77	2.72	2.30	2.57	6.50	11.38%	673.15
3.10	2.08	2.84	2.88	2.39	2.66	6.59	12.87%	673.15
3.20	2.39	2.86	2.99	2.42	2.77	6.80	15.04%	673.15
3.33	2.43	3.01	3.05	2.54	2.87	6.60	16.40%	683.15
3.32	2.35	2.95	2.77	2.45	2.77	6.00	17.62%	703.15
3.16	2.32	2.91	2.71	2.31	2.69	5.89	19.24%	723.15
2.92	2.08	2.67	2.61	2.14	2.49	5.82	20.87%	753.15
2.49	1.92	2.38	2.50	1.96	2.25	5.98	21.54%	763.15
1.85	1.38	1.81	1.46	1.03	1.51	4.82	27.37%	853.15
1.67	1.38	1.76	1.42	1.15	1.47	4.65	30.62%	873.15
1.67	1.45	1.78	1.46	1.05	1.48	4.50	32.11%	883.15
1.56	1.30	1.76	1.47	1.04	1.43	4.46	33.20%	903.15

τ(GPa) (021)	(101)	(130)	(131)	(112)	τ(GPa) (average)	P (Gpa)	Strain	T(K)
1.29	1.23	1.44	1.26	0.82	1.21	4.59	34.42%	923.15
1.04	1.11	1.18	1.09	0.70	1.02	4.68	59.89%	948.15
0.86	0.97	0.96	0.96	0.65	0.88	4.53		968.15
0.83	0.94	0.85	0.91	0.65	0.84	4.41		968.15
1.08	1.03	1.06	1.06	0.91	1.03	4.22		963.15
1.22	1.21	1.15	1.17	1.00	1.15	4.14		973.15
1.14	1.12	1.13	1.10	0.92	1.08	4.28		1003.15
1.01	1.10	1.00	0.95	0.81	0.97	4.20		1013.15
0.86	0.91	0.83	0.80	0.71	0.82	4.14		1033.15
0.55	0.63	0.55	0.51	0.45	0.54	3.78		1113.15
0.54	0.68	0.54	0.52	0.45	0.55	3.81		1133.15
0.93	1.07	0.94	0.96	0.80	0.94	2.57		1173.15
0.43	0.46	0.38	0.42	0.35	0.41	1.65		1253.15
0.31	0.42	0.22	0.23	0.17	0.27	1.46		1243.15
0.38	0.46	0.30	0.35	0.29	0.36	1.48		1233.15
0.48	0.60	0.45	0.44	0.32	0.46	1.50		1213.15
0.80	0.83	0.77	0.72	0.68	0.76	1.46		1183.15
0.62	0.82	0.56	0.88	0.64	0.70	1.58		1153.15

Table D-7B Data table for San122, fine grain.

No.		Detector 1					Detector 2			
Peak	Time(s)	(021)	(101)	(130)	(131)	(112)	(021)	(101)	(130)	(131)
22\mca\SAN122.002		3.89261	3.72413	2.77508	2.51628	2.46308	3.88926	3.72431	2.77332	2.5193
SAN_122_00012.med	13586	3.82906	3.68954	2.73218	2.48167	2.43455	3.82817	3.68651	2.73187	2.48191
SAN_122_00014.med	14388	3.82577	3.68723	2.72944	2.47912	2.43274	3.82345	3.6828	2.72885	2.47902
SAN_122_00016.med	15034	3.8176	3.68332	2.72297	2.4734	2.42781	3.81557	3.67729	2.72301	2.47365
SAN_122_00018.med	15670	3.80973	3.68084	2.71713	2.46947	2.42421	3.80806	3.67598	2.71808	2.46899
SAN_122_00019.med	16596	3.79981	3.6751	2.7112	2.46495	2.42016	3.80032	3.67295	2.70897	2.46488
SAN_122_00021.med	17240	3.79783	3.6746	2.70882	2.46348	2.41911	3.79697	3.67141	2.70888	2.46337
SAN_122_00023.med	17897	3.79612	3.67253	2.70792	2.46174	2.41863	3.79571	3.67071	2.70833	2.46167
SAN_122_00025.med	18532	3.79715	3.67183	2.70814	2.46107	2.41899	3.79755	3.67155	2.70889	2.46262
SAN_122_00027.med	19181	3.79734	3.67301	2.70843	2.53602	2.46148	3.7981	3.66924	2.70925	2.46358
SAN_122_00029.med	19817	3.79909	3.67513	2.70837	2.46331	2.4216	3.79882	3.67204	2.70948	2.46426
SAN_122_00031.med	20451	3.79991	3.67361	2.70945	2.46503	2.42263	3.79871	3.67437	2.71087	2.46626
SAN_122_00033.med	21089	3.79935	3.67491	2.70911	2.46611	2.42288	3.79922	3.67173	2.71153	2.46603
SAN_122_00035.med	21729	3.7999	3.67318	2.70937	2.4657	2.42192	3.80044	3.67303	2.7106	2.4669
SAN_122_00037.med	22360	3.7983	3.67562	2.7094	2.46524	2.4213	3.79834	3.67237	2.71086	2.46691
SAN_122_00039.med	22990	3.79997	3.67543	2.71166	2.46681	2.42262	3.80159	3.67296	2.7128	2.46831
SAN_122_00041.med	23630	3.80588	3.67648	2.71392	2.46986	2.42494	3.80727	3.67611	2.71495	2.4707
SAN_122_00043.med	24268	3.81131	3.6798	2.71865	2.47179	2.42694	3.81232	3.68034	2.71973	2.4726
SAN_122_00045.med	24919	3.81449	3.68115	2.72218	2.47494	2.42982	3.81696	3.68218	2.72335	2.47606
SAN_122_00047.med	27645	3.84155	3.7037	2.73843	2.48784	2.44081	3.82792	3.68522	2.73182	2.48306
SAN_122_00049.med	28250	3.84601	3.69933	2.74058	2.48945	2.44225	3.83388	3.68825	2.73606	2.48557
SAN_122_00050.med	29014	3.84579	3.69986	2.74197	2.49276	2.44334	3.83782	3.69302	2.73966	2.48917
SAN_122_00051.med	29198	3.84423	3.69928	2.74139	2.49119	2.44202	3.83865	3.69394	2.73938	2.48862

No.	Detector 1					Detector 2				
Peak	Time(s)	(021)	(101)	(130)	(131)	(112)	(021)	(101)	(130)	(131)
SAN_122_00053.med	29823	3.84284	3.69847	2.74002	2.49062	2.44232	3.83852	3.6932	2.73931	2.48945
SAN_122_00055.med	30480	3.84821	3.70264	2.74269	2.49211	2.44435	3.84082	3.69649	2.74066	2.49072
SAN_122_00057.med	31202	3.85169	3.70591	2.74567	2.4963	2.44719	3.84545	3.70004	2.74492	2.49551
SAN_122_00059.med	31849	3.85884	3.71101	2.74983	2.49952	2.449	3.85072	3.70068	2.74839	2.49865
SAN_122_00061.med	32517	3.86316	3.71225	2.75231	2.50258	2.45121	3.85434	3.70372	2.75054	2.50114
SAN_122_00063.med	33155	3.86724	3.72002	2.75382	2.50244	2.45367	3.8571	3.70342	2.75064	2.50174
SAN_122_00065.med	33827	3.85417	3.7078	2.75531	2.51273	2.45469	3.85712	3.69089	2.74943	2.51106
SAN_122_00066.med	34803	3.85391	3.71541	2.74214	2.51269	2.45354	3.85619	3.71541	2.74214	2.51188
SAN_122_00068.med	35483	3.85351	3.7096	2.74064	2.51154	2.45306	3.8528	3.71017	2.74834	2.50881

Continued

Detector 3					Detector 4					
(112)	(021)	(101)	(130)	(131)	(112)	(021)	(101)	(130)	(131)	(112)
2.46382	3.89696	3.72911	2.77133	2.51951	2.46322	3.89516	3.73142	2.77587	2.52051	2.46627
2.43438	3.85499	3.70504	2.74233	2.49576	2.44627	3.84573	3.70371	2.74334	2.49238	2.44435
2.43222	3.85606	3.70836	2.74257	2.49618	2.44677	3.8473	3.70658	2.74509	2.49238	2.4449
2.42747	3.85383	3.70948	2.7445	2.49688	2.44764	3.85018	3.70631	2.74596	2.49381	2.4461
2.42543	3.85394	3.70655	2.74539	2.4978	2.44799	3.8507	3.70766	2.74689	2.49425	2.44664
2.4218	3.85644	3.7082	2.74709	2.49701	2.44735	3.85178	3.70387	2.7482	2.49457	2.44637
2.42052	3.85938	3.71042	2.74684	2.49735	2.44774	3.85177	3.70493	2.7468	2.49525	2.44657
2.42074	3.85314	3.70695	2.74687	2.49714	2.44721	3.85253	3.70535	2.74665	2.49476	2.44566
2.42184	3.85424	3.70933	2.74596	2.49896	2.44773	3.85063	3.70383	2.74714	2.49533	2.44592
2.42407	3.85883	3.70475	2.74587	2.4993	2.44749	3.84849	3.70425	2.74599	2.49543	2.44579

Detector 3					Detector 4					
(112)	(021)	(101)	(130)	(131)	(112)	(021)	(101)	(130)	(131)	(112)
2.42282	3.857	3.70956	2.74647	2.49905	2.44767	3.85006	3.70303	2.74603	2.49567	2.44612
2.42458	3.85667	3.71324	2.74602	2.49902	2.44766	3.85138	3.70254	2.74594	2.49621	2.44641
2.42306	3.85931	3.72106	2.7473	2.49977	2.4488	3.85114	3.70823	2.74604	2.49672	2.4477
2.42461	3.85697	3.71338	2.74832	2.49954	2.4488	3.85265	3.70779	2.74876	2.49535	2.44692
2.42547	3.85875	3.71201	2.74698	2.50033	2.4494	3.853	3.70755	2.74734	2.49716	2.44778
2.425	3.85825	3.7132	2.74962	2.50182	2.45055	3.8547	3.70525	2.74854	2.49869	2.44839
2.42707	3.86404	3.71944	2.74961	2.50248	2.451	3.85714	3.70975	2.75069	2.49735	2.4485
2.42885	3.86214	3.7175	2.75137	2.50211	2.45122	3.85752	3.71037	2.75142	2.49831	2.45014
2.43123	3.86465	3.71653	2.75075	2.50373	2.45173	3.85668	3.70934	2.75128	2.49777	2.44997
2.43492	3.8686	3.72059	2.75276	2.50669	2.45547	3.86441	3.71472	2.75245	2.50321	2.45332
2.43854	3.86785	3.72325	2.75107	2.50658	2.45472	3.8618	3.71489	2.75197	2.50298	2.45366
2.44033	3.87128	3.72699	2.74939	2.50624	2.45412	3.86189	3.71671	2.74972	2.50239	2.45181
2.4401	3.87134	3.72171	2.74937	2.50783	2.45448	3.86198	3.71397	2.75208	2.50113	2.45139
2.44135	3.87298	3.72322	2.7515	2.50839	2.45512	3.86359	3.71585	2.75455	2.50312	2.45261
2.4425	3.86989	3.71817	2.75282	2.50966	2.45681	3.8646	3.71563	2.75573	2.50374	2.45399
2.44566	3.87266	3.72111	2.75253	2.50849	2.45691	3.86681	3.71491	2.75645	2.50765	2.45557
2.44822	3.87378	3.71788	2.75618	2.5115	2.45737	3.87015	3.72087	2.75702	2.5074	2.45596
2.45001	3.87253	3.72324	2.75611	2.51126	2.45798	3.87334	3.72078	2.75793	2.50871	2.4573
2.45061	3.87758	3.71661	2.75629	2.5114	2.45768	3.87199	3.72557	2.76057	2.51005	2.45865
2.45391	3.89097	3.71465	2.76058	2.51323	2.46513	3.87747	3.72204	2.76058	2.51403	2.46309
2.45261	3.90263	3.73228	2.77536	2.51349	2.46398	3.88921	3.72716	2.77536	2.51499	2.46494
2.45191	3.87098	3.72494	2.77579	2.51253	2.46429	3.87673	3.71832	2.77579	2.51439	2.46451

(Continued)

τ(GPa) (021)	(101)	(130)	(131)	(112)	τ(GPa) (average)	P (GPa)	Strain	T(K)
0.18	0.28	-0.03	0.13	0.08	0.13	0		298.15
0.81	0.79	0.61	0.74	0.72	0.73		0.55%	673.15
1.01	1.09	0.83	0.92	0.88	0.95		0.36%	673.15
1.32	1.34	1.26	1.32	1.27	1.30		0.36%	672.15
1.63	1.39	1.62	1.62	1.49	1.55		1.09%	674.15
2.03	1.56	2.14	1.88	1.72	1.87		3.28%	672.15
2.18	1.69	2.17	2.00	1.82	1.97		4.56%	671.15
2.14	1.68	2.21	2.09	1.78	1.98		6.57%	671.15
2.07	1.70	2.18	2.15	1.76	1.97		8.76%	673.15
2.10	1.63	2.12	-0.14	0.25	1.19		11.86%	670.15
2.05	1.59	2.14	2.04	1.64	1.89		14.05%	666.15
2.05	1.65	2.05	1.94	1.55	1.85		16.06%	677.15
2.10	2.00	2.08	1.95	1.68	1.96		18.61%	673.15
2.05	1.82	2.20	1.89	1.63	1.92		21.90%	673.15
2.16	1.74	2.11	1.98	1.67	1.93		23.72%	673.15
2.08	1.70	2.10	1.97	1.70	1.91		26.82%	693.15
2.01	1.85	2.03	1.79	1.57	1.85		29.93%	713.15
1.78	1.63	1.82	1.69	1.50	1.68		32.66%	743.15
1.66	1.51	1.59	1.51	1.34	1.52		34.31%	763.15
1.16	1.11	0.98	1.16	1.08	1.10		45.07%	853.15
0.91	1.21	0.74	1.02	0.90	0.95		49.09%	873.15
0.90	1.21	0.49	0.79	0.72	0.82		53.28%	873.15
0.92	1.01	0.58	0.86	0.77	0.83		54.74%	873.15

τ(GPa) (021)	(101)	(130)	(131)	(112)	τ(GPa) (average)	P (GPa)	Strain	T(K)
1.01	1.13	0.74	0.93	0.78	0.92		57.30%	878.15
0.83	0.83	0.70	0.90	0.78	0.81		61.68%	898.15
0.77	0.72	0.51	0.71	0.63	0.67		65.88%	913.15
0.62	0.64	0.41	0.61	0.52	0.56			933.15
0.51	0.66	0.31	0.47	0.45	0.48			953.15
0.45	0.44	0.34	0.50	0.39	0.43			968.15
1.02	0.91	0.45	0.10	0.62	0.62			968.15
1.44	0.67	1.80	0.11	0.72	0.95			968.15
0.75	0.56	1.69	0.19	0.76	0.79			968.15

Table D-8 Data table for San123.

No.	time(s)	Detector 1					Detector 2			
Peak		(021)	(101)	(130)	(131)	(112)	(021)	(101)	(130)	(131)
SAN__123_0002.med		3.88369	3.71378	2.76793	2.51912	2.45994	3.87953	3.71897	2.7691	2.51682
SAN__123_0004.med	18446	3.88923	3.74311	2.77264	2.52364	2.48011	3.84647	3.70495	2.77363	2.53668
SAN__123_0005.med	19157	3.87612	3.73684	2.76713	2.51782	2.4725	3.84661	3.69226	2.76617	2.53477
SAN__123_0007.med	21604	3.83524	3.68033	2.73206	2.48625	2.42883	3.83524	3.68033	2.71839	2.48199
SAN__123_0008.med	22337	3.82562	3.65863	2.73405	2.46701	2.41877	3.82562	3.61187	2.72116	2.48475
SAN__123_0009.med	22684	3.81195	3.68336	2.73528	2.46959	2.41675	3.82302	3.69951	2.72121	2.47489
SAN__123_0011.med	23474	3.80904	3.67978	2.72368	2.46889	2.41856	3.81894	3.64658	2.72269	2.4653
SAN__123_0013.med	24252	3.80577	3.68012	2.71101	2.47253	2.41472	3.81536	3.64077	2.71612	2.4809
SAN__123_0015.med	24603	3.79946	3.67634	2.70809	2.47245	2.42095	3.79835	3.62937	2.71286	2.45755

No. Peak	time(s)	Detector 1					Detector 2			
		(021)	(101)	(130)	(131)	(112)	(021)	(101)	(130)	(131)
SAN__123_0016.med	25017	3.79682	3.67378	2.70658	2.46588	2.42191	3.79686	3.67378	2.71009	2.46588
SAN__123_0017.med	25425	3.79765	3.67486	2.70803	2.46944	2.42248	3.79672	3.68237	2.70862	2.46676
SAN__123_0019.med	25724	3.80104	3.67389	2.70832	2.4687	2.42182	3.79655	3.69041	2.70827	2.46654
SAN__123_0020.med	27699	3.8044	3.67967	2.71198	2.46849	2.42567	3.7899	3.67967	2.70211	2.46711
SAN__123_0022.med	29877	3.80203	3.68905	2.7105	2.47129	2.42465	3.78612	3.66808	2.70894	2.45994
SAN__123_0024.med	30212	3.80487	3.68652	2.71264	2.46738	2.42376	3.77885	3.66394	2.7112	2.46789
SAN__123_0026.med	30538	3.80546	3.68589	2.71223	2.4668	2.42384	3.77912	3.66558	2.71108	2.46742
SAN__123_0028.med	30863	3.80521	3.68284	2.71189	2.46655	2.42375	3.77935	3.66496	2.71168	2.4678
SAN__123_0030.med	31184	3.80692	3.6849	2.712	2.4673	2.42494	3.78232	3.66931	2.71209	2.46721
SAN__123_0032.med	31514	3.80834	3.68609	2.71194	2.46727	2.42598	3.78371	3.66946	2.7127	2.46481
SAN__123_0034.med	31848	3.81063	3.69056	2.71172	2.46723	2.42779	3.7912	3.67915	2.71348	2.46447
SAN__123_0036.med	32184	3.81395	3.69197	2.71257	2.46683	2.42894	3.79976	3.68372	2.71356	2.4642
SAN__123_0038.med	32513	3.81441	3.69784	2.71266	2.46772	2.4282	3.80339	3.69107	2.71244	2.46504
SAN__123_0040.med	32836	3.81683	3.70164	2.71345	2.46882	2.42841	3.80631	3.69714	2.71234	2.46629
SAN__123_0042.med	33166	3.81927	3.69576	2.714	2.46955	2.42907	3.80868	3.70316	2.71317	2.46756
SAN__123_0044.med	33527	3.81947	3.68952	2.71548	2.47062	2.42929	3.81151	3.70426	2.71494	2.4683
SAN__123_0046.med	33848	3.82208	3.69039	2.71727	2.47218	2.43145	3.81428	3.70051	2.71713	2.4695
SAN__123_0048.med	34177	3.82396	3.69251	2.71938	2.47253	2.43122	3.81528	3.69727	2.71888	2.47084
SAN__123_0050.med	34501	3.82374	3.69515	2.72091	2.47347	2.4314	3.81534	3.69719	2.72113	2.47252
SAN__123_0052.med	34824	3.82214	3.69779	2.72129	2.4745	2.43208	3.81515	3.69526	2.7221	2.47385
SAN__123_0054.med	35155	3.82235	3.69774	2.72378	2.47556	2.4324	3.81613	3.69532	2.72465	2.47612
SAN__123_0056.med	35483	3.82446	3.70149	2.72556	2.47702	2.43418	3.81534	3.69348	2.7266	2.47852
SAN__123_0058.med	35816	3.82611	3.70332	2.72742	2.47845	2.43579	3.81712	3.69515	2.72952	2.48007
SAN__123_0060.med	36147	3.82985	3.70791	2.72893	2.47907	2.43887	3.8192	3.69769	2.73166	2.47976
SAN__123_0062.med	36471	3.83357	3.70808	2.73085	2.47962	2.4403	3.82168	3.70473	2.73397	2.48095

No. Peak	time(s)	Detector 1					Detector 2			
		(021)	(101)	(130)	(131)	(112)	(021)	(101)	(130)	(131)
SAN__123_0064.med	36801	3.83712	3.709	2.73294	2.48069	2.44212	3.82651	3.70299	2.73504	2.48285
SAN__123_0066.med	37141	3.85261	3.71246	2.73487	2.51238	2.47632	3.85231	3.70899	2.73787	2.51232
SAN__123_0068.med	37478	3.90505	3.73891	2.78052	2.52501	2.47639	3.8993	3.73192	2.77818	2.52436
SAN__123_0070.med	37799	3.91069	3.74251	2.78448	2.52865	2.47858	3.907	3.7363	2.7813	2.52734
SAN__123_0071.med	38150	3.91258	3.7433	2.78551	2.52876	2.47757	3.9098	3.73612	2.78146	2.52744
SAN__123_0073.med	38475	3.90727	3.74167	2.78229	2.52657	2.47608	3.9082	3.73709	2.77947	2.52513
SAN__123_0075.med	38801	3.90292	3.73624	2.77909	2.52396	2.47427	3.90178	3.73042	2.77631	2.5221
SAN__123_0077.med	39127	3.89676	3.73424	2.77537	2.5212	2.47288	3.89761	3.72674	2.77265	2.5193
SAN__123_0079.med	39460	3.89112	3.72681	2.77517	2.5176	2.47039	3.89467	3.72457	2.7681	2.51618
SAN__123_0081.med	39782	3.88466	3.72452	2.77083	2.5141	2.46865	3.89395	3.72354	2.76356	2.51254
SAN__123_0083.med	40111	3.87809	3.72071	2.76464	2.51086	2.46736	3.88101	3.72127	2.75874	2.50937
SAN__123_0085.med	40433	3.87156	3.7203	2.75921	2.5076	2.46557	3.87423	3.71835	2.75426	2.50648
SAN__123_0087.med	40755	3.86542	3.7157	2.75391	2.50465	2.46327	3.86871	3.71576	2.74976	2.5028
SAN__123_0089.med	41177	3.8625	3.71316	2.75052	2.50049	2.45995	3.86386	3.70577	2.74941	2.4985
SAN__123_0091.med	41507	3.86459	3.70915	2.74889	2.49777	2.45497	3.8615	3.69951	2.74922	2.49531
SAN__123_0093.med	41906	3.86303	3.70745	2.74434	2.49488	2.45304	3.85111	3.69346	2.74391	2.49113
SAN__123_0095.med	42230	3.86068	3.70408	2.7405	2.49267	2.45124	3.84662	3.69108	2.74078	2.48919
SAN__123_0097.med	42562	3.85695	3.70245	2.73818	2.49089	2.44913	3.84129	3.6857	2.73712	2.48685
SAN__123_0099.med	42883	3.82465	3.69349	2.72871	2.47804	2.43494	3.81763	3.67924	2.727	2.47632
SAN__123_0101.med	43208	3.8239	3.69214	2.7264	2.47638	2.4374	3.81605	3.67846	2.72517	2.47442
SAN__123_0103.med	43536	3.8205	3.6901	2.72575	2.47367	2.4363	3.81263	3.67369	2.72346	2.47194
SAN__123_0105.med	43860	3.81624	3.68646	2.72373	2.47162	2.43413	3.80924	3.67312	2.72119	2.46972
SAN__123_0107.med	44198	3.81231	3.68339	2.72195	2.46935	2.43273	3.80505	3.66894	2.71879	2.46739
SAN__123_0109.med	44532	3.80823	3.68422	2.72021	2.46714	2.43091	3.8027	3.6669	2.71686	2.46536
SAN__123_0111.med	44861	3.80507	3.68346	2.71886	2.46597	2.43025	3.8	3.66696	2.71487	2.46352

No. Peak	time(s)	Detector 1 (021)	(101)	(130)	(131)	(112)	Detector 2 (021)	(101)	(130)	(131)
SAN__123_0113.med	45186	3.80345	3.68264	2.71782	2.46474	2.43244	3.79711	3.66424	2.7132	2.46205
SAN__123_0115.med	45577	3.80806	3.68065	2.71422	2.46826	2.43109	3.80332	3.67456	2.70493	2.4591
SAN__123_0117.med	46069	3.80657	3.67979	2.71273	2.46671	2.42861	3.79964	3.67077	2.70367	2.45749
SAN__123_0119.med	46433	3.79368	3.66796	2.71296	2.45867	2.42498	3.78729	3.66044	2.70847	2.45752

(Continued)

Detector 3 (112)	(021)	(101)	(130)	(131)	(112)	Detector 4 (021)	(101)	(130)	(131)	(112)
2.45594	3.88335	3.72603	2.76805	2.51166	2.45827	3.87365	3.69151	2.76495	2.51077	2.45747
2.47906	3.96645	3.70402	2.75391	2.52033	2.46866	3.87121	3.66106	2.75391	2.51207	2.44513
2.47489	3.89256	3.74004	2.75634	2.52029	2.46938	3.89256	3.74004	2.75652	2.51478	2.44729
2.42955	3.87092	3.68074	2.76952	2.51204	2.46653	3.87092	3.69155	2.77429	2.48889	2.47039
2.43754	3.87864	3.7147	2.75592	2.53434	2.47205	3.88258	3.72716	2.75847	2.52176	2.45967
2.43309	3.88491	3.70731	2.75175	2.54239	2.47147	3.88898	3.71937	2.75587	2.52049	2.45753
2.41874	3.88733	3.72111	2.77277	2.52004	2.47819	3.89076	3.72193	2.75666	2.52191	2.45199
2.44862	3.90002	3.71555	2.76804	2.47425	2.43968	3.88582	3.71928	2.75672	2.51009	2.44935
2.42517	3.89397	3.71603	2.76261	2.52163	2.45657	3.8731	3.72314	2.75629	2.50887	2.45378
2.42191	3.89771	3.7163	2.76073	2.51108	2.45274	3.87032	3.72371	2.75523	2.5164	2.45691
2.42238	3.89713	3.70562	2.75913	2.50678	2.45093	3.87208	3.72659	2.75745	2.51311	2.45715
2.42023	3.8967	3.70711	2.75984	2.50284	2.44899	3.87328	3.72769	2.75775	2.51092	2.45694
2.42443	3.89674	3.71289	2.7637	2.49747	2.44533	3.87638	3.72958	2.75999	2.51611	2.46151
2.41772	3.87367	3.71571	2.75348	2.50803	2.44787	3.8729	3.71171	2.75774	2.50353	2.45498
2.42183	3.87184	3.70986	2.7542	2.50344	2.45028	3.87166	3.71089	2.75257	2.50789	2.45209
2.42047	3.87181	3.70877	2.75473	2.50335	2.45026	3.873	3.71191	2.75402	2.50808	2.4524

Detector 3					Detector 4					
(112)	(021)	(101)	(130)	(131)	(112)	(021)	(101)	(130)	(131)	(112)
2.42262	3.87414	3.70968	2.75561	2.5054	2.45155	3.87339	3.7093	2.75572	2.50852	2.45277
2.42273	3.87312	3.70918	2.75604	2.50629	2.45258	3.87321	3.71117	2.75609	2.50842	2.45331
2.42136	3.87633	3.71344	2.75794	2.50694	2.45325	3.87371	3.71414	2.7573	2.50938	2.45348
2.42384	3.87749	3.71863	2.75912	2.50779	2.45462	3.87546	3.71588	2.75806	2.51	2.45456
2.42221	3.87983	3.71779	2.75992	2.50893	2.45576	3.87824	3.71834	2.75887	2.51139	2.45663
2.42384	3.88286	3.71844	2.76128	2.50939	2.45665	3.88073	3.72058	2.75951	2.51098	2.45813
2.42491	3.88531	3.72079	2.76309	2.51024	2.45691	3.882	3.72154	2.76082	2.51141	2.46076
2.4275	3.88765	3.72023	2.76504	2.51047	2.45724	3.88433	3.72326	2.76213	2.51301	2.46265
2.42899	3.88855	3.72397	2.76718	2.51166	2.45739	3.88606	3.72527	2.7641	2.51482	2.46288
2.43118	3.89292	3.72648	2.76926	2.51391	2.45826	3.88897	3.72652	2.76609	2.51592	2.46252
2.43417	3.89521	3.72742	2.77131	2.5154	2.46005	3.89113	3.72754	2.76845	2.51737	2.46262
2.43542	3.89703	3.73044	2.77362	2.51787	2.46201	3.89256	3.724	2.77039	2.51794	2.46281
2.43437	3.89887	3.73517	2.77547	2.51924	2.46268	3.89361	3.72387	2.7731	2.51862	2.46312
2.43613	3.89759	3.73382	2.77685	2.52113	2.46413	3.89628	3.72394	2.77495	2.51928	2.46363
2.4381	3.9028	3.73626	2.77835	2.52183	2.46492	3.89854	3.72704	2.77703	2.52082	2.46481
2.44297	3.89917	3.73646	2.77986	2.52167	2.4665	3.8985	3.72899	2.77883	2.52162	2.46535
2.44457	3.90045	3.73999	2.7818	2.52207	2.46778	3.89905	3.73139	2.78106	2.52239	2.46611
2.44604	3.9004	3.74044	2.78376	2.52373	2.4697	3.90047	3.73326	2.78274	2.52416	2.46839
2.44468	3.90464	3.74347	2.78401	2.52433	2.47013	3.90198	3.73461	2.78471	2.52637	2.47123
2.47803	3.91984	3.75393	2.79446	2.53707	2.48299	3.91793	3.75107	2.79246	2.53633	2.47999
2.47454	3.93549	3.76712	2.79674	2.54455	2.49083	3.93793	3.76281	2.79879	2.54036	2.49028
2.47638	3.92939	3.76447	2.79589	2.5422	2.48913	3.93593	3.76272	2.79693	2.53897	2.4893
2.47623	3.93	3.75978	2.79521	2.54064	2.48765	3.93085	3.75725	2.79517	2.53779	2.4875
2.47481	3.93056	3.75806	2.79432	2.54009	2.48714	3.9288	3.75644	2.79421	2.53728	2.48717
2.47263	3.93119	3.75563	2.79312	2.53926	2.48703	3.92797	3.75536	2.79321	2.53695	2.48661

Detector 3					Detector 4					
(112)	(021)	(101)	(130)	(131)	(112)	(021)	(101)	(130)	(131)	(112)
2.47038	3.92833	3.75712	2.79315	2.53897	2.48684	3.92764	3.75582	2.79281	2.53676	2.48605
2.46792	3.92977	3.7568	2.79328	2.53903	2.48632	3.92771	3.75532	2.79303	2.53724	2.48614
2.46675	3.92855	3.75745	2.79499	2.53964	2.48658	3.92838	3.75649	2.79335	2.53751	2.48599
2.46607	3.92895	3.75917	2.79652	2.54001	2.48622	3.92951	3.75505	2.79407	2.53785	2.48569
2.46412	3.928	3.76005	2.79777	2.54042	2.48562	3.93023	3.75734	2.79473	2.53831	2.48514
2.4618	3.92928	3.76183	2.79891	2.54106	2.48463	3.93038	3.75577	2.79627	2.53891	2.48467
2.4603	3.92793	3.76277	2.79922	2.54058	2.48381	3.92703	3.75455	2.79968	2.53877	2.48371
2.45965	3.92218	3.75761	2.79891	2.54012	2.48415	3.92047	3.75411	2.80165	2.53884	2.48344
2.45031	3.92136	3.75636	2.79824	2.53869	2.48218	3.91962	3.75366	2.80152	2.53897	2.48211
2.44751	3.92117	3.75515	2.7974	2.53757	2.48063	3.92125	3.75285	2.80047	2.53814	2.48081
2.44379	3.92072	3.75453	2.79567	2.53581	2.47885	3.92009	3.75248	2.79897	2.53665	2.47907
2.43316	3.89904	3.72955	2.77622	2.51794	2.4677	3.89994	3.73045	2.77429	2.5192	2.46559
2.43204	3.90167	3.72973	2.77512	2.51664	2.46683	3.89844	3.73149	2.77346	2.51874	2.46479
2.42832	3.89774	3.73367	2.76907	2.51316	2.46253	3.89702	3.7324	2.77013	2.51389	2.46501
2.42833	3.89683	3.72858	2.76878	2.51341	2.4621	3.89636	3.73186	2.76997	2.51367	2.46487
2.42693	3.89923	3.72761	2.76875	2.51339	2.46165	3.89577	3.73047	2.76955	2.51336	2.46442
2.42421	3.89424	3.7285	2.76779	2.51329	2.46097	3.89546	3.73005	2.76896	2.51269	2.46374
2.42458	3.89385	3.72904	2.76732	2.51203	2.45992	3.89469	3.72961	2.76812	2.51192	2.46325
2.42399	3.89352	3.72913	2.76643	2.5112	2.45943	3.89409	3.72952	2.76686	2.51061	2.46242
2.41689	3.89198	3.72898	2.76717	2.51627	2.45967	3.89008	3.72344	2.76821	2.51266	2.45751
2.4175	3.89024	3.72879	2.7663	2.51492	2.45894	3.88798	3.72369	2.76669	2.51155	2.45675
2.42219	3.88679	3.72517	2.76169	2.50672	2.45601	3.88986	3.72838	2.76123	2.50686	2.45986

(Continued)

τ(GPa) (021)	(101)	(130)	(131)	(112)	τ(GPa) (average)	P(Gpa)	Strain%	T(K)
-0.11	-0.36	-0.11	-0.39	0.00	-0.19			298
1.76	-2.02	-1.05	-0.79	-1.43	-0.71	1.83		674
1.10	1.18	-0.56	-0.50	-0.97	0.05	1.94	0.00%	673
1.30	0.29	2.56	0.98	2.52	1.53	0.94	2.16%	675
1.99	4.19	1.65	3.02	2.43	2.66	3.68	2.27%	672
2.51	1.05	1.43	3.42	2.56	2.20	3.71	4.11%	672
2.72	2.82	2.30	3.16	3.02	2.80	3.91	6.39%	671
2.97	2.76	2.73	0.94	0.85	2.05	3.69	7.90%	672
3.10	3.24	2.76	2.98	2.11	2.84	5.09	8.98%	673
3.19	2.22	2.80	2.84	2.16	2.64	5.29	10.06%	673
3.20	1.81	2.82	2.49	2.08	2.48	5.26	14.39%	671
3.15	1.69	2.85	2.35	2.11	2.43	5.23	14.94%	673
3.27	1.99	3.08	2.33	1.86	2.51	4.81	14.50%	675
2.93	1.70	2.59	2.41	2.00	2.33	5.56	17.75%	692
2.96	1.70	2.35	2.28	1.87	2.23	5.76	21.10%	713
2.97	1.68	2.42	2.31	1.93	2.26	5.80	31.17%	733
3.02	1.73	2.48	2.38	1.91	2.30	5.78	30.41%	758
2.91	1.60	2.48	2.40	1.92	2.26	5.80	30.84%	773
2.92	1.74	2.55	2.52	1.95	2.34	5.78	30.84%	798
2.78	1.55	2.59	2.57	1.89	2.28	5.79	31.28%	843
2.64	1.45	2.60	2.66	2.00	2.27	5.87	31.93%	873
2.66	1.20	2.69	2.61	2.05	2.24		31.06%	903
2.62	1.03	2.75	2.57	2.10	2.22		31.71%	933

τ(GPa) (021)	(101)	(130)	(131)	(112)	τ(GPa) (average)	P(Gpa)	Strain%	T(K)
2.61	1.06	2.79	2.57	2.06	2.22	5.82	32.14%	963
2.60	1.32	2.81	2.59	2.01	2.27		32.03%	993
2.62	1.47	2.80	2.60	1.89	2.28		32.36%	1023
2.65	1.54	2.81	2.63	1.85	2.30		33.12%	1048
2.70	1.47	2.81	2.64	1.87	2.30	5.51	33.55%	1073
2.78	1.56	2.89	2.62	1.92	2.35		33.77%	1103
2.79	1.53	2.83	2.59	1.91	2.33		34.31%	1138
2.89	1.61	2.81	2.54	1.85	2.34		34.96%	1163
2.76	1.58	2.77	2.47	1.70	2.25		35.39%	1193
2.69	1.54	2.77	2.49	1.61	2.22		35.82%	1213
2.59	1.42	2.74	2.53	1.65	2.19		36.80%	1243
2.54	1.54	2.71	2.52	1.73	2.21	4.66	36.80%	1263
2.30	1.92	3.04	1.36	0.26	1.78	3.93	37.77%	1363
1.16	1.33	0.95	0.98	0.91	1.07		43.29%	1398
0.80	1.09	0.70	0.69	0.71	0.80		44.16%	1418
0.64	0.85	0.60	0.61	0.65	0.67		45.78%	1383
0.74	0.81	0.69	0.71	0.71	0.73		46.32%	1348
0.92	1.01	0.80	0.83	0.81	0.88		46.65%	1323
1.04	1.18	0.99	0.98	0.90	1.02	1.91	46.97%	1283
1.21	1.39	1.12	1.18	1.04	1.19		47.19%	1253
1.33	1.50	1.41	1.41	1.14	1.36		47.51%	1223
1.69	1.65	1.76	1.61	1.18	1.58		47.51%	1193
1.92	1.80	2.07	1.81	1.26	1.77		48.16%	1163
2.14	1.97	2.40	2.03	1.36	1.98	1.60	48.16%	1143
2.20	2.26	2.59	2.25	1.46	2.15		48.59%	1103

τ(GPa) (021)	(101)	(130)	(131)	(112)	τ(GPa) (average)	P(Gpa)	Strain%	T(K)
2.01	2.37	2.68	2.41	1.64	2.22	1.03	48.81%	1073
2.19	2.52	2.93	2.59	1.90	2.42		48.59%	1033
2.34	2.61	3.07	2.65	1.96	2.53		49.13%	1003
2.47	2.75	3.16	2.69	2.04	2.62	1.52	49.03%	973
2.80	2.07	2.59	2.42	2.09	2.40	3.70	49.03%	933
2.86	2.15	2.66	2.48	2.00	2.43	3.56	52.49%	903
2.90	2.42	2.48	2.41	2.03	2.45	3.77	52.49%	873
3.02	2.40	2.59	2.54	2.08	2.53	3.66	52.49%	843
3.20	2.52	2.70	2.67	2.15	2.65		52.71%	813
3.23	2.56	2.76	2.78	2.26	2.72		52.92%	783
3.32	2.58	2.82	2.81	2.22	2.75		53.03%	763
3.39	2.67	2.84	2.83	2.12	2.77		53.25%	733
3.09	2.32	3.24	3.02	2.26	2.79		53.46%	703
3.13	2.44	3.26	3.04	2.28	2.83	4.26	53.03%	673
3.58	3.00	2.85	2.93	2.25	2.92		54.00%	633

Table D-9 Data table for San131.

No.	Time(s)	Detector 1					Detector 2		
Peak		(021)	(101)	(130)	(131)	(112)	(021)	(101)	(130)
SAN_131_0003.med		3.88824	3.72446	2.77322	2.51643	2.46285	3.88529	3.72976	2.77058
SAN_131_0009.med	14700	3.80643	3.67484	2.71919	2.46263	2.42288	3.80773	3.67974	2.7116
SAN_131_0010.med	15150	3.80279	3.67609	2.71804	2.46046	2.4201	3.80632	3.68169	2.70863
SAN_131_0011.med	15595	3.79638	3.67745	2.71521	2.45926	2.42326	3.82226	3.6877	2.71391
SAN_131_0012.med	15917	3.79505	3.68187	2.71377	2.45913	2.42302	3.80744	3.68538	2.71648
SAN_131_0013.med	16233	3.79338	3.67871	2.71504	2.45778	2.4205	3.8018	3.68262	2.71724
SAN_131_0014.med	16550	3.79057	3.67745	2.7149	2.45763	2.42286	3.79971	3.67677	2.71689
SAN_131_0015.med	16866	3.79116	3.68072	2.7128	2.45674	2.42333	3.79904	3.67433	2.71668
SAN_131_0016.med	17183	3.79456	3.67895	2.71239	2.45872	2.42589	3.79773	3.67436	2.71553
SAN_131_0017.med	17499	3.79484	3.67711	2.71185	2.45945	2.42454	3.79972	3.67474	2.71532
SAN_131_0018.med	17816	3.79396	3.6757	2.71214	2.46029	2.42363	3.8012	3.67477	2.71471
SAN_131_0019.med	18133	3.7926	3.67624	2.71193	2.46159	2.42272	3.80062	3.67299	2.71464
SAN_131_0020.med	18449	3.79055	3.67668	2.71195	2.46077	2.42079	3.80077	3.67103	2.71429
SAN_131_0021.med	18766	3.78817	3.67797	2.71095	2.46043	2.42134	3.7981	3.67043	2.71227
SAN_131_0022.med	19082	3.78879	3.67616	2.70983	2.46088	2.42354	3.79103	3.67286	2.71044
SAN_131_0023.med	19399	3.789	3.67849	2.70947	2.45947	2.42173	3.79038	3.67218	2.70987
SAN_131_0024.med	19715	3.7886	3.67765	2.70936	2.45903	2.42081	3.79011	3.67324	2.71001
SAN_131_0025.med	20032	3.78918	3.67708	2.7096	2.4601	2.42188	3.79028	3.67492	2.70973
SAN_131_0026.med	20348	3.78913	3.67821	2.70952	2.45946	2.42226	3.78848	3.67651	2.71005
SAN_131_0027.med	20664	3.7898	3.68024	2.70932	2.46127	2.42356	3.78691	3.67955	2.71067
SAN_131_0028.med	20981	3.79084	3.6813	2.70951	2.46133	2.4238	3.78741	3.6786	2.71147
SAN_131_0029.med	21297	3.79093	3.68228	2.71017	2.46193	2.42446	3.78918	3.68123	2.7116
SAN_131_0030.med	21614	3.79381	3.68315	2.711	2.4622	2.42544	3.78881	3.68189	2.71202
SAN_131_0031.med	21930	3.79481	3.68368	2.71124	2.46256	2.42657	3.78932	3.68224	2.71269

No. Peak	Time(s)	Detector 1					Detector 2		
		(021)	(101)	(130)	(131)	(112)	(021)	(101)	(130)
SAN_131_0032.med	22247	3.79714	3.68384	2.71196	2.46239	2.42712	3.78972	3.68306	2.71346
SAN_131_0033.med	22563	3.79798	3.68247	2.71282	2.46306	2.42804	3.79056	3.68278	2.7137
SAN_131_0034.med	22880	3.79828	3.68099	2.71325	2.46402	2.42636	3.79128	3.68234	2.71437
SAN_131_0035.med	23196	3.79923	3.67996	2.71364	2.4645	2.42601	3.79385	3.68255	2.71423
SAN_131_0036.med	23513	3.80183	3.68249	2.71448	2.46506	2.42769	3.79561	3.68322	2.71438
SAN_131_0037.med	23829	3.80266	3.68382	2.71493	2.46539	2.42927	3.79827	3.68441	2.7155
SAN_131_0038.med	24146	3.80401	3.68363	2.71592	2.46575	2.42926	3.79895	3.68461	2.71676
SAN_131_0039.med	24462	3.80356	3.68685	2.71703	2.46655	2.43103	3.80122	3.68656	2.71806
SAN_131_0040.med	24779	3.80448	3.68429	2.71835	2.46745	2.43041	3.80291	3.6869	2.71873
SAN_131_0041.med	25096	3.80458	3.68448	2.71854	2.46774	2.42858	3.80356	3.68737	2.71937
SAN_131_0044.med	27291	3.80771	3.68989	2.71999	2.46854	2.431	3.79248	3.67416	2.71238
SAN_131_0045.med	27607	3.8099	3.6921	2.72079	2.47	2.43216	3.79364	3.6738	2.71301
SAN_131_0046.med	27924	3.8117	3.69214	2.72215	2.47087	2.43174	3.79424	3.67502	2.71394
SAN_131_0047.med	28241	3.81356	3.69554	2.72348	2.47188	2.43314	3.79631	3.67568	2.71498
SAN_131_0048.med	28557	3.81478	3.69059	2.7245	2.47242	2.43429	3.80114	3.6811	2.71713
SAN_131_0049.med	28873	3.81762	3.69412	2.72517	2.47317	2.43578	3.8039	3.6827	2.71938
SAN_131_0050.med	29190	3.81883	3.69474	2.72607	2.47447	2.43825	3.8079	3.68346	2.72146
SAN_131_0051.med	29506	3.82383	3.69636	2.72703	2.4756	2.44306	3.81043	3.68393	2.7228
SAN_131_0052.med	29823	3.82576	3.69437	2.72904	2.47793	2.4458	3.81468	3.686	2.72411
SAN_131_0053.med	30140	3.83086	3.69696	2.72996	2.47942	2.44682	3.81682	3.68632	2.72553
SAN_131_0054.med	30456	3.83406	3.69895	2.73202	2.48025	2.44759	3.82075	3.68836	2.72676
SAN_131_0055.med	30773	3.8367	3.69972	2.73363	2.48282	2.44632	3.82452	3.68925	2.72841
SAN_131_0056.med	31089	3.84029	3.69841	2.73559	2.48512	2.45108	3.82905	3.6907	2.73052
SAN_131_0057.med	31406	3.84226	3.70271	2.73748	2.48589	2.45191	3.83223	3.6924	2.7336
SAN_131_0058.med	31723	3.84555	3.70415	2.73994	2.48918	2.45707	3.83537	3.69558	2.7366

No. Peak	Time(s)	Detector 1 (021)	(101)	(130)	(131)	(112)	Detector 2 (021)	(101)	(130)
SAN_131_0059.med	32039	3.84965	3.70641	2.74301	2.49202	2.45673	3.83988	3.69718	2.73934
SAN_131_0060.med	32356	3.85191	3.7122	2.74671	2.49519	2.46036	3.84354	3.70079	2.74289
SAN_131_0061.med	32672	3.8586	3.71562	2.7512	2.4974	2.45911	3.84798	3.70556	2.74641
SAN_131_0062.med	32989	3.86384	3.71841	2.75456	2.50012	2.46028	3.85408	3.70701	2.75009
SAN_131_0063.med	33306	3.86842	3.72029	2.75807	2.50308	2.4608	3.86093	3.71011	2.75378
SAN_131_0064.med	33622	3.87428	3.72336	2.76106	2.50614	2.46225	3.86765	3.7134	2.75732
SAN_131_0065.med	33938	3.87694	3.72422	2.76461	2.50911	2.4636	3.87317	3.71659	2.76077
SAN_131_0066.med	34255	3.882	3.72867	2.76677	2.51162	2.46449	3.87743	3.71919	2.76316
SAN_131_0067.med	34571	3.88498	3.72797	2.76761	2.51342	2.46488	3.87859	3.72011	2.76441
SAN_131_0068.med	34888	3.88156	3.72599	2.76618	2.51196	2.46303	3.87638	3.7189	2.76295
SAN_131_0069.med	35204	3.879	3.72387	2.76365	2.50952	2.46105	3.87178	3.71625	2.76053
SAN_131_0070.med	35521	3.87683	3.72248	2.76035	2.50704	2.45894	3.86861	3.71207	2.75738
SAN_131_0071.med	35838	3.8704	3.72059	2.75711	2.50455	2.45754	3.86342	3.70816	2.75363
SAN_131_0072.med	36154	3.86486	3.71747	2.75314	2.50133	2.45457	3.858	3.70393	2.7499
SAN_131_0073.med	36470	3.85934	3.71586	2.74914	2.49785	2.45209	3.85242	3.70061	2.74538
SAN_131_0074.med	36787	3.85318	3.7127	2.74517	2.49498	2.45068	3.84668	3.69681	2.74102
SAN_131_0075.med	37103	3.84826	3.70919	2.74098	2.49119	2.44775	3.84166	3.69382	2.73791
SAN_131_0076.med	37420	3.84498	3.70765	2.73947	2.48969	2.44681	3.83923	3.69318	2.73671
SAN_131_0077.med	37737	3.84569	3.70563	2.73904	2.48895	2.4454	3.83852	3.6925	2.73597
SAN_131_0078.med	38053	3.84341	3.70482	2.73871	2.4886	2.44583	3.83766	3.69182	2.7356
SAN_131_0079.med	38369	3.84273	3.70302	2.73719	2.48742	2.44455	3.83616	3.69025	2.73417
SAN_131_0080.med	38686	3.83728	3.70084	2.73432	2.48501	2.44271	3.8319	3.68626	2.73144
SAN_131_0081.med	39003	3.8344	3.69668	2.73088	2.48172	2.43979	3.82643	3.68501	2.72833
SAN_131_0082.med	39319	3.82768	3.69646	2.72783	2.47872	2.43709	3.82167	3.68078	2.72516
SAN_131_0083.med	39635	3.82391	3.69611	2.72686	2.47729	2.43302	3.81918	3.68163	2.72417

(Continued)

Detector 3					Detector 4					
(131)	(112)	(021)	(101)	(130)	(131)	(112)	(021)	(101)	(130)	(131)
2.51701	2.46285	3.89585	3.73622	2.77286	2.51436	2.46344	3.88868	3.72281	2.77106	2.51673
2.47936	2.42496	3.88464	3.73124	2.76123	2.51374	2.45117	3.89141	3.73193	2.77905	2.51902
2.47056	2.42508	3.88184	3.73297	2.76815	2.51219	2.45312	3.88934	3.72841	2.78023	2.51892
2.46252	2.42024	3.88386	3.73337	2.76872	2.51165	2.45767	3.88395	3.72294	2.77575	2.51597
2.46256	2.42343	3.88543	3.7304	2.77226	2.51205	2.45777	3.88487	3.71658	2.77111	2.51457
2.46318	2.42457	3.88782	3.72969	2.7766	2.5101	2.45781	3.88592	3.71616	2.77003	2.51355
2.46221	2.42325	3.88861	3.73024	2.77641	2.50922	2.45862	3.88532	3.71716	2.76892	2.5127
2.46193	2.42616	3.88941	3.72998	2.77532	2.51139	2.45939	3.8858	3.71554	2.7691	2.51275
2.46128	2.42614	3.89061	3.72404	2.77292	2.51197	2.45923	3.88888	3.70829	2.7693	2.51214
2.46227	2.42649	3.89072	3.71458	2.7726	2.51214	2.45942	3.89031	3.70807	2.77021	2.51171
2.46116	2.42654	3.89148	3.72172	2.77102	2.51335	2.45997	3.89106	3.70551	2.77082	2.51209
2.46105	2.42739	3.89153	3.71507	2.77046	2.51226	2.4599	3.89171	3.70595	2.77121	2.51236
2.45969	2.42689	3.89248	3.7219	2.77062	2.51343	2.45986	3.8931	3.70818	2.7713	2.51238
2.45956	2.42457	3.8893	3.71817	2.76714	2.51075	2.45786	3.8948	3.7067	2.76904	2.51197
2.45862	2.42572	3.88707	3.71097	2.76662	2.51068	2.45693	3.89474	3.70496	2.76756	2.5121
2.45871	2.42619	3.88816	3.71578	2.76782	2.51136	2.45765	3.89598	3.70838	2.76843	2.51205
2.45774	2.42166	3.88929	3.71237	2.76954	2.51278	2.45893	3.89749	3.709	2.76927	2.51099
2.45962	2.42581	3.89004	3.71874	2.77038	2.51258	2.45922	3.89802	3.71241	2.77095	2.51102
2.45977	2.42353	3.88925	3.71789	2.77252	2.51299	2.45935	3.89822	3.71829	2.77246	2.51197
2.46014	2.42316	3.89055	3.71622	2.77351	2.51479	2.4608	3.89824	3.72233	2.77356	2.51275
2.46129	2.42493	3.89226	3.72024	2.77499	2.51457	2.4601	3.89862	3.72738	2.77508	2.51305
2.46045	2.42171	3.8927	3.72516	2.77604	2.51542	2.45941	3.89949	3.72653	2.7763	2.51351
2.46072	2.41919	3.89392	3.72645	2.77685	2.51568	2.45821	3.90011	3.72735	2.77789	2.51474
2.46104	2.42057	3.89561	3.73179	2.77839	2.51653	2.459	3.90062	3.72766	2.77984	2.51628

Detector 3					Detector 4					
(131)	(112)	(021)	(101)	(130)	(131)	(112)	(021)	(101)	(130)	(131)
2.46132	2.42219	3.89572	3.73313	2.77991	2.51907	2.46048	3.90155	3.73176	2.78102	2.51729
2.46206	2.42348	3.89637	3.73273	2.7814	2.51956	2.46143	3.90249	3.73254	2.78128	2.51829
2.463	2.42637	3.89886	3.73414	2.78113	2.51955	2.46177	3.90367	3.73567	2.782	2.51889
2.46335	2.42314	3.8998	3.73555	2.78089	2.52097	2.46291	3.90502	3.73761	2.78205	2.51962
2.4641	2.42673	3.8999	3.7374	2.77974	2.52212	2.46307	3.90557	3.73589	2.78172	2.52049
2.46402	2.42756	3.90228	3.73221	2.77967	2.52155	2.46321	3.90617	3.73774	2.78216	2.52108
2.46465	2.42936	3.90216	3.73615	2.78061	2.52216	2.46408	3.90569	3.73603	2.78208	2.52159
2.4661	2.43459	3.90272	3.73756	2.78115	2.52152	2.46439	3.90615	3.73674	2.78152	2.52255
2.46691	2.43014	3.90407	3.7387	2.78203	2.52183	2.465	3.90674	3.73661	2.78303	2.52324
2.46748	2.42869	3.90403	3.73936	2.78209	2.52237	2.46483	3.90746	3.73744	2.78353	2.52416
2.46013	2.42405	3.90671	3.73536	2.77991	2.52464	2.46725	3.90445	3.73603	2.78322	2.5254
2.4608	2.425	3.90741	3.73743	2.77947	2.52517	2.46772	3.90386	3.73564	2.78358	2.52623
2.46099	2.42542	3.90767	3.74015	2.77973	2.52548	2.46787	3.9043	3.73643	2.78418	2.52597
2.46187	2.42664	3.90801	3.73825	2.77983	2.52572	2.46759	3.90488	3.73737	2.78462	2.5256
2.46322	2.42648	3.90678	3.73733	2.78042	2.52669	2.46858	3.90422	3.73743	2.78487	2.52613
2.46799	2.43256	3.90718	3.72951	2.78045	2.52609	2.46873	3.90268	3.7391	2.78494	2.52679
2.46907	2.43373	3.90507	3.73927	2.78086	2.52734	2.46959	3.90069	3.73961	2.78512	2.5269
2.47374	2.43803	3.90657	3.73558	2.78004	2.52764	2.47021	3.90017	3.73971	2.78437	2.52749
2.47542	2.43908	3.90376	3.73898	2.78023	2.52728	2.47073	3.89952	3.74135	2.78447	2.52764
2.47675	2.44112	3.90506	3.74032	2.78048	2.52712	2.47128	3.89958	3.74074	2.78414	2.52716
2.47892	2.44353	3.90522	3.73753	2.781	2.52748	2.47171	3.89927	3.7392	2.78443	2.52714
2.48073	2.44512	3.90166	3.74039	2.78111	2.52702	2.4722	3.89749	3.73992	2.7844	2.52691
2.48238	2.44662	3.90032	3.73988	2.78147	2.52656	2.47248	3.89847	3.74012	2.78428	2.52652
2.48448	2.44752	3.90067	3.74019	2.78132	2.5261	2.47278	3.89686	3.73895	2.78381	2.52649
2.48733	2.45067	3.8997	3.74106	2.7815	2.52542	2.47282	3.89739	3.73849	2.78315	2.52622

Detector 3					Detector 4					
(131)	(112)	(021)	(101)	(130)	(131)	(112)	(021)	(101)	(130)	(131)
2.4899	2.45353	3.90056	3.74129	2.78157	2.52497	2.4727	3.8963	3.73883	2.78229	2.52507
2.4925	2.45423	3.89689	3.73776	2.78029	2.52469	2.47285	3.89521	3.73585	2.78143	2.52406
2.49558	2.457	3.8964	3.73604	2.77914	2.5238	2.47288	3.89545	3.73606	2.78025	2.52354
2.49831	2.45744	3.89279	3.73342	2.77756	2.52266	2.47301	3.89552	3.73566	2.77922	2.52296
2.50138	2.4591	3.89944	3.73426	2.77748	2.52177	2.4729	3.89585	3.73472	2.77868	2.52261
2.50451	2.4605	3.89796	3.73578	2.77744	2.52164	2.47298	3.89694	3.73594	2.77896	2.5225
2.50705	2.45969	3.89791	3.73697	2.77704	2.52217	2.47338	3.89778	3.73645	2.77905	2.52279
2.50967	2.46112	3.89985	3.73915	2.77723	2.52237	2.47349	3.89976	3.73823	2.77941	2.52304
2.51081	2.46209	3.8973	3.73618	2.77641	2.52302	2.47339	3.89943	3.73627	2.77924	2.52328
2.50901	2.46189	3.89701	3.73765	2.77595	2.5231	2.47297	3.89834	3.73674	2.77866	2.52295
2.50711	2.45897	3.89708	3.73642	2.77565	2.52289	2.47228	3.89816	3.73573	2.77863	2.52298
2.50446	2.45723	3.89839	3.73506	2.776	2.52302	2.47205	3.89753	3.73443	2.77902	2.52308
2.50056	2.45394	3.89793	3.73752	2.77626	2.52336	2.47205	3.89807	3.7361	2.77949	2.52355
2.49746	2.45222	3.90013	3.73834	2.77751	2.52419	2.47188	3.89856	3.73595	2.78019	2.52432
2.49419	2.45012	3.90073	3.73886	2.77864	2.52463	2.47185	3.89982	3.73606	2.78149	2.5251
2.4904	2.44708	3.90197	3.73923	2.78054	2.52545	2.47155	3.90042	3.73695	2.78247	2.52592
2.48717	2.44434	3.90375	3.74005	2.78178	2.52651	2.47126	3.90161	3.73622	2.78359	2.52658
2.48579	2.44329	3.90452	3.73747	2.78183	2.52642	2.47088	3.90237	3.73528	2.78348	2.52645
2.48503	2.44196	3.90188	3.74031	2.78152	2.52574	2.47011	3.90102	3.73509	2.78293	2.5259
2.48483	2.44198	3.90075	3.73837	2.78097	2.52548	2.46974	3.89991	3.73353	2.78241	2.52546
2.48356	2.44101	3.89954	3.73747	2.78047	2.52533	2.46942	3.89987	3.73311	2.78224	2.52542
2.48083	2.43908	3.90142	3.74063	2.78078	2.52542	2.46947	3.90066	3.73478	2.7823	2.5256
2.47853	2.43716	3.90228	3.7398	2.78036	2.52573	2.46929	3.90151	3.73413	2.78241	2.52565
2.47532	2.43358	3.90151	3.73799	2.78003	2.52516	2.46856	3.90184	3.73333	2.7818	2.52555
2.47483	2.43398	3.90614	3.74172	2.78054	2.5261	2.46865	3.90082	3.73324	2.78199	2.52546

(Continued)

(112)	τ(GPa) (021)	(101)	(130)	(131)	(112)	τ(GPa) (average)	P(GPa)	Strain Strain%	T(K)
2.46048	0.19	0.11	0.00	-0.07	-0.06	0.04	0		298
2.44362	2.94	2.58	3.03	2.68	1.56	2.56	5.79	4.31%	673
2.44622	2.95	2.46	3.36	2.96	1.79	2.71	5.16	5.35%	673
2.44979	2.72	2.17	3.19	3.15	2.11	2.67	4.62	5.99%	673
2.4529	3.06	1.90	3.13	3.13	2.11	2.67	4.38	6.78%	673
2.45694	3.26	2.02	3.15	3.07	2.28	2.76	3.69	7.74%	673
2.46064	3.36	2.23	3.13	3.05	2.39	2.83	3.40		673
2.46028	3.38	2.17	3.18	3.15	2.29	2.83	3.58		673
2.4599	3.41	1.90	3.16	3.11	2.19	2.75	3.81	9.50%	673
2.45771	3.39	1.71	3.20	3.05	2.16	2.70	3.95		673
2.45674	3.41	1.85	3.19	3.10	2.17	2.74	4.16		673
2.45621	3.46	1.74	3.19	3.04	2.16	2.72	4.20	11.65%	673
2.45563	3.53	1.99	3.20	3.14	2.22	2.82	4.28	12.05%	673
2.45249	3.60	1.85	3.14	3.07	2.12	2.76	4.84	13.89%	673
2.45004	3.69	1.63	3.18	3.09	1.90	2.69	5.13	14.29%	691
2.4504	3.73	1.78	3.26	3.14	1.98	2.78	5.01	14.60%	707
2.45084	3.79	1.71	3.32	3.20	2.21	2.85		14.76%	727
2.45225	3.80	1.91	3.39	3.10	2.09	2.86		15.08%	744
2.45517	3.82	1.96	3.47	3.16	2.25	2.93		15.64%	760
2.45716	3.86	1.89	3.52	3.16	2.33	2.95	4.78	16.04%	777
2.45832	3.87	2.10	3.56	3.12	2.27	2.99		16.44%	795
2.45965	3.85	2.10	3.60	3.17	2.38	3.02		16.92%	809
2.46045	3.84	2.11	3.62	3.19	2.42	3.04		17.48%	833
2.46066	3.84	2.22	3.69	3.24	2.37	3.07		17.88%	853

(112)	τ(GPa) (021)	(101)	(130)	(131)	(112)	τ(GPa) (average)	P(GPa)	Strain Strain%	T(K)
2.46035	3.81	2.32	3.71	3.33	2.33	3.10	4.65		873
2.45981	3.80	2.37	3.73	3.33	2.27	3.10			883
2.45951	3.84	2.52	3.71	3.29	2.23	3.12		18.83%	898
2.45959	3.82	2.62	3.69	3.32	2.39	3.17			918
2.46045	3.74	2.54	3.63	3.34	2.24	3.10			933
2.4623	3.73	2.40	3.59	3.33	2.22	3.06		20.59%	953
2.46436	3.68	2.45	3.55	3.33	2.26	3.05	4.99		968
2.46547	3.66	2.38	3.48	3.27	2.07	2.97		20.91%	983
2.46598	3.65	2.45	3.49	3.24	2.27	3.02		21.55%	993
2.46678	3.64	2.47	3.48	3.26	2.40	3.05		21.95%	1003
2.46954	3.79	2.54	3.57	3.55	2.63	3.22		24.66%	1013
2.47005	3.72	2.53	3.53	3.52	2.59	3.18		24.98%	1033
2.47049	3.69	2.58	3.48	3.49	2.61	3.17		25.62%	1043
2.47074	3.63	2.46	3.43	3.43	2.52	3.10		26.02%	1063
2.47097	3.49	2.43	3.36	3.42	2.53	3.04	5.35	26.50%	1073
2.47144	3.37	2.17	3.28	3.25	2.30	2.87		27.06%	1093
2.47187	3.20	2.37	3.21	3.22	2.22	2.84		27.45%	1108
2.4723	3.08	2.23	3.11	3.06	1.95	2.69		27.93%	1123
2.47246	2.91	2.35	3.02	2.94	1.85	2.61		28.49%	1138
2.47234	2.80	2.29	2.96	2.84	1.76	2.53		29.21%	1153
2.47292	2.66	2.10	2.89	2.76	1.69	2.42		29.61%	1168
2.47306	2.46	2.14	2.80	2.61	1.70	2.34	5.19	30.25%	1173
2.47285	2.30	2.13	2.69	2.47	1.50	2.22		30.81%	1193
2.47291	2.19	1.97	2.54	2.37	1.46	2.10		31.52%	1208
2.47317	2.06	1.87	2.37	2.16	1.20	1.93		32.08%	1223

(112)	τ(GPa) (021)	(101)	(130)	(131)	(112)	τ(GPa) (average)	P(GPa)	Strain Strain%	T(K)
2.47331	1.90	1.79	2.19	1.96	1.12	1.79		32.48%	1233
2.47319	1.71	1.42	1.94	1.75	0.99	1.56		33.28%	1253
2.47343	1.51	1.19	1.66	1.56	0.95	1.37	5.12	34.08%	1273
2.47306	1.24	1.02	1.40	1.35	0.89	1.18		34.88%	1293
2.4728	1.16	0.90	1.19	1.14	0.81	1.04		35.43%	1303
2.4727	0.93	0.81	1.02	0.96	0.72	0.89		36.31%	1323
2.4731	0.80	0.76	0.82	0.82	0.72	0.78		37.27%	1343
2.47385	0.70	0.68	0.71	0.69	0.68	0.69	5.28	38.15%	1353
2.47377	0.58	0.57	0.63	0.63	0.63	0.61		39.03%	1333
2.47292	0.65	0.68	0.68	0.71	0.66	0.68		39.66%	1303
2.47262	0.78	0.74	0.80	0.83	0.78	0.79	5.10	40.22%	1273
2.47231	0.88	0.81	1.00	0.99	0.88	0.91		40.46%	1253
2.47203	1.09	1.05	1.21	1.20	1.02	1.11		40.54%	1223
2.47189	1.33	1.23	1.47	1.42	1.16	1.32		40.70%	1193
2.47198	1.56	1.36	1.76	1.65	1.31	1.53	4.84	40.94%	1173
2.4718	1.81	1.56	2.06	1.89	1.44	1.75		41.18%	1143
2.47135	2.04	1.71	2.33	2.15	1.60	1.96		41.26%	1113
2.47079	2.17	1.69	2.40	2.23	1.63	2.02		41.66%	1093
2.47027	2.10	1.81	2.41	2.24	1.68	2.05	4.47	41.58%	1063
2.46967	2.12	1.77	2.40	2.23	1.64	2.03		41.58%	1043
2.46955	2.14	1.82	2.47	2.30	1.70	2.08		41.58%	1013
2.46958	2.36	2.07	2.63	2.46	1.82	2.27	4.31	41.82%	983
2.46919	2.54	2.17	2.81	2.64	1.96	2.42			953
2.46861	2.74	2.22	2.96	2.80	2.13	2.57			903
2.46864	2.92	2.29	3.03	2.89	2.25	2.67	4.27	41.74%	893